Universitat Autònoma de Barcelona

Computational Study of the Properties of Cu-Peptide Complexes Relevant to Alzheimer's Diseases

Andrea Mirats Arce

Universitat Autònoma de Barcelona

Computational Study of the Properties of Cu-Peptide Complexes Relevant to Alzheimer's Diseases

Andrea Mirats Arce

Tesi Doctoral

Estudi de Doctorat en Química

Directors:

Mariona Sodupe Roure

Luis Rodríguez Santiago

Departament de Química

Facultat de Ciències

2016

Universitat Autònoma de Barcelona

Departament de Química

Unitat de Química Física

Memòria presentada per aspirar al Grau de Doctor per Andrea Mirats Arce,

Andrea Mirats Arce

Vist i plau,

Mariona Sodupe Roure **Luis Rodríguez Santiago**

Bellaterra, 18 de Novembre de 2016

Als meus pares i parella

Preface

Alzheimer's disease is a neurodegenerative disorder characterized by progressive cognitive and memory impairment. One of its main hallmarks is the presence of extracellular deposits of the amyloid-beta peptide (Aβ), in which metal cations have been shown to play an important role. In particular, the interaction of the redox active Cu^{2+} metal cation with Aβ has been found to interfere in amyloid aggregation and to lead to reactive oxygen species (ROS). Thus, a detailed knowledge of the structure of Cu-$A\beta_{1-16}$ complexes is essential to get a better understanding of this critical process. In the last decade many conflicting coordination spheres on the Cu^{2+}-Aβ complexes have been proposed, but the structure of these complexes is still disputed and highly pH dependent.

The present thesis is structured in seven chapters. Chapter 1 introduces the AD framework in which the thesis is located, pointing out the importance of the presence of metal ions in the Aβ deposits and its role in the ROS formation, as well as the most relevant treatments used until now. Then, Chapter 2 introduces the goals that this thesis aims. After that, Chapter 3 overviews the general theoretical aspects behind it, such as electronic structure with quantum mechanics or molecular mechanics and molecular dynamics methods, as well as homology modeling technics. However, the computational details are described in each results topic, which encloses four chapters. The first one, Chapter 4, presents the building and characterization of the 3D structure of Cu^{2+}-$A\beta_{1-16}$ complexes. In the next chapter, Chapter 5, the study of the Cu^{+}-$A\beta_{1-16}$ species obtained by reduction of Cu^{2+}-$A\beta_{1-16}$ complexes from the last chapter along with the redox properties of this couple, as well as the stability of these species, is reported. Then, Chapter 6 investigates the role of these species in the catalytic cycle of the H_2O_2 formation; specially, the O_2 activation in order to obtain the superoxide specie. Lastly, some peptides are studied as Cu chelates as possible AD treatment in Chapter 7. Finally, Chapter 8 addresses general conclusions of the present thesis. Moreover, there is a reference section with all the references cited in this thesis, as well as Appendix parts that support the information given in Chapters 4 to 7.

Acknowledgements

Primer de tot m'agradaria donar les gracies als meus directors, sense els quals aquesta tesis no hauria estat possible, la Prof. Mariona Sodupe, que a fet possible la meva incorporació al departament i m'ha donat aquesta increïble oportunitat de seguir formant-me (que tenint en compte els temps que corren, no es fàcil trobar-les), i el Prof. Luis Rodríguez Santiago, per tot el suport i els consells que m'ha donat. Com no podia ser d'una altra manera, també vull agrair al nostre estimat col·laborador i coautor en tots els treballs realitzats en aquest projecte, el Prof. Jorge Alí Torres de la Universidad Nacional de Colombia, per les seves valuoses contribucions als diversos treballs presentats en aquesta tesis.

A més, també he d'agrair a tots els companys del despatx totes els dubtes que m'han resolt al llarg d'aquest període, així com tots els moments viscuts. Sense ells aquesta experiència no hagués estat igual. Tampoc em puc oblidar del Dr. Giovanni La Penna, qui hem va donar l'oportunitat d'ampliar la meva formació en una estada doctoral a Florència.

D'altra banda, vull expressar el meu agraïment per l'oportunitat que se m'ha donat de poder assistir a diferents congressos com a doctorant, gracies al meu grup de recerca "Computational Studies of (Bio)inorgànic Systems" (GETAB group) i a les subvencions que ha rebut a través dels projectes del Ministeri de Ciència i Innovació (CTQ2011-24847 i CTQ2011-23336) i de la Generalitat de Catalunya (2009SGR-0638), així com al Subprograma d'Ajudes FPI-MICINN del Gobierno de España per la beca doctoral (BES-2012-052853). També estic agraïda al Consorci de Serveis Universitaris de Catalunya (CSUC) pels recursos computacionals proporcionats per l'assoliment d'aquesta tesis.

Per últim, agrair a tots els meus amics i familiars tot el suport prestat durant aquest temps, un pilar fonamental durant tots aquest anys. El seu recolzament ha estat molt gratificant.

Andrea Mirats Arce

Bellaterra, Novembre del 2016

List of Abbreviations

	Meaning
AD	Alzheimer's Disease
AIMD	*Ab initio* Molecular Dynamics
APP	Amyloid Precursor Protein
ATCUN	Amino Terminal Cu^{2+}-binding motif
Aβ	Amyloid beta
BBB	Blood Brain Barrier
CC	Coupled Cluster
CI	Configuration Interaction
CQ	Clioquinol
CV	Cyclic Voltammetry
DFT	Density Functional Theory
EA	Electron Affinity
EPR	Electronic Paramagnetic Resonance
FF	Force Field
GGA	Generalized Gradient Approximation
HF	Hartree-Fock
HK	Hohenberg-Kohn
HM	Homology modeling
IE	Ionization Energy
IR	Infrared light
KS	Kohn-Sham
LCAO	Linear Combination of Atomic Orbitals
LDA	Local Density Approximation
LSDA	Local Spin Density Approximation
MBPT	Many Body Perturbation
MD	Molecular Dynamics
MM	Molecular Mechanics
MP	Moller-Plesset
MPAC	Metal-Protein Attenuating Compounds

	Meaning
NMR	Nuclear Magnetic Resonance
NPA	Natural Population Analysis
ONIOM	Our N-layered Integrated Molecular Orbitals and Molecular Mechanics
PBC	Periodic Boundary Conditions
PCM	Polarizable Continuum Model
PDB	Protein Data Bank
PES	Potential Energy Surface
QM	Quantum Mechanics
ROS	Reactive Oxygen Species
SA	Simulated Annealing
SCE	Saturated Calomelan Electrode
SCF	Self-Consistent Field
SMD	Universal Solvation Model
SRP	Standard Reduction Potential
ThT	Thioflavin-T
UFF	Universal Force Field

List of Abbreviations of Amino Acids

	Symbol	
Amino Acid	**1- letter**	**3-letter**
Alanine	A	Ala
Arginine	R	Arg
Aspargine	N	Asn
Aspartic Acid (Aspartate)	D	Asp
Cysteine	C	Cys
Glutamic Acid (Glutamate)	E	Glu
Glutamine	Q	Gln
Glycine	G	Gly
Histidine	H	His
Isoleucine	I	Ile
Leucine	L	Leu
Lysine	K	Lys
Methionine	M	Met
Phenylalanine	F	Phe
Proline	P	Pro
Serine	S	Ser
Threonine	T	Thr
Tryptophan	W	Trp
Tyrosine	Y	Tyr
Valine	V	Val
Any Amino Acid	X	Xaa
Termination codon		Term

Contents

1

INTRODUCTION

Alzheimer's disease (AD) is the most common form of neurodegenerative dementia, usually affecting people over 65 years. Due to the increased life expectancy, the number of new and existing cases of AD will grow in the next years, leading to a serious health problem. This thesis is based on computational approaches to shed some light in the atomistic behavior of several metal complexes related to AD.

This first chapter is devoted to make a general introduction to different aspects of the disease, beginning with a brief introduction about the AD concept. Then, the hypotheses about the causes of the disease are presented. In particular, the influence of the metal ions in AD and its role in oxidative stress processes will be discussed in detail. Finally, a possible therapeutic treatment for AD, which is metal chelation, will be described.

1.1. ALZHEIMER'S DISEASE

Alzheimer's disease is a degenerative brain disease and the most common cause of dementia.[1] Originally, dementia was related to old-age. In fact, the first steps toward classification of dementia were done during the Greco-Roman period, with Galen identifying dementia in the *senium* as a mental disease.[2] In the 17th century, the dissection of the human body started to be tolerated, which promoted an increase in the search for underlying physiological changes in the brain that might be the source of mental disorders.[3] From the late 19th century, a series of events enabled to progress defining the bases of all mental disorders, including senile dementia. Specifically, in 1892, the recently discovered carmine stain helped to describe a novel pathological feature which consisted in the accumulation of an undefined substance into plaques in the brain.[4,5] Then, Fisher suggested that this neuropathology could be considered as a marker for senile dementia.[6] Meanwhile, in 1903, Bielschowsky improved the silver stain discovered by Golgi in 1873,[7] enabling to clearly visualize cellular components of neurons for the first time.[8] In 1907, using the Bielschowsky stain, Alois Alzheimer described a new pathology in the brain of a recently deceased woman (Auguste Deter, 1850-1906) who died a few years after developing a clinically unusual dementia at age of 51. This novel neuropathological feature that Alzheimer observed consisted of tangles of fibrils within the cytoplasm of neurons. In addition to these neurofibrillary tangles, Alzheimer also noted the widespread presence of plaque pathology extensively described in senile dementia by Fischer[6]. In the next five years following Alzehimer's initial description, eleven similar cases of pre-senile dementia (*i.e.*, onset before 65) accompanied by neuropathological features of plaques and tangles were reported in the medical literature. It seemed that many others pathologists were considering the illness described by Alzheimer to be, indeed, a unique disease and several of them already referred to this condition as "Alzheimer's disease".[3] The official acceptance of this disease is ascribed to Emil Kraeplin, the foremost psychiatrist in the world at that time (and today considered one of the founders of modern psychiatry), by his inclusion of "Alzheimer's disease" in the eighth edition of his *Textbook of Psychiatry*, published in 1910.[9]

Nowadays, AD is described as an irreversible and progressive disease associated with the deterioration of memory, language, problem-solving and other cognitive skills that affect a person's ability to perform everyday activities. At present, due to the advances in

medicine and medical technology, as well as social and environmental conditions, people that may survive into their 80s, 90s and beyond is expected to rise dramatically. Hence, the number of new and existing cases of AD will grow substantially. For instance, approximated 5.3 million Americans of all ages had AD in 2015[10] including an estimated 5.1 million people over age 65 and approximately 200,000 individuals under age 65.[11] It is difficult to determine how many deaths are caused by AD. The National Center for Health Statistics of the *Centers for Disease Control and Prevention* (CDC) consider that a person have died from AD if the death certificate identifies Alzheimer's as the underlying cause of death, defined by the *World Health Organization* (WHO) as "the disease or injury which initiated the train of events leading directly to death".[12] All of this implies that in 2050, the disease may increase until 24.6 million of new cases each year[13] unless the disease will come better understood and a cure or a drug that delay the disease progression is found.

AD and normal age-related cognitive impairment are produced by damage in the neurons involved in cognitive function causing, in the end, their death. Nevertheless, they differ in that the first neurons to malfunction in AD are usually neurons related in forming new memories which cause that the most common initial symptom of AD is a gradually aggravating ability to remember new information.[14] In particular, *postmortem* studies of AD patients' brain tissue exhibit two main histopathological features, shown in *Figure 1.1*:

a) **Intraneuronal fibrillar tangles** composed of hyperphosphorilated tau protein.[15,16] Tau protein is important for the structural integrity of microtubules in the neuron cytoskeleton. Like most microtubule-associated proteins, tau is normally regulated by phosphorylation.[17] However, in AD patients, twisted strands of hyperphosphorylated tau are accumulated inside nerve cell bodies known as neurofibirillary tangles,[17,18] which are commonly observed upon neurodegeneration.

b) **Extracellular deposits** of fibrillar amyloid beta (Aβ) peptide called senile plaques.[15,19] Aβ is a 39- to 43-residue peptide derived from sequential proteolytic cleavage from the C-terminal region of a much larger protein, the Amyloid Precursor Protein (APP),[20,21] which is found in the membrane of cells and organelles such as mithochondria.[18,22] Aβ monomers are soluble. However, at sufficiently high

concentration; they aggregate to form amyloid fibrils suffering dramatically conformational changes.[23] Nevertheless, amyloid plaques are also not unique to AD, because 20-40% of unaffected elderly individuals can own as many amyloid plaques as AD patients.[24]

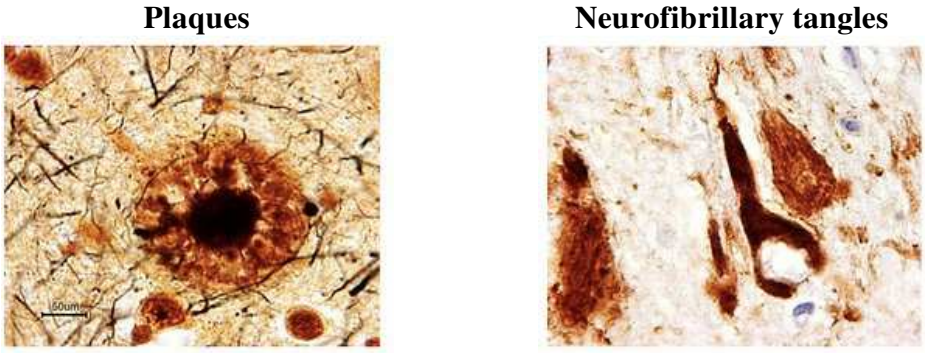

Figure 1.1. Visualization of the two main hallmarks of Alzheimer's Disease, obtained from the Ref. *25*.

In summary, it is believed that senile plaques and neurofibrillary tangles prompt the injury and death of neurons, and as consequence memory loss and behavioral symptomatic changes. During the past years, several hypotheses, such as the neuronal cytoskeletal degeneration hypothesis[26] and *Amyloid Beta Synergistic Endothelial and Neuronal Toxicity* (ABSENT) hypothesis,[27] emerged in order to explain these brain changes.[18,28] Nevertheless, nowadays, the most accepted is the amyloid cascade hypothesis.[29–31]

1.2. AMYLOID CASCADE HYPOTHESIS

This hypothesis states that the deposition of Aβ is the cause of AD; that is, the rest of the disease processes, including the formation of neurofibrillary tangles, vascular damage, cell loss and dementia, are consequence of a series of events that follow this deposition.[32]

Aβ is a product of the larger APP protein,[33] a type I transmembrane glycoprotein.[34] Its cleavage can be produced by two main pathways, as it is illustrated in *Figure 1.2*, the amyloidogenic which comes from the β-secretase cleavage and the non-amyloidogenic which goes through α-secretase. Both of them occur in the normal healthy organism.[35–38] Usually, a major rout of APP cleavage proceeds through the non-amyloidogenic path where the α-secretase cuts on the C-terminal side of residue 16 of the Aβ peptide.[39] After that, the γ-secretase releases the P3 peptide, which contains the C-terminal region of the

Aβ sequence,[40] and the *intracellular APP domain* (ADIC).[41] Therefore, the Aβ peptide formation is prevented. However, the amyloidogenic path produce the most abundant fragments of Aβ peptide which are $A\beta_{1-40}$ and $A\beta_{1-42}$, the latter being considerably more neurotoxic and prone to aggregation than the former,[42,43] possibly due to the two additional hydrophobic amino acids.[44,45] The human $A\beta_{1-42}$ sequence is:

DAEFRHDSGY EVHHQKLVFF AEDVGSNKGA IIGLMVGGVV IA
10 20 30 40

Aβ peptides can be found in different aggregation states, such as soluble oligomers, protofibrils and fibrils or extracellular aggregates. The most neurotoxic ones are the oligomeric forms which can lead to neurodegeneration by different ways[38] including the formation of Reactive Oxygen Species (ROS).[46]

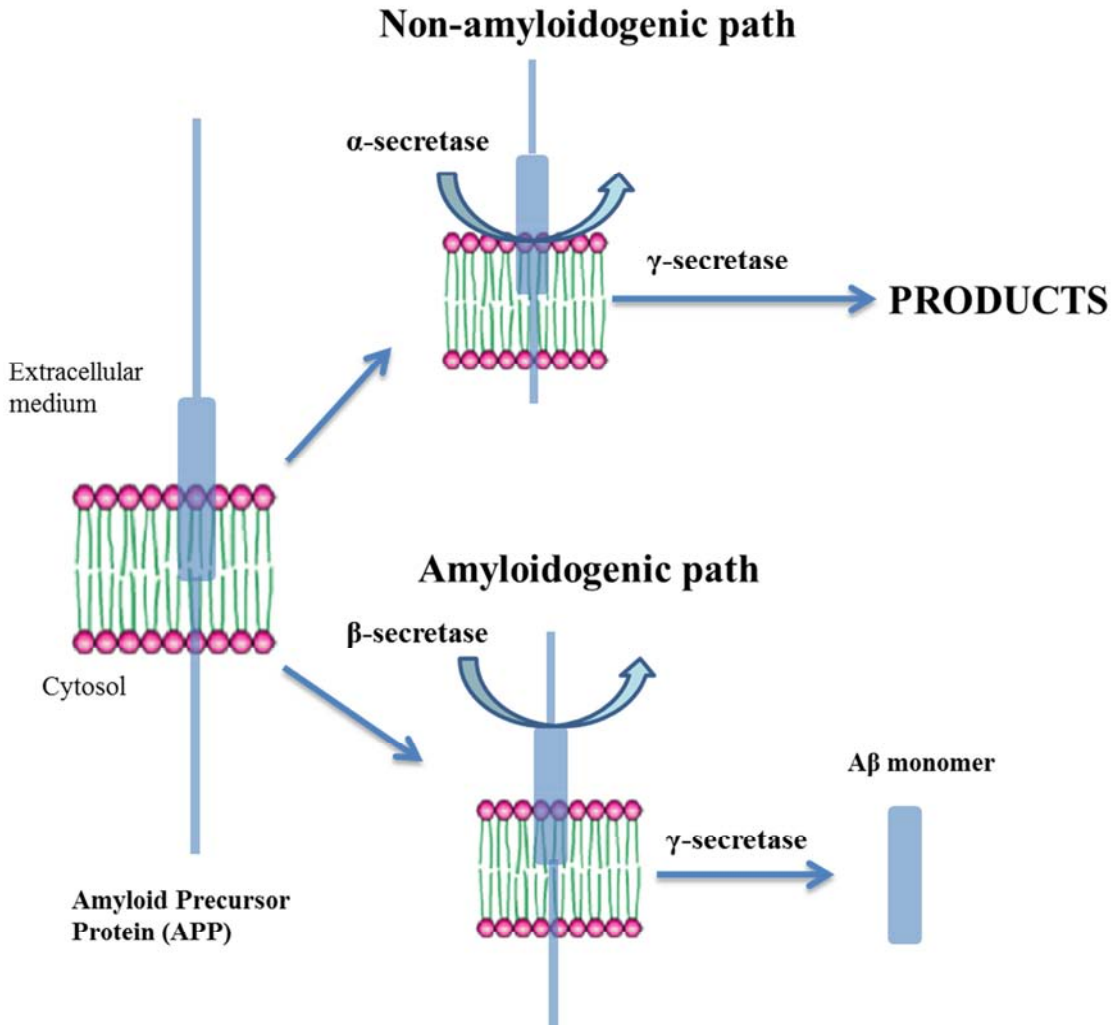

Figure 1.2. Description of the APP cleavage to form Aβ.

Normally, Aβ peptide is degraded through different routes. One of them is its cleavage by a series of proteases present in the brain. A second minor route is the Aβ traffic by the *InterStitial Fluid* (ISF) into the *CerebroSpinal Fluid* (CSF) via bulk flow. The route for Aβ clearance is direct trafficking out of the brain via the Blood-Brain Barrier (BBB) into peripheral circulation,[47] the Aβ production and cleavage being in equilibrium in order to avoid its accumulation.[35] An imbalance of both mechanisms, however, can produce the Aβ aggregation leading to the amyloid plaques formation.[38] Therefore, the neurodegenerative process is the result of an imbalance between the formation and clearance of Aβ in the brain.[36]

1.3. THE ROLE OF METAL IONS IN ALZHEIMER'S DISEASE

Healthy brain is the richest part of the body in transition metal ions, specifically on Zn, Cu and Fe.[48] They are in the brain at low concentrations but are completely necessary for organism vital functions; for example, Fe and Zn play an important role in the *Central Nervous System* (CNS). However, these metals are not equally distributed; for instance, the hippocampus, which is a region for memory and one of the first struck in AD, is further enriched in Zn and Cu.[49] An imbalance in their concentrations may become in serious problem health.[38]

Postmortem brain analysis of AD patients have shown high Fe concentrations and accumulation of Cu and Zn in the senile plaques.[50] Moreover, *in vitro* studies have shown that metal ions such as Zn or Cu can favor the Aβ aggregation, while Cu and Fe may promote the neurotoxic redox activity of Aβ and the stable oligomeric production.[50] All these observations suggested that metal dyshomeostasis for Zn, Cu and Fe combined with Aβ imbalance may influence the AD pathogenesis.[51] Nevertheless, there are some controversy on formation or inhibition of Aβ aggregation induced by metal ions.[52,53] In general, quick aggregation leads to amorphous fibrils which do not produce senile plaques because they need a more organized structure. Hence, metal ions can raise Aβ aggregation inducing an organized conformation, which implies a solubility decrease that means more Aβ precipitation, or they can inhibit fibril formation stabilizing a more amorphous configuration.[54] Hence, the exact role of metal ions is controversial.

Multiple observations show that Zn(II) and Cu(II) can be involved on the formation and structural integrity of amyloid aggregates, oligomers and fibrils.[53,55–62] The Zn-Aβ complexes usually seems to be nontoxic whereas Cu-Aβ complexes are neurotoxic.[63] Additionally, if one considers that Cu present higher affinity for Aβ than Zn and that Cu exhibits a high redox activity,[64] it is apprehensible that Cu-Aβ complexes has been the most intensively studied. In particular, the study of Cu-Aβ interaction and the mechanism that lead to the production of ROS are central to understand the role of copper in AD. Several investigations have used truncated peptides of Aβ, such as $A\beta_{1\text{-}16}$[65] or $A\beta_{1\text{-}28,}$[61] to study its interaction with Cu(II) because they are more soluble than $A\beta_{1\text{-}42}$. These intermediate systems include the first 16 amino acids of Aβ. This region constitute the hydrophilic motif of the peptide, known to interact with metal cation, then called the metal ion affinity region.[66]

Experimental techniques, for instance *Nuclear Magnetic Resonance* (NMR),[67] *Electronic Paramagnetic Resonance* (EPR),[68] *Attenuated Total Reflectance-Fourier Transform InfraRed* (ATR-FTIR) spectroscopy [69] or *HYperfine Sub-level CORrelation* (HYSCORE) spectroscopy,[68] have been used to study the metal environment and the conformational changes of Aβ in Cu^{2+}-$A\beta_{1\text{-}16}$ complexes.[46,68] Initial investigations already suggested that Cu^{2+}-$A\beta_{1\text{-}16}$ complexes formed a 3N1O coordination environment,[70] where the 3N coordination could be given by the three His residues[71] or by two His and the N-terminal.[72] However, there was controversy in order to explain the oxygen coordination. On the one hand, it was proposed that the O could come from a carboxylic group of the Asp1, Asp7, Glu3 or Glu11 residues.[73] In contrast, other studies proposed that the Tyr10 residue was the O donor,[71,73] but recent researches have rejected this possibility.[74–76] Later, O form carbonyl groups of the amide were suggested as another possible ligand for the Cu coordination.[77,78]

More recent investigations, based in EPR and HYSCORE spectroscopy[68,74,78] combined with ^{15}N, ^{13}C and ^{17}O isotopic labeling, have allowed to describe the most reliable coordination environment for the Cu^{2+}-$A\beta_{1\text{-}16}$ complexes.[68] Thus, the coexistence of different species in equilibrium has been observed. These species are sensitive to the pH variation and two of them are considered the most dominant ones, called component I and II. *Figure 1.3. s*hows the major coordination environments proposed from EPR

experiments. At physiological pH, near 6-7, the major specie is component I[65,68] which enclose two different configurations in equilibrium, component Ia and Ib,[74] as it is illustrated in *Figure 1.3. a.* These two configurations involve the coordination of two imidazole N of the His (His6 and His13/14, depending if it is Ia/Ib),[74,79] the N-terminal[80] and the O of the carbonyl group of Asp1.[69] Furthermore, a fifth coordination position is possible. Firstly, the carbonyl of the peptide bond of the non-coordinated His was proposed; but, then, the carboxylate of Asp1 in axial position has been suggested as the fifth coordination position.[78,81] At higher pH, the predominant specie is component II which present some controversies in the coordination environment because two different structures depending on the pH have been proposed, as it is outlined at *Figure 1.3. b.* One, at pH ~8, which involves the coordination of three His and the carbonyl group of Ala2[78] and the second one, at pH~9, which involves the coordination of His 6, the carbonyl group of the peptide bond between Ala2 and Glu3, a deprotonated amide, the N-terminal and, probably, the carboxylate group of Asp1.[80,82]

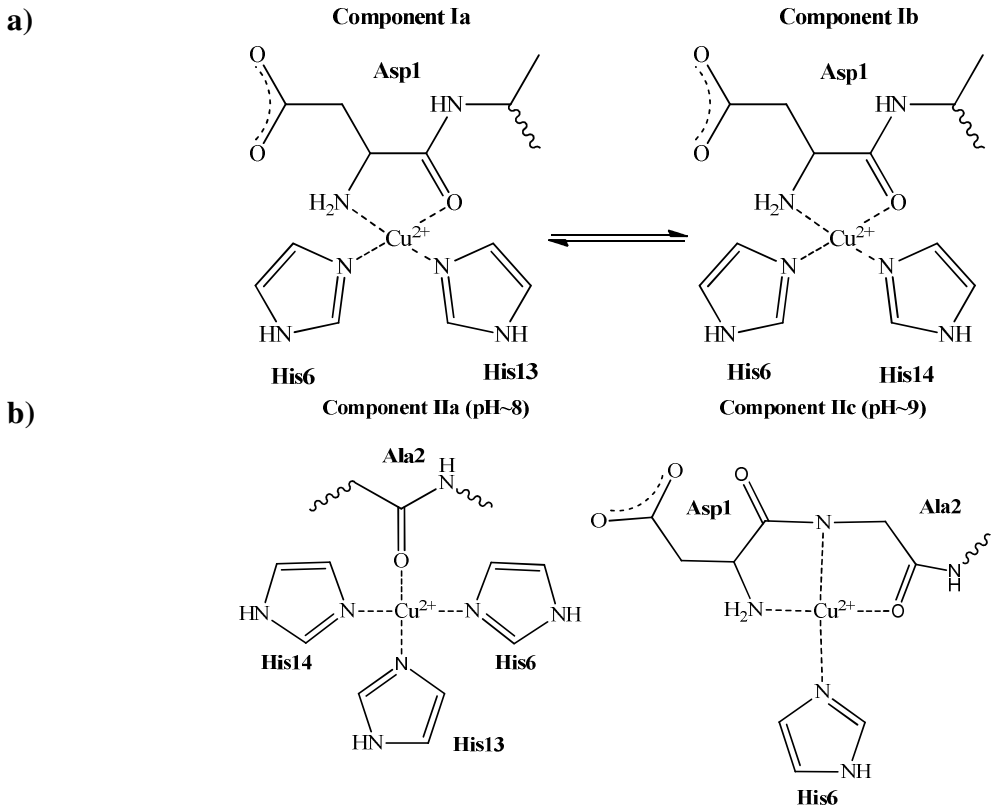

Figure 1.3. a) Possible coordination environments for component I. **b)** Possible coordination environments for component II.

Finally, experimental observations based on ATR-FTIR spectroscopy indicate that at low pH the coordination mode of His6 is through N_ε while the coordination of His13 and 14

is through N_δ. The nomenclature of the possible coordinating nitrogens of His is illustrated in *Figure 1.4.* The His6 coordination mode keep constant during pH 6.5 to 9, whereas the coordination mode of His13 and 14 can change along the pH range.[69]

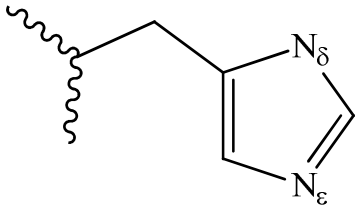

Figure 1.4. Nomenclature of the possible coordinating nitrogens of His.

Parallel to the experimental work, theoretical studies have been performed to analyze the stability of different coordination environments and provide insights on the electronic and molecular structure of the Cu^{2+}-$A\beta_{1-16}$ complexes. In order to reduce the computational costs and the complexity of the system, the first investigations[83,84] were performed with small models that only involve the first coordination metal sphere. These studies allowed describing the metal coordination environment, as well as the ligand-metal affinity. For example, the metal affinity for His13 and 14 was analyzed at the B3LYP level considering the solvent as a Polarizable Continuum Model (CPCM). These calculations suggested that the most stable coordination was through the N_δ atom of both His and involve the O of the carbonyl group of the peptide producing a distorted square planar coordination. Moreover, Cu environment was best represented as distorted square planar coordination.[83] A subsequent study addressed the structures, the ligand affinity and the reduction potentials of Cu^{2+} in Cu^{2+}-Aβ complexes using, again, small models with quantum calculations (DFT and Möller-Plesset) and a polarizable continuum water model (IEFPCM). Results proposed that component I coordination would be the preferred one and that Asp1 would not participate in the coordination environment of Cu^{2+} in component II.[84]

Other investigations considered the whole system using classical mechanics calculations in order to study the Cu-Aβ interaction. One of them considered the interaction of Cu with $A\beta_{1-42}$ and $A\beta_{1-40}$ employing Molecular Dynamics (MD) simulations in aqueous environment. The results manifested that $A\beta_{1-42}$ monomer presents β-sheet regions, which are paired in antiparallel fashion by hydrogen bonds, whereas the $A\beta_{1-40}$ system show different collapsed coil. Furthermore, it was shown the Cu^{2+} binding can disrupts the β-sheet formation in the N- and C- terminal regions.[85]

1.4. OXIDATIVE STRESS AND ALZHEIMER'S DISEASE

The brain comprises 2% of the total body mass and it is the most aerobically active organ due to its high rate of oxidative metabolism, consuming about 20% of total body oxygen.[86] The oxygen consumption is related to the high brain energy demand, which is produced in ATP form in the respiratory chain. This process is an overall redox reaction of NADH and succinate with oxygen. However, this reaction is slow though it can be metal catalyzed or induced by light. As light does not penetrate into most parts of human body, in most places redox active metal ions, specially Cu and Fe which have the ability to occupy multiple valance states and are present in a diversity of enzymes,[87] can accelerate the reaction by mediating electron transfer. As a consequence, Cu and Fe not only dissipate energy, but can also produce radicals by one-electron reduction producing the so-called ROS,[38] which the most important forms are outlined in *Figure 1.5*. Notable ROS are superoxide ($O_2^{\bullet-}$), which is the one-electron-reduced radical anion form of normal triplet dioxygen, dihydrogen peroxide (H_2O_2) and hydroxyl radical ($OH^{\bullet}$).[88,89] These are formed mainly in the mitochondria as a side product of oxidative metabolism.

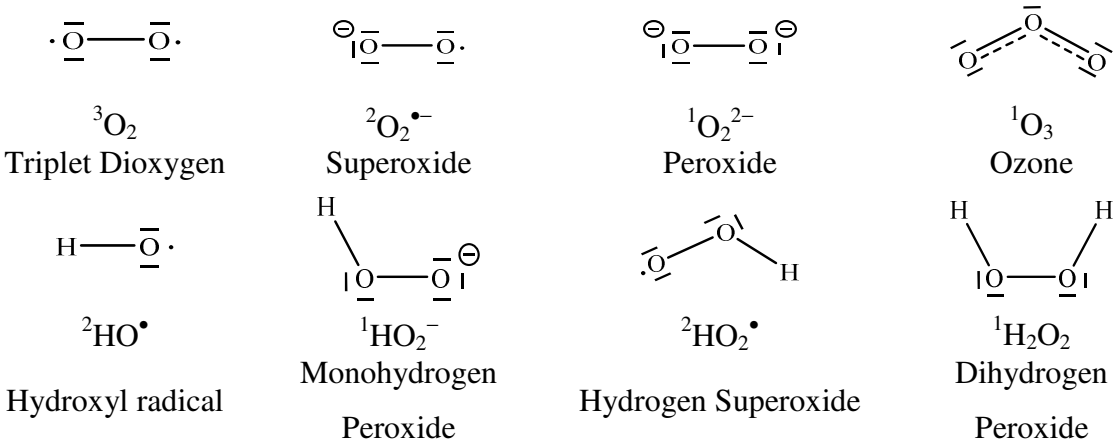

Figure 1.5. Chemical and electronic structures of normal atmospheric $^3O_2$ and ROS. The spin multiplicity is given as a superscript before the molecular formula.

Under certain conditions ROS production is required, for instance in the defense reaction of phagocytes against pathogens. Furthermore, the ROS byproducts from the respiratory chain might be a feedback signal for discerning its integrity, for example an increment of ROS might signal malfunctioning.[90] Usually, there are mechanisms that degrade ROS, but they can escape the organisms' antioxidants defenses and degrade proteins and lipids or nucleic acids of the DNA, leading to mutations.[91] Then, oxidative stress can be defined

as a disturbance in the balance between the systemic manifestation of ROS and a biological system's ability to readily detoxify the reactive intermediates or to repair the resulting damage.[92] It can be enhanced by the age, the gens or the environment resulting in accumulated gene defects and declining mitochondrial functions that subsequently leads to neurological disorders, either gradually or when reaching a critical threshold that initiates apoptosis in neurons.[93,94] In summary, oxidative stress pathogenesis can be produced by ROS formation along with metal ion dyshomeostasis, which shifts balance from bound to free metal ions.[88]

As mentioned, oxidative stress in AD patients may be intensified by the production of H_2O_2 catalyzed by metal-Aβ complexes enclosing redox-active metal cations[95,96] which, in turn, derives in the production of ROS through Fenton and Haber-Weiss-like reactions.[97–101] This oxidative damage, which precedes Aβ deposition,[51,102] can cause the typical ROS injury such as oxidation of proteins and DNA[95] and increase lipid peroxidation. These processes are one of the earliest and the most fatal symptoms observed in the development of the AD.[103] Although oxidative stress somehow precedes Aβ toxicity, both effects are combined to enhance, creating an unfavorable positive feedback.[104]

In order that Cu^{2+}-Aβ complex catalyze ROS formation, the metal cation in the complex should be reduced. Early studies reported Standard Reduction Potential (SRP) values around of 0.72 to 0.77 V versus Standard Hydrogen Electrode (SHE) for the Cu^{2+}-Aβ/ Cu^{+}-Aβ couple.[71] Initially, this reduction was suggested to be induced by Aβ itself,[97] through the oxidation of some residues such as Tyr10 and Met35. Nevertheless, Aβ itself does not probably reduce Cu^{2+} through Tyr10 and Met35 due to their high redox potentials (0.95 and 1.5 V, respectively).[99,105] More recent studies have proposed SRP values ranging from 0.28 to 0.34 V.[99,101] On the other hand, similar SRP values were found for truncated complexes, such as Cu^{2+}-$Aβ_{1-16}$ and Cu^{2+}-$Aβ_{1-28}$. Therefore, the involvement of external reducing agents, usually found in the cerebral medium, in the ROS fomration mechanism has been suggested.[106] *X-ray Absorption Near Edge Structure* (XANES) experiments have been used to study the substrate mediated reduction of Cu^{2+} in Cu^{2+}-Aβ complexes by relating the intensity and position of near-edge features. This

study indicated that Cu^{2+}-Aβ complex can be reduced by ascorbate and 6-hydroxydopamine but not by dopamine and cholesterol.[107]

The reduced complex backs to Cu^{2+}-Aβ oxidized system across the reaction with the dissolved oxygen and the protons in the medium, resulting in a catalytic cycle that would generate hydrogen peroxide in excess,[98] as it is illustrated in *Figure 1.6.* In principle, this process only involves the reaction between the reduced Cu^{+}-Aβ system with oxygen in a single-electron process and should yield superoxide, $O_2^{\bullet-}$, as product. However, instead of the superoxide, the two-electron reduction product, hydrogen peroxide, is observed.[108,109]

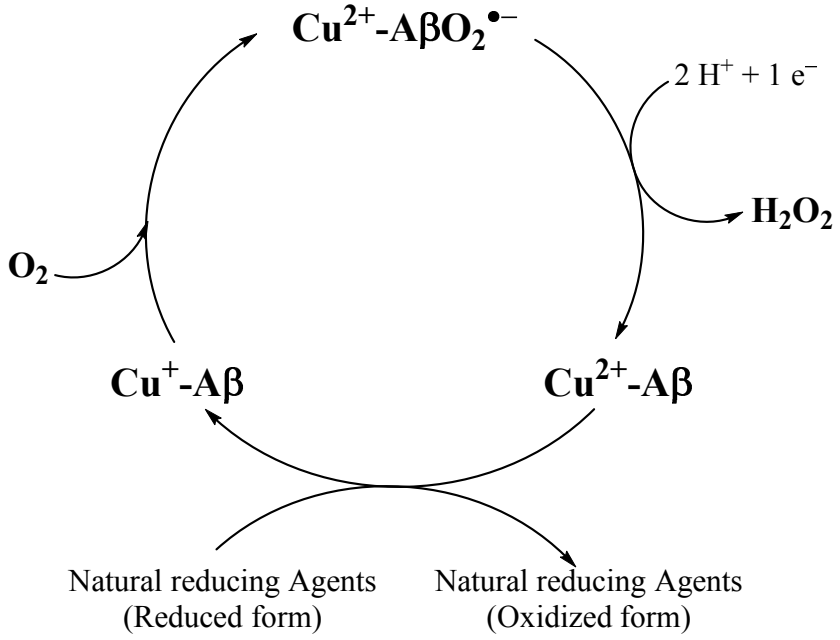

Figure 1.6. Putative mechanism scheme for H_2O_2 formation catalyzed by Cu-Aβ.

The SRP versus SHE for the couple O_2/H_2O_2 is 0.30 V at physiological pH.[110] This implies that the SRP of the copper complex has to be higher than those of the external reducing agents and lower than that for the O_2/H_2O_2 couple to favor the formation of H_2O_2. The SRP of the Cu-Aβ complex depends on the coordination environment of the metal cation. For instance, the SRP values for several cluster models of Cu-Aβ complexes, based on different coordination spheres, have been computationally determined obtaining values that range from -0.07 to 0.63 V.[84] Similarly, a spectroscopic and electrochemical study of Cu-Aβ complexes, enclosing the proposed experimental coordination modes,[74,78,80,82] as function of the pH reveals a SRP value of 0.255 V (*vs*

SHE) for component I and -0.153 V (*vs* SHE) for component II, which highlights that coordination mode might change the redox behavior of the complex.[111]

1.5. CHELATORS: METAL CATIONS AS THERAPEUTIC TARGETS

The multifactorial nature of AD process hinders the identification of clear therapeutic targets for pharmaceutical intervention. Nevertheless, the engagement of metal ions in oxidative stress and Aβ aggregation plays an important role in AD. Hence, metal ions are a promising therapeutic target.[112] This idea is not new. In fact, since the 1960s, transfusion-related iron overload in diseases such as β-thalassemia have been treated with iron chelators. However, more recently, their practice has been extended to other diseases as cancer and neurodegeneration.[113]

By the end of the 1990s, it was reported that the presence of metal chelators reverse Zn(II)- or Cu(II)-induced Aβ aggregation *in vitro.*[114,115] These encouraging results spread the hypothesis that chelating agents could induce the solubilization of Aβ plaques. These compounds, however, must satisfy various conditions; for instance, they should be specific to the target metal ion and not toxic for the human body, they should present proper hydrophobicity to be able to cross the BBB because the drug should be supplied via oral administration and have reasonable small molecular weight among other typical criteria of drug-likeness.[116–118] The approach of chelator introduction to disrupt specific abnormal metal-protein interactions is referred to Metal-Protein Attenuating Compound (MPAC) therapy. It is distinct from the process of chelation and excretion of bulk metal ions because its traditional mechanism consist on sequester peripherally and, then, eliminate by excretion, whereas the MPAC therapy disrupt the abnormal metal-protein interaction to achieve a subtle redistribution of metals and a subsequent normalization of metal function.[97] With this purpose, different studies tried to solubilize plaques in *postmortem* brain tissue with different metal-binding agents, such as BAPTA (1,2-bis(o-aminophenoxy)ethane-N,N,N',N'-tetraacetic acid), bathocuproine (2,9-dimethyl-4,7-diphenyl-1,10-phenanthroline) and bathophenanthroline (4,7-diphenyl-1,10-phenanthroline),[115] which are outlined in *Figure 1.7.* These chelators, however, are unsuitable for *in vivo* application due to their poor permeability through the BBB and the lack of specificity for individual metal ions. Shortly after, a small lipophilic molecule that binds Cu(II) and Zn(II), called clioquinol (5-chloro-7-iodo-8-hydroxoquinoline, CQ,

Figure 1.7), was verified to be particularly useful for these purposes.[119] The ability to cross the BBB and its approbation by the U.S. FDA (*Food and Drug Administration*) are some of the most valuable advantages of this molecule[119]. Despite the promising properties of CQ in clinical trials, its use as metal chelator was discontinued due to synthetic difficulties and toxicity.[120]

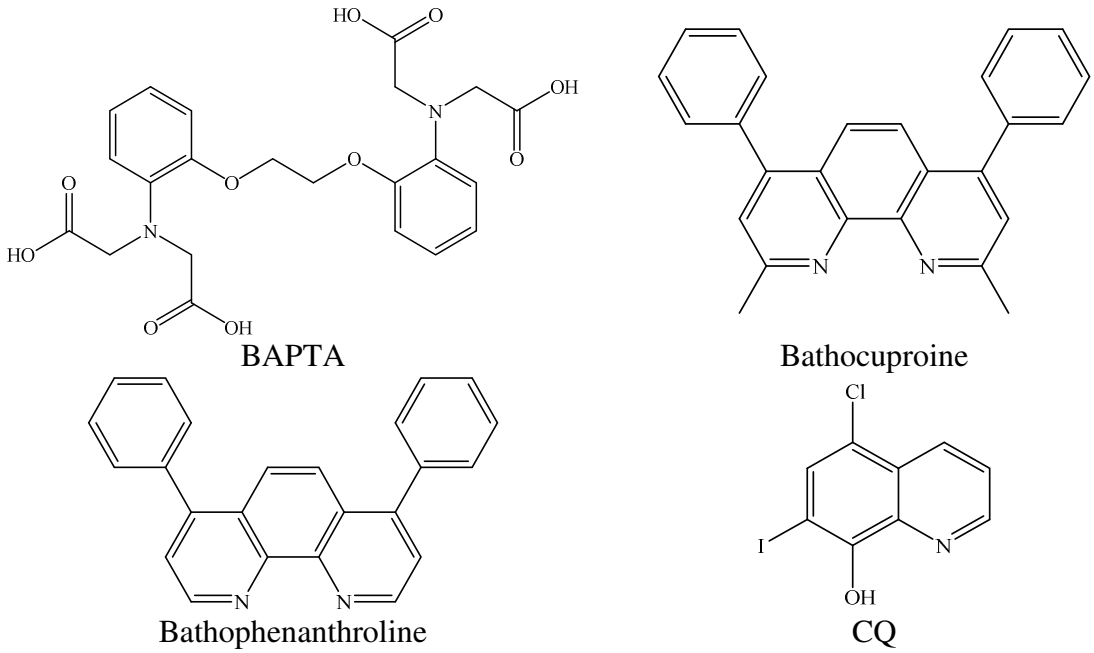

Figure 1.7. First metal-binding chelators proposed to solubilize the Aβ deposits. Obtained from Ref. *113*.

The aforementioned ligands could be presented as molecular scaffolds for the subsequent generation of metal-binding agents. Improvements on the CQ derived in a new chelator called PBT2,[121] whose structure is related to CQ and is shown in *Figure 1.8*. This new agent is a Cu and Zn metal binding agent with antioxidant activity which decreases the H_2O_2 production and prevents the Cu- and Zn- Aβ aggregates. Furthermore, it transports the metals into the cell which can activate a cell signaling cascade that, in turns, generate a range of proteases that normally degrade Aβ in the brain.[122] However, it is still in clinical trial phases.

DP-109, a diester derivative of BAPTA calcium chelator, had greater chelating efficiency for Zn(II) and Cu(II) than for other divalent metals and effective permeability through the BBB. *In vivo* trials showed that this ligand decreases the amount of insoluble Aβ peptide and reduces neuronal damage.[116] Unfortunately, no cognitive testing or further studies has demonstrated the beneficial neurological effects in AD therapy. Instead of bathocuproine and the bathphenantroline, different 1,10-phenantroline derivatives, have been studied

due to their ability to coordinate particularly copper.[123] Specifically, 1,10-phenantroline moieties and bis-tosylate linker were used to prepare both 3-propyl-Clip-Phen and Cyclo-bi-Phen ligands. Nevertheless, the Cyclo-bi-Phen ligand did not show significant plaque reduction and 3-propyl-Clip-Phen increased the Aβ brain deposits.[124] All structures of the described derivatives are shown in *Figure 1.8*.

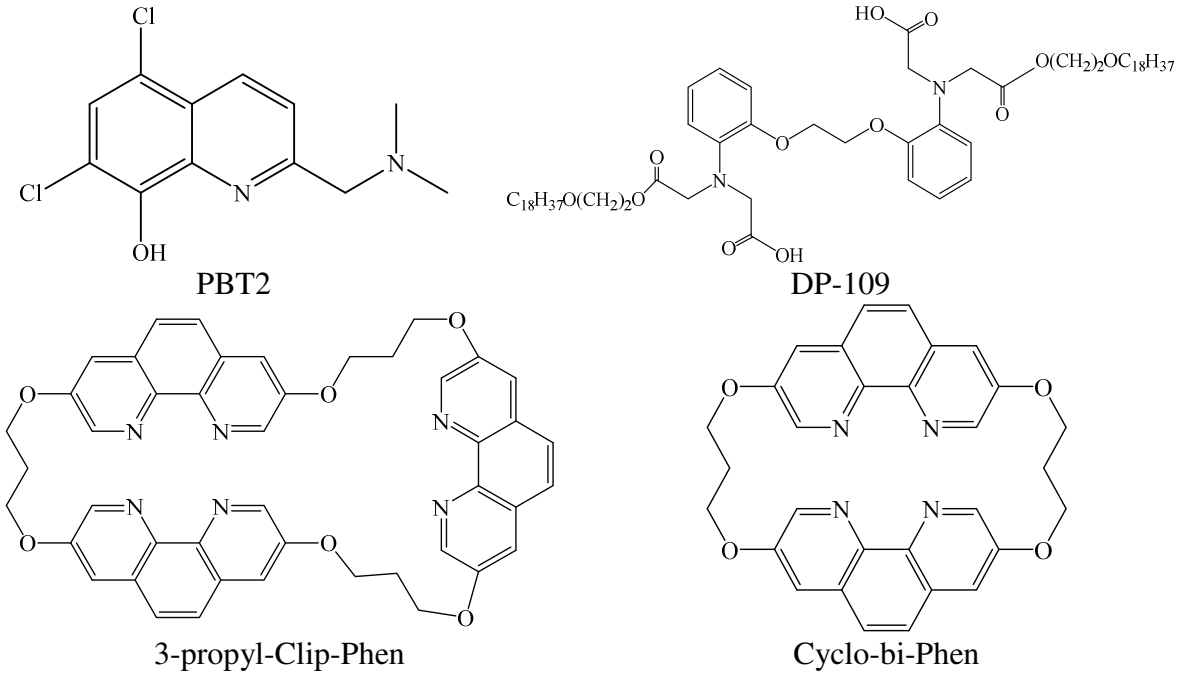

Figure 1.8. Metal chelators derived from the first metal-binding chelators. Obtained from Ref. *125*, for PBT2, and *113*, for the rest of species.

Another chelating approach is based on the use of antioxidants, which may act in various ways including prowling ROS or their precursors, inhibiting ROS formation or binding metal ions needed for the catalysis of ROS generation.[126] Moreover, they are part of our regular dietary requirements and do not have side effects.[127–129] Similarly, the beneficial properties of flavonoids[130] have been shown, which are basically polyphenolic compounds derived from plants and fruits (*Figure 1.9*); such as, catechin (EGCG, (-)-epigallocatechin-3-gallete)[131] a green tea constituent, myricetin[132] in grape seed extract and red wine and curcumin in curry powder.[133,134] Flavonoids have shown strong anti-Aβ aggregation *in vitro* effects,[131,135] as well as anti-oxidative and anti-inflammatory properties and the ability to attenuate the Aβ production.[135–137]

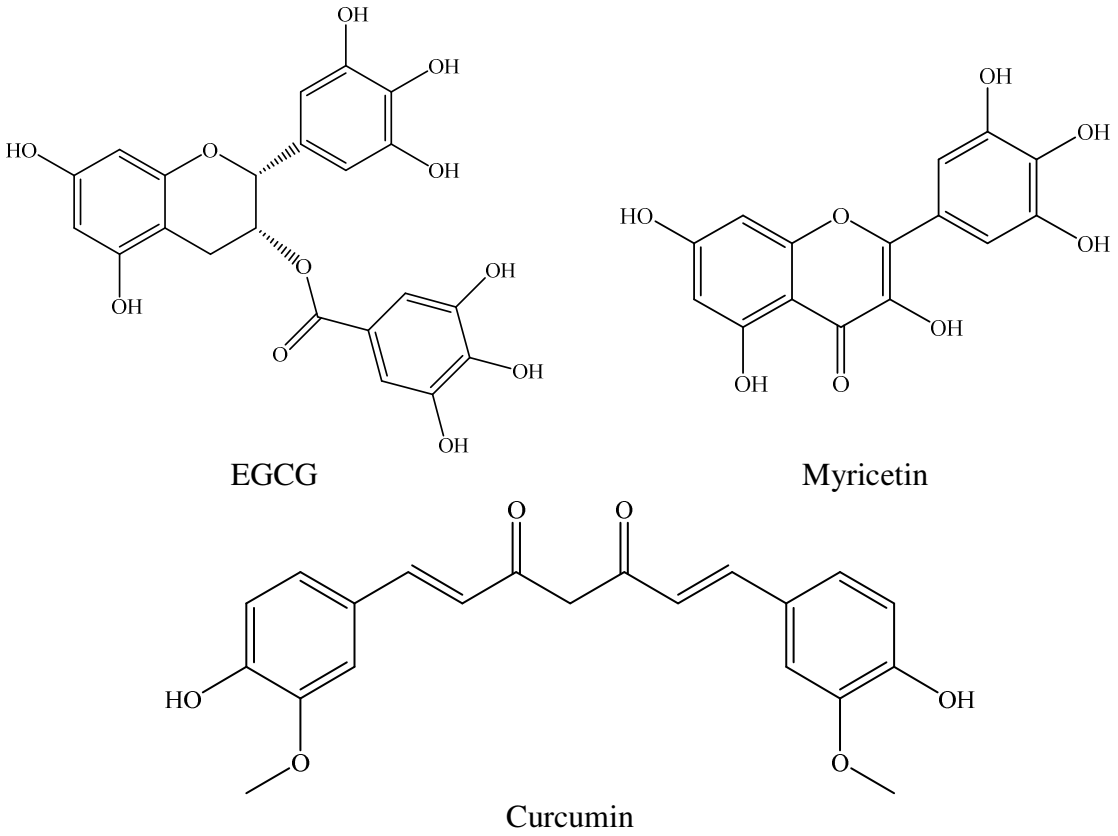

Figure 1.9. Metal chelators derived from flavonoids. Obtained from Ref. *113*.

Finally, some studies have considered the use of small peptides as MPACs. For instance, prochelators as agents that do not interact with metal ions until its activation under specific conditions, for example elevated H_2O_2 levels. This can improve the fact that general metal chelation strategies have a deficiency in their ability to differentiate metals associated with normal metal homeostasis from those toxic metals associated with Aβ plaques.[138,139] With this purpose, a prochelator SWH have been studied. The SWH abbreviation comes from the known APP Swedish mutant sequence (abbreviated SW), EVNLDAEF, where the second glutamic acid has been replaced by a histidine. This prochelator is activated by β-secretase and can sequester Cu from Aβ, prevent and undo aggregate formation and protect against Cu promoted H_2O_2 and $OH^{\bullet}$ formation.[140] Equally, a study based in glycine, glutamate, histidine or cysteine amino acid residues as metal chelators showed that they can suppress the effect of metal-induced $A\beta_{1\text{-}42}$ aggregates that stimulate their fibrillation.[63]

The design of efficient chelating ligands requires a proper knowledge of the electronic and molecular structure of the complex formed. In this line, several *in silico* studies have been performed in our group.[141–144] For instance, a proposed protocol that allows

identifying commercial compounds, which act as metal chelator, with suitable coordination and pharmacokinetic properties, was developed.[141] This protocol combines quantum chemical calculations with the search of commercial compounds of different databases via virtual screening. Quantum mechanical calculations are useful to determine the structure of metal complexes and evaluating their stability constants. Other study uses DFT (B3LYP) calculations to analyze the coordinative properties of a set of chelating ligands, which are based on the main structural and aromatic features of *Thioflavin-T* (ThT) and CQ, towards Cu^{2+}. Results indicate that those chelating ligands containing fewer aromatic moieties form more stable complexes.[142] Moreover, the coordinative properties of CQ interacting with Zn^{2+} in aqueous solution have been analyzed by means of static DFT (BLYP) calculations and *ab initio* MD simulations showing that coordination properties of $Zn(CQ)_2$ is delicate. Results from static calculations suggest that the preferred metal coordination is tetrahedral, while the more realistic *ab initio* MD simulations propose that proper description of the penta, $Zn(CQ)_2(H_2O)$, and hexa, $Zn(CQ)_2(H_2O)_2$ coordinated complexes are major quasi degenerate structures and, thus, they are expected to coexists in aqueous solution.[143]

Although several chelators have been proposed, there is little information about small peptide as metal chelators. Because of their similarity to natural body metal-peptide structures, small peptides can be suitable chelators to compete with the toxic complexes, such as Cu-Aβ. For example, the amino terminal Cu^{2+}-binding (ATCUN) motif is a structural sequence of type Xaa–Xaa–His (Xaa means any amino acid) present in proteins, which was first identified in metal-transport albumins, including human serum albumin (HSA).[145,146] It was subsequently found in other natural proteins,[146,147] such as neuromedins C and K,[148] histatins[149] and human sperm protamine P2a.[150] Furthermore, the metal ions can be released in the presence of appropriate ligands,[151] reflecting the role of ATCUN motif as a transport site.[152] Various other properties of Cu^{2+}-bound ATCUN motifs have been reported (apart from metal transport), illustrating their great biological significance.[146] For instance, it has been shown that they are capable of cleaving DNA in the presence of ascorbate by the production of hydroxyl radicals,[153,154] most likely through a Fenton-like mechanism.[155,156] As a result of their attractive (biological) properties, ATCUN-based compounds have been developed as potential metallodrugs.[157,158] For example, a Gly-Gly-His Cu^{2+}-ATCUN unit has been conjugated

to a RNA-binding peptidic sequence, *i.e.* the YrFK-amide (Tyr–D-Arg–Phe–Lys-NH_2), to generate an active antiviral molecule (against hepatitis C virus).[159,160] However, their structure determination is difficult because their high flexibility. For that reason, computational studies can provide a conformational insight about these kinds of peptides.

Considering the background given before, this thesis presents some possible 3D structures of Cu^{2+}-Aβ_{1-16} complexes and their reduced species, Cu^{+}-Aβ_{1-16}, along with the redox properties of this couple. After the study of these species, their role in the catalytic cycle of the H_2O_2 formation; specially, the O_2 activation in order to obtain the superoxide specie, is analyzed. Finally, the study of a set of peptides which enclose three amino acids have been considered. This last work has been done in collaboration Patrick Gamez of UB (Universitat de Barcelona) and Gonzalo Guirado from UAB (Universitat Autònoma de Barcelona).

2

OBJECTIVES

One of the challenges in AD is the determination of both the 3D structure and the reactivity of Cu-Aβ complexes. However, the progress in the research of these systems has been hindered because there are not X-ray data available, as aforementioned. Within these conditions computational modeling can provide useful structural information in addition to an in-depth about interaction mechanisms which allows understanding the metal ion role in the aggregation, as well as in the related reactions as Cu-Aβ induced ROS formation. All these information will enable to design a more efficient and selective Cu chelates as therapeutic strategy against the disease.

In this context, this thesis has the purpose of treating several relevant aspects in AD, such as the specific $Cu^{+/2+}$ coordination environment in Cu-Aβ complexes and the exhaustive

analysis of the electronic structure and redox properties of these complexes. Likewise, a family of possible chelates has been also studied.

Previous studies only considered the first coordination sphere of Cu^{2+}. Many of these studies provided interesting and useful insights. However, the derived results have limited scope. This promoted a study using more realistic models; that is, considering all the metal affinity region of the Aβ peptide which is the first 16 amino acids. For that reason, it was necessary to apply a protocol which enables to build and evaluate such models in order to obtain significant information about the metal coordination effect in the $A\beta_{1-16}$ and the properties of the procured complexes.

In this sense, the main goals of this thesis are summarized in the following points:

I. Building 3D Cu^{2+}-$A\beta_{1-16}$ complexes based on the experimental metal coordination environments and the RMN structures of the Zn^{2+}-$A\beta_{1-16}$ complex deposited in the PDB using homology modeling techniques. Moreover, providing detailed electronic and geometric structure description of such complexes.

II. Determining the 3D structure of the Cu^{+}-$A\beta_{1-16}$ species obtained through the reduction of the most stable Cu^{2+}-$A\beta_{1-16}$ complexes found in the above point, their stability and the influence of the metal coordination sphere in the SRP values. Furthermore, evaluating if these complexes can catalyze the ROS formation.

III. Describing the putative mechanism of H_2O_2 formation through the study of the superoxide formation by using model systems, as well as providing a detailed description of the role of the first and the second sphere of the $Cu^{+/2+}$-$A\beta_{1-16}$ complexes in the O_2 activation.

IV. Exploring the coordination and electrochemical properties of a possible family of Cu chelates consisting of a tripeptide with different sequences that allows sequestering the metal by using DFT calculations.

3

THEORETICAL BACKGROUND

Theoretical chemistry applies quantum mechanics, classical mechanics and statistical mechanics as conceptual and mathematical tools to explain the structures and dynamics of chemical systems as well as to understand and predict their thermodynamic and kinetic properties; while computational chemistry transforms these tools into efficient numerical algorithms that assist, through computer simulation, in solving chemical problems.

The aim of this chapter is to make a general review on the computational techniques used in the present thesis. It starts with the description of electronic structure methods. On the other hand, as the present thesis considers structures of Cu-Aβ complexes and its properties, QM/MM hybrid methods, Homology Modeling (HM) and Molecular Dynamic (MD) simulations are also explained. Nevertheless, the specific details of the employed basis sets and every approximation are detailed in each results chapter section. This

revision is not a monographic work about computational methods. Thus, if the reader wants to deepen in the topics, the most relevant references are cited.

3.1. QUANTUM MECHANICS

Similar to Newton's second law in classical mechanics, Erwin Schrödinger published in 1926 one of the most important equations in physics which is in the base of Quantum Mechanics (QM).[161] The partial differential equation describes the state of a chemical system as a wave function which evolves in time:

$$i\hbar\frac{\partial}{\partial t}\Psi(\vec{q},t) = \hat{H}\Psi(\vec{q},t) \tag{3.1}$$

Where Ψ is the wave function of the system, $\vec{q}$ is the collective coordinates used to represent the position of both nuclei and electrons on a molecule and $\hat{H}$ is the Hamiltonian operator. However, if the molecular Hamiltonian has not time dependence and the system is described as an eigenstate of the Hamiltonian, it is possible to obtain an equation which describes the motion of electrons in a system where the electrons and nuclei are interacting and do not have temporal coordinates. This equation is called the *time-independent non relativistic Schrödinger equation:*[162]

$$\hat{H}\Psi(\vec{q}) = E\Psi(\vec{q}) \tag{3.2}$$

Where Ψ continues being the wave function of the system and $\hat{H}$ is the Hamiltonian operator for this system in the absence of electromagnetic fields, which can be expressed as the sum of kinetic energy of the nuclei ($\hat{T}_n$) and of the electrons ($\hat{T}_e$) as well as the potential terms for coulomb attraction between electrons and nuclei ($\hat{V}_{ne}$) and repulsion between electrons ($\hat{V}_{ee}$) and nuclei ($\hat{V}_{nn}$):[163]

$$\hat{H} = \hat{T}_n + \hat{T}_e + \hat{V}_{ne} + \hat{V}_{ee} + \hat{V}_{nn} \tag{3.3}$$

Even with the simplification of the time-space separation in *equation 3.2*, the resolution still becomes unfeasible. Nevertheless, in 1927, Max Born and J. Robert Oppenheimer assumed that the electronic and nuclear coordinate separation was possible because nuclei are so much more massive than electrons; they must accordingly move more slowly. Hence, it is considered that the nuclei are fixed and only the electronic motion has to be solved. This is known as the *Born-Oppenheimer approximation.*[164] Then, the first term of

equation 3.3, the kinetic energy of the nuclei, can be separated and the last term, the repulsion between the nuclei, can be considered constant at a given configuration of the nuclei:

$$\hat{H}_e = \hat{T}_e + \hat{V}_{ne} + \hat{V}_{ee} \tag{3.4}$$

The wave function can be expressed as the product of an electronic wave function $\left(\Psi_e(\vec{r};\vec{R})\right)$, which depends on both the electronic coordinates explicitly and on the nuclear coordinates parametrically, and a nuclear wave function $\left(\Psi_n(\vec{R})\right)$:

$$\Psi_{tot}(\vec{r};\vec{R}) = \Psi_e(\vec{r};\vec{R}) \cdot \Psi_n(\vec{R}) \tag{3.5}$$

Where $\vec{R}$ and $\vec{r}$ denote the nuclear and the electronic coordinates, respectively. Then, if the electronic Hamiltonian is applied to the electronic wave function, the electronic state of the molecule is obtained by solving *the electronic Schrödinger equation*:

$$\hat{H}_e\Psi_e(\vec{r};\vec{R}) = E_e(\vec{R})\Psi_e(\vec{r};\vec{R}) \tag{3.6}$$

Finally, the total energy $U_n(\vec{R})$ of the system, also known as potential energy, can be calculated as the sum of the electronic energy, $E_e(\vec{R})$, and the coulombic repulsion between nuclei, $\hat{V}_{nn}(\vec{R})$, for a fixed nuclear coordinates. However, the exact solution of the electronic Schrödinger equation is limited to the case of H_2^+, which is a monoelectronic system, while quantum chemistry is faced with many-electron problems.[165] Therefore, several methods to obtain approximate solutions to the electronic Schrödinger equation have been developed. In the following sections, the most popular electronic structure methods are briefly presented (wave function-based methods and density functional methods).

3.1.1. MANY-ELECTRON WAVE FUNCTION-BASED METHODS

Different *ab initio* methods were proposed to overcome the impossibility of exactly solving the electronic Schrödinger equation for many electrons systems. Some of them are based on the Hartree-Fock (HF) theory. Despite the fairly fundamental assumption of this theory, it provides a well-defined basis on which would be supported more sophisticated theories.[166]

3.1.1.1. Hartree-Fock method

The simplest antisymmetric wave function, which can be used to describe the ground state of an N-electron system, is a single Slater determinant; *i.e.*, the antisymmetric product of N-orthonormal one-electron wave functions (spin-orbitals, χ_i), which in turn are defined by the product of spatial function, $\phi_i(\vec{r})$, and spin function, $\alpha(s)$ or $\beta(s)$.[165] In the HF method, the Slater determinant that yields the lowest energy is obtained by minimizing the energy with respect to the spin-orbitals, under the condition that during the minimization they must remain orthonormal.[165,166] The resulting equations are the HF equations:

$$\hat{f}\chi_i = \varepsilon_i\chi_i, \qquad \text{i = 1,2,...,N} \tag{3.7}$$

This process generates N equations, where N is the number of electrons of the system. ε_i are the corresponding spin-orbital energies and $\hat{f}$ is the Fock operator, which includes the average potential created by the nuclei and the rest of the electrons over the electron *i*. To solve the HF equations, an iterative process known as Self Consistent Field (SCF) method, to determine the spin-orbitals, χ_i , is needed.[165]

Moreover, Roothaan and Hall proposed to express each molecular orbital as linear combination of functions, which are in general atomic orbitals (LCAO). Those orbitals constitute the basis set to solve the HF equations.[167,168]

$$\phi_i = \sum_{\upsilon}^{K} c_{\upsilon i}\varphi_\upsilon \tag{3.8}$$

In *equation 3.8*, the coefficients $c_{\upsilon i}$ are variationally determined through the SCF method and φ_υ are the basis functions. The lowest possible energy through the HF approximation is obtained from considering an infinite number of basis sets and is referred to the limit HF. Practically, a finite number of basis has to be chosen. The minimum basis set consists of one basis function per orbital. Nevertheless, it can be improved by using more extensive basis functions, such as double-ζ, triple-ζ, etc. depending if each atomic orbital is characterized by two, three, etc. basis functions. Moreover, polarization functions, which are higher angular momentum functions that describe the distortion of electronic distribution due to the bonds, can be added.

Finally, diffuse functions with lower exponents, but same angular momentum, can define a more extended electronic density.

3.1.1.2. Electron correlation

As mentioned, the HF method is the simplest approach to describe most of the chemical systems in QM. This method treats the electrons as independent particles that move in an average field and thus, does not consider the instant correlation between electrons. Hence, the correlation energy is defined as the difference between the non-relativistic exact energy (E_0) and the limit HF energy (E_{HF}):

$$E_{corr} = E_0 - E_{HF} \tag{3.9}$$

The correlation energy can be dived into two contributions: one called dynamic correlation which is related to the correlation of electron's motion and the other one, the non-dynamic (static) correlation, associated to the fact that sometimes more than one nearly degenerative Slater determinant is needed to describe the ground state.[163]

3.1.1.3. Post Hartree-Fock methods

Post Hartree-Fock methods include the correlation energy based on the HF method. The most important ones are: the variational method of *Configuration Interaction* (CI),[169] the perturbative *Møller-Plesset* method (MP)[170] and the *Coupled Cluster* method (CC).[171,172] For the last one there is a multiconfigurational variant that allows including the non-dynamic correlation, however this thesis only considers the monodeterminal formalism.

CI method is the simplest *post* Hartree-Fock method. It defines the wave function (Ψ_{CI}) as a linear combination of Slater determinants representing different electronic configurations:

$$\Psi_{CI} = \sum_I c_I \varphi_I \tag{3.10}$$

The solution consists in determining the eigenvalues of the system once the Hamiltonian representation matrix has been expressed on the basis of the configurations of determinants. Nevertheless, a Slater determinant is not always an

eigenfunction of $\hat{S}^2$. Therefore, when working with determinants, it should be taken into account that the spin-adapted configurations frequently include more than one determinant; meaning that the complete configuration has to be included in the expansion in order to preserve the space and symmetry properties of the wave function.

MP method is based in the Many Body Perturbation Theory (MBPT), which consists in expressing the Hamiltonian as the sum of two contributions: the zero-order Hamiltonian $\left(\hat{H}^{(0)}\right)$, whose eigenvalues $\left(E_i^{(0)}\right)$ and eigenfunctions $\left(\Psi_i^{(0)}\right)$ are known, and a perturbation operator $\left(\hat{V}\right)$. The exact energy and wave function can be expanded in an infinitive series whose elements are the zeroth-order energy and the wave function and the successive corrections, expressed through increasing powers of the perturbation operator.

$$\Psi_i = \Psi_i^{(0)} + \Psi_i^{(1)} + \Psi_i^{(2)} + \cdots \tag{3.11}$$

$$E_i = E_i^{(0)} + E_i^{(1)} + E_i^{(2)} + \cdots \tag{3.12}$$

In the MP method the zeroth-order Hamiltonian is taken as the sum of the Fock one-electron operator:

$$\hat{H}^{(0)} = \sum_i \hat{f}(i) \tag{3.13}$$

With this election, the sum of $E^{(0)}$ and $E^{(1)}$ gives the HF energy, thus higher-order corrections should be taken into account in order to incorporate the electronic correlation. Therefore, if the partition between the zeroth-order Hamiltonian and the perturbation is appropriate, this method enables to estimate the electron correlation effect on the energy and the wave function with a limited expansion. However, it is a non-variational method which avoids knowing the sign error on the estimated energy and, also, the convergence of higher order corrections is not ensured. Second-order MP (MP2) method is the most used.

CC method was introduced in the 1950s and is one of the methods that includes the electronic correlation in greater depth. The CC method inserted the concept of wave function operator $\left(\hat{T}\right)$ as an operator that transforms the reference wave function,

which can be the HF wave function, into the exact one. The wave function is expressed as:

$$\Psi_{CC} = e^{\hat{T}}\Psi_{HF} \tag{3.14}$$

$\hat{T}$ can be expanded as a sum of cluster operators for each possible excitation, where the subscript indicates the excitation order:

$$\hat{T} = \hat{T}_1 + \hat{T}_2 + \hat{T}_3 + \cdots \tag{3.15}$$

And the exponential can be expanded in a Taylor series:

$$e^{\hat{T}} = \hat{1} + \hat{T} + \frac{1}{2!}\hat{T}^2 + \frac{1}{3!}\hat{T}^3 + \cdots = \sum_{k=0}^{\infty}\frac{1}{k!}\hat{T}^k \tag{3.16}$$

Equaling the same excitation level terms, the degree-of-excitation relations are obtained. Hence, the exponential operator may be written as:

$$e^{\hat{T}} = 1 + \hat{T}_1 + \left(\hat{T}_2 + \frac{1}{2}\hat{T}_1^2\right) + \left(\hat{T}_3 + \hat{T}_2\hat{T}_1 + \frac{1}{6}\hat{T}_1^3\right) + \cdots \tag{3.17}$$

Within these expressions, two types of contributions can be observed: the so-called *linked* or *connected* cluster component of the i^{th} excitation degree $\left(\hat{T}_i\right)$ seen in *equation 3.15*, which corresponds to the simultaneously excitation of *i* electrons, and the *disconnected* components $\left(\hat{T}_k\hat{T}_j\right)$, which are products of lower excitation operators that may reach the same degree of i^{th} excitation degree.

The most used CC method, due to its less computational cost, is that which includes the simple and double excitations (CCSD).[173] Nowadays there are methods that include the effect of triple excitations, in an exact form (CCSDT) or approximately such as CCSD(T),[172] where the triple excitations are considered perturbatively.

Although the correlation energy represents only ~1% of the total system energy, it is crucial for calculating energy differences. For that reason, wave-function methods that include the correlation energy are very useful. However, these methods are computationally very costly and can only be applied to molecular systems of limited size. A cheaper alternative to include the correlation energy is the use of electronic density based methods which are described in the next section.

3.1.2. DENSITY FUNCTIONAL THEORY

During the last decades, the Density Functional Theory (DFT) has become a very popular tool to calculate systems of medium to large size. The success of DFT is based on the calculation of electronic properties from the electron density, instead of the wave function. Hence, for a system composed by N electrons, the density only depends on three coordinates regardless the electron number of the system; while the wave function methods implies the computation of the wave function for a given nuclear coordinates, which are function of 4N coordinates (3 coordinates for each electron and one more if the spin is considered).[163] Moreover, the electron density is an observable and can be measured experimentally (*i.e.* by X rays).

The electron density $\rho(\vec{r})$ is defined as the multiple integral over the spin variables of all electrons and over all but one of the spatial coordinates:

$$\rho(\vec{r}) = N \int \cdots \int |\Psi(\vec{x}_1, \vec{x}_2, \ldots, \vec{x}_N)|^2 ds_1 d\vec{x}_2 \ldots d\vec{x}_N \tag{3.18}$$

In this manner, $\rho(\vec{r})d\vec{r}$ represents the probability of finding any of the N electrons of the system within the volume element $d\vec{r}$ but with arbitrary spin, regardless the position of the other N-1 electrons. Furthermore, since the electrons are indistinguishable, the probability of finding any electron at that position is just N times the probability for one particular electron. Hence, $\rho(\vec{r})$ is a non-negative function of only three spatial coordinates that vanishes at infinity and integrates to the total number of electrons:

$$\rho(\vec{r} \to \infty) = 0 \tag{3.19}$$

$$\int \rho(\vec{r})d\vec{r} = N \tag{3.20}$$

The Thomas-Fermi (TF) model of a uniform electron gas[174,175] and the Slater local exchange approximation[176] are the conceptual roots in DFT. A formalistic evidence for the correctness of the Thomas-Fermi model was provided by the Hohenberg-Kohn (HK) theorems,[177,178] which along with the Kohn-Sham (KS) formalism[179] constitute the two core elements of DFT, which will be described in the next sections.

3.1.2.1. The Hohenberg-Kohn theorems

Hohenberg and Kohn stated two theorems that represent the theoretical bedrock of DFT.

The first HK theorem postulates that any observable of a stationary non-degenerate ground state for an electronic system of N particles can be determined from the electronic density of this ground state. Particularly, the electronic energy can be expressed as:

$$E[\rho] = T[\rho] + V_{ee}[\rho] + V_{ne}[\rho] \tag{3.21}$$

Where $T[\rho]$ is the kinetic energy functional and $V_{ee}[\rho]$ is the functional that represents the electron-electron interactions, which can be decomposed into two components: a coulombic one and a component that include all non-classical bielectronic repulsions. Finally, $V_{ne}[\rho]$ is the interaction energy with an external potential, normally due to the nuclei-electron interaction. If the terms that are dependent on the external potential are separated from those which are independent on it, the independent terms can be collected into a new quantity, the Hohenberg-Kohn functional, $F_{HK}[\rho]$:

$$E_v[\rho] = F_{HK}[\rho] + \int \rho(\vec{r})v(\vec{r})d\vec{r} \tag{3.22}$$

Where $E_v[\rho]$ indicates that, for a specific external potential $v(\vec{r})$, the energy is a functional of density. If $F_{HK}[\rho]$ is known, then the Schrödinger equation can be solved exactly.

The second HK theorem establishes that the electronic energy, calculated using *equation 3.21*, for any proof density $(\tilde{\rho})$ will be always greater or equal than the ground state energy (E_0). It means that the ground state energy can be obtained from the minimization of the $F_{HK}[\rho]$ functional at the ground state density:[180]

$$E_0 \leq E[\tilde{\rho}] = T[\tilde{\rho}] + V_{ee}[\tilde{\rho}] + V_{ne}[\tilde{\rho}] = F_{HK}[\tilde{\rho}] + \int \tilde{\rho}(\vec{r})v(\vec{r})d\vec{r} \tag{3.23}$$

These two theorems based the relation between the electronic density and the ground state energy; however they did not set the $F_{HK}[\rho]$ functional form. In 1965, W. Kohn

and L. Sham proposed a method that allowed the practical implementation of the HK theorems using atomic orbitals.

3.1.2.2. The Kohn-Sham formalism

KS method is based in the formulation of the TF and Thomas-Fermi-Dirac (TFD) methods[174,181,182] and it proposes the use of an estimated expression for the $F_{HK}[\rho]$ functional to solve the N-electron problem approximately. As above mentioned, the problem that arises is that the exact expression relating $F_{HK}[\rho]$ is not known. KS suggested calculating this kinetic energy using a reference system which involves N electrons that do not interact among themselves and which is described by one-electron orbital functions (the KS orbitals, ϕ_i); in such a way that it has an equal overall ground state density $\rho_s(\vec{r})$ than the density of the real system where electrons interact, $\rho(\vec{r})$:

$$\rho_s(\vec{r}) = \sum_{i=1}^{N} |\phi_i|^2 = \rho(\vec{r}) \tag{3.24}$$

Thus, the energy functional is redefined as:

$$E[\rho] = T_s[\rho] + V_{ne}[\rho] + J[\rho] + E_{XC}[\rho] \tag{3.25}$$

Where $T_s[\rho]$ corresponds to the kinetic energy of the non-interacting electrons system, $V_{ne}[\rho]$ accounts for the nuclear-electron interactions, $J[\rho]$ is the classical electron-electron Coulomb interactions functional and $E_{XC}[\rho]$, which is known as exchange-correlation functional, considers all quantum mechanical terms not included in $J[\rho]$; that is, it includes all non-classic corrections to the electron-electron interactions (*i.e.*, exchange and Coulomb correlations and the correction to the unphysical self-interaction contribution) and the kinetic correlation which implies the correction to the kinetic energy arising from the interacting nature of the electrons. The description of this last term is the most challenging aspect of DFT.

The electronic density can be calculated solving the N monoelectronic equations that results from applying the variational principle to the electronic energy, with the charge density given by *equation 3.24*:

$$\hat{h}_{KS}\phi_i = \varepsilon_i\phi_i, \qquad \text{i} = 1,2,\ldots, \text{N} \tag{3.26}$$

This is the KS equation where $\hat{h}_{KS}$ represents the KS Hamiltonian and ε_i is the KS orbital energy associated. This equation is iteratively solved starting from any proof density $(\tilde{\rho})$ which can be obtained from the density superposition of constituent atoms for a molecular system. Moreover, the KS orbitals are expressed as linear combination of a basis set. In this way, the KS equation solution corresponds to the coefficients determination of the linear combination, similarly to the HF process.

Several DFT methods use different approximations of $E_{XC}[\rho]$ term to apply the KS approach. Usually, this energy is split in two contributions: the exchange term, E_X, which is known as exchange functional and it is associated to the interactions between electrons with the same spin, and the correlation term, E_C, which is also called correlation functional and it considers the opposite spin electronic interactions.

$$E_{XC}[\rho] = E_X[\rho] + E_C[\rho] \tag{3.27}$$

Both contributions can be of two distinct types: local functionals, which depend only on the electron density, ρ, and gradient corrected functional, depending on both ρ and its gradient, $\nabla\rho$. These types of functionals are those that KS proposed to estimate the Schrödinger solution and will be explained in more detail in the next section.

3.1.2.3. Exchange-correlation potential approximations

The form of exchange-correlation functionals is often designed to have a certain limiting behavior and fitting parameters to known accurate data. In the next few pages, the different types of exchange-correlation functionals and the approximations that are behind them will be explained.

Local Density Approximation (LDA) constitutes the simplest approach to represent the exchange-correlation functional. The exchange energy estimation was proposed by Dirac[182] and assumes that density can be locally treated as homogeneous and constant using an electron gas model:

$$E_X^{LDA}[\rho] = -\frac{3}{4}\left(\frac{3}{\pi}\right)^{1/3}\int \rho^{4/3}(r)dr \tag{3.28}$$

As far as the correlation part E_C^{LDA} is concerned, no expression for the energy is known. However, there are accurate numerical quantum Monte Carlo simulations from which analytical expressions based of interpolation schemes have been developed;[183] one of the most widely used is the Vosko-Wilk-Nusair (VWN) functional.[184]

In the LDA, the total density is considered to be the sum of α and β spin densities. Nevertheless, when these densities are not equal, as for open-shell systems, the *Local Spin Density Approximation* (LSDA) is more appropriated because it introduces spin dependence into the functionals. The exchange energy in the LSDA is:

$$E_X^{LSDA}[\rho] = -(2)^{1/3}\frac{3}{4}\left(\frac{3}{\pi}\right)^{1/3}\int\left[{\rho_\alpha}^{4/3}(r) + {\rho_\beta}^{4/3}(r)\right]dr \tag{3.29}$$

Despite the simplicity of these approximations, they provide acceptable results for a large number of systems. A partial explanation of it resides in the systematic error cancelation. In fact, LDA underestimates E_X but overrates E_C generating a surprising correct value for E_{XC}.

Generalized Gradient Approximation (GGA) considers that exchange and correlation terms not only depend on the electron density, but also on its derivatives; whereas LDA assumes that the exchange-correlation energy effects are local and only depend on the value of the electron density at each point. It means that GGA take into account the variations in the densities around each point of the system. The general expression for the exchange-correlation functional in the GGA is:

$$E_{XC}^{GGA}[\rho] = \int f(\rho, \nabla\rho)d\vec{r} = E_X^{GGA}[\rho] + E_C^{GGA}[\rho] \tag{3.30}$$

Most of the GGA exchange functionals are developed following two main philosophies. The first one, which was initially proposed by Becke, is based on fitting empirical parameters usually considering experimental data for a huge set of atoms or model molecules. Some examples of exchange functionals that follow this philosophy are the Becke88 (B88),[185] the modified Perdew-Wang (mPW)[186] and the OptX (O),[187] while in the exchange-correlation functional highlights of Perdew-Wang (PW).[188] On the other side, the second philosophy considers that the development of exchange functional should be based on principles derived from QM. The most common exchange functional is the Becke86 (B86),[189] while the extremely popular correlation

functional is the Lee-Yang-Parr (LYP)[190] and one of the most utilized exchange-correlation functional is the Perdew-Burke-Ernzerhof (PBE).[191] In principle, all the correlation functionals could be combined with any of the exchange functionals, but in practice, only some combinations are currently in use.

GGA corrections improve the geometries, frequencies and LDA charges densities and work reasonably well for systems with hydrogen bonds, although they fail to describe van der Waals complexes.

Meta-GGA (M-GGA) methods are based on the GGA but also include additional semi-local information beyond the first-order density gradient contained in the GGAs. Thus, the *meta*-GGA functionals depend on the density, the higher order density gradients $\left(\nabla^2\rho(r)\right)$ and the kinetic energy density, τ:

$$E_{XC}^{meta-GGA}[\rho] = \int f(\rho, \nabla^2\rho, \tau)d\vec{r} \tag{3.31}$$

Some examples of these types of functionals are the exchange-correlational functionals Becke98 (B98);[192] Tao, Perdew, Staroverov and Scuseria (TPSS)[193] and Van Voorhis and Scuseria (VSXC).[194]

Hybrid density functional (H-GGA) methods are characterized by combining the exchange-correlation of a conventional GGA method with a percentage of exact exchange (Hartree-Fock). In fact, the amount of exact exchange is fitted empirically because it cannot be assigned from first-principles.

Currently, one of the most popular hybrid functional is the Becke's 3-parameters method (B3LYP), which uses the B88 exchange functional and the LYP correlation functional with a 20% of exact exchange. As the LYP functional contains a local part besides of the correction to the gradient, the LSDA-based correction functional derived from VWN functional is also added in order to subtract this local part. The exchange-correlation energy for the B3LYP is expressed as:

$$E_{XC}^{B3LYP} = aE_X^{exact} + (1-a)E_X^{LSDA} + b\Delta E_X^{B88} + cE_C^{LYP} + (1-c)E_C^{VWN} \tag{3.32}$$

The *a, b* and *c* values were parameterized to reproduce a series of properties such as energies, ionization potential and protonic affinities. The *a* coefficient determines the

exact exchange percentage of the functional (20%, in this case). In the last years, it has been by far the most popular and widely used functional. However it fails in certain aspects, like the non-covalent interactions description which is not very accurate.

Hybrid-meta GGA (HM-GGA) methods represent one of the newest class of DFT functionals. Based on a similar concept to the M-GGA functionals, HM-GGA methods depend on the exact exchange (represented in the *equation 3.33* as λ), the electron density and its gradient, and the kinetic energy density:

$$E_{XC}^{HM-GGA}[\rho] = \int f(\lambda, \rho, \nabla\rho, \tau) d\vec{r} \tag{3.33}$$

Some functionals belonging to this category are the Minnesota M06 family developed by Truhlar,[195] which accounts for short-range dispersion and better describes non-covalent interactions. This family includes four functionals: M06-L,[196] without exact exchange (thus, it would be a M-GGA functional); M06,[195] with 27% of exact exchange; M06-2X,[195] with 54% of exact exchange; and M06-HF,[197] with 100% of exact exchange. These methods represent an improvement over the previous formalisms, particularly, in the determination of barrier heights and atomization energies. The exchange-correlation energy for the M06 functionals (except M06-L) can be written as:

$$E_{XC}^{M06X} = \frac{X}{100} E_X^{exact} + \left(1 - \frac{X}{100}\right) E_X^{M06} + E_C^{M06} \tag{3.34}$$

Where E_X^{exact} is the exact exchange energy, X is the percentage of exact exchange of the hybrid functional and E_X^{M06} and E_C^{M06} are the exchange and correlation energy of the M06 functional, respectively.

3.1.2.4. Limitations of DFT

a) Dispersion: DFT functionals are not able to describe the van der Waals interactions, which derive from electron correlation at "medium" to "long range", accurately. In addition to the Truhlar's functionals, which partially recover these contributions, there are other ways of improving the description of non-covalent interactions in DFT.[198–201] Among them, probably the most popular is the dispersion correction method (DFT-D), commonly known as Grimme's dispersion correction.[198] The

correction consists in adding to the Kohn-Sham energy a dispersion energy term defined as:

$$E_{disp} = -s_6 \sum_{i=1}^{N_{at}-1} \sum_{j=i+1}^{N_{at}} \frac{C_6^{ij}}{R_{ij}^6} f_{dmp}(R_{ij}) \tag{3.35}$$

Where s_6 is a global scaling factor that only depends on the density functional used, N_{at} is the number of atoms in the system, C_6^{ij} denotes the dispersion coefficient for ij atom pair, R_{ij} indicates the interatomic distance and f_{dmp} is a damping function to avoid unphysical behavior of the dispersion term for small distances. This last term is an exponential function that goes down quickly when the interatomic distances are short; hence, the dispersion correction for the *i* and *j* atoms, which are under the van der Waals distance, is zero. Then, the common bonds are not affected by the dispersion.

Recently, some additional corrections have been added to this term resulting in a considerably improvement of the performance of these dispersion corrected density functionals.[202–204]

b) Self-interaction error: another problem that one can find using a DFT functional is the so-called *self-interaction error*, which may be especially important in open-shell systems as those used in this thesis. The inclusion of high exact exchange percentage corrects rigorously the self-interaction error.

Probably, the easiest way of understanding this error is to consider the particular case of a one-electron system. In accordance with HF method, the electronic energy of the system is given by:

$$E_{HF} = \sum_{i=1}^{N} \varepsilon_i - \frac{1}{2} \sum_{i=1}^{N} \sum_{j=1}^{N} (J_{ij} - K_{ij}) \tag{3.36}$$

Where ε_i is the energy of electron *i* and *J* and *K* are the Coulomb and exchange integrals, respectively. In a monoelectronic system, since there is no electron-electron repulsion, the terms *J* and *K* in *equation 3.36* are equal and different of zero, which leads to the complete cancellation of the self-interaction of the electron *i*. In the KS scheme (*equation 3.25*), the term $J[\rho]$ is also different to zero, because

it contains the false interaction of the density with itself, and it must be equal with opposite sign to E_{XC} to be completely cancelled. However, as the exact form of the exchange-correlation functional is not known, and estimated approximations must be used, the difference between $J[\rho]$ and E_{XC} fails to completely vanish.

The self-interaction error correction is uncomplete in LDA and GGA functional and leads to an overstabilization of the delocalized situations. In fact, studies developed by our group in Cu^{2+}-ligand systems have demonstrated that functionals with different exact exchange percentage can provide important differences in the results regarding to charge and spin delocalization.[205–208] In these cases, the inclusion of exact exchange percentage reduces the self-interaction error leading to better results compared with the CCSD(T) method.[209]

3.2. MOLECULAR MECHANICS

Molecular Mechanics (MM) uses classical mechanics to model molecular systems. It is based upon a rather simple model of the interactions within a system with contributions from processes such as the stretching bonds, the opening and closing of angles and the rotation about single bonds. This method ignores the electronic motions and calculates the energy of a system as a function of the nuclear position only. Therefore, it can be used to study large biological systems or material assemblies with thousand atoms. However, the MM method cannot be used to predict any property depending on the electronic distribution, including reactive processes.[210]

3.2.1. FORCE FIELDS

Force Field (FF) methods deal with molecules as mechanically connected systems of atoms where electrons are not treated explicitly but together with the nuclei as effective atoms. Hence, the calculation of the electronic energy (E_{el}) for solving the electronic Schrödinger equation is bypassed by writing E_e as a parametric function of the nuclear coordinates where the parameters that enter the function are fitted to experimental or higher computational data level.[211–213] Therefore, FF methods are also referred to MM methods because the quantum aspects of nuclear motion is neglected which means that the dynamics of the atoms is treated by classical mechanics.

The foundation of FF methods is that molecules tend to be composed of structural units which are similar in different molecules. This idea is implemented in FF models as *atom types*. The *atom type* depends on the atomic number and the type of involved chemical bonding. The *type* may be denoted either by a number or by a simple letter code. Furthermore, FF calculations enable predictions of relative energies and barriers for interconversion of different conformations.[163]

3.2.2. FORCE FIELD ENERGY

The force field energy includes bonded terms for interactions of atoms that are linked by covalent bonds, non-bonded terms that describe the long-range electrostatic and van der Waals forces and it can be writing as a sum of terms:

$$E_{FF} = E_{str} + E_{bend} + E_{tors} + E_{cross} + E_{vdw} + E_{electros} \quad (3.37)$$

E_{str} is the energy function for stretching a bond between two atoms and E_{bend} represents the energy required for bending an angle. These are the bond and angle term, respectively, and are usually modeled by quadratic energy functions that do not allow bond breaking. E_{tors} is the torsional energy for rotation around a bond and E_{cross} describes coupling between these first three terms. Those four terms are the bounded related terms. E_{vdw} is usually computed with a Lennard-Jones potential and $E_{electros}$ is commonly calculated by Coulomb's law. Both terms describe the non-bonded atom-atom interactions. Minimizing E_{FF} as a function of the nuclear coordinates makes possible to locate the stable structures that correspond to minima on the potential energy surface.[163]

3.2.3. DIFFERENCES IN FORCE FIELDS

Nowadays, there are many different force fields in use. They differ in three main aspects:

a) The functional form of each energy term.
b) The number of cross terms included.
c) The type of information used for fitting the parameters.

There are two general trends; one designed primarily to treat large systems where the functional forms are kept as simple as possible. This means that only harmonic functions are used for E_{str} and E_{bend} and no cross terms are included as well as Lennard-Jones potential is used for E_{vdw}. Such force fields are often called "harmonic" or "Class I". The second trend consists on reproducing small to medium size molecules to a high degree of precision. These force fields will include a number of cross terms, use at least cubic or quartic expansions of E_{str} and E_{bend}, and possibly an exponential type potential for E_{vdw}. Such FFs are often called "Class II".[163]

The first use of a FF is attributed to M. Levitt and S. Lifson, when in 1969 refined the conformation of a protein from its X-ray structure.[214] One year later, A. Warshel published the first consistent FF[215] and N. L. Allinger and J. T. Spargue implemented in 1973 the MM1 force field in the first MM software package.[216] Up to now, several FFs have been developed, published and incorporated into various molecular modeling packages. For simulation on biomolecular systems, the most noteworthy FFs are the *Assisted Model Building with Energy Refinement* (AMBER),[217,218] *Chemistry at HARvard Molecular Mechanics* (CHARMM),[219] *GROningen MOlecular Simulation* (GROMOS)[220] and *Optimized Potential for Liquid Simulations* (OPLS).[221] All of them belong to Class I. Each of them has different parameters or even different atom types and these variations cause that the information transfer between them become arduous. However, some comparative studies of different FFs reveal that, in spite of some discrepancies, the global result is usually similar for all of them.[222]

The main advantage of FF methods is the speed at which calculations can be performed which enables large systems to be treated. Transferability of FF enables a set of parameters developed and tested on a relatively small number of cases to be applied to a much wider range of problems.[210] Nevertheless, if the molecule is slightly out of the ordinary, it is very likely that only poor quality parameters or none at all, exist. Hence, FF do not present a total transferability and the quality of the result can only be judged by comparison with other calculations on similar types of molecule, for which relevant experimental data exist.[163]

3.3. QM/MM HYBRID METHODS

Despite the great progress of computational chemistry; accurate atomistic description of huge systems continues being an important challenge. During the last years only force-field-based MM methods, which are based in classical mechanics, are able to achieve these kinds of simulations. However, such methods are unsuitable to describe chemical reactions and electronic processes as charge transfer. As it has been mention before, those electronic processes need QM methodology. Nevertheless, QM methods are restricted to systems of up to a few hundred atoms. For that reason, combined Quantum-Mechanics/Molecular-Mechanics (QM/MM) approaches have become the method of choice for modeling reactions in biomolecular systems.[223,224]

The basic idea of the QM/MM methodology is to use a QM method for the chemical active region also called inner region (*I*), usually a DFT method due to its favorable computational-effort/accuracy ratio, and a MM treatment for the surroundings which is considered the outer region (*O*). Hence, this approach implies a reasonable computational effort while it provides the necessary accuracy.

Owing to the interactions between the QM and the MM regions, the total energy of a system (*S*) cannot be simple written as the sum of the energies of the subsystems. There are two schemes to deal with this: the *subtractive* and the *additive*. *Subtractive* QM/MM model requires an MM calculation on the entire system and both QM and MM calculation on the inner system. Therefore, the energy can be expressed as:

$$E_{QM/MM}^{sub} = E_{MM}(S) + E_{QM}(I) - E_{MM}(I) \tag{3.38}$$

The main advantage of the subtractive scheme is its simplicity inasmuch it can be seen as an MM approach where certain region of space has been cut out and is treated at QM level. But, a complete set of MM parameters for the inner subsystem is needed and the coupling between the subsystems is handled entirely at the MM level which implies a particular problem for the electrostatic interaction. One of the most popular QM/MM method based in this arrangement is *Our N-layered Integrated molecular Orbital and Molecular mechanics* (ONIOM) method.

On the other hand, the basic energy expression for an additive QM/MM scheme is:

$$E_{QM/MM}^{add} = E_{MM}(O) + E_{QM}(I) + E_{QM-MM}(I,O) \tag{3.39}$$

In this case, the MM calculation is only performed on the outer subsystem and appears an explicit coupling term $E_{QM-MM}(I,O)$ which considers the interaction between the two subsystems. The exact form of the last term defines a particular QM/MM method. It includes bonded, van der Waals and electrostatic interactions.[224] Hence, the interaction between the QM and the MM region is critical.

3.3.1. BOUNDARY TREATMENT

There are different approaches to treat the boundary between the QM and MM regions.[225] One of them is the *link atom* approach[166] which consists in the introduction of a hydrogen atom into the quantum system at the location of the boundary between the QM and MM regions; that is, the hydrogen atom saturate the broken bonds in the frontier atoms. This link atom is usually a hydrogen atom which involves a parametrized semiempirical Hamiltonian[226] or a parametrized Effective Core Potential (ECP)[227,228] adjusted to mimic the properties of the original bond being cut. This method is simple and widely used.

An alternative to the *link atom* method are the Local Self-Consistent Field (LSCF) methods developed by V. Thery and coworkers.[229] These methods use local orbitals which are more fundamental because they provide a QM description of charge distribution around the QM/MM boundary. A more generalized form of this implementation was Generalized Hybrid Orbitals (GHO) presented by Gao et al.[230] in which a set of hybrid orbitals are used at the boundary region. In this approach, a set of four hybrid orbitals is assigned to each MM boundary atom and the one that is directed toward the frontier QM atom is called the active orbital. Hence, the four orbitals are included in the QM calculation, but only the active orbital participates in the SCF procedure.

An appropriate boundary election is really important and there are some general rules to choose it. The more important ones are that the QM/MM frontier should be as distant from the active region as possible controlling the size of QM part and that the bond being cut should be non-polar and not involved in conjugated interactions.

3.3.2. ELECTROSTATIC COUPLING SCHEMES

The electrostatic coupling between the QM charge density and the charge model used in the MM region can be managed at different levels which are classified as: *mechanical, electrostatic* or *polarized embeddings.*[224]

The *mechanical embedding* is characterized by the application of the same charge model of the MM method, which is typically the rigid atomic point charges, to the QM region. It means that the interactions between the QM and the MM regions are treated at MM level. The main limitation is that charges in the outer region do not interact with the QM density, which is not directly influenced by the electronic environment.

Nevertheless, the *electrostatic embedding* avoids the *mechanical embedding* problem because, in this approach, the inner region can adapt to changes in the charge distribution environment and is automatically polarized by it. The QM-MM electrostatic interaction is treated at the QM level, which provides a more advanced and accurate description of the interaction, adding a monoelectronic operator in the QM Hamiltonian. Despite the increase in computational demand, the *electrostatic embedding* is the most used embedding scheme nowadays.

The most sophisticated approach is the *polarized embedding* which introduces a flexible MM charge model that is polarized by the QM charge distribution. It can be divided into two approximations; one where the polarizable charge model in the MM region is polarized by the QM electric field but does not act back on the QM density, and an ideal fully self-consistent formulation that includes the polarizable model into the QM Hamiltonian which allows for mutual polarization. However, there are yet no generally established polarizable biomolecular force fields.

3.4. SOLVENT EFFECTS

The appropriate description of the solvent effects is essential for the study of the structure and reactivity of biological systems in the presence of solvent. In order to consider the solvent effects, there are two alternatives. One of them implies the use of individual solvent molecules explicitly, which considerably increase the computational cost. The other alternative is more affordable because it treats the solvent as a continuous medium; that is the reason why is named as *continuum methods*.

The explicit solvent methods employ hundreds or thousands of discrete solvent molecules which are described using either empirical potentials, which includes several fitted parameters, or *Ab initio* potentials, which are computationally more expensive. Among them, there are a variety of potential functions to describe intermolecular liquid water interactions. These models differ regarding the number of interactions sites, the geometric arrangements and the parametrization of the charge sites.[231] The simplest possible model for water uses a Lennard-Jones sphere with two embedded charges of equal magnitude and opposite sign to mimic water's dipole moment. Thus, a solute molecule sees three interaction sites: the center of the sphere and the two point charges.[166] One of them is the *Transferable Intermolecular Potential* 3-point model (TIPS3), which has positive charges on the hydrogens and a negative charge on oxygen.[232] Subsequently, Berendsen used the same model, but optimized the parameters to improve the energy for liquid water obtaining the *Simple Point Charge* (SPC) potential.[233] More recently, TIPS3 was reparametrized to meliorate the energy and the density of liquid water, which has been called TIP3P.[232] However, four site models give better results to describe liquid water. Hence, the first 4-site form was proposed by Bernal and Fowler based on calculations of properties of the monomer, dimer and ice, which was called BF potential.[234] Nevertheless, there is an alternative parametrization, called TIP4P, which yields a slightly higher density.[232] The remaining 5-site model function is the ST2 potential of Stillinger and Rahman.[235] An extra site increases the complexity and, thus, the computational cost.

Continuum methods consider the solvent as a uniform polarizable medium with a dielectric constant, ϵ, where the solute is placed in a suitable shaped hole in the medium. The solvation free energy can be calculated as the sum of different energy contributions:

$$\Delta G_{solv} = \Delta G_{cav} + \Delta G_{disp-rep} + \Delta G_{elec} \tag{3.40}$$

In this expression, ΔG_{cav} corresponds to the energetic cost that is needed to create the cavity for the solute and, for that reason, it is always a non-stabilizing term. The second term, $\Delta G_{disp-rep}$, is associated with the dispersive-repulsion interactions between solute and solvent and, also, contributes positively to the solvation. These two terms are also called steric or non-electrostatic contributions. Finally, ΔG_{elec} is a stabilizing term which refers to the electrostatic interactions between the solute and the solvent. Concretely, it includes two components. The work necessary to create the solute's gas-phase charge

distribution in solution and the work required to polarize the solute charge distribution by the solvent.[236] Therefore, the wave function optimization is performed as an iteratively repeated process until the mutual polarization between the solute and the solvent achieves the self-consistency. This process is known as Self-Consistent Reaction Field (SCRF).[237]

Within SCRF method, there are different models depending on several features. Among them, the most common ones are: the *Polarizable Continuum Model* (PCM),[238] the *COnductor-like Screening MOdel* (COSMO)[239] and the recently developed universal *Solvation Model Density* (SMD).[240] This last model is the one used in this thesis.

The PCM model defines the cavity for the solute as the union of a series of interlocking spheres centered on the atoms. There are other variants of PCM solvent model, such as *Integral-Equation-Formalism* PCM (IEF-PCM) which includes other properties of the specific liquid besides the permittivity to treat anisotropic environments and can be generalized to be used in many other environments.[241] The COSMO model considers the solvent as a conductor; thus, the electrostatic equations are considerably simpler. On the other hand, SMD model is based on the polarized continuous quantum mechanical charge density of the solute and does not utilize partial atomic charges causing that its applicability does not depend on the availability of reasonable charges for a given level of theory.[242]

As we mentioned before, to create the cavity of the solvent, an overlapping sphere model is used, for which is necessary to describe the radii of these spheres. There are different radii types[242,243], but in this thesis the Universal Force Field (UFF)[244] radii have been used, which places a sphere around each solute atom with the radii scaled by a factor of 1.1. This radii type is employed as default in the *Gaussian09* package.[245]

3.5. MOLECULAR DYNAMICS

Molecular Dynamics (MD) methodology is based on the application of the classical mechanics laws to microscopic systems which enable to predict macroscopic thermodynamic and dynamic observables for a wide variety of systems at finite temperature.[246] Moreover, MD is useful as a guide toward understanding the mechanisms underlying a given chemical process. In addition, it permits direct visualization of the

detailed motions of individual atoms in a system, thereby providing a window into the microscopic world. Many of these applications address important problems in biology, such as protein and nucleic acids folding, as well as in material science, like surface diffusion and catalysis. Hence, MD simulations provide the methodology for performing time-evolution studies of systems at the atomic scale (femtoseconds to microseconds) and the trajectories of atoms are determined by solving the Newton's equations of motion for a N-particle system which for particle *i* takes the form:

$$m_i \frac{d^2 r_i}{dt^2} = F_i\left(r_1, \ldots, r_N, \frac{dr_i}{dt}\right) \tag{3.41}$$

Where m_i is the mass of the particle i, r_i is its position, $v_i = dr_i/dt$ is its velocity and $a_i = d^2r_i/dt^2$ is its acceleration; finally, F_i is the force experimenting the i^{th} particle due to all of the other particles in the system. Moreover, the gradient of the potential energy, E, of the whole system, acting on particle i, represents the force F_i exerted on particle i:

$$F_i = -\nabla_i E \tag{3.42}$$

Once the *equation 3.41* and *3.42* are combined, the relationship between the potential energy and the positions of the particles is:

$$-\frac{dE}{dr_i} = m_i \frac{d^2 r_i}{dt^2} \tag{3.43}$$

To start a simulation, the initial coordinates and velocities need to be assigned to all the particles in the system. Unfortunately, the interparticle forces are highly nonlinear functions of the N particle positions so that *equation 3.43* possesses enormous dynamical complexity and obtaining an analytical solution is hopeless. Thus numerical methods, for instance *Verlet*[247] or *leap-frog*[248] algorithms, are used to solve the classical equations of motion. Nowadays, the methodology is capable of performing many different types of MD calculations.

All the above mentioned treatments can be merged with MD obtaining the MM, QM and QM/MM molecular dynamics. Specifically, one of the major milestones in molecular dynamics is the *ab initio* or first-principles MD within the Born-Oppenheimer

approximation for the valence electrons treatment (here simplified as AIMD).[249] AIMD simulations can avoid the MD problems to predict chemical bonding processes because the forces are computed from the electronic structure "on the fly" as simulation proceeds, thereby enabling to treat explicitly the breaking and formation of chemical bonds. However, the increased accuracy and predictive power of AIMD comes at significant computational cost. For that reason, approximation schemes, such as DFT methods, are widely used to solve the electronic Schrödinger equation.[250]

3.5.1. THERMODYNAMIC ENSEMBLES

Classically, the microscopic state of a system is a function of the momenta and coordinates of its particles which form the phase space. Each state of the system is represented by a single point in the phase space. Thus, a collection of a huge number of single points in the phase space, satisfying the conditions of a specific thermodynamic state, is needed. This collection is called ensemble.

The basis of the ensemble concept originally introduced by Gibbs is the idea that macroscopic observables of a system are not sensitive to precise microscopic details. More formally, an ensemble is a collection of systems described by the same set of microscopic interactions and sharing a common set of macroscopic properties. Each system evolves under the microscopic laws of motion from a different initial condition so that at any point in time, every system has a unique microscopic state. Once an ensemble is defined, macroscopic observables are calculated by performing averages over the system in the ensemble. They can be defined for a wide variety of thermodynamic situations. Some of them with different characteristics are described below.[251]

The *microcanonical ensemble* (NVE) is used to represent the possible states of a mechanical system characterized by fixed values of the N identical particles in a container of volume, V, with a total internal energy, E. The N, V and E variables are all macroscopic thermodynamic quantities referred to *control variables* which are simply quantities that characterize the ensemble and that determine other thermodynamic properties of the system. The main disadvantage of this ensemble is that experiments are not performed under constant total energy conditions. Therefore, the development of

different ensembles that have different sets of thermodynamic *control variables* in order to reflect more common experimental setups is important.

The *canonical ensemble* (NVT) describes a system in contact with an infinite thermal bath whose *control variables* means a constant number of particles, *N*, constant volume, *V*, and constant temperature, *T*. In addition, it forms the basis for the *isothermal-isobaric* (NPT) and the *gran canonical* (μVT) ensembles. The first one maintains a constant number of particles, *N*, a constant pressure, *p*, and a constant temperature, *T*, in the system. Whereas the second one characterizes a system that maintains the thermodynamic equilibrium with a reservoir; thus, the system is open to exchange energy and particles with the reservoir at chemical potential, μ.

When a system is in thermal contact with an infinite external heat source, as in the three last mentioned ensembles, its energy will fluctuate so that its temperature remains constant. In order to generate these fluctuations several methods have been proposed. One of the most accurate and efficient method is the Nosé-Hoover thermostat,[210] which was originally introduced by Nosé in 1984[252] and subsequently modified by Hoover in 1985.[253]

3.6. HOMOLOGY MODELING

The 3D structures of proteins provide important information about their function and molecular properties, which allow obtaining proper starting points for experimental design, such as directed mutagenesis, mutation studies related to diseases or specific inhibitor design based in the proteins structure. However, the experimental methods, as X–rays techniques or NMR spectroscopy, do not always lead to the 3D structure procurement because its high complexity. Nowadays, near 67.000 3D structures exist in the Protein Data Bank (PDB),[254,255] but this number is small compared with the known sequences number deposited in the UniProt, which in 2010 had close to 4.2 million of series.[256] For that reason, in the last years, molecular modeling techniques have become a very useful tool to obtain 3D structures from known chains.

One of those methodologies is the Homology Modeling (HM) method, whose aim is to build 3D models for an unknown structure (*target*) based on its sequence similarity with one or more protein of established structure (*template*).[257–260] This method is based on the

idea that the higher the similarity of the chains between proteins, the higher the structural similarity. Therefore, two conditions must be achieved. Firstly, the similarity between the *template* and the *target* must be considerable; in general, sequences with less similarity than the 20% give significantly different 3D structures. Secondly, the amino acid alignment between the *template* and the *target* must be correct, since diversity on the sequences could result in significant differences in their 3D structures.[261] For that reason, HM methods consist in four sequential steps: identification of the *template* related to the *target*, alignment between the *target* and the *template* sequence, model *target* building based on the *template* 3D structure and model evaluation,[262] which will be explained in detail in the fourth chapter of the thesis.

Nowadays, there are several programs that use HM techniques to build model protein structures; among them, SwissModel,[263] Composer,[264,265] 3D-JIGSAW[266] and Modeller.[267] Within these programs, Modeller is particularly interested because it can include additional constrains, like distances or dihedral angles to build the model, as well as stereochemistry restrains.[268,269] This program uses as starting information the *target* sequence alignment with the *template* chain. The result, if no additional data are added, is the 3D *target* model including all heavy atoms of both the backbone and the side chains.

In order to explore the conformational space, Modeller restrains many distances and dihedral angle on the *target* sequence. This constrains were derived from the statistics analysis of the relationships between many pairs of proteins, obtained from a database of proteins with known 3D structures, which contain highly similarity fragments with the *target* protein.[270] These relations are expressed as conditional probability density function and can be used directly as space restrains. After that, the spatial constrains and CHARMM 23[219] energy terms, enforcing proper stereochemistry,[271] are combined into a *target* function. In this way, the model is obtained optimizing the *target* function into the space. This optimization employs conjugated gradient methods[272] and Simulated Annealing (SA)[273,274] molecular dynamics. This last method is a sequential stochastic search technique designed to avoid local optima. In SA techniques, the initial temperature is chosen to be high and during the MD process it is slowly reduced (by analogy with annealing in metals). This implies that the molecule may initially move over a large area, but as the temperature is decreased, it becomes trapped in a minimum. Therefore,

reaching the optimal solution can be labored because optimal results require that the temperature decreases very slowly from iteration to iteration.

After the conformational search, several conformations can be obtained. Therefore, a clustering analysis should be done in order to select some of the most relevant conformations for further studies. The objective of cluster analysis is to assign observations to groups ("clusters") so that observations within each group are similar to one another with respect to variable or attributes of interest and the groups themselves stand apart from one another. In other words, the aim is to divide the observations into homogeneous and distinct groups. Cluster analysis seeks to discover the number and composition of the groups.[275]

In this case the clustering method employed is *NMRClust*[276] which ensemble members into conformationally-related sub-families. All structures are superposed in a pairwise manner and the resulting Root Mean Square (RMS) distances between each pair are calculated. *Average linkage* cluster analysis, which considers the distance between two clusters as the average of the distances of all pairs of observations, is used in conjunction with a penalty function to automatically determine a cut-off in the clustering hierarchy. Once the models are clustered, the one closest to the centroid of the largest cluster is selected as the most representative.

In this chapter, a general methodology has been presented in order to understand the theory behind the computational details used in this thesis which will be described more explicitly in each result chapters.

4

3D Cu^{2+}-Aβ_{1-16} STRUCTURES

The elucidation of the Cu^{2+} coordination to Aβ is essential to understand the metal ion role on the peptide aggregation and for the design of new strategies against AD. Because of that, many experimental works have focused on determining the coordination environment of Cu^{2+} interacting with Aβ. EPR experiments reveal the existence of two main species in the physiological pH range: one referred to component I at low pH, which involve the terminal amino group, an oxygen atom from Asp1, His6 and His13 or His14 (depending if it is component Ia or Ib, respectively), and a second one related to component II at higher pH, where two possible coordination environment have been proposed, component IIa that involves three histidine residues and the carbonyl group of Ala2 and component IIc that only involve one histidine along with the N_{tern}, the deprotonated amide nitrogen of Ala2 and carbonyl oxygen (see *Figure 1.3*).[68,78] Nevertheless, as important as characterizing the

first metal coordination sphere, is the determination of the entire structure of Cu-Aβ complexes, since the conformation adopted by the peptide upon copper attachment may also influence the physicochemical properties of the formed complexes. For instance, the information could be useful as starting point for understanding the role of metal cation interactions in the initial stages of nucleation and plaque formation as well as to explain the metal complexes mediation in redox activity. It has not been possible to obtain by experimental methods, such as NMR or X-ray, the monomeric 3D Cu-Aβ structure. All of these leaded the group to start a research to determine the 3D structure of these complexes. Dr. Jorge Alí Torres studied, during his PhD thesis, the different ligand affinity according the experimental data of that moment (3 His and 1 O as metal coordination environment),[77] as well as the redox properties of Cu-$A\beta_{1-16}$ complexes. Therefore, theoretical methods can play an important role in the determination of such structures.

In this chapter, the most plausible 3D Cu^{2+}-$A\beta_{1-16}$ structures will be proposed. As the number of possible Cu-Aβ structures is noticeably elevated, the computational modelling of these complexes requires addressing two fundamental aspects: the metal coordination sphere and the conformation adopted by the peptide. To perform this, strategies that combine experimental data, QM and HM methods should be used.

4.1. COMPUTATIONAL APPROACH

The protocol to build the 3D Cu^{2+}-$A\beta_{1-16}$ structures starts by studying the model systems that include the first coordination sphere of the metal, proposed experimentally, with QM techniques. Afterwards, the entire Cu^{2+}-$A\beta_{1-16}$ complex is generated using HM approaches. Finally, the obtained complexes are refined with QM calculations.

This multiscale protocol shares common grounds with the one reported in a previous study of the group on component IIa.[277] However, the present procedure has been improved with finer optimizations of the conformation of the Cu^{2+}-$A\beta_{1-16}$ structural loops and including solvent effects.

4.1.1. ELECTRONIC STRUCTURE METHODS

Cu^{2+} is an open-shell metal cation ($3d^9$), which shows a particular flexibility in its coordination environments. In most cases, the tetracoordinate Cu^{2+} environment is a

square-planar geometry, whereas the Cu^{+} (d^{10}, close-shell) tends to form tetracoordinate complexes in tetrahedral coordination, tricoordinate species as trigonal plane geometries or dicoordinate complexes in linear environments.[278]

Usually, the electronic structure methods used are based on DFT since they provide a good relationship between computational cost and accuracy. However, because of the Cu^{2+} nature, its electronic description is delicate. Previous studies of Cu^{2+}-L systems, which have been performed in our research group, have demonstrated that GGA functionals or hybrid functionals with low percentage of exact exchange tend to overstabilize lower coordinated Cu^{2+} structures due to the wrong cancellation of the self-interaction in the exchange-correlation functional. In particular, for $Cu^{2+}(H_2O)_n$ clusters,[279] it was found that the relative energies of different coordinating systems were, in general, better described with functionals that involve a large amount of exact exchange such as BHLYP or MPWB1K, which exhibit 50% and 40% of exact exchange, respectively.

In addition, the functional chosen should provide a good description of hydrogen bonding and dispersion forces to properly account for the peptide configuration and stability if the whole bioinorganic moiety is considered at the DFT level. However, the latest functionals do not properly describe the dispersion forces. Then, HM-GGA functionals have been used.

More recently developed functionals such as M06 are able to include dispersion forces at least, mid-range, and thus, a study of model systems that only enclose the metal coordination environment has been performed with the M06 family of functionals (M06-L, M06 and M06-2X) which include 0 %, 28 % and 54 % exact exchange, respectively. Overdelocalization of the electron density can lead to a wrong characterization of the metal-ligand electrostatic interactions. Therefore, the spin densities of the model systems have been examined. These values have demonstrated that all the functionals mostly locate the spin density on the Cu atom, regardless the model system, values oscillating between 0.6 and 0.8. As expected, the lower value is proportionated by the functional with less exact exchange (M06) and the higher result is related to the functional with large amount of exact exchange (M06-2X).

Furthermore, two basis sets have been used. In one case, it has employed the LANL2DZ pseudopotential and its related basis for the Cu, (5s5p5d)/[3s^{3}p2d],[280] and the 6-31G(d) basis set for the rest of atoms. In the second basis set has used the larger LANL2TZ, (5s5p5d)/[5s5p3d], for Cu[281] supplemented with an *f* function[282] and the 6-311++G(d,p) basis set for all the rest of atoms. Hereafter, the two basis sets used will be referred to as small basis set one (SB_1), in order to distinguish for the other small basis set used in the folowwing chapters, and large basis set (LB), respectively.

The geometrical parameters of the considered model systems at different level of theory are described in detail in *Figure A1* from the *Appendix A* section. All the model systems show a distorted square-planar geometry, with the sum of the four angles around Cu near 360º and Cu^{2+}-ligand distances about 2.00 Å. Overall, it can be considered that there are minor structural differences; *i.e.*, the different functionals and basis set strategies provide very similar geometrical parameters. Therefore, the following optimizations and frequencies calculations have been carried out with the SB_1 basis set, in order to reduce the computational cost, and energies have been refined by performing single-points calculations with the LB basis. In all cases, energies the M06-2X functional have been used, which is the one that gives a better description of the non-covalent interactions, and provide smaller spin overdelocalization.

Thermodynamic corrections were obtained assuming unscaled harmonic vibrational frequencies, which enable to confirm that all structures are true minima, and the rigid rotor approximation was obtained by standard statistical methods. Cu^{2+} calculations, as it is an open-shell ion, were based on an unrestricted formalism. All electronic calculations have been done with *Gaussian09* package program.[245] Atomic charges and spin densities were obtained from Natural Population Analysis (NPA). Moreover, the solvent effect, specifically water, is included with the SMD continuum model.

4.1.2. HOMOLOGY MODELING SIMULATIONS

As mentioned in the introduction section, HM simulations are widely used in biochemistry and pharmacology to generate 3D models of unknown structure proteins (*target*) from similar structures which are experimental recognized (*template*). Therefore, HM simulations have been performed using the $A\beta_{1-16}$ peptide conformation of the NMR Zn^{2+}-$A\beta_{1-16}$ structure as *template* obtained from the PDB with code

1ZE9[283] and including the geometric constrains (distance and angles) from the model systems explained before. HM techniques cannot reproduce structures in which the reorganization of the protein in the *target* is significantly different of the *template*. However, several evidences have suggested that the peptide differences between Cu^{2+}-$A\beta_{1-16}$ and Zn^{2+}-$A\beta_{1-16}$ complexes should be small. Specifically, the experimental structures of free $A\beta_{1-16}$ (PDB code: 1ZE7) and Zn^{2+}-$A\beta_{1-16}$ complexes have shown that the main conformational change of the peptide in the Zn^{2+}-$A\beta_{1-16}$ structure is the expected peptide compaction due to the metal coordination.[283] Hence, the metal coordination essentially produces the reorganization of the side chains of the peptide with respect to the non-coordinated peptide form. For that reason, a similar behavior is expected for the Cu^{2+}-$A\beta_{1-16}$ complexes on the peptide backbone.

Taking into account all these considerations, HM simulations have been carried out using *Modeller9v11*[284] program. For all the models, different combinations of δ/ε coordination of the imidazole nitrogens of the participant histidines have been evaluated. In order to better understand the process, the specific case of component Ia with N_δ coordination for both histidines, [CO^{D1}, N_{term}, N_δ^{H6}, N_δ^{H13}], is explained in detail.

After aligning the residues of the *target*, with respect to the $A\beta_{1-16}$ sequence of the *template* and including the coordination restrictions; 500 models were generated, which guarantees a great exploration of the conformational space, by fixing the metal coordination sphere and leaving the side chains move freely. Considering all the configurations for all the components, a total of 9.000 hypothetical candidates for Cu^{2+}-$A\beta_{1-16}$ complexes were generated.

Once the 500 models were obtained, the most probable one was selected to be subsequently treated. The selection method consists of a clustering analysis using the *NMRClust* implemented in *Chimera1.6,*[285] which groups the models according to their RMS values. Then, the representative structure of each cluster, which is the one closest to the centroid of the group in question, is evaluated energetically and geometrically. The energetic evaluation is based on the CHARMM energy (E_{CHARMM}) generated by *Modeller* in the model building process, whereas the geometric appraisal uses the DOPE, *Discrete Optimized Protein Energy,* value (E_{DOPE}), which is also implemented in *Modeller* and uses probability density functions to punctuate the models according to

the deviations that present its secondary structures with respect to structures that are contained in a crystallographic data base. In the case that concerns us, component Ia, 48 clusters were generated of which the most populated ones are disclosed in *Table 4.1*.

Table 4.1. Representative structure evaluation of the most populated clusters for component Ia. The energies are in kcal·mol^{-1}.

Cluster elements	Representative specie	E_{CHARMM}	E_{DOPE}
213	**496**	**261.2**	**-584.1**
91	132	335.4	-549.2
74	201	432.7	-517.2
18	291	487.3	-373.2
13	39	475.4	-338.7

In order to improve the peptide description, a *loop* refinement has been performed. Therefore, the most representative structure of the 500 models was submitted to the same preceding protocol, but in this case only the most flexible loops can move and 100 models have generated. In the case of component Ia the most representative structure was the structure number 496 that was subsequently used for the *loop* refinement obtaining 25 cluster of which the most populated ones are shown in *Table 4.2*.

Table 4.2. Representative structure evaluation of the most populated clusters for component Ia derived from the *loop* refinement. The energies are in kcal·mol^{-1}.

Cluster elements	Representative specie	E_{CHARMM}	E_{DOPE}
18	**75**	**22.5**	**-689.0**
18	49	32.1	-683.3
14	58	27.8	-629.4
11	7	48.3	-606.1

It is possible to observe that, for component Ia, the most representative structure is the number 75 which has been used for the following calculations. In this case, the E_{CHARMM} is lower than the previous, because the complex is not built from scratch but the complex is refined from the previous one already assembled.

This process has been employed for the rest of component Ia configurations as well as for the rest of the configurations of the components. The evaluation results for all these configurations are exhibited in *Table A1* and *A2* from *Appendix A* section. However, for component IIa the calculations had already been performed by Jorge Alí Torres. Then, the results were obtained from his thesis.[277]

Up to this point, the models have not included the effects of the electronic structure of the metal coordination sphere in the whole complex structure. These effects are

included by means QM methods. That is**,** QM optimizations have been carried out at the M06-2X/SB_1 level and the final energies have been refined with the LB basis set, as aforementioned. All these QM calculations include the solvent effect with the SMD continuum model, and thus residues are considered in the protonation states expected in solution at physiological pH. Starting structures in these optimizations have been taken from HM simulation and, to save computer time, they have been first relaxed with ONIOM (M06-2X:UFF) in the gas phase, with the first coordination sphere in their neutral form. The overall process is summarized in *Scheme 4.1*.

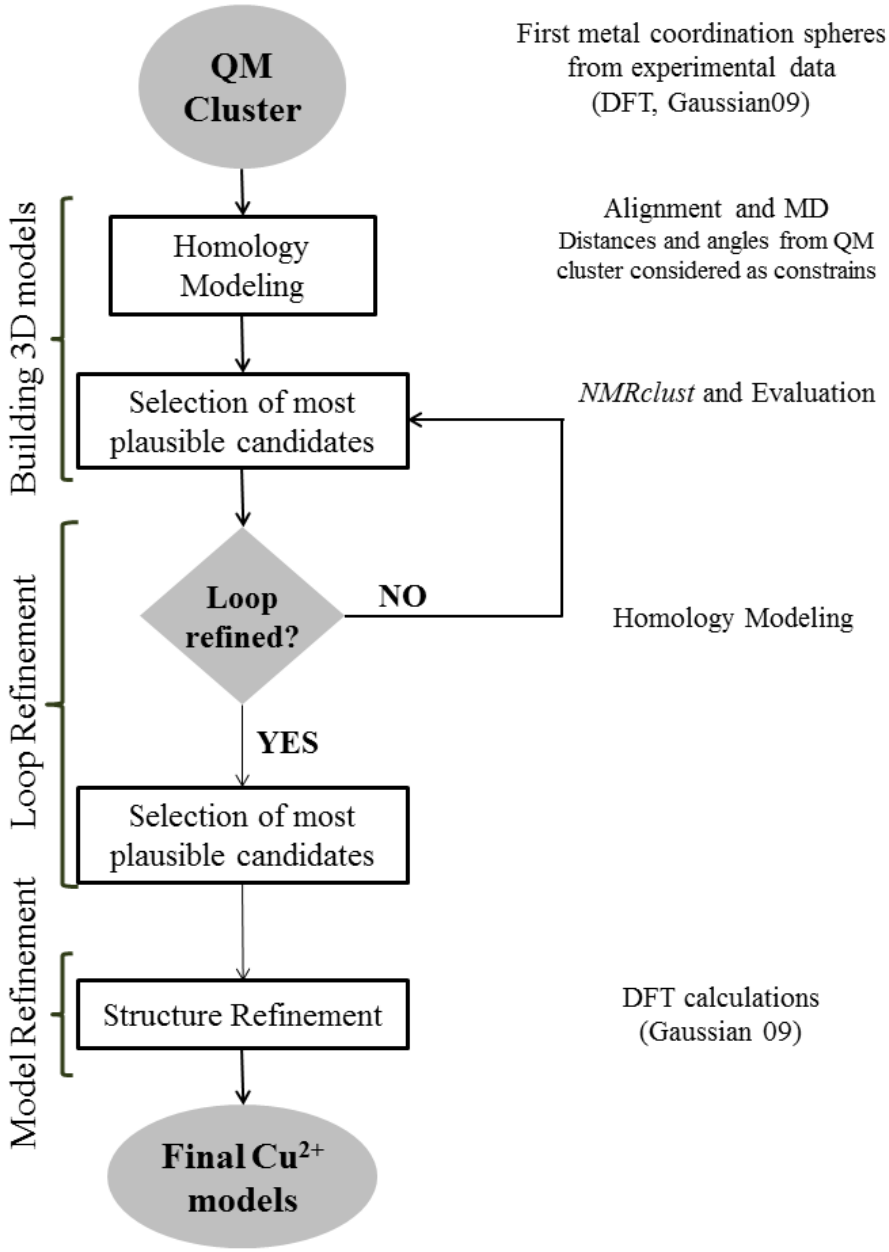

Scheme 4.1. Summary of the protocol used for the construction and evaluation of the Cu^{2+}-$A\beta_{1-16}$ complexes.

Notably, in few cases the optimized structure showed low imaginary frequencies (less than 50 cm^{-1} in absolute value). Because of the size of the system, reoptimizations to find the true minima were not performed. Instead, and because the imaginary frequencies were all small, their contribution to the molar enthalpy was considered to be *RT* and their contribution to the entropy was estimated considering a frequency of 10 cm^{-1} for each imaginary one.[286]

In addition, single point calculations of the metal coordination sphere at the optimized geometry of the Cu^{2+}-$A\beta_{1-16}$ complexes, as well as the peptide, acquired from the remaining peptide moiety, have been executed including the solvent effect in order to analyze the influence of both motifs in the complex stabilization.

The results obtained for all the components using this methodology are discussed in the following sections.

4.2. Cu^{2+}-$A\beta_{1-16}$ COMPLEXES

In this section, the different models built for Cu^{2+}-$A\beta_{1-16}$ complexes will be presented. Aforementioned, the construction of these complexes are based on the experimental metal coordination spheres, which are included as constrains in the homology modeling simulations. As it was commented, experimental studies have revealed the existence of two main species in the physiological pH range (see *Figure 1.3*). One referred to component I at lower pH (6.3-6.9). A second one named component II at higher pH (8-9), for which two metal coordination environments have been proposed (there noted component IIa and IIc).

4.2.1. LOW pH SPECIES

Component Ia and Ib have generated four subgroups for each studied case as a result of all the possible combination of the δ/ε nitrogen coordination of the histidines. The first subgroup involves the N_δ coordination of histidines 6 and 13 or 14, the second and the third group implicates different nitrogen coordination, the N_δ for His 6 and the N_ε for His 13 or 14 and vice versa. Finally, the last subgroup is associated to the N_ε coordination for both histidines. Therefore, the nomenclature used for the complexes is the name of the related component; that is, Ia, Ib, IIa or IIc, and the δ/ε nitrogen

coordination as subscript, where the first indicates the coordination of His6 and the second one, the coordination of His13 or 14.

Once the methodology was applied, the most stable structures for each component were obtained. For component Ia, the most stable structure was **$Ia_{\delta\delta}$**; whereas for component Ib was **$Ib_{\delta\varepsilon}$**, which are shown in *Figure 4.1*. The geometry descriptions of the less stable conformations as well as the detailed geometry description of all obtained structures are illustrated in *Figures A2* and *A3* from the *Appendix A* section.

If the geometric parameters of all the structures shown in the *Figure A2* and *A3* from the *Appendix A* section are analyzed, one can observe that the metal center presents a distorted square planar geometry with the sum of angles around Cu near 360º and Cu-ligand distances around 2.00 Å. Moreover, N_1-Cu-N_2 and O_1-Cu-N_3 angles are between 170-150º.

Structure $Ia_{\delta\delta}$

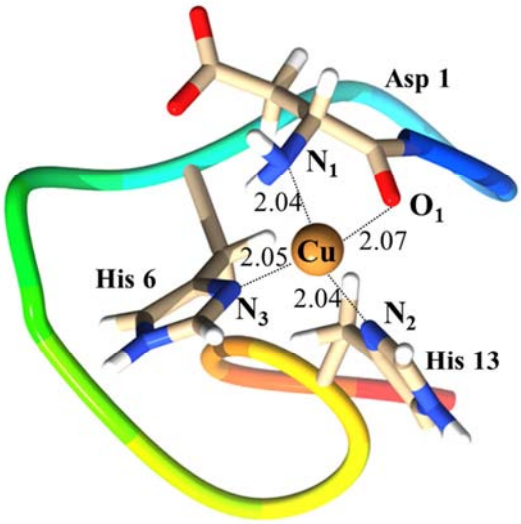

N_1-Cu-N_2: 168.0, **O_1-Cu-N_3:** 151.5
Σα: 362.5

Structure $Ib_{\delta\varepsilon}$

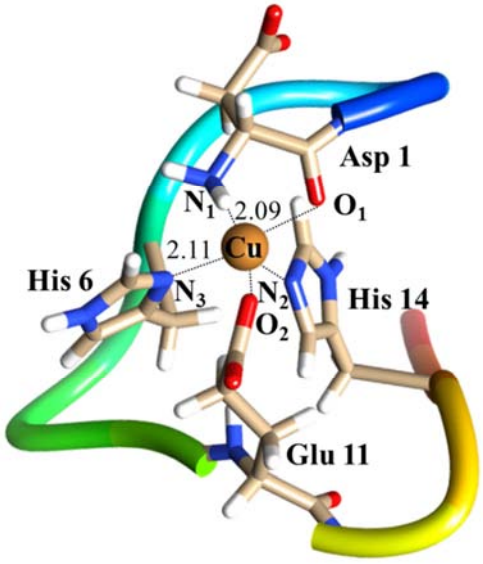

O_1-Cu: 2.08, **N_2-Cu:** 2.05, **O_2-Cu:** 2.19
N_1-Cu-N_2: 156.6, **O_1-Cu-N_3:** 167.5
Σα: 356.8

Figure 4.1. The most stable conformations for component Ia and Ib obtained by the application of the methodology explain before. Distances are in angstroms and angles in degrees. Σα means the sum of all the angles around Cu.

The exception is the structure **$Ib_{\delta\varepsilon}$** of component Ib (Σα: 356.8º), which shows a square-based pyramid pentacoordination due to the additional interaction of the carboxylate group of the Glu11 residue, as it is shown before in the *Figure 4.1*. Moreover, the distortion can be appreciated if these complexes are compared with the related model

system, because the O_1-Cu-N_3 angle have slightly decreased in most of the structures from 174.7º in model system to ~150.0º in the complexes. It is important to note that all structures present a spin density of 0.7-0.8 mainly localized at Cu^{2+}.

The relative energies of the different configurations of each component are disclosed in *Table 4.3*. This table also includes the relative contributions of the metallic (ΔE_{MC}) and peptidic (ΔE_{pept}) moiety, which are both calculated as it was mention before. In addition, this table shows the total number of the stabilizing non-covalent interactions ($N_{non\text{-}covalent}$) of the peptide characterized by the hydrogen bonds. More detailed analysis of these interactions is summarized in the *Table 4.4.*

Table 4.3. Relative energies summary of the configurations of components Ia and Ib, as well as the thermodynamic data. All the energies are in kcal·mol^{-1}.

	ΔE	**ΔE_{MC}**	**$\Delta E_{pept.}$**	**ΔH**	**TΔS**	**ΔG**	**$N_{non\text{-}covalent}$**
	Component Ia						
δδ	**0.0**	0.0	**0.0**	**0.0**	**0.0**	**0.0**	**10**
δε	19.1	-4.1	21.8	18.3	13.7	4.6	6
εδ	23.8	0.2	26.7	23.8	9.8	13.9	3
εε	18.4	**-6.6**	22.5	18.4	8.0	10.4	5
	Component Ib						
δδ	35.0	-4.3	37.8	34.5	18.0	16.5	3
δε	16.0	-2.1	30.0	15.7	13.1	**2.6**	1
εδ	**14.1**	**-5.6**	**24.3**	**13.2**	**7.6**	5.6	**3**
εε	21.9	-3.5	28.7	20.3	12.8	7.5	3

The relative metal center energies are all lower than 7 kcal·mol^{-1}, in absolute value, whereas the peptide energies can reach 38 kcal·mol^{-1} indicating that the relative energies related to the metal center are minor compared to the peptidic moiety. This conclusion is also supported by the fact that the geometry of the metal coordination environment does not differ overmuch between the complex and the model system. Accordingly, the complex stability is given by the peptide conformation rather than by the metal coordination center.

On the other hand, the values shown in *Table 4.3* indicate that relative enthalpies are similar to the relative potential energies; while the Gibbs energies, although they follow the same trend, exhibit lower values due to the smaller entropy energies of those systems containing more stabilizing interactions. In this regard, the final stability results from a balance between the energy gained due to the formation of such stabilizing motifs and the free energy lost associated with the entropic terms. Among the

stabilizing motifs, the interactions that have been considered are represented in *Figure 4.2*:

- NH_3^+ - X
- CO - HX
- COO^- - HX

Hydrogen bonds (HB)

- COO^- - NH_3^+ ⟶ Salt bridge (SB)

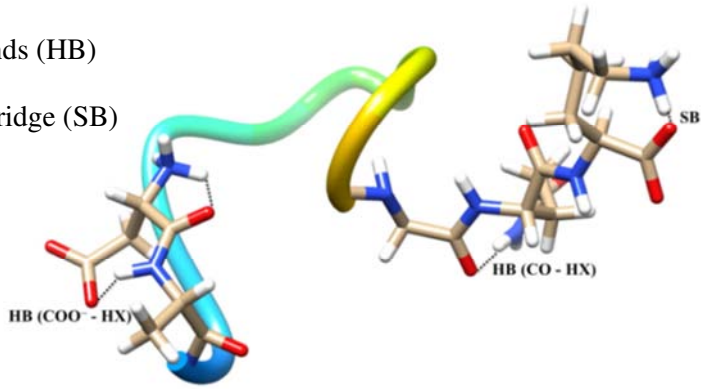

Figure 4.2. Representation of hydrogen bonds (HB) and salt bridge (SB) in the peptide, where X is any element.

Table 4.4. Detailed description of the stabilizing motifs of the peptide for each configuration of Component Ia and Ib. HB present all the considered hydrogen bonds and SB indicate salt bridge interactions.

	HB			SB
	NH_3^+-X	CO-HX	COO^--HX	COO^--NH_3^+
	Component Ia			
δδ	0	4	4	2
δε	1	3	2	0
εδ	0	0	2	1
εε	0	1	4	0
	Component Ib			
δδ	1	1	1	0
δε	0	1	0	0
εδ	0	1	1	1
εε	0	2	0	1

Among all four structures of component Ia, the most stable one is structure **Ia$_{\delta\delta}$**, corresponding to the coordination of δ nitrogen of both histidines. However, it does not exhibit the most stable coordination environment (ΔE_{MC}). A detailed analysis of the different structures revealed that the peptide configuration in this structure shows a large number of hydrogen bonds (see *Table 4.4*); specifically two salt bridges, one between Glu3 and Lys16 and the other between Arg5 and Asp7, largely contributing to the stability of the complex.

In the case of the component Ib, relative potential energies (ΔE) indicate that these models lie higher in energy than the most stable conformation of component Ia, despite the fact that their metal site (ΔE_{MC}) is more stable. This is due to the larger stability of the peptide moiety in component Ia cause by the presence of more stabilizing

interactions than component Ib, particularly salt bridge interactions. Indeed, structure **$Ia_{\delta\delta}$** is 14-24 kcal·mol^{-1} more stable than the structures which only have one salt bridge (**$Ia_{\varepsilon\delta}$**, **$Ib_{\varepsilon\delta}$** and **$Ib_{\varepsilon\varepsilon}$**) and is up to 35 kcal·mol^{-1} more stable than structure **$Ib_{\delta\delta}$**, with no salt bridges. This fact highlights the magnitude of the salt bridge interaction.

A particular case is the structure **$Ib_{\delta\varepsilon}$,** because despite not presenting any salt bridge interaction its relative potential energy with respect to structure **$Ia_{\delta\delta}$** is only 16 kcal·mol^{-1}. Furthermore, the most stable configuration changes, in terms of free Gibbs energy, and becomes the configuration **$Ib_{\delta\varepsilon}$**. This evidence can be explained through the particular case of this configuration which shows a pentacoordinate metal sphere geometry, as it is illustrated in *Figure 4.1*, which provides an extra stabilization to the complex becoming the more stable configuration for component Ib. In fact, the inclusion of thermal effects modifies their relative stability in such a way that it lies only 2.6 kcal·mol^{-1} higher than configuration **$Ia_{\delta\delta}$**, in terms of Gibbs free energies.

The axial coordination of the carboxylic group is not found in other configuration which can be due to the delicate balance between the $Cu^{2+} - COO^{-}$ and the solvent interactions with the carboxylate. The coordination of Glu11 may be due to the restrictions imposed by the peptide over this side chain, doing that it is sufficiently close to the metal to coordinate it.

4.2.2. HIGH pH SPECIES

At high pH values, two possible different components have been experimentally proposed, component IIa and IIc, as mentioned before. The nomenclature employed for these complexes uses three subscripts for component IIa, referred to each His coordination, and one for component IIc because it only has one His in the metal coordination environment. The most stable structure for each component has been illustrated in *Figure 4.3*.

For component IIa, which seems to dominate at pH near 8, eight subgroups were generated considering all the possible coordinations of the three histidines. All the structures, which are geometrically detailed in *Figure A4* from the *Appendix A* section, exhibit a distorted square-planar coordination with the sum of angles around Cu near 360º, Cu-ligand distances near 2.00 Å and spin density mainly localized at the metal

center (0.7 to 0.8). While for most configurations the distortion is minor (angles, N_1-Cu-N_2 and O_1-Cu-N_3, between 165.2º and 176.4º), for **IIa$_{\delta\delta\delta}$**, **IIa$_{\varepsilon\varepsilon\delta}$** and **IIa$_{\delta\varepsilon\varepsilon}$** the coordinating angles have decreased to between 109.7º and 143.7º, which indicate that the distortion is significant. This can be produced by the limited mobility of the side chains of the residues that coordinates to the metal imposed by the peptide configuration. Nevertheless, the distances are very similar to the model system. The **IIa$_{\varepsilon\varepsilon\varepsilon}$** configuration, illustrated in *Figure 4.3*, was determined the most stable structure.

Structure IIa$_{\varepsilon\varepsilon\varepsilon}$ **Structure IIc$_{\delta}$**

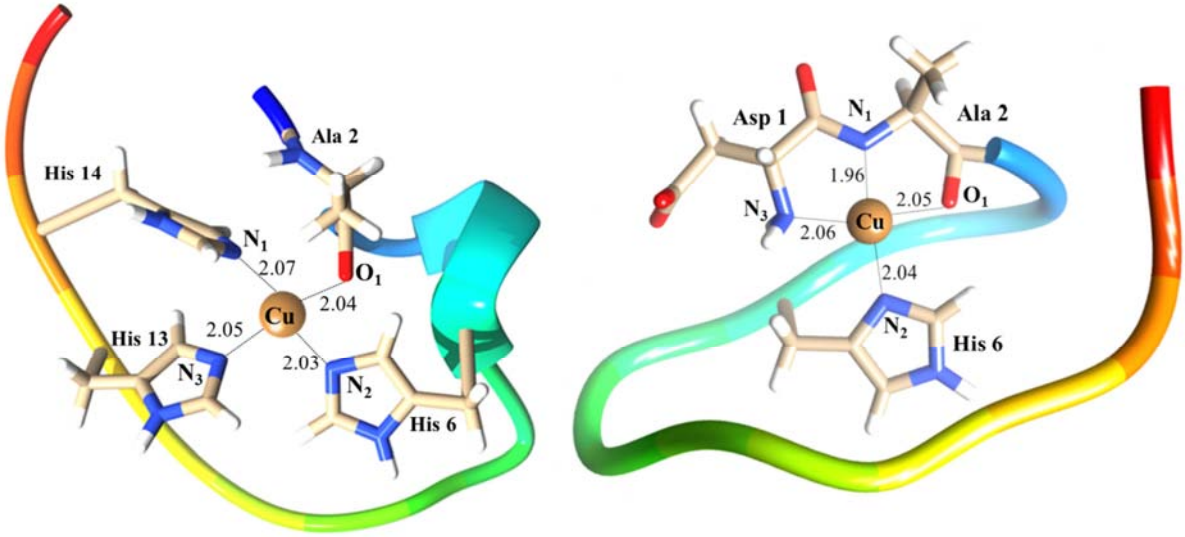

N_1-Cu-N_2: 165.2, **O_1-Cu-N_3:** 165.2
Σα: 364.8

N_1-Cu-N_2: 169.6, **O_1-Cu-N_3:** 162.3
Σα: 359.7

Figure 4.3. The most stable configuration for component IIa and IIc. Distances are in angstroms and angles in degrees. Σα means the sum of all the angles except those that are explicitly described.

On the other hand, for component IIc, which is dominant at about pH 9 and only present one histidine in the coordination sphere, exclusively two configurations were obtained, which are geometrically detailed in *Figure 4.3* and *Figure A5* from the *Appendix A* section. Both conformations present a square-planar geometry, with the high rigidity of the Asp1-Ala2 fragment hindering significant distortions, and the spin density mainly also localized at Cu^{2+}. The **IIc$_{\delta}$** configuration, shown in *Figure 4.3*, is the most stable structure.

Finally, the relative energies of the whole system, the metal center and the peptide, as well as the total number of the stabilizing non-covalent interactions ($N_{non\text{-}covalent}$) of the peptide, are disclosed in *Table 4.5*. More detailed analysis of these stabilizing interactions is summarized in the *Table 4.6*.

Table 4.5. Relative energies summary of the configurations of component IIa and component IIc, as well as the thermodynamic data. All the energies are in kcal·mol^{-1}.

	ΔE	**ΔE_{MC}**	**$\Delta E_{pept.}$**	**ΔH**	**TΔS**	**ΔG**	**$N_{non\text{-}covalent}$**
	Component IIa						
δδδ	21.0	5.1	16.0	21.8	21.8	4.2	0
δδε	10.6	-1.7	10.4	8.5	6.8	1.7	4
δεδ	30.4	0.7	23.3	32.4	-0.7	33.1	4
δεε	11.4	1.6	12.6	12.3	0.4	11.8	**8**
εδδ	19.3	-2.9	24.1	20.3	**-1.8**	22.1	5
εδε	7.3	**-4.8**	10.2	7.2	7.9	**-0.7**	3
εεδ	35.3	7.9	27.7	34.9	8.2	26.7	5
εεε	**0.0**	0.0	**0.0**	**0.0**	0.0	0.0	6
	Component IIc						
δ	**0.0**	0.0	**0.0**	**0.0**	**0.0**	0.0	**4**
ε	13.9	**-0.7**	8.9	10.6	11.5	**-0.9**	3

As for low pH components, the final stability of the structures depends on the peptide configuration, being mainly determined by the stabilizing non-covalent interactions. In addition, thermal contributions play a crucial role in the relative stabilities of the derived model.

Among all the structures of component IIa, those which present a major distortion, structures **$IIa_{\delta\delta\delta}$**, **$IIa_{\delta\varepsilon\varepsilon}$** and **$IIa_{\varepsilon\varepsilon\delta}$**, are which show higher ΔE_{MC} and, thus, less stable metal sites. Furthermore, when no thermal effects are considered, the structure **$IIa_{\varepsilon\varepsilon\varepsilon}$**, which corresponds to the coordination of ε nitrogen of all the histidines present in the metal coordination sphere, is the most stable. However, the inclusion of thermal contributions modifies this preference, with structure **$IIa_{\varepsilon\delta\varepsilon}$**, corresponding to the ε, δ and ε nitrogen coordination of the histidines 6, 13 and 14, respectively, becoming slightly more stable in terms of Gibbs energies by -0.7 kcal·mol^{-1}.

For component IIc, due to the presence of the tricoordinating fragment, the interaction of His6 through δ or ε coordination has a minor influence on the relative stability of the metal site. Then, the final stability of the complex is determined by the peptide configuration. However, entropic contributions are crucial to determine the final stability; because structure **IIc_{ε}** is slightly more stable in terms of Gibbs energies by -0.9 kcal·mol^{-1}.

Table 4.6. Detailed description of the stabilizing motifs of the peptide for each configuration of Component IIa and IIc. HB presents all the considered hydrogen bonds and SB indicates salt bridge interactions.

	HB			SB
	NH_3^+-X	CO-HX	COO^--HX	COO^--NH_3^+
	Component IIa			
δδδ	0	0	0	0
δδε	0	0	2	2
δεδ	1	1	2	0
δεε	1	1	4	2
εδδ	2	0	2	1
εδε	0	0	1	2
εεδ	0	1	2	2
εεε	0	1	2	3
	Component IIc			
δ	1	2	1	0
ε	1	1	1	0

Configuration **IIc$_\delta$** is the most stable structure in terms of potential energy because it presents more stabilizing motifs. However, model **IIa$_{\varepsilon\varepsilon\varepsilon}$**, which is the most stable configuration according to potential energy, does not present the maximum stabilizing elements. As it is demonstrated before, some stabilizing motifs have more influence than others; for instant, salt bridges. Therefore, structure **IIa$_{\varepsilon\varepsilon\varepsilon}$** is more stable because it has more salt bridges than the rest of structures. Then, the results enable to conclude the different influence of the peptide stabilizing motifs, which is as follows:

$$NH_3^+ - COO^- > NH_3^+ - X/COO^- - HX > CO - HX$$

On the other hand, component IIa and IIc were compared considering the IIa → IIc + $2H^+$ reaction. The relative free energies for the most stable structures, which are **IIa$_{\varepsilon\delta\varepsilon}$** and **IIc$_\varepsilon$**, are -1.2, -3.9 and -6.6 kcal·mol^{-1} at pH 7, 8 and 9, respectively. This values show that component IIc becomes progressively more stable as the pH increases. However, these small values do not enable to conclusively determine which the most stable binding site for component II at this pH range is.

4.2.3. INFRARED SPECTRA

Last but not least, the *InfraRed* (IR) spectra of each conformation have been simulated. The IR spectra of the most stable species of each component are represented in *Figure 4.4*, whereas the rest of the configurations are in the *Appendix A* section in *Figures A6*

and *A7*. For component IIa, only the IR of the most stable configurations, at potential and Gibbs energy terms (structures **IIa$_{\varepsilon\delta\varepsilon}$** and **IIa$_{\varepsilon\varepsilon\varepsilon}$**), have been simulated.

Despite of the frequency overlap along the spectrum, four different regions can be characterized. The first one, which is at 1400 cm^{-1} approximately, corresponds to the symmetric stretching of the carboxylate groups. A second region, which appears between 1480 and 1550 cm^{-1}, belongs to the bending of the NH peptide bond. The third group of bands, which is at 1600 cm^{-1}, coincides with the antisymmetric stretching of the carboxylate groups and, finally, a region between 1650 and 1710 cm^{-1} appears which corresponds to the stretching of the carbonyl group of the peptide bond.

Moreover of these defined bands, there are others that overlap with them as, for example, the hydrogen wagging of the R_2-CH_2 at 1300-1400 cm^{-1} or the bending of the same hydrogens at 1500 cm^{-1}. On the other hand, there are bands observed between 3000 and 3500 cm^{-1}, which concern to the CH stretching (ν CH), and a region around 3400 cm^{-1}, which correspond to NH stretching (ν NH). These bands are typical in the proteins structures because they are associated to the peptide bonds movements.

As one can observe, all the structures evince similar IR spectra. However, the most relevant peak is at 2500-2800 cm^{-1}, which corresponds to the salt bridge. In the case of the structure **Ib$_{\varepsilon\varepsilon}$**, which involves the coordination of the ε nitrogens of both histidines of the component Ib, the single peak of the salt bridge is overlapped with a set of bands that corresponds to the CH stretching (ν CH) and it appears at large frequency, 3016 cm^{-1} (see *Figures A6* of *Appendix A* section). Similarly, the two configurations of the component IIa has this signal at 2968 and 2993 cm^{-1}, referring to the most and the less stable configuration, respectively (see *Figure 4.4* and *Figure A7* of *Appendix A* section, respectively).

Structure $Ia_{\delta\delta}$

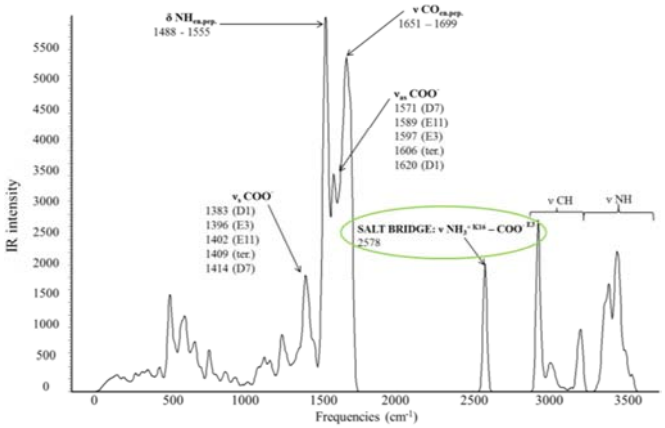

Structure $Ib_{\delta\varepsilon}$

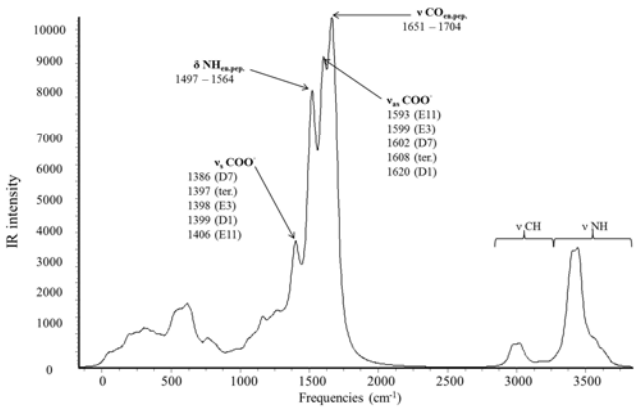

Structure $IIa_{\varepsilon\delta\varepsilon}$

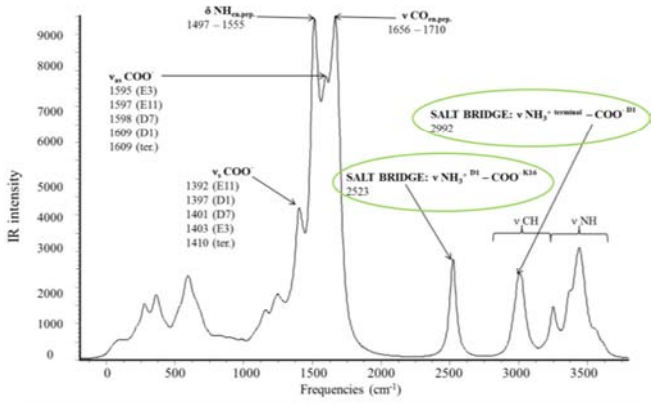

Structure IIc_{ε}

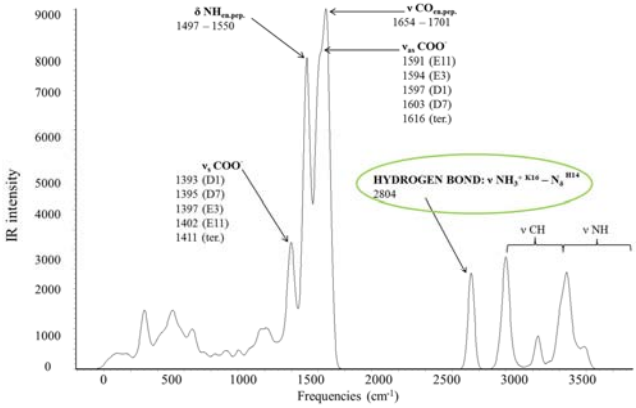

Figure 4.4. IR spectra for the most stable structures of all considered components, where ν indicates a stretching movement and δ a bending movement. The highlighted bands correspond to salt bridges, except for structure **IIc_{δ}** which refers to a hydrogen bond.

4.3. CONCLUSIONS

In this study, different 3D structures of Cu^{2+}-$A\beta_{1-16}$ complexes have been theoretically determined, involving the metal sphere coordination experimentally proposed at different pH values. The used protocol has been proposed by our group in the Jorge Alí Torres thesis, where Homology Modeling and Quantum Mechanics calculations have been combined, and has provided us with the exploration of the conformational space and the modelling of the fine electronic effects necessary to generate plausible models. This methodology has been improved by employing the M06 family of functionals and including the solvent effect with the SMD continuum model. After some model system explorations, the M06-2X functional has been chosen for the QM simulations.

Summarizing, the most stable configurations of each component based on the possible nitrogen coordination of the histidines, it is as follows. For component Ia the most stable

structure is **Ia_{δ}**, which involves the N_{δ} coordination of the two imidazole. For component Ib, the most stable configuration is **Ib_{de}**, which includes the N_{δ} coordination of the His6 and the N_{ε} coordination of the His14. For component IIa, the most stable model is **$IIa_{\delta\varepsilon\delta}$**, which comprehends the N_{δ} coordination of histidines 6 and 14 and N_{ε} for histidine 13. Finally, for component IIc, the most stable structure is **IIc_{ε}**, which implicates the N_{ε} coordination of the coordinated histidine.

This study has enabled to determine that the final stability of the complexes results from a balance between the metal coordination site and amyloid folding upon complexation, illustrating the importance of the second coordination sphere in defining the relative stability between complexes. In fact, the stabilizing motifs analysis shows that the most important element that contributes to the peptide stabilization is the salt bridge. Furthermore, the IR spectra have been simulated which can be helpful to the experimentalist to know what they have in solution.

The obtained structures allow us to study the potential standard reduction of these complexes with the corresponding description of the Cu^{+}-$A\beta_{1-16}$ complexes, which in turns can be implicated in the ROS production and oxidative stress.

5

Cu^{+}-Aβ_{1-16} SPECIES AND REDOX PROPERTIES

As aforementioned, Cu-Aβ complex can be involved in the increase of oxidative stress observed in AD patients by catalyzing the Reactive Oxygen Species (ROS) formation. It has been proposed that Cu^{2+}-Aβ complex is reduced to Cu^{+}-Aβ by reducing agents present in the media. Subsequently, it can react with the dissolved oxygen to give the oxidized system, resulting in a catalytic cycle that would generate hydrogen peroxide in excess. Hence, the first step of this mechanism is the reduction of Cu^{2+}-Aβ complex. The Cu^{2+}/Cu^{+} redox cycling critically depends on the binding mode of Cu^{2+} in the Cu^{2+}-Aβ complexes because different coordination environments are expected to present different redox properties.

Moreover, reduction can lead to tetrahedral tetracoordinated, tricoordinated or linear dicoordinated species. DFT calculations,[208] as well as different experiments,[287] have shown the propensity of Cu^{+} complexes to adopt near-linear two coordinated structures. However, these linear dicoordinated complexes have been found to be inert toward dioxygen[288] hindering the redox cycling of $Cu^{+/2+}$-Aβ. On the other hand, tricoordinated structures seem to be involved in the redox cycling.[289–291] Therefore, a key issue in the redox activity of $Cu^{+/2+}$-Aβ complexes is the nature and stability of these reduced Cu^{+}-Aβ species.

In this chapter, two fundamental aspects have been addressed. The first one is the determination of the *Standard Reduction Potential* (SRP) of the $Cu^{2+/+}$-Aβ_{1-16} couple to discuss their possible influence in the ROS formation, considering the Cu^{+}-Aβ_{1-16} species from the reduction of the oxidized complexes. The second one is the elucidation and stability of transient tricoordinated species of Cu^{+}-Aβ_{1-16} species.

5.1. COMPUTATIONAL DETAILS

Cu^{+}-A$\beta_{1–16}$ structures have been obtained by reduction of Cu^{2+}-A$\beta_{1–16}$ complexes by DFT methods. Then, QM/MM MD simulations have been performed to determine the stability of these reduced species. Finally, the SRP have been calculated at the same level of theory.

5.1.1. STATIC CALCULATIONS

Equally to the last chapter, fully geometry optimizations have been carried out using the M06-2X functional, which appropriately describes the coordination properties at the metal site and the non-covalent interactions of the peptide, as explained in the last chapter. The used basis set is the SB_1, which is the LANL2DZ pseudopotential and its related basis for the Cu, (5s5p5d)/[3s^3p2d],[280] and the 6-31G(d) basis set for the rest of atoms. Subsequently, the energies have been refined by performing single-points calculations with the LB basis set, which are the larger LANL2TZ, (5s5p5d)/[5s5p3d], for Cu[281] supplemented with an *f* function[282] and LANL2DZ pseudopotential[280] and the 6-311++G(d,p) basis set for all the rest of atoms. The solvent effect has been included with the SMD continuum model and thus, residues have been considered in the protonation states expected in solution at physiological pH.

Thermodynamic corrections were obtained assuming unscaled harmonic vibrational frequencies, which enable to confirm that all structures are true minima, and the rigid rotor approximation was obtained by standard statistical methods. Cu^{2+} calculations, as it is an open-shell ion, were based on an unrestricted formalism. All electronic calculations have been done with *Gaussian09* package program.[245] Atomic charges and spin densities were obtained from Natural Population Analysis (NPA).

Standard Reduction Potentials calculations: after obtaining the Cu^{+}-$A\beta_{1\text{-}16}$ complexes as well as their thermochemical properties, the SRP values are computed. The SRP versus the *Standard Hydrogen Electrode* (SHE) was estimated considering the following semi-reactions:

$$Cu^{2+}\text{-}A\beta_{1\text{-}16\ (aq)} + e^{-} \rightarrow Cu^{+}\text{-}A\beta_{1\text{-}16\ (aq)} \qquad \Delta G^{Cu} \qquad (5.1)$$

and

$$H^{+} + e^{-} \rightarrow 1/2\ H_2 \qquad \Delta G^{SHE} \qquad (5.2)$$

where the ΔG^{Cu} and ΔG^{SHE} are the free-energy changes for the semi-reactions, ignoring the electron. Hence, the SRP is calculated using the following equation:

$$E^{0}(Cu^{2+/+} - A\beta_{1-16}) = -\left(\frac{\Delta G^{0}_{Cu} - \Delta G^{0}_{SHE}}{F}\right) \qquad (5.3)$$

where F is the Faraday constant, which is 23.061 kcal·V^{-1}·mol^{-1}. For the reduction of the proton in aqueous solution, the experimental value, ΔG^{SHE} = -99.9 kcal·mol^{-1},[98,292] was used.

To account on the limitations of the level of theory used, the SRP values have been corrected taking as reference the reduction potential of copper in water, modeled through the $[Cu^{2+}(H_2O)_4]/[Cu^{+}(H_2O)_4]$ couple, whose experimental value is 0.16 V.[293] The calculated SRP value for this couple at the present level of theory is 0.060 V; that difference of 0.10 V is determined, which was added as an empirical correction to the computed SRP of the different Cu-$A\beta_{1\text{-}16}$ complexes.

5.1.2. MOLECULAR DYNAMIC SIMULATIONS

The stability of the reduced Cu^{+}-$A\beta_{1\text{-}16}$ singlet complexes was analyzed by performing *Ab initio* molecular dynamics (AIMD) according to the Born-Oppenheimer approach

using the CP2K program[294] with the Quickstep algorithm,[294] which employs a mixed Gaussian and plane-waves basis set and norm-conserving pseudopotentials, to solve the electronic structure problem. In those simulations performed in collaboration with Jorge Alí-Torres, each structure was placed in a box of water solvent molecules, as is shown in *Figure 5.1*. The size of the box depends on the size of the metal-peptide complex and was set to reproduce the density of water at ambient conditions. The complex was treated quantum mechanically and the solvent molecules using MM through a QM/MM scheme. For the QM region, the PBE-D3 level was used; that is, by using the PBE functional[191], which provides accurate results for closed shell systems, supplemented with Grimme's D3 correction for the dispersion[203]. In this case, the M06-2X functional is overly expensive to be used and is not implemented in CP2K. Moreover, present MD calculations are carried out to determine the stability of reduced Cu^{+}-Aβ_{1-16} complexes, and since they are close shell systems, they do not suffer from spin overdelocalization. The force field of the MM region was based on the TIP3P water model.[232] Short range molecularly optimized double-ζ valence polarized (DZVP)[295] Gaussian basis functions were used to represent the orbitals and up to 300 Ry cut-off was used for the plane waves expansion.

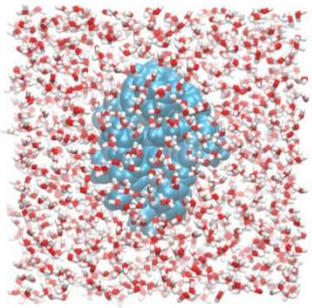

Figure 5.1. Snapshot of the Cu^{+}-Aβ solvated model. The simulation cell is periodically repeated in space.

The simulation cell was treated under Periodic Boundary Conditions (PBC), which employ translational symmetry to ensure that the system is periodical in all directions to approximate its infinite size by using a small unit cell.[163] The intrinsic periodicity in the plane wave is removed by using a fit to atom-centered Gaussians, which reproduces the long-range electrostatic potential of the original density of the molecule.[296] Core electrons were described by pseudopotentials[297–299] and wave function optimization was achieved through the orbital transformation method,[300] where the convergence criterion for the electronic gradient was set to $5 \cdot 10^{-7}$. The QM/MM coupling is described by using a real space multigrid approach[301] and the *Gaussian Expansion of the*

Electrostatic Potential (GEEP) with a modified Ewald lattice summation,[302] which are implemented in CP2K. The QM box was cubic and large enough to guarantee the decay of the electron density at the boundaries.

Initially, each structure underwent 500 ns classical MD simulation, within the canonical (NVT) ensemble, keeping the complex fixed at the implicit solution optimized structure, in order to equilibrate the system. The final conformation was used to start 20 ps of QM/MM MD simulation within the canonical ensemble at a target temperature of 300 K with a MD time-step of 1fs for the integration of the equations of motion and using a coupling constant of 10 fs for the velocity-rescaling thermostat.

5.2. Cu^{+}-Aβ_{1-16} SPECIES

The most stable configurations of the Cu^{2+}-Aβ_{1-16} complex identified in the last chapter have been reduced in order to obtain the Cu^{+}-Aβ_{1-16} structures. These configurations are **Ia$_{\delta\delta}$**, **Ib$_{\delta\varepsilon}$**, **IIa$_{\varepsilon\delta\varepsilon}$**, **IIa$_{\varepsilon\varepsilon\varepsilon}$**, **IIc$_{\delta}$** and **IIc$_{\varepsilon}$**, following the same nomenclature used in the last chapter. Optimized geometries are presented in *Figure 5.2*. Additionally, frequency calculations were performed to estimate the thermodynamic corrections to the potential energy which will be analyzed in the redox properties section.

One can observe that metal cation reduction induces significant changes in the coordination environment. The major geometrical change is associated to the Cu-O_1 distances, which increase from ~2 Å, in Cu^{2+}-Aβ_{1-16} structures, to approximately 3 Å or more, in Cu^{+} species. The only component that does not follow this behavior is component IIc, since the Cu-O_1 distance only increases to 2.6 Å in the reduced complex, due to the presence of the tridentate ligand that hinders a larger distancing from the metal. Nevertheless, it is possible to conclude that the reduction induces a decrease in the metal coordination number, from tetracoordinated in the Cu^{2+}-Aβ_{1-16} complexes to tricoordinated in the reduced species, most of them exhibiting T-shaped geometries, because of the decoordination of the involved carbonyl group. Particularly, configuration **Ib$_{\delta\varepsilon}$**, which involves an axial fifth coordination of the carboxylate group of Glu11, changes from a pentacoordinated metal sphere in the oxidized complexes to tetracoordinated in the Cu^{+}-Aβ_{1-16} complexes. Furthermore, the Cu-N distances in the reduced species (2.05 - 2.26 Å) are larger than those in the oxidized ones (1.95 - 2.12 Å)

due to the smaller electrostatic interaction and higher Pauli repulsion in the Cu^{+}-A$\beta_{1–16}$ complexes.

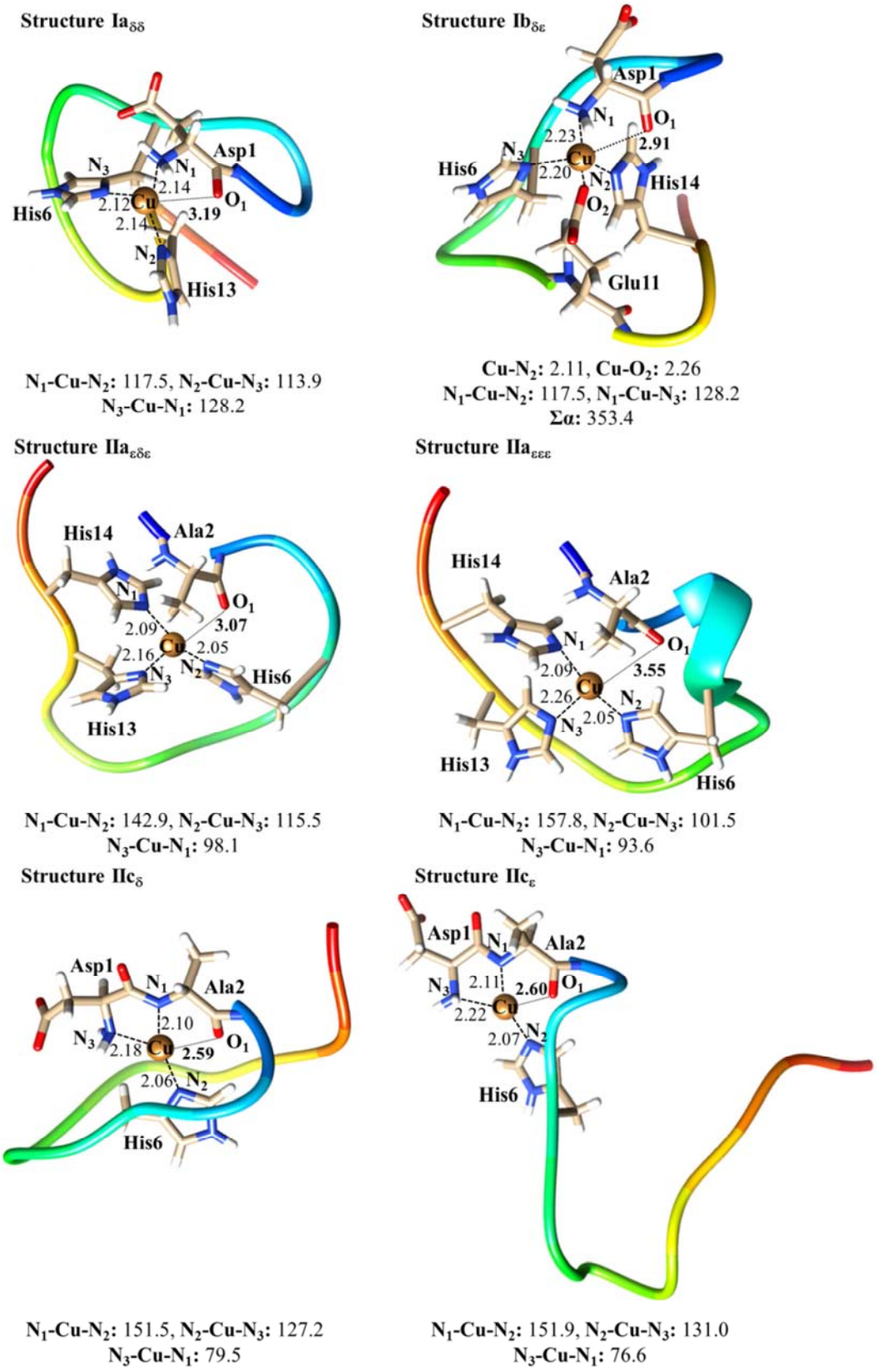

Figure 5.2. Optimized structures for Cu^{+}-A$\beta_{1\text{-}16}$ complexes. Distances are in angstroms and angles in degrees.

On the other hand, the peptide conformation exhibits minor changes upon reduction. Superimposed models of the oxidized and reduced species, as illustrated in *Figure 5.3*, show very similar peptide backbone.

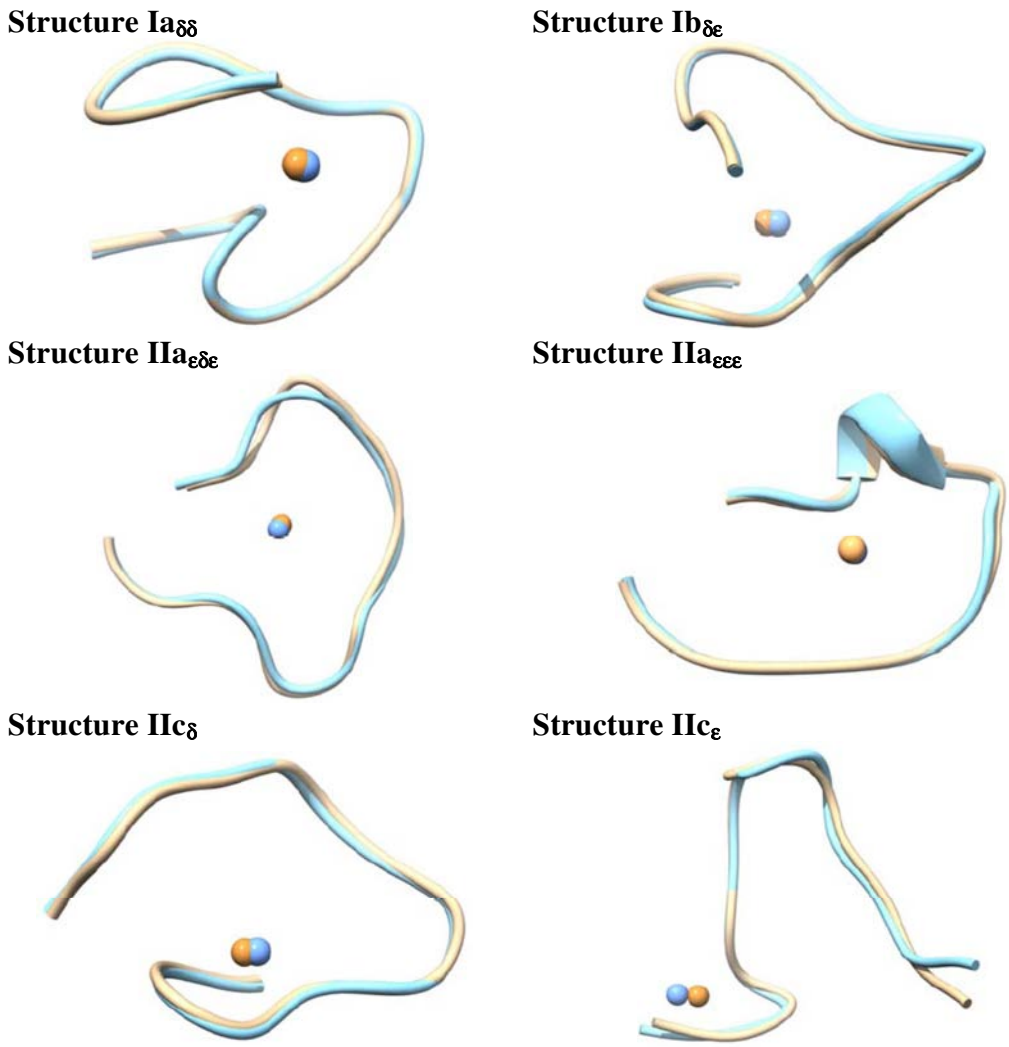

Figure 5.3. Superimposed backbones of Cu^{2+}-$A\beta_{1-16}$ complexes, in beige, and Cu^{+}-$A\beta_{1-16}$ complexes, in light blue, for the different selected configurations.

This reduction in the coordination number for the Cu^{+}-$A\beta_{1-16}$ complexes is in agreement with X-ray absorption spectroscopy experiments for model systems, which involve the Cu^{+} interaction with His-His fragments. The X-ray results are consistent with either a two-coordinate linear geometry or three-coordinate T-shaped structures[287,290,303]. Moreover, DFT calculations for Cu^{+} systems have also demonstrated the propensity of Cu^{+} complexes to adopt near-linear dicoordinate or distorted T-shaped structures[208,304,305]. Therefore, the stability of these species has been analyzed by MD in order to confirm or not the prevalence of the T-shaped geometry. This is important because transiently three-coordinate species seem to be the most influential ones in the redox cycling,[289,291] given

that they are more reactive towards oxygen.[287,290] Moreover, the structures showed above were obtained considering only the solvent as a uniform polarizable medium with a dielectric constant. However, this not represents the reality because the molecules of the solvent can compact the protein or even could interact with the metal center. Hence, the MD simulations including explicit solvent allow us studying also the effect of the solvent molecules about the protein.

5.3.STABILITY OF Cu^{+}-Aβ SPECIES: MD SIMULATIONS

In this section, the stability of Cu^{+}-Aβ_{1-16} complexes has been analyzed by running QM/MM MD simulations for some representative species, which are **Ia$_{\delta\delta}$**, **IIa$_{\delta\delta\delta}$**, **IIa$_{\varepsilon\varepsilon\varepsilon}$** and **IIc$_{\varepsilon}$**. The starting geometry for the MD simulations has been obtained from the geometry of the oxidized species of these structures. After equilibration of the solvent, 20 ps QM/MM MD simulation was run. *Figure 5.4* and *Figure 5.5* show the evolution of the most relevant Cu-ligand geometrical parameters during the simulations.

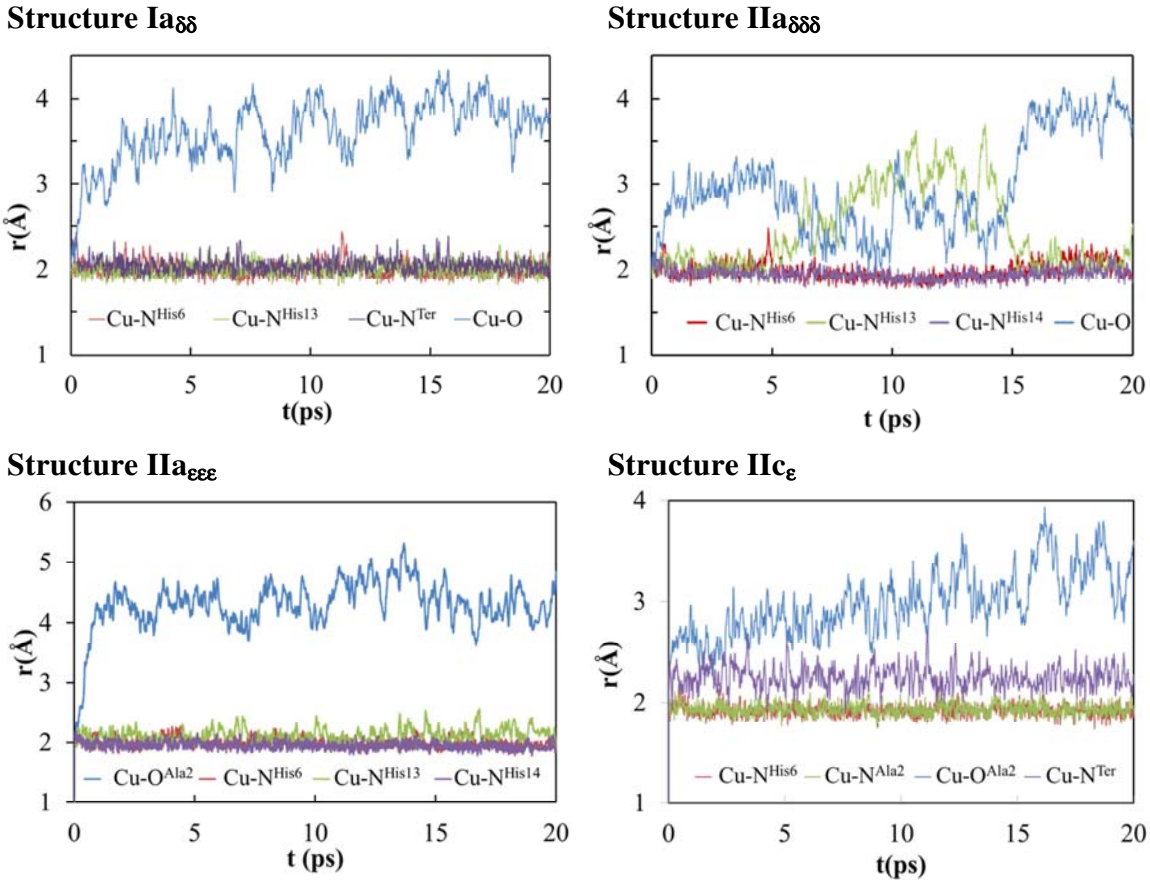

Figure 5.4. Evolution of the relevant Cu-ligand distances during the simulation of the structures **Ia$_{\sigma\sigma}$**, **IIa $_{\delta\delta\delta}$**, **IIa$_{\varepsilon\varepsilon\varepsilon}$** and **IIc$_{\varepsilon}$**.

In all the structures, after the reduction of the complex, the carbonyl group of the peptide, initially coordinated to the metal cation, decoordinates resulting in a tri-coordinated structure in the first few steps, which is almost maintained during the rest of the simulation (blue line). After the decoordination of the carbonyl group, structure **$Ia_{\delta\delta}$** presents a T-shaped geometry which evolves to a trigonal-planar arrangement in about 5 ps, as one can see in the angle variation scheme of *Figure 5.5* where all the angles evolve to approximate 120º. In the case of structure **$IIa_{\delta\delta\delta}$**, in the central part of the simulation which means around 10 ps, the oxygen atom and the nitrogen of His13 move away from Cu to about 2.5 – 3.5 Å. After about 5 ps, the N^{His13} atom coordinates again the metal cation giving rise to a tri-coordinated structure. Among all the structures, this is the one showing more tendency to adopt linear dicoordinated geometry and, thus, is less prone to interact with O_2 and generate the superoxide intermediate.

Structure $Ia_{\delta\delta}$

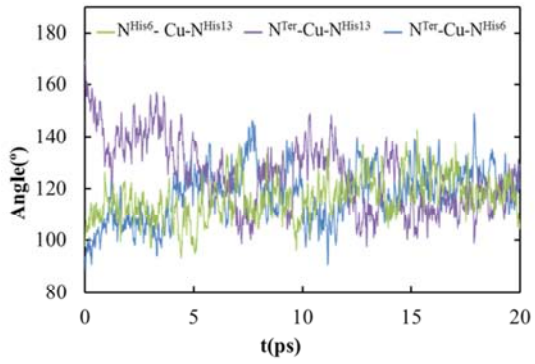

Structure $IIa_{\delta\delta\delta}$

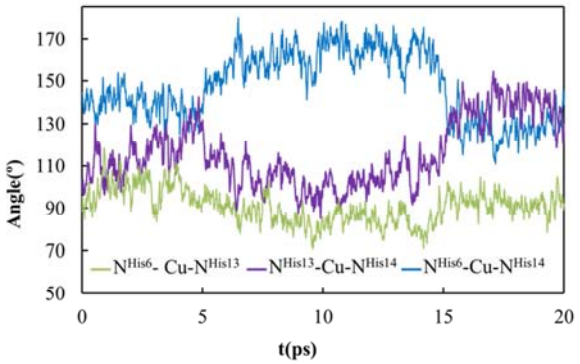

Structure $IIa_{\varepsilon\varepsilon\varepsilon}$

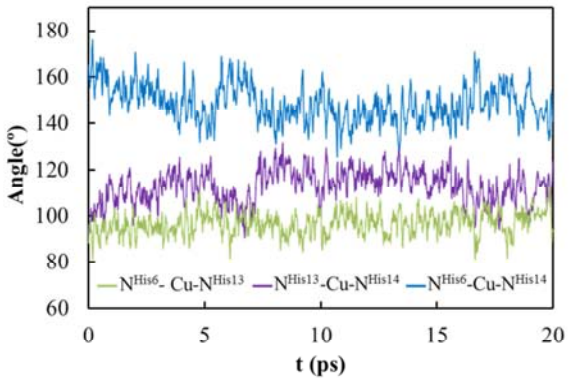

Structure IIc_{ε}

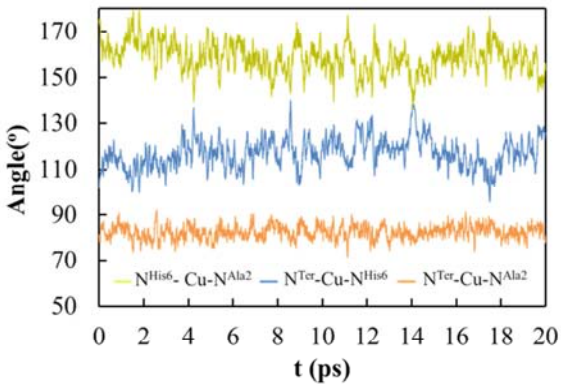

Figure 5.5. Evolution of the relevant Cu-ligand bond angles during the simulation of the structures **$Ia_{\sigma\sigma}$**, **IIa $_{\delta\delta\delta}$**, **$IIa_{\varepsilon\varepsilon\varepsilon}$** and **$IIc_{\varepsilon}$**.

On the other hand, structure **IIa$_{\varepsilon\varepsilon\varepsilon}$** present a distorted T-shaped coordination environment of Cu^{+}, after the decoordination, with one of the angles, N^{His6}-Cu-N^{His14}, considerably larger than the others. Finally, in structure **IIc$_{\varepsilon}$**, the elongation of the Cu-O bond is smaller due to the restrain imposed by the Asp1-Ala2 fragment which is acting as tridentate ligand in the initial structure and despite the cleavage of the Cu-O bond, the oxygen cannot move too far away, as observed in the optimization of the reduced complexes (see above). Furthermore, this structure also exhibit a distorted T-shaped structure with the N^{His6}-Cu-N^{Ala2} angle of about 160º and the other two angles around 90-110º, displaying significantly smaller values than the other structures due to the restriction imposed by the Asp1-Ala2 fragment.

To conclude, the MD simulations confirm that the reduction of Cu^{2+}-Aβ_{1-16} complexes occurs through the decoordination of the O ligand from the CO group, maintain during all the simulation a tricoordinated geometry. The exception is **IIa$_{\delta\delta\delta}$**, which present a linear coordination during an appreciable time of the simulation.

5.4. SRP FOR Cu-Aβ_{1-16} COMPLEXES

The SRP values have been calculated from static calculations as mentioned in *Computational details* section. The computed SRP values are given in *Table 5.1* along with the reaction energies (ΔE, ΔH and ΔG) associated with the reduction process. Moreover, the reduction energy without geometrical changes (ΔE_{ver}) has also been included to evaluate which coordination environments are more prone to capture one electron. For comparison, and to analyze the influence of Aβ peptide on the SRP value, the SRP for models systems that only include the first metal coordination sphere have also been calculated.

In general, the computed SRP values for complexes **Ia$_{\delta\delta}$**, **IIa$_{\varepsilon\delta\varepsilon}$** and **IIa$_{\varepsilon\varepsilon\varepsilon}$** are in pretty good agreement with the most recent experimental values determined for $Cu^{2+/+}$-Aβ_{1-16} complexes couple, which range from 0.28 to 0.34 V.[99,101,291] However, structures **Ib$_{\delta\varepsilon}$**, **IIc$_{\delta}$** and **IIc$_{\varepsilon}$** show more negative SRP values.

Table 5.1. Reaction energies (in kcal·mol^{-1}) and SRP vs SHE (in V) for the different considered structures of Cu^{2+}/Cu^{+} complexes couple. The subscript *corr* means that the empirical correction has been considered. The values in parenthesis correspond to the results for the computed model systems.

System	ΔE_{ver}	ΔE	ΔH	$T\Delta S$	ΔG	E^0_{corr}
$[Cu^{2+/+}(H_2O)_4]$		-95.7	-98.1	3.1	-101.2	0.16
Ia$_{\delta\delta}$	-76.9 (-75.6)	-99.1 (-92.1)	-100.4 (-93.4)	3.7 (3.3)	-104.0 (-96.7)	0.28 (-0.04)
Ib$_{\delta\varepsilon}$	-74.5 (-72.3)	-91.7 (-91.1)	-92.9 (-92.0)	1.9 (2.3)	-94.8 (-94.3)	-0.12 (-0.14)
IIa$_{\varepsilon\delta\varepsilon}$	-72.5 (-77.7)	-96.0 (95.6)	-98.3 (-96.4)	4.0 (2.7)	-102.3 (-99.1)	0.21 (0.07)
IIa$_{\varepsilon\varepsilon\varepsilon}$	-79.7 (-77.7)	-99.1 (-95.6)	-100.1 (-96.4)	1.8 (2.7)	-101.8 (-99.1)	0.19 (0.07)
IIc$_{\delta}$	-65.9 (-69.4)	-87.7 (-86.3)	-90.0 (-87.2)	-0.9 (1.9)	-89.1 (-89.1)	-0.37 (-0.37)
IIc$_{\varepsilon}$	-64.7 (-69.4)	-85.5 (-86.3)	-84.7 (-87.2)	-5.8 (1.9)	-78.8 (-89.1)	-0.81 (-0.37)

Complex relaxation, after the reduction, defined as the difference between ΔE and ΔE_{ver}, which range from -17 to -22 kcal·mol^{-1}, is principally driven by changes on the metal active site as demonstrated by the values of the relaxation energies in the model systems, which extend from -17 to -19. In fact, this is in agreement with the great similarity of the backbone configuration for the oxidized and reduced complexes shown before. Nevertheless, the reduction of the metal cation seems to be more favored in the peptide complex for structures **Ia$_{\delta\delta}$**, **IIa$_{\varepsilon\delta\varepsilon}$** and **IIa$_{\varepsilon\varepsilon\varepsilon}$**, whose SRP values are larger by 0.12 to 0.32 V as compared with those of the model systems. This behavior is due to several factors, such as the distortion of the square planar coordination of Cu^{2+}-Aβ_{1-16} complexes induced by the peptide, the contribution of peptide relaxation and thermal effects. For structures **Ib$_{\delta\varepsilon}$** and **IIc$_{\delta}$**, the values of the SRP are very similar to those obtained for the model systems. This is due to the higher rigidity of the coordination sphere, which seems to be less influenced by the presence of the peptide. Noteworthy, for **IIc$_{\varepsilon}$**, the SRP value is smaller than that corresponding to the model system due to entropic effects. Hence, this comparison with the model systems highlights the importance of the changes induced by the peptide moiety.

Overall, differences on the $Cu^{2+/+}$-Aβ_{1-16} SRP are mainly due to the metal coordination environment; which means that changes in the interaction between the Cu atom and the coordinated ligands before and after the reduction process influence the SRP values. For instance, there is a stronger electrostatic interaction between Cu^{2+} and negatively charged ligands (such as in structures **Ib$_{\delta\varepsilon}$**, **IIc$_{\delta}$** and **IIc$_{\varepsilon}$**) than between Cu^{+} and the same negatively charged ligands in the reduced complexes. This loss in the electrostatic interaction upon reduction is significantly higher than that produced in structures **Ia$_{\delta\delta}$**, **IIa$_{\varepsilon\delta\varepsilon}$** and **IIa$_{\varepsilon\varepsilon\varepsilon}$**, where Cu^{2+} and Cu^{+} atoms are interacting with neutral ligands. As a consequence, Cu^{2+}-Aβ_{1-16}/Cu^{+}-Aβ_{1-16} reaction energies are more negative for those structures with neutral ligands than for those with negatively charged ligands which leads to higher SRP for the structures that involve neutral ligands. These observations confirm that differences on the SRP for the considered complexes mainly arise from the differences in the metal environment and more particularly, on the nature of the ligands.

In order to know if these complexes can catalyze ROS formation, the SRPs for all complexes should be lower than 0.30 V[110], which is the SRP value for the O_2/H_2O_2 couple. As they are, the reduction of O_2 to H_2O_2 is thermodynamically favored for all the considered complexes. However, as mentioned, the first step in this process is the reduction of Cu^{2+}-Aβ_{1-16} complexes, which can be done by reducing agents available in the cellular environment or by oxidizable aminoacids present in Aβ. Computed values indicate that the process of metal reduction could not be facilitated by any of the oxidizable amino acids present in the Aβ peptide such as Tyr10 because its SRP is determined to be 0.95 V[99], which is higher than the SRP of the complexes. Consequently, the participation of external reducing agents is required. Nevertheless, the reduction of the metal center by typical external reducing agents would not be favorable for all systems. For instance, structures **IIc$_{\delta}$** and **IIc$_{\varepsilon}$** would not be reduced by any of the reducing agents existing in the cerebral medium because all of them have higher SRP than those values given by the component IIc. Thus, they do not seem to be plausible candidates for participating in the reactions associated with the neurological damage observed in AD.[97] Structure **Ib$_{\delta\varepsilon}$** could be reduced by agents such as NAD^{+} (SRP = -0.32 V) and FAD (SRP = -0.33 V),[306] among others with SRP values lower than -0.12 V. This species are typically present in the mitochondria of the neurons, taking part in the respiratory chain.[307] Finally, structures **Ia$_{\delta\delta}$**, **IIa$_{\varepsilon\delta\varepsilon}$** and **IIa$_{\varepsilon\varepsilon\varepsilon}$** can be reduced by most of

the reducing species found in the cerebral medium such as ascorbic acid (SRP = 0.05 V),[308] cytochrome b (SRP = 0.04 V), myoglobin (SRP = 0.01 V), glutathione (SRP = -0.23 V) and vitamin B12 (SRP = -0.24 V)[306] among others, which are exposed in the extracellular medium, besides the mitochondrial species previously mentioned.

5.5. CONCLUSIONS

In this chapter, the SRPs of the most representative structures of the oxidized complexes obtained in the last chapter have been computed with the aim of getting new insights into the relation between their structure and their redox behavior. In order to calculate the SRP, the Cu^{+}-$A\beta_{1-16}$ complexes were accurately described by performing optimizations and frequency calculations at M06-2X/SB_1 level of theory and refined, through single point calculations, with a LB basis set. The results show that the copper reduction induces the $CO_{backbone}$ decoordination leading to tri-coordinated species, in most cases with T-shaped geometry. This is also supported by AIMD simulations which confirm that this geometry is stable for a period of time long enough to be attacked by O_2, since tricoordinated structures are those that can be oxidized by dioxygen while linear dicoordinated species seem to be resistant to O_2 induced oxidation.

The SRP results highlight the importance of the nature of the ligands being significantly lower for those structures which exhibit negatively charged ligands, such as structures **IIc$_{\delta}$**, **IIc$_{\varepsilon}$** and **Ib$_{\delta\varepsilon}$**, than those which present neutral ligands, structures **Ia$_{\delta\delta}$**, **IIa$_{\varepsilon\delta\varepsilon}$** and **IIa$_{\varepsilon\varepsilon\varepsilon}$**. The SRP values of the structures which involve neutral ligands are in better agreement with the reported experimental data and are consistent with the production of H_2O_2 related to the oxidative stress characteristic of the AD.

6

O_2 ACTIVATION INDUCED BY Cu-A$\beta_{1\text{-}16}$ COMPLEXES

After the reduction of Cu^{2+}-A$\beta_{1\text{-}16}$ complexes by external reducing agents, a cascade of reactions is triggered to produce ROS.[97–99,101,309] The first step of this cascade of reactions seems to be the interaction of the dissolved oxygen with Cu^{+}-Aβ complex to form a Cu bound superoxide species. That is, once triplet dioxygen reaches the Cu^{+} coordination site, the final Cu oxidation depends on the chance of an efficient electron transfer to the bound dioxygen:

$$\mathbf{R_1:}\quad Cu^{+}\text{-}A\beta\cdots O_2 \rightarrow Cu^{2+}\text{-}A\beta O_2^{-\bullet} \tag{6.1}$$

Experimentally, the superoxide formation is very elusive presumably because of the product of *reaction 6.1* reacts with the protons in the medium and one additional molecule of reductant in a fast and very exothermic process.[98] Indeed, only Reybier and coworkers have reported the detection of superoxide as an intermediate.[310] Next step is identified as a globally down-hill proton-coupled electron transfer reaction:[43]

$$\mathbf{R_2}: \quad Cu^{2+}\text{-}A\beta O_2^{-\bullet} + 2\ H^+ + 1\ e^- \rightarrow Cu^{2+}\text{-}A\beta O_2H_2 \tag{6.2}$$

Then, the oxidation is propagated to form hydrogen peroxide which can be eventually split into the hydroxyl radical by other Cu^+ complexes in the environment.[311] Finally, the Cu^{2+}-Aβ specie is recovered and thus, it can be reduced again by external reducing agents. Hence, the catalytic cycle is restarted.

$$\mathbf{R_3}: \quad Cu^{2+}\text{-}A\beta O_2H_2 \rightarrow Cu^{2+}\text{-}A\beta + H_2O_2 \tag{6.3}$$

This redox catalytic cycle critically depends on the binding mode of Cu^{2+} in the Cu^{2+}-Aβ_{1-16} complexes, because this specie must have an appropriate SRP to be reduced by ascorbate and oxidized by O_2 and the SRP is determined by the coordination environment of the complex, as it has been mentioned in the last chapter.

Since superoxide intermediate has not been detected in vivo, computational techniques may shed some light on the formation and characterization of this key step in the proposed mechanism. Hence, in this chapter, model systems were used to analyze the O_2 activation for every proposed Cu^{2+}-Aβ_{1-16} coordination spheres commented in *Chapter 4* and, then, the whole Cu-Aβ_{1-16} complexes have been considered.

6.1. COMPUTATIONAL APPROACH

The standard 6-31+G(d) basis set for H, C, N and O atoms and the LANL2DZ pseudopotential with its associated basis set (5s5p5d)/ [3s3p2d][280] for Cu were used for geometry optimizations and frequencies calculations. Hereafter, it will be referred as SB_2 in order to differentiate it from the basis set used in the other chapters. After that, single point calculations with the LB basis set, which are the larger LANL2TZ, (5s5p5d)/[5s5p3d], for Cu[281] supplemented with an *f* function[282] and LANL2DZ pseudopotential[280] and the 6-311++G(d,p) basis set for all the rest of atoms, were

performed to refine the energies. All the calculations were done considering the aqueous solvent effect using the SMD implicit solvent model.

The functional chosen for this work needs to properly describe the properties of the metal site, particularly the formation of the charged transfer Cu^{2+}-A$\beta O_2^{-\bullet}$ superoxide complex. For that, both the second *Ionization Energy* (IE) of Cu and the O_2 *Electron Affinity* (EA) were chosen as the parameters to analyze the functional description. *Table 6.1* discloses the second IE of Cu and the O_2 EA computed with different functionals and with the SB_2 and LB basis set.

Table 6.1. Ionization Energy (IE) of Cu and Electronic Affinity (EA) of O_2 in gas phase in eV at different levels of calculation with the SB_2 and LB basis sets. The references for the experimental data are a) Ref. [312] b) Ref. [313].

	IE		**EA**	
	SB_2	**LB**	**SB_2**	**LB**
Exp.	20.3[a]		-0.4[b]	
M06-L	20.2	20.1	-0.2	-0.2
M06	20.7	20.6	-0.6	-0.5
M06-2X	20.6	20.5	-0.4	-0.4
B3LYP	20.8	20.6	-0.6	-0.6

Results evince that the two basis set employed show similar values, as in previous sections. This is the reason why the following optimizations and frequencies calculations have been carried out with the SB_2 basis set, in order to reduce the computational cost, and energies have been refined by performing single-points calculations with the LB basis. In addition, different functionals provide similar IE. Notably, hybrid functionals, such as M06, M06-2X and B3LYP (considering LB basis set), give an IE around 0.2 – 0.3 eV larger than the experimental value; while M06-L, with no exact exchange percentage, is 0.2 eV lower than the experimental value. On the other hand, concerning EA, the M06-2X value seems to be the one that better compares to the experimental result. Furthermore, M06-2X functional has been shown to provide a good description of charge transfer complexes[314] and is able to account for mid-range dispersion forces.[195] Additionally, as it has been commented of about Cu^{2+} complexes studies in *Chapter 4*, GGA functionals or hybrid functionals with a low percentage of exact exchange tend to exhibit too large spin delocalization, situations that are overstabilized due to a bad cancellation of the self-interaction part by the exchange functional. Thus, M06-2X functional was chosen to analyze O_2 activation by Cu^{+}-Aβ complexes.

Thermodynamic corrections were obtained assuming unscaled harmonic vibrational frequencies, which enable to confirm that all structures are true minima, and the rigid rotor approximation was obtained by standard statistical methods. Cu^{2+} calculations, as it is an open-shell ion, were based on an unrestricted formalism. All electronic calculations have been done with *Gaussian09* package program.[245] Atomic charges and spin densities were obtained from Natural Population Analysis (NPA).

6.2. O_2 ACTIVATION

The identification of superoxide as an intermediate has always been difficult, even *in vitro*.[309] Therefore, there is a debate about the lifetime of the initially Cu-superoxide complex and the accessibility to superoxide species by other reactant molecules in the synaptic region. Computational models are particularly useful to elucidate mechanisms that involve labile intermediates. However, computational results strongly depend on the chosen model; for instance, chemical groups in the second coordination sphere can influence in the reactivity of Cu. Therefore, this study extends the range of hypothetical Cu-Aβ-O_2 metal coordination spheres proposed by A. Rauk and coworkers,[43,98] and shows the most popular coordination spheres proposed in the literature for the Cu^{2+}-Aβ species and other truncated models proposed by G. LaPenna.[311]

Furthermore, once the most stable orientation of O_2 was determined for model systems, the inclusion of the full peptide in the Cu-Aβ_{1-16} complexes was considered to study of O_2 activation.

6.2.1. INFLUENCE OF METAL COORDINATION

In this section, the optimized structures for the mentioned model systems of Cu^{+}-Aβ$\cdots O_2$ and Cu^{2+}-A$\beta O_2^{-\bullet}$, which are relevant species for the study of superoxide formation, are analyzed. This study has been developed in collaboration with Dr. Giovanni La Penna at the Institute for Chemistry of Organometallic Compounds of the *National Research Council* (CNR) in a predoctoral short visit of three months in Florence.

In order to analyze the influence of metal coordination, models considered in this section only include the first metal coordination sphere. The model construction has been performed *via* two different approaches. That is, a group of model systems have

been built by adding dioxygen to the most stable truncated Cu^{+}-Aβ_{1-16} complexes obtained in the last chapter (models **Ia$_{\delta\delta}$**, **IIa$_{\delta\varepsilon\delta}$** and **IIc$_{\varepsilon}$**, hereafter the subscript "δ" or "ε" will be omitted for simplicity), which only include the groups interacting in the first coordination sphere. Different orientations of the incoming O_2 molecule with respect to the other Cu^{+} coordinating ligands have been considered, as outlined in *Figure 6.1,* considering the steric hindrance of the peptide in the full complexes to the O_2 entrance. For instance, model Ia presents two different orientations; one that analyzes the entrance of the oxygen between the two histidines (**Ia1**) and other where the oxygen approaches from the space left by the decoordinated O of the CO group (**Ia2**). Model **IIa** only exhibits one possible oxygen entrance with less steric hindrance. However, model **IIc** also shows two different approaches; one between the N-terminal and the histidine (**IIc1**) and a second approach where oxygen comes from the space left by the decoordinated O of the CO group (**IIc2**), similarly to model **Ia2**.

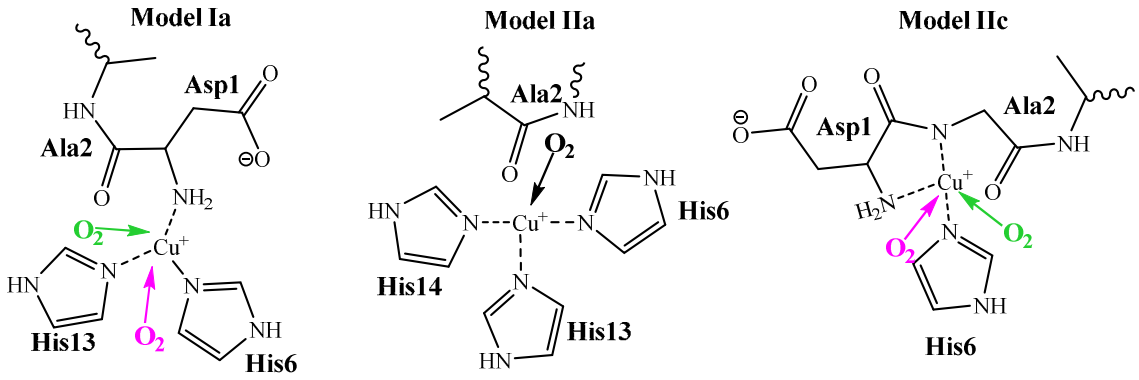

Figure 6.1. Different O_2 approaches to Cu^{+} considered in the present study. When different orientations are possible, position 1 is shown in pink and position 2 in green.

While the fist models comes from Cu^{2+}-Aβ_{1-16} monomers obtained in the last chapter, the initial structure of the second kind of models (models **1-15**) has been obtained from other Cu-Aβ states of hydroperoxide in Cu^{+}-Aβ_{1-16} complexes, from Ref. [311], and substituting hydroperoxide by dioxygen keeping the bath of 311 water molecules. These initial configurations also include information concerning Aβ dimers. Among the 16 configurations obtained in Ref. [311], only those with O_2 in the first Cu-coordination sphere were considered whereas configurations with O_2 in the second sphere (**3**, **4**, **6**, **12** and **16**) have not been used as models for the dioxygen binding to Cu^{+}. Therefore, only 11 configurations were evaluated, which were truncated including only the relevant

residues for coordination (Asp1, His6, His13 and His14) and water molecules within a range of 2 Å from the dioxygen molecule.

The latter configurations (models **1-15**) were geometrically restricted by fixating the C_β atoms of His sidechains and Asp1 to mantain the original peptide configuration. In these models, Cu ligands were simplified by substituting His sidechains by 4-methyl-imidazole, which involves the δ or ε coordination of the nitrogens ($metIm_{\delta/\varepsilon}$), and Ala2 by $NHCH_3$. However, the first models (**Ia**, **IIa** and **IIc**) do not include this methyl in the imidazole groups; then, the geometrical restrictions of the peptide cannot be considered, as well as the δ or ε coordination.

The most representative Cu^+-Aβ···O_2 and Cu^{2+}-A$\beta O_2^{-\bullet}$ structures (**Ia1**, **IIa, IIc2** and **11**) have been outlined in *Figure 6.2.* The rest of complexes are shown in *Figures B1* and *B2* in *Appendix B* section. These structures have been selected because **Ia1**, **IIa** and **IIc2** are the ones that most stabilize the formation of superoxide. On the other hand, structure **11** is the only one that Cu^{2+}-$O_2^{-\bullet}$ system has not been found.

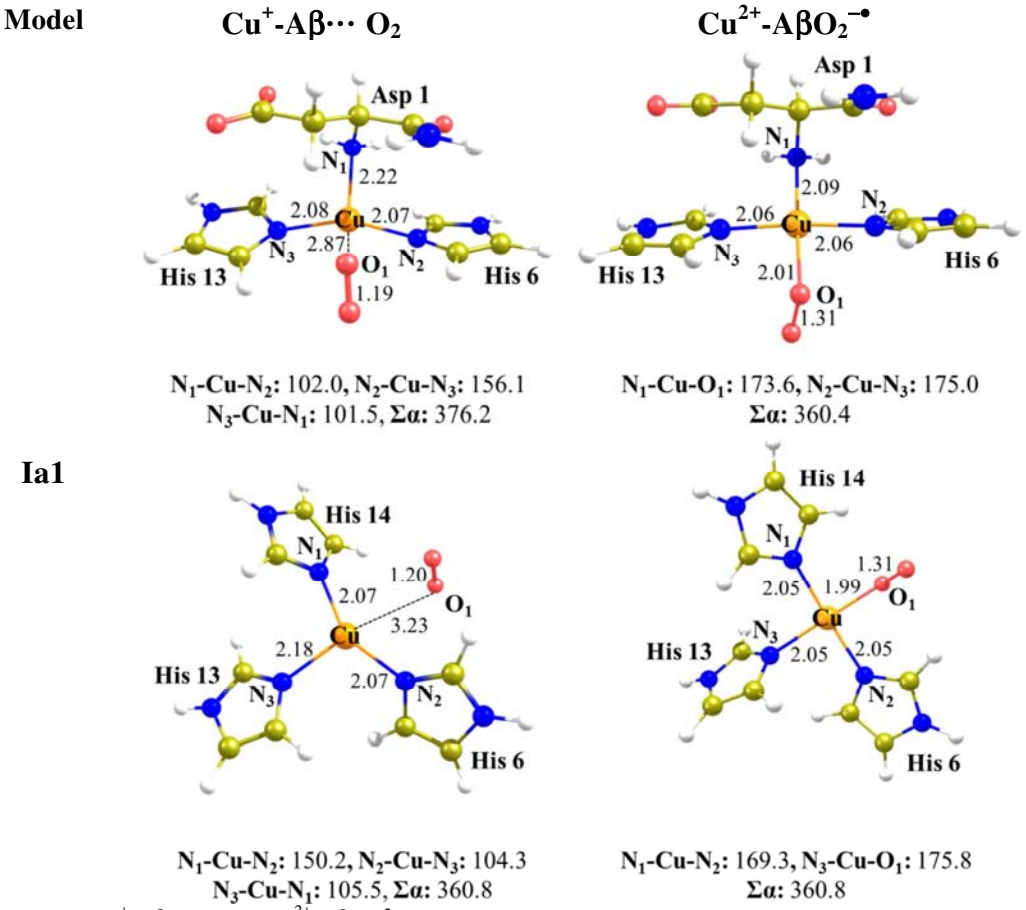

Figure 6.2. Cu^+-Aβ···O_2 and Cu^{2+}-A$\beta O_2^{-\bullet}$ optimized structures for the considered O_2 orientations. Distances are in angstroms and angles in degrees. Σα means the sum of all the angles around Cu.

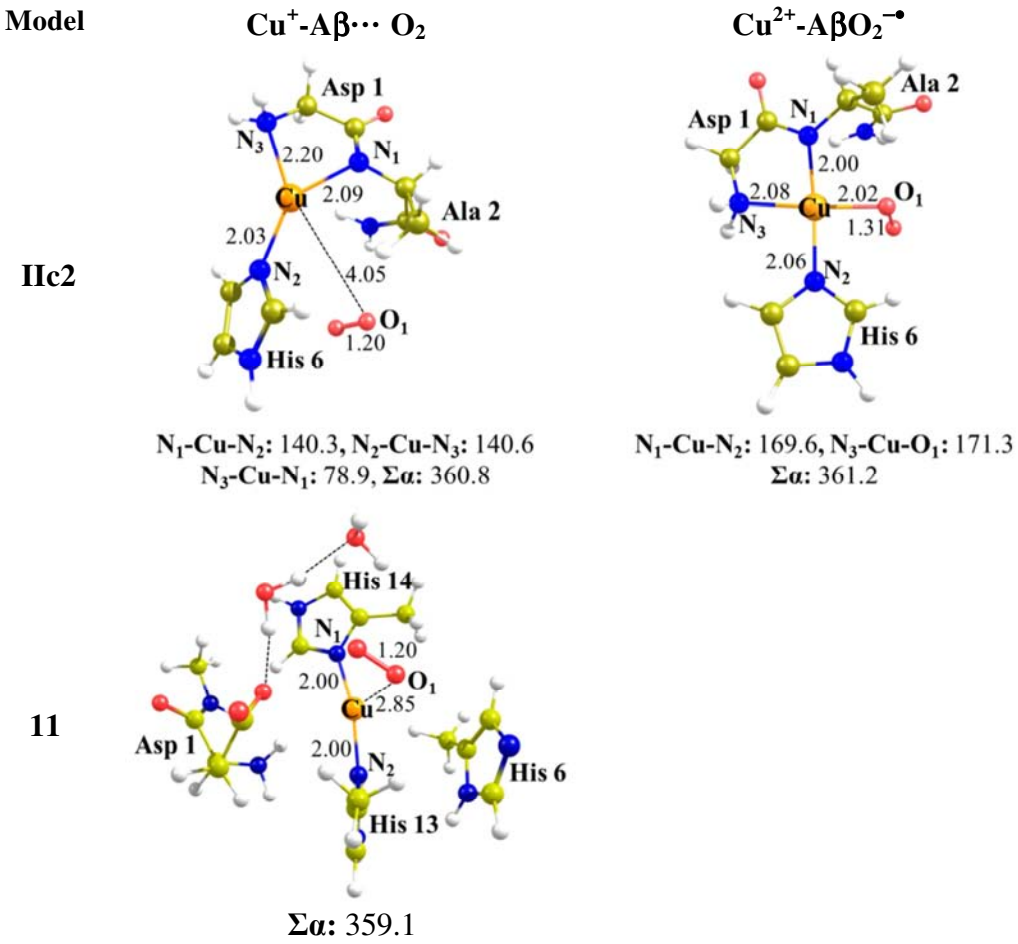

Figure 6.2. Continuation.

All the Cu^{+}-Aβ··· O_2 complexes present a Cu-O_2 distance larger than 2.80Å and can be considered that the oxygen is not bound to Cu. However, Cu^{2+}-A$\beta O_2^{-\bullet}$ species show a Cu-O_2 distance around 2.00 Å, like the other ligands bound to Cu. Notably, all models present an O-O distance for the O_2 about of 1.20 Å in the O_2 unbound systems, in agreement with the value of the distance for the gas phase O_2 molecule, which is 1.208 Å.[315] In contrast, for the O_2 bound complexes, this distance increase to 1.31 Å in accordance with an electron transfer to an antibonding π orbital to form superoxide. Moreover, all the Cu^{2+} considered models present a Cu spin density between 0.66-0.76, indicating a strong Cu^{2+} character as well as a strong charge transfer to oxygen as is also shown in the values of the O_2 charge in the bound complexes, which are near 0.77. The Cu^{+}-O_2 species show a Cu spin density around 0.00 and O spin density in the O_2 moiety around 1.99.

It can be observed in *Figure 6.2* that for **Ia** and **IIa** models, Cu^{+}-Aβ···O_2 shows a slightly distorted T-shaped geometry. However, the coordination of amino terminal

group and the deprotonated amide nitrogen of the same ligand favor distorted trigonal type coordination for **IIc** model. In all cases, one of the Cu^+-N distances is significantly larger, 2.18-2.22 Å, than the others, 2.03-2.09 Å, according to the linear dicoordination preference of Cu^+-O_2 to minimize metal-ligand repulsion. Moreover, the oxygen in these Cu^+-O_2 species is oriented to form a planar geometry because the sum of the four angles around Cu (Σα) in Cu^+ complexes are near to 360º, except in model **Ia** which presents higher Σα values. On the other hand, Cu^{2+}-$O_2^{-\bullet}$ complexes evince in all cases regular square-planar geometries with Σα near 360º and four similar metal ligand distances, around 2.00 Å.

The potential energy change in the dioxygen activation (E_{R1}) has been also estimated as the energy cost for superoxide formation in the Cu^{2+}-$O_2^{-\bullet}$ bound state with respect to the Cu^+-O_2 unbound state, following the *reaction 6.1*. These results are summarized in *Table 6.2*.

Table 6.2. Potential energy difference between Cu-O_2 bound and unbound states (E_{R1}) and the list of Cu ligands complementing the O_2 binding. Moreover, for models **Ia**, **IIa** and **IIc**, free energies are shown in parenthesis. *Im* refers to the imidazole group of the His sidechain. Energies are in kcal·mol^{-1}.

Model	Group	E_{R1}	Cu coordination
Models derived from truncated Cu^+-Aβ_{1-16} complexes			
Ia1	*C*	-3.7 (-0.5)	2 Im + N/O_δ^{Asp1}
Ia2	*C*	-1.7 (2.3)	2 Im + N/O_δ^{Asp1}
IIa	*A*	-5.7 (-1.0)	3 Im
IIc1	-	-8.2 (-5.8)	1 Im
IIc2	-	-8.6 (-6.1)	1 Im
Models derived from Aβ monomers			
1	*A*	4.5	3 Im
2	*B*	1.7	2 Im + H_2O
5	*B*	7.3	2 Im + H_2O
7	*B*	13.8	2 Im + H_2O
8	*C*	1.0	2 Im + N^{Asp1}
Models derived from Aβ dimers			
9	*C*	2.3	2 Im + N^{Asp1}
10	*D*	5.1	Im + N^{Asp1}
11	*B*	–	2 Im
13	*A*	3.0	3 Im
14	*D*	-0.7	Im + N/O_δ^{Asp1}
15	*A*	-0.6	3 Im

In the case of models **Ia**, **IIa, IIc**, **14** and **15**, the process is exothermic corresponding to a favorable superoxide formation. Moreover, for models **Ia**, **IIa** and **IIc**, the entropic effects favor the Cu^+-O_2 system increasing the reaction energies between 2.4 (**IIc1**) to

4.7 (**IIa**) kcal·mol^{-1}. The observed trends would be similar regardless of consider Gibbs or potential energies.

The reason for the differences in binding energy can be understood if the 11 models are divided in four groups, according to the respective coordination topology and ranked in order of the decreasing number of His binding Cu.

Group A is referred to those configurations where Cu is bound to 3 imidazole rings of three different His and the fourth Cu valence is filled by O_2, which are models **1**, **13** and **15**. Also, model **IIa** can be included. Models **1** and **13** exhibit that Cu^{2+}-$O_2^{-\bullet}$ system is slightly higher in energy compared to the Cu^{+}-O_2, due to the restrictions in the metal coordination environment that prevent the formation of a regular square-planar coordination for Cu^{2+}. Models **15** and **IIa** present favorable reaction energies, particularly model **IIa** showing that more favorable square-planar coordination for Cu^{2+} can be achieved if no restrictions are considered.

Group B, which implies models **2**, **5** and **7**, represent the configurations that display, additionally to O_2, two imidazole rings and one water molecule bound to Cu. The E_{R1} energy suggest that the unbound state is more stable that the bound one, which means that there is a notable conformational change from Cu^{+}-O_2 to Cu^{2+}-$O_2^{-\bullet}$ system in all models. In fact, the metal coordination environment in the Cu^{+}-O_2 species is not planar ($\Sigma\alpha$ is far from 360º) and need a significant reorganization to accommodate O_2 in Cu^{2+}-$O_2^{-\bullet}$ complexes. On the other hand, model **11** has been also included in this group. However, it lacks of water molecule as third ligand forming a linear coordination, which is inert toward dioxygen as mentioned in the last chapter. Therefore, no Cu^{2+}-$O_2^{-\bullet}$ system has been found.

Models **8** and **9** form *group C*, which are structures with two imidazoles bound to Cu along with N_{term} of Asp1 besides O_2, similarly to model **Ia**. As in the case of *group A*, the reaction energy is unfavorable for models **8** and **9**, but favorable for model **Ia**. This is probable due to the restrictions imposed in models **1 – 15** whose β carbon atoms have been fixed at their initial position in the Cu^{+} complexes.

Finally, *group D*, which involves models **10** and **14**, evince one single imidazole as well as the N_{term} and either the O of the carbonyl group or the O_δ of the carboxylate group of

Asp1, respectively. In this case, the energy related to the O_2 activation shows that Cu^+-O_2 is again more stable than Cu^{2+}-$O_2^{-\bullet}$ in model **10**; in contrast, in model **14** superoxide formation is favorable by 0.2 kcal·mol^{-1}. This favorable O_2 activation is caused by the *anti* coordination of the carboxylate group with respect to the end-on O_2 that stabilize the Cu^{2+}-$O_2^{-\bullet}$ complex. In fact, model IIc that also present a negatively charged ligand in the metal coordination sphere imply favorable reaction energy.

Generally, results indicate that superoxide formation is more favorable in His rich coordination environments, as in model **IIa** and **15**, or when there are negatively charged coordinating ligands, such as in model **IIc** or **14**.

6.2.2. ENERGY BARRIERS FOR THE SUPEROXIDE FORMATION

In addition, the energy barrier for the superoxide intermediate formation has also been study. *Figure 6.3* outlines the PES (*Potential Energy Surface*) curves for the approach of O_2 to the Cu^{2+} in the most stable model systems orientations, which are **Ia1**, **IIa** and **IIc2.** These curves have been obtained by performing relaxed PESs starting for both Cu^+-A$\beta\cdots O_2$ and Cu^{2+}-A$\beta O_2^{-\bullet}$species shortening and lengthening the Cu-O distance, respectively. Therefore, the maximum of each curve corresponds to the crossing point of both PESs and represents the approximation to the transition state for the superoxide formation process.

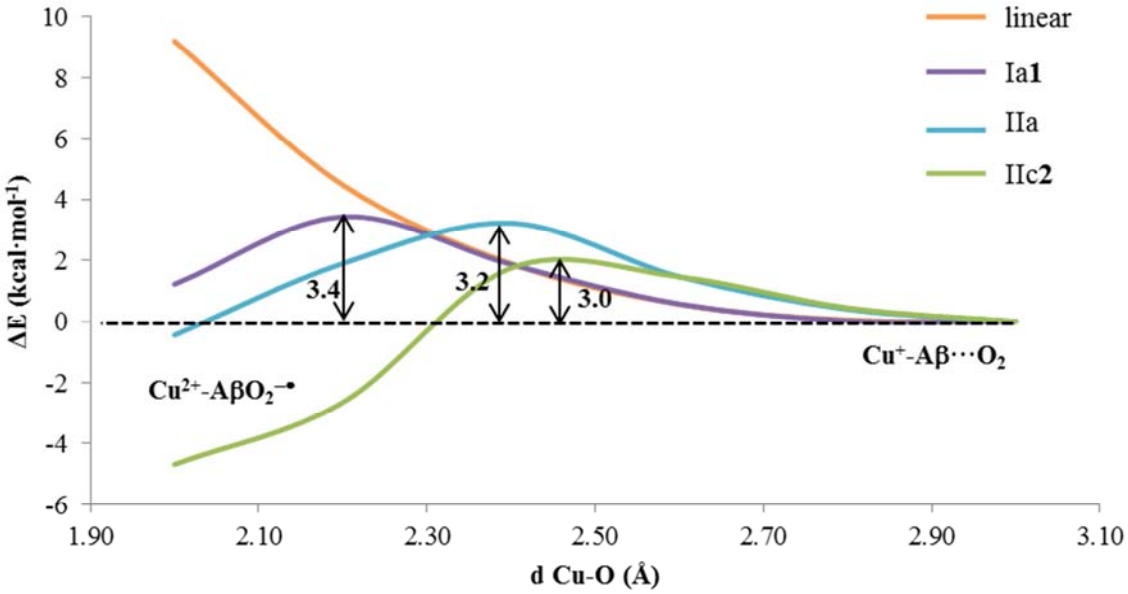

Figure 6.3. Potential-energy curves corresponding to the coordination of O_2 to Cu^+ in the most favorable orientations of O_2 for the considered model systems of Cu^+Aβ (energetic barriers are in kcal·mol^{-1}).

The approximate potential energy barriers for O_2 activation are similar for all models, **Ia**, **IIa** and **IIc**; and range between 3.0 and 3.4 kcal·mol^{-1}. These values indicate a fast process at room temperature and, hence, population of both states is only determined by their corresponding relative energies. Moreover, the interaction of O_2 with a system enclosing a His-His linear geometry through the N_δ coordination of imidazole has been considered, named linear in *Figure 6.3*. In this case, no minimum is found, according to experimental studies supporting that linear two coordinate structures are inert toward dioxygen.[288]

The entropic effects have not been considered. But, as note for the reaction energies, these effects should slightly favor Cu^+-A$\beta\cdots O_2$ with respect to the transition state increasing somewhat the energy barriers. However, small differences between potential and Gibbs energies are expected, which would not change the observed trends.

6.2.3. INFLUENCE OF SECOND SPHERE INTERACTION

Once the influence of metal coordination sphere in the O_2 activation has been studied, the interaction of the second sphere has been taken into account considering the influence of the full peptide. Results of the AIMD calculations have shown that the final structures of Cu^+-A$\beta_{1\text{-}16}$ are very similar to those obtained by the reduction of Cu^{2+}-A$\beta_{1\text{-}16}$. Therefore, the tricoordinated Cu^+-A$\beta_{1\text{-}16}$ complexes obtained from the QM reduction of Cu^{2+}-A$\beta_{1\text{-}16}$ in the last chapter have been used as starting structures for O_2 activation. Furthermore, only the most favorable orientations have been analyzed.

Figure 6.4 outlined the optimized structures for the real Cu^+-A$\beta_{1\text{-}16}\cdots O_2$ and Cu^{2+}-A$\beta_{1\text{-}16}O_2^{-\bullet}$ complexes. The metal coordination spheres are similar to those found for the model systems; that is, the unbound system corresponds to the same tricoordinated structures, while the O_2 bound complexes evince regular square-planar geometries ($\Sigma\alpha$ near 360º). Moreover, the O-O distances in the O_2 moiety are maintained; it means 1.20 Å in the unbound system and 1.30 Å in the bound complexes. Frequency calculations on the real systems have not been performed due to their large size. However, since O_2 coordination to Cu^+ mainly implies geometrical changes on the first metal coordination sphere, the inclusion of entropic effects would follow similar trends than for the model systems.

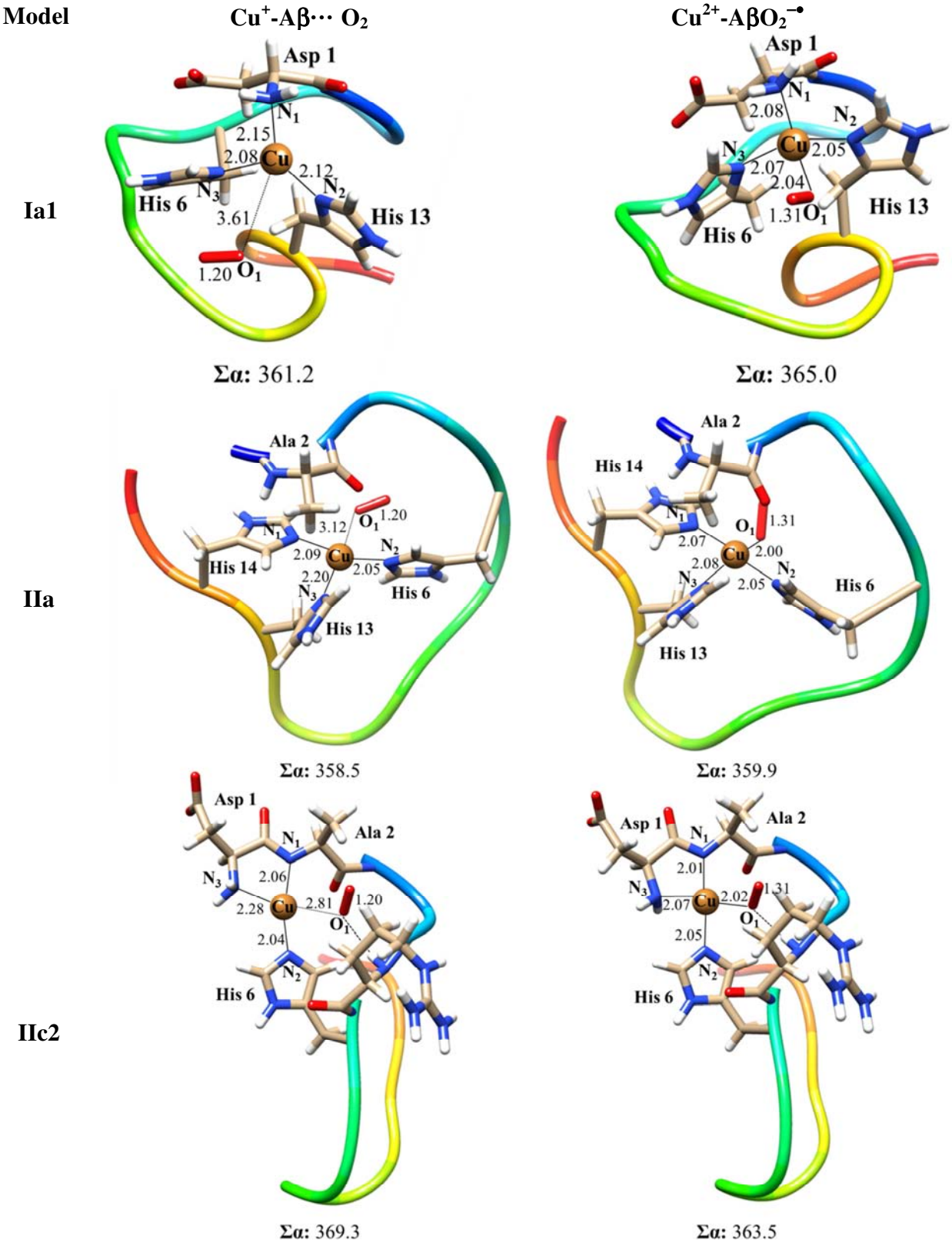

Figure 6.4. Cu^{+}-Aβ···O_2 and Cu^{2+}-A$\beta O_2^{-\bullet}$ optimized structures of the real system. Distances are in angstroms and angles in degrees. Σα means the sum of all the angles around Cu.

The potential reaction energy corresponding to O_2 activation, which corresponds to R_1 in the *reaction 6.1*, has been computed for the entire system. *Table 6.3* summarizes the obtained results, which also includes the values for model systems to compare.

Table 6.3. Potential reaction energy of O_2 activation in kcal·mol^{-1} for the different coordination spheres considered. [a]Cu spin density for the Cu^{2+}-A$\beta O_2^{-\bullet}$ specie. [b]Charge of O_2 in Cu^{2+}-A$\beta O_2^{-\bullet}$ complexes.

	Model system			Real system	
	E_{R1}	Spin (Cu)[a]	q (O_2)[b]	E_{R1}	Spin (Cu)[a]
Ia1	-3.7	0.73	-0.76	0.3	0.69
Ia2	-1.7	0.73	-0.76		
IIa	-5.7	0.74	-0.76	-5.6	0.74
IIc1	-8.2	0.74	-0.77		
IIc2	-8.6	0.73	-0.77	-16.1	0.70

Explicit inclusion of the full peptide in the models induces different effects depending on the electrostatic interactions exerted by charged residues of the second sphere as a result of the peptide conformation adopted in the different coordination modes. *Figure 6.5* presents the electrostatic potential maps of the Cu^{2+}-A$\beta O_2^{-\bullet}$ complexes that show these interactions. For instance, for component **Ia1** the peptide disfavors the superoxide formation by 4.0 kcal·mol^{-1} because the O_2 moiety is exposed to negatively charged ligands around it, due to the carboxylate groups. Thus, superoxide formation results in an increase in the electrostatic repulsion due to the interaction between $O_2^{-\bullet}$ and the carboxylate groups of the second sphere ligands, which hinders the O_2 activation. The distances between the end O atom of superoxide and the C atom of the carboxylate group range between 4.7 and 11.6 Å. Similarly, component **IIa** is slightly disfavored when the peptide is included, only 0.1 kcal·mol^{-1}. In this case the negatively charged regions near to O_2 are around 5.7-13.5 Å. Hence, there are not as close as in model **Ia1**. Thus, the peptide does not overly disfavor the superoxide formation. The opposite effect can be observed when the O_2 is located in the vicinity of a positively charged region. For instance, in the case of component **IIc2**, the inclusion of the full peptide greatly favors the reaction by 7.5 kcal·mol^{-1} owing to the side chain of Arg5, which stabilizes the superoxide formation. Moreover, in the case of model **IIc2**, one of the oxygen atoms of O_2 evince a weak interaction with the NH group of Arg5 (1.96 Å).

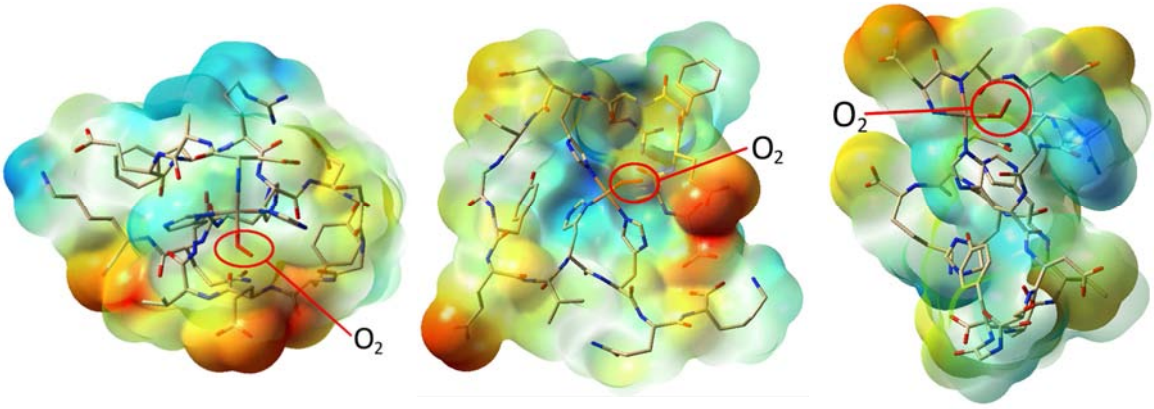

Model Ia1 **Model IIa** **Model IIc2**

Figure 6.5. Electrostatic potential maps of the Cu^{2+}-A$\beta O_2^{-\bullet}$ structures. Red and blue colors indicate negative and positive electrostatic potential, respectively.

Summarizing, the superoxide formation is more favorable in **IIc** type environments, where Cu^{2+} is largely stabilized by the presence of negatively charged ligand in the coordination sphere and O_2 ligand is located in vicinity of a positively charged region. However, this structure is not the predominant one at physiological pH. Furthermore, it has a low SRP to be reduced by external reducing agents present in the medium. On the contrary, model **Ia** show slightly unfavorable superoxide formation, indicating that this type of coordination is less prone to it. Nevertheless, the subsequent protonation and reduction steps of the mechanism, which are referred to the *reactions 6.2* and *6.3*, are largely favorable providing the driving force of the global process.

6.3. CONCLUSIONS

Reduction of Cu^{2+}-Aβ_{1-16} and activation of O_2 by the resulting Cu^{+}-Aβ_{1-16} complex have been proposed as the key steps in the H_2O_2 formation mechanism that, in turns, produce ROS which lead to the oxidative stress typical of AD. In this chapter, the O_2 binding to Cu^{+}-Aβ_{1-16} complex has been studied by performing optimizations and frequency calculations at M06-2X/SB_2 level of theory and refined, through single point calculations, with a LB basis set.

The most stable Cu^{2+}-Aβ_{1-16} complexes obtained from the last chapter have been considered. In addition, small models that only include the ligands of the first metal coordination sphere have also been analyzed in order to understand the role of the second sphere interactions. Both small, which involve a range of hypothetical configurations based on experimental data, and real Cu-Aβ_{1-16} models indicate that superoxide formation

is more favorable in His rich coordination environments, like model **IIa**, or when negatively charged ligands are near to the metal, such as model **IIc**. However, the binding O_2 to Cu^{+}-$A\beta_{1-16}$ for model **Ia1**, which enclose the N terminus and histidines 6 and 13, is slightly unfavorable (0.3 kcal·mol^{-1}). In all cases, spin density values indicate a significant Cu^{2+} character and, consequently, a charge transfer to superoxide. In addition, the energy barrier for the superoxide formation of models **Ia1**, **IIa** and **IIc2** are less than 4 kcal·mol^{-1} and, thus, kinetically affordable.

Furthermore, comparison of the reaction energy values for the small and real models show that peptide configuration induces different effects depending on the coordination mode considered. Electrostatic potential maps evince that this behavior is due to the different second sphere interactions with O_2 in each model. In fact, model **Ia1** is in vicinity of negatively charged regions which produce that the superoxide formation is disfavor; whereas in model **IIc2**, the metal center is near to a positively charged Arg5 which favors the O_2 activation.

7

COPPER CHELATORS

As mentioned, a potential treatment for AD consists in lowering extracellular copper levels and restoring homeostasis in the brain via efficient chelators. These kind of ligands are known as *Metal Protein Attenuating Compounds* (MPACs) and seem highly promising. They should be able to translocate Cu^{2+} from the extracellular environment to inside the cell reducing the Aβ toxicity because, inside the cell, the metals induce a neuroprotective signaling cascade that lead to the degeneration of Aβ. Among all the possible MPACs, the development of short peptide-based chelators shows important advantages because they are easy to synthesize and less likely to be immunogenic.

Several proteins that interact with metal ions present a typical peptidic sequence called ATCUN motif. The ATCUN metal-binding site, which is known for more than 55 years,[316] is characterized by a coordination donor-set composed of a free NH_2 terminus, two

deprotonated amide nitrogen atoms from two amino acids at positions 1 and 2, and an imidazole from a histidine residue at the third position (*Figure 7.1*).[317,318] These four N-atoms can specifically and strongly interact with Cu^{2+} ions, generating very stable square-planar complexes.[319]

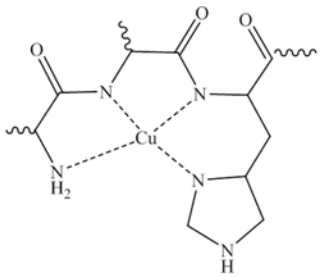

Figure 7.1. Schematic representation of Cu^{2+}-bound ATCUN motif.

In the present study, tripeptides including two histidines and either one tryptophan or one alanine have been selected to investigate the influence of the peptidic sequence on the copper-binding and redox properties of the well-known peptidic triad. Tryptophan has been chosen as a potential fluorescent reporter to allow metal-binding studies by fluorescence spectroscopy in the future. Hence, the behavior of four different tripeptides, namely His–Trp–His (HWH), Trp–His–His (WHH), His–His–Trp (HHW) and AcHis–Trp–His (Ac-HWH), interacting with copper has been examined in great detail (see *Figure 7.2*), both theoretically and experimentally, in collaboration with Patrick Gamez and Ana Belén Caballero from the Universitat de Barcelona and Silvia Mena and Gonzalo Guirado from the Universitat Autónoma de Barcelona.

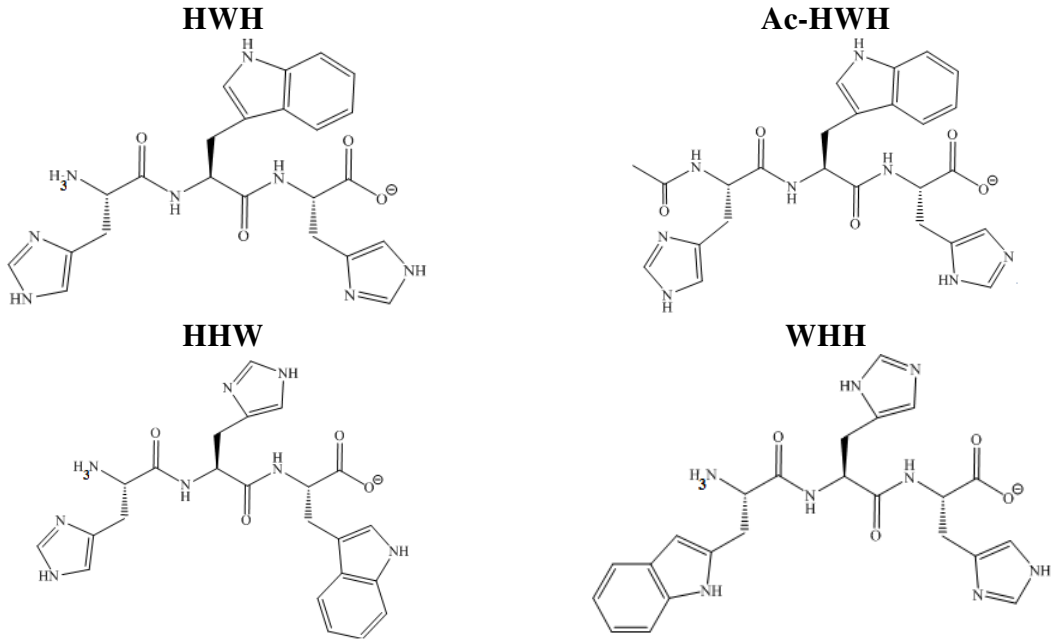

Figure 7.2. Scheme of the peptide sequences studied in this work**.**

7.1. COMPUTATIONAL DETAILS

All the optimizations have been performed using the M06-2X functional, which appropriately describe the coordination properties at the metal site and the non-covalent interactions of the peptide, as explained in the previous chapters. The used basis set are the LB basis set, which is the LANL2TZ, (5s5p5d)/[5s5p3d], for Cu[281] supplemented with an *f* function[282] and LANL2DZ pseudopotential[280] and the 6-311++G(d,p) basis set for all the rest of atoms. The aqueous solvent effect is considered by using the SMD implicit solvent model.

Thermodynamic corrections were obtained assuming unscaled harmonic vibrational frequencies, which enable to confirm that all structures are true minima, and the rigid rotor approximation was obtained by standard statistical methods. Cu^{2+} calculations, as it is an open-shell ion, were based on an unrestricted formalism. All electronic calculations have been done with *Gaussian09* package program.[245] Atomic charges and spin densities were obtained from Natural Population Analysis (NPA).

The SRP values are computed following the equation:

$$E^0(Cu^{2+/+} - A\beta_{1-16}) = -\left(\frac{\Delta G^0_{Cu} - \Delta G^0_{SHE}}{F}\right) \quad (7.1)$$

where *F* is the Faraday constant, 23.061 kcal·V^{-1}·mol^{-1}. For the reduction of the proton in aqueous solution, the experimental value, ΔG^{SHE} = -99.9 kcal·mol^{-1},[98,292] was used.

Similar to what was performed in *Chapter 5*, the SRP values have been corrected taking as reference the reduction potential of copper in water; that is by adding an empirical correction of -0.07 V. Moreover, the experimental potentials are estimated versus the *Saturated Calomelan Electrode* (SCE), while the theoretical potentials are calculated versus *Standard Hydrogen Electrode* (SHE). Hence, a correction of -0.24 V has been added to the theoretical potentials to compare with the experimental ones.

7.2. ELECTROCHEMICAL RESULTS

In the Master final project of Silvia Mena,[320] the four different tripeptides shown in *Figure 7.2.* have been analyzed by *Cyclic Voltammetry* (CV) in order to study the activity of the metal-chelate complexes. The potentials are estimated versus the SCE, using glassy

carbon (electrode diameter, ϕ = 1 cm) as working electrode and Pt (ϕ < 1 cm) as counter electrode disc. Most relevant results are summarized below.

First, it should be mentioned that Cu^{2+}-tripeptide complexes exhibit a significant different behavior depending on the sequence of the tripeptide. For the case of **Cu^{2+}-HWH** complex, the cyclic voltammogram does not show a reduction process of Cu^{2+} to Cu^{+}, but presents two successive oxidative bands at low scan velocities, as one can see in *Figure 7.3*.

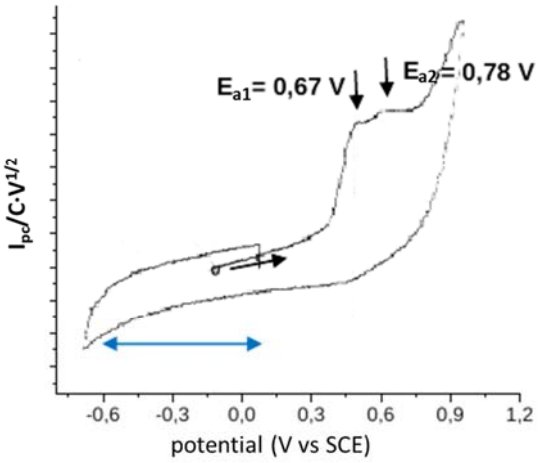

Figure 7.3. Cyclic voltammogram trace of aqueous solution of Cu^{2+}-HWH complex in 0.05M TRIS and 0.1 M $NaClO_4$ at physiological pH, v = 1 $V \cdot s^{-1}$.

The first oxidation peak corresponds to the oxidation of Cu^{2+} to Cu^{3+} with a potential E_{a1} = 0.67 V. The second oxidation band is related with the oxidation of the indole group (the electrochemical active moiety of the tryptophan) with a potential E_{a2} = 0.78 V.

In addition, **Cu^{2+}-HAH** complex was analyzed by CV in order to observe the influence of the Trp. The cyclic voltammogram is shown in *Figure 7.4*.

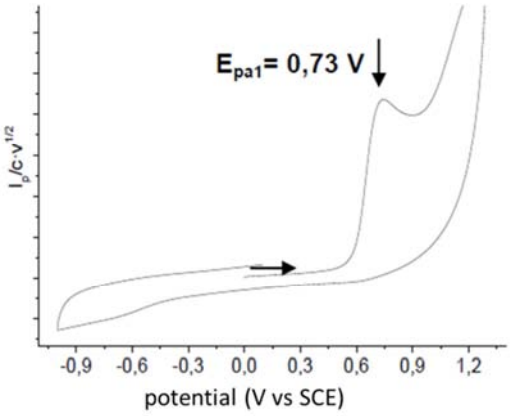

Figure 7.4. Cyclic voltammogram trace of aqueous solution of Cu^{2+}-HAH complex in 0.05M TRIS and 0.1 M $NaClO_4$ at physiological pH, v = 100 $mV \cdot s^{-1}$.

Equally to **Cu^{2+}-HWH** complex, the reduction process of Cu^{2+} to Cu^{+} is not observed. However, an oxidation peak is also obtained, which corresponds to the oxidation of Cu^{2+} to Cu^{3+} with a potential E_a = 0.73 V. It means, that the second sphere does not overly interfere in the SRP; thus, it is expected that the difference in the potential peaks between HAH and HWH complexes will be small.

The electrochemical analysis of **Cu^{2+}-Ac-HWH** shows a pseudo-reversible reduction of Cu^{2+} to Cu^{+}, the cathodic potential being E_c = -0.24 V and anodic potential E_{a1} = 0.22. Moreover, another anodic oxidation peak is observed with E_{a2} = 0.80 V which corresponds to the oxidation of the tryptophan amino acid (see *Figure 7.5*).

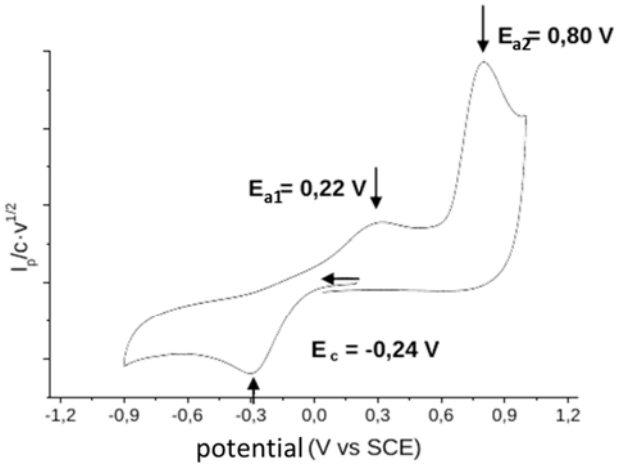

Figure 7.5. Cyclic voltammogram trace of aqueous solution of Cu^{2+}-Ac-HWH in 0.05 M TRIS and 0.1 M $NaClO_4$ at physiological pH, v = 300 $mV \cdot s^{-1}$.

The CV analysis of **Cu^{2+}-HHW** complex also shows a pseudo-reversible reduction with a cathodic potential of E_c = -0.90 V and anodic potential of E_a = 0.23 V.

Finally, the CV analysis of **Cu^{2+}-WHH** complex shows a different behavior depending on the pH. At basic pH (pH = 10.2), and similarly to **Cu^{2+}-HWH**, two successive oxidation bands, which correspond to the anodic potentials E_{a1} = 0.65 V and E_{a2} = 0.79, are observed. Again, these values are related to the oxidation of Cu^{2+} to Cu^{3+} and the oxidation of the Trp amino acid, respectively. Moreover, there is not any reduction process. On the other hand, at pH 4.80, a pseudo-reversible reduction of Cu^{2+} to Cu^{+} is observed with E_{a1} = 0.23 V and E_c = -0.08 V. In addition, the anodic scan show a second oxidation with E_{a2} = 0.92 V, that corresponds to the Trp amino acid oxidation. The cyclic voltammogram traces are shown in *Figure 7.6*.

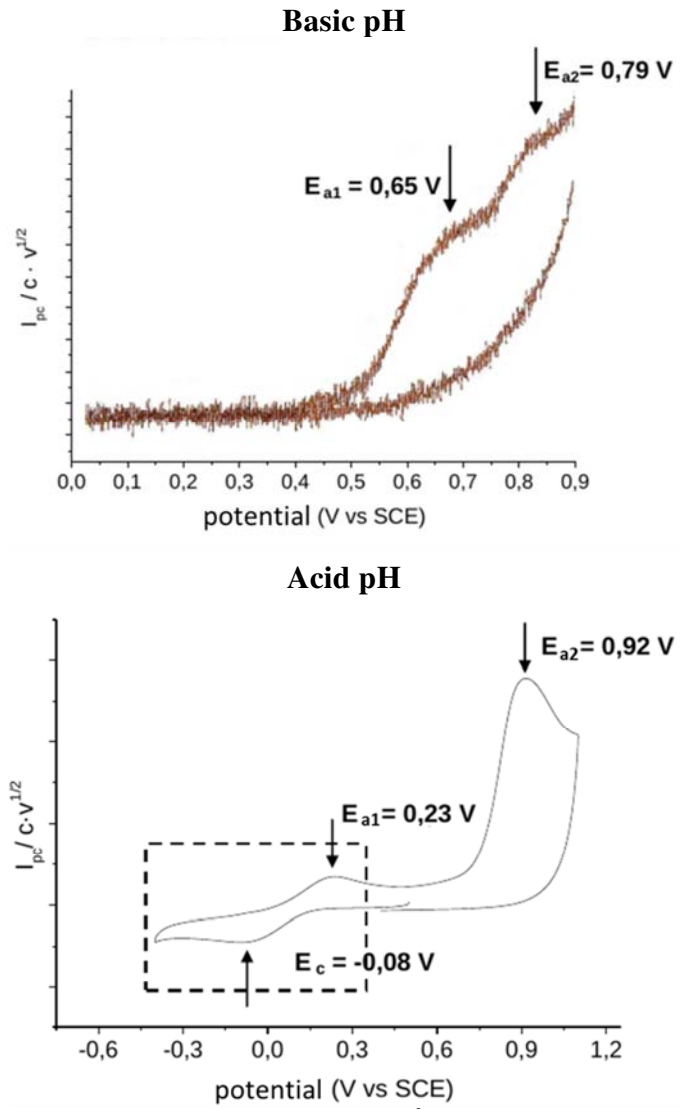

Figure 7.6. Cyclic voltammogram trace of aqueous solution of Cu^{2+}-WHH in 0.05 M TRIS and 0.1 M $NaClO_4$ at both acid and basic pH, v = 100 mV·s^{-1} (acid) and v = 500 mV·s^{-1} (basic).

However, a physiological pH (5.5 < pH < 9.5) there are intermediate potential values between the two mentioned above. Upon increasing the basicity of the medium, potential peaks are shifted to more negative values, the intensity of the bands in the pseudo-reversible reduction decreases and another anodic peak corresponding to the oxidation process of Cu^{2+} to Cu^{3+} appears. This behavior is also observed by analyzing the spectrophotometry response of different aqueous solutions that contain this complex. In general, these metallopeptides show absorbance values between 520 nm < λ < 600 nm, depending on the basicity of the electrolytic medium. Particularly, in the UV-Vis characterization of the **Cu^{2+}-WHH** complex, the maximum absorbance is shifted to shorter wavelengths with increasing basicity of electrolytic medium (see *Figure 7.7*).

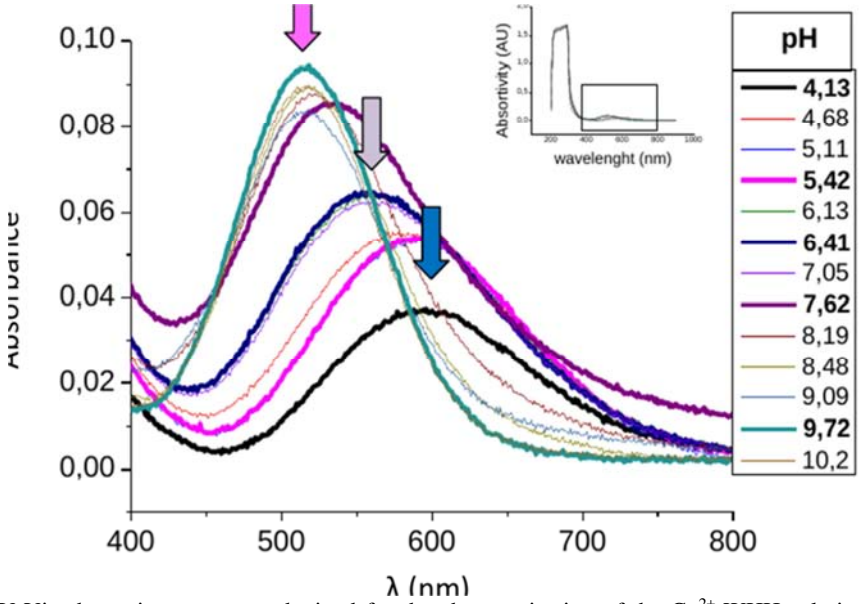

Figure 7.7. UV-Vis absorption spectrum obtained for the characterization of the Cu^{2+}-WHH solution in electrolytic medium varying the pH from 4.13 to 10.2.

That is, at acid pH, the absorbance values are 580 nm < λ < 600 nm, while at basic pH, the values are near 520 nm. However, at physiological pH the wavelengths show intermediate values between the acid and basic pH wavelengths which reflect the different metal coordination environment present in this complex.

These results show that the redox properties of the complexes and, therefore, the coordination environment of the metal depend on the peptide sequence. Moreover, in the case of **Cu^{2+}-WHH** redox and spectroscopic properties change with the pH indicating that the complex structure depends on the pH value. Thus, computational methods have been used to get a deeper insight into the atomic structure of the different complexes and to rationalize the different redox behavior.

7.3. THEORETICAL RESULTS

All complexes presented in the experimental section, that is, **Cu^{2+}-HAH**, **Cu^{2+}-HWH**, **Cu^{2+}-Ac-HWH**, **Cu^{2+}-HHW** and **Cu^{2+}-WHH,** have been studied at DFT level of theory and considering solvent effects using implicit solvation model. For all these complexes different metal coordination environments have been studied in order to try to explain the redox behavior observed in the CV analysis.

7.3.1. Cu^{2+}-HAH COMPLEXES

Since minor differences on the coordination properties are expected between HAH and HWH, first exploration has been done for the HAH tripeptide. Different configurations of Cu^{2+}-HAH have been explored in order to know which the most relevant one is. These configurations have been built considering different coordinating centers based on NMR experiments performed by Patrick Gamez and Ana Belén Caballero from the Universitat de Barcelona. These experiments show that the most probable Cu coordinating ligands are the N^{term}, His1, His3, N^- from the amide of the backbone or O from the carbonyl group of the backbone. However, the results are not conclusive. Therefore, a configurational search considering all the possible combinations of the coordinating ligands has been performed. The first configuration considered, hereafter referred to structure **1**, involves the N-terminal, His1, His3 and the O from the carbonyl of Ala2. Structure **2** involves the N-terminal, the deprotonated N from the amide of Ala2, the O from the carbonyl of Ala2 and His3, whereas structure **3** corresponds to the ATCUN motif, which involes the N-terminal, His3 and the deprotonated N from the amide of both Ala2 and His3. Finally, structure **4** involves His1, His3, the deprotonated N from the amide of Ala2 and the O from the carbonyl of Ala2. These coordination environments are shown in *Figure 7.8.*

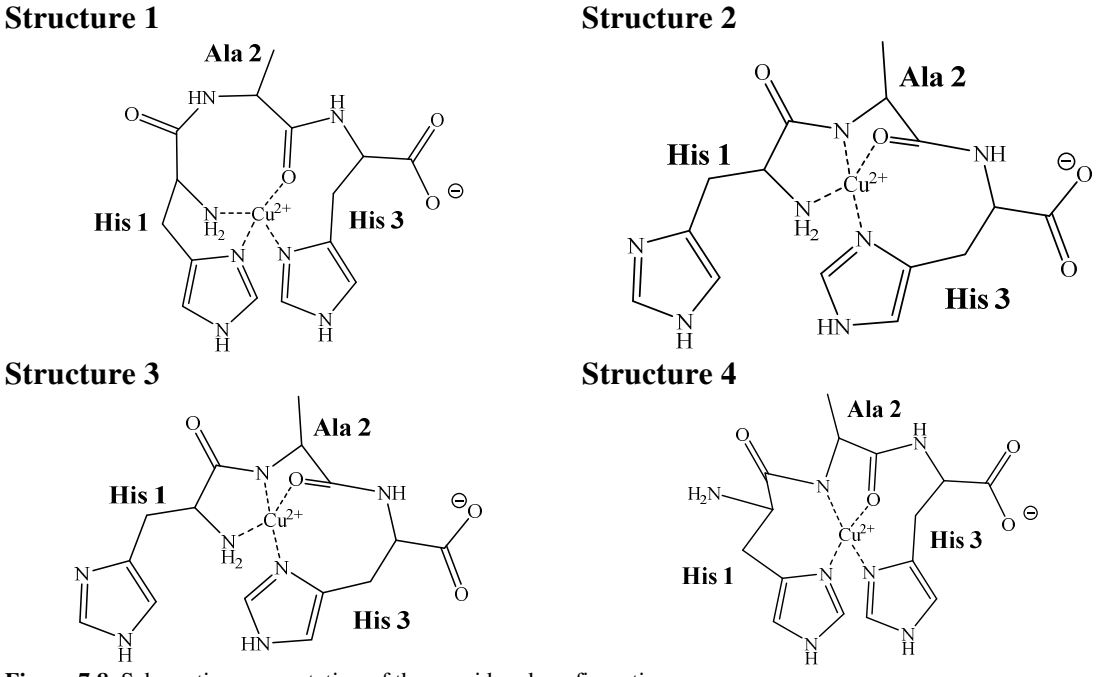

Figure 7.8. Schematic representation of the considered configurations.

For all cases, all the possible combination of the δ/ε nitrogen coordination of the histidines have also been considered, which is indicated as subscript. The geometrical parameters of the most stable structures of each group and the corresponding reduced complexes are reported in *Figure 7.9*, while the rest of structures are shown in *Figure C1* of *Appendix C* section.

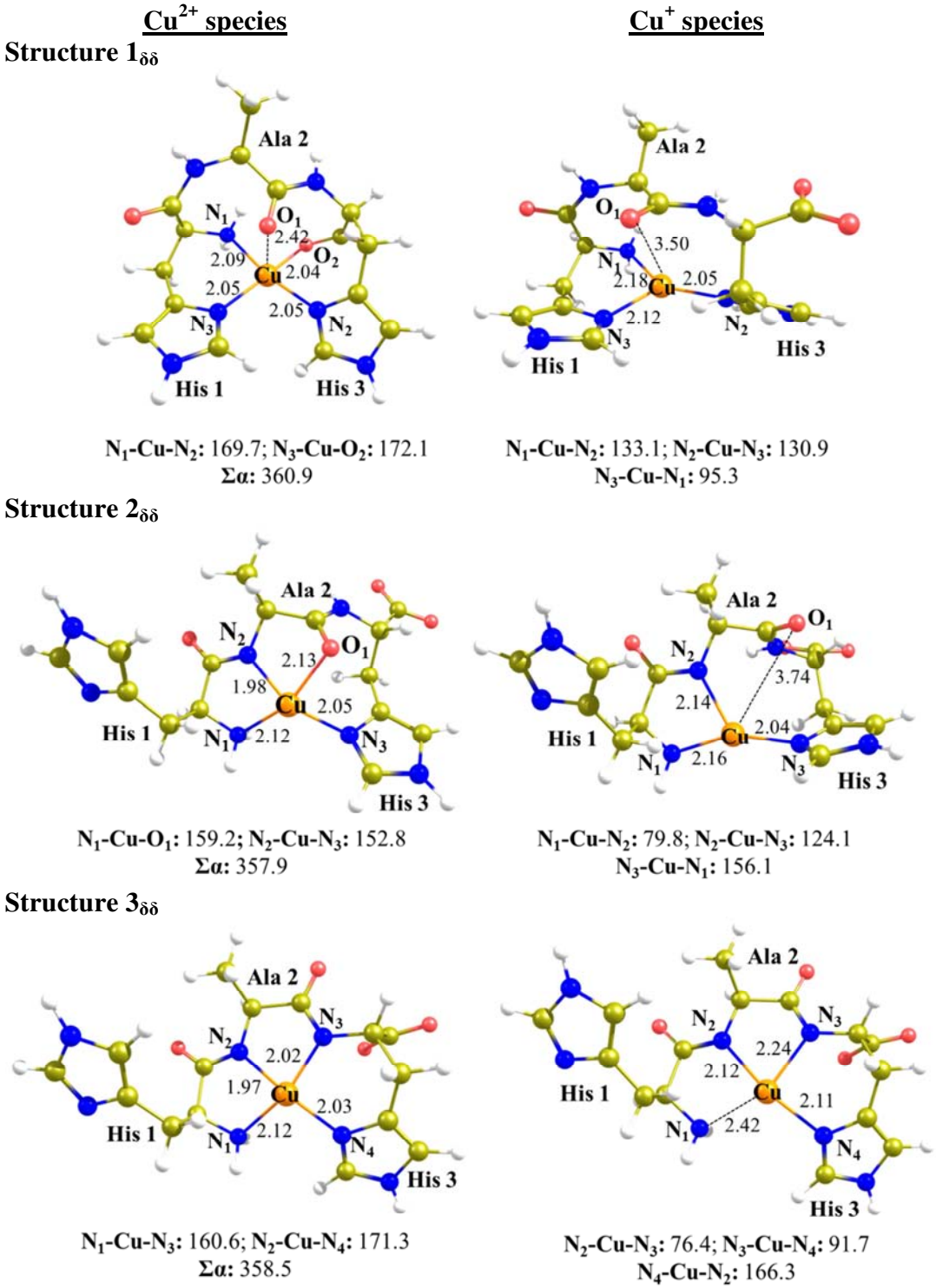

Figure 7.9. Optimized structures for all the considered Cu-HAH peptides. Distances are in angstroms and angles in degrees. Σα means the sum of all the angles around Cu.

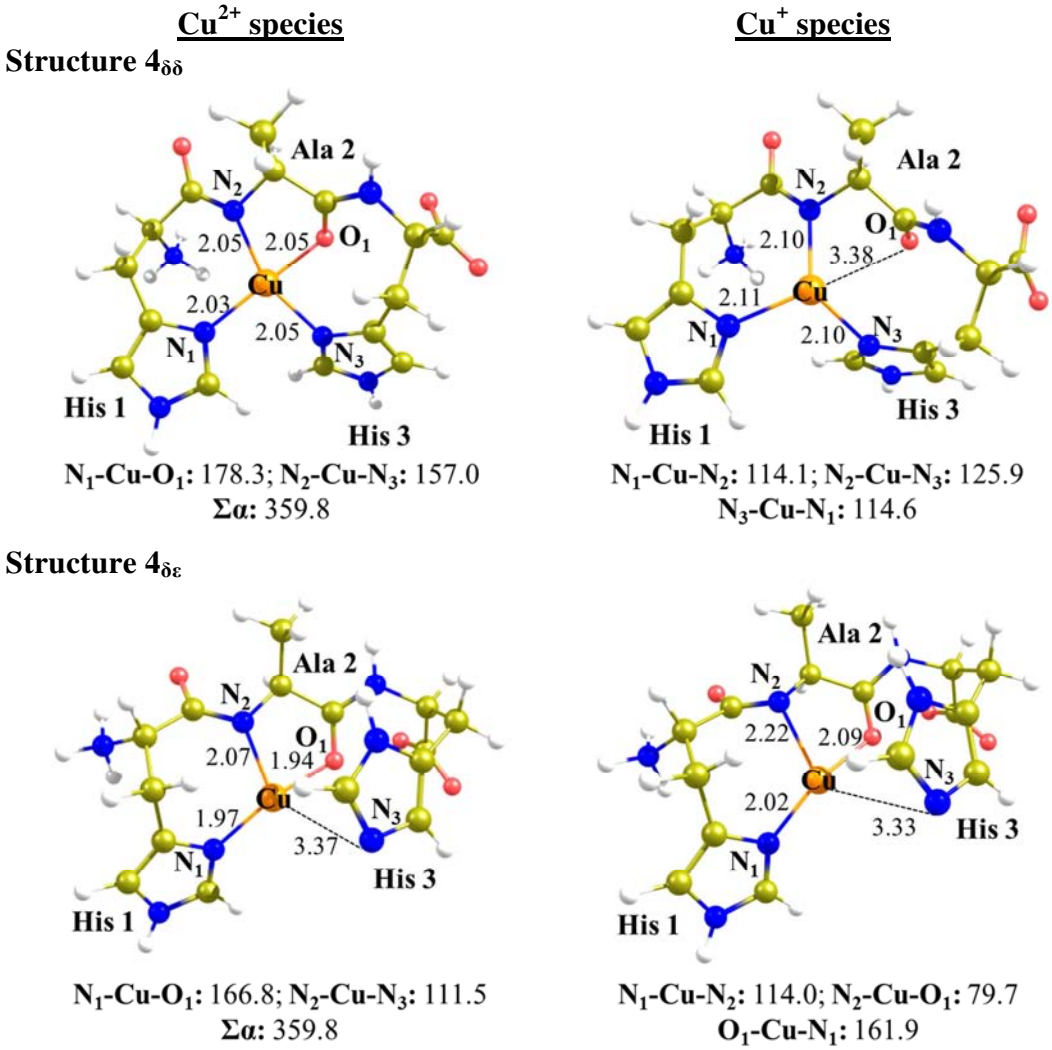

Figure 7.9. Continuation.

All the Cu^{2+} structures show a typical distorted square-planar coordination environment with all Cu-ligands distances being around 2.00 Å. Surprisingly, structure **4** present two conformations very near in energy which are $\mathbf{4_{\delta\delta}}$ and $\mathbf{4_{\delta\varepsilon}}$. The first one shows a distorted square-planar geometry, similarly at the rest of configurations. However, structure $\mathbf{4_{\delta\varepsilon}}$ exhibits a tricoordinated T-shaped geometry because the ε deprotonated N of His3 cannot coordinate by σ interaction due to the steric hindrance; thus, this histidine is decoordinated. The other structures showing different coordination of the histidine nitrogens have been represented in *Figure C1* of the *Appendix C* section. All these structures present a Cu spin density between 0.76 and 0.87.

Note that, the Cu^{+} complexes obtained after the reduction, which can be observed in *Figure 7.9*, present a tricoordinate structure with a CO backbone decoordination or a N ligand elongation (in the case that the complexes do not involve any O ligand, structure

3). However, in the case of structure $\mathbf{4_{\delta\varepsilon}}$, as the Cu^{2+} coordination is already tricoordinated, an elongation of all the ligands is observed for the Cu^{+} complex.

Relative energies reported in *Table 7.1,* indicate that, in all cases, the most stable structure is that in which the imidazole group coordinates through the nitrogen δ, except for structure **4** that exhibit a tricoordinated structure in the most stable configuration due to the ε deprotonated N of His3. However, structure **4** present two conformations very near in energy, as commented before, which one of them is the structure $\mathbf{4_{\delta\delta}}$. The most stable configuration of each complex has been considered to calculate the SRP values.

Table 7.1. Relative energy summary for Cu^{2+} binding HAH complexes and reaction energies for Cu^{2+}/Cu^{+} couple (in kcal·mol^{-1}), as well as the SRP (in V) vs SHE ($\boldsymbol{E^0_{SHE}}$) and vs SCE ($\boldsymbol{E^0_{SCE}}$) for the different considered structures of Cu^{2+}/Cu^{+} HAH couple.

	$\boldsymbol{\Delta E^{Cu^{2+}}}$	$\boldsymbol{\Delta G^{Cu^{2+}}}$	$\boldsymbol{E^0_{SHE}}$	$\boldsymbol{E^0_{SCE}}$
Structure 1				
δδ	**0.0**	**0.0**	**0.15**	**-0.09**
δε	9.6	8.5		
εδ	43.8	43.5		
εε	32.4	31.1		
Structure 2				
δ	**0.0**	**0.0**	**0.11**	**-0.13**
ε	3.0	5.8		
Structure 3				
δ	**0.0**	**0.0**	**-1.24**	**-1.48**
ε	15.1	14.1		
Structure 4				
δδ	0.6	1.5	0.11	-0.13
δε	**0.0**	**0.0**	**0.07**	**-0.17**
εδ	14.9	16.7		
εε	24.4	27.3		

The computed SRP obtained for the $Cu^{2+/+}$ couple allows us identifying the most probable structure by comparing with the experimental results shown in *Figure 7.4*. In this case, the reduction of Cu^{2+} to Cu^{+} is not observed experimentally, which means that the reduction potential must be very negative, *i.e.*, it should present a value lower than -1.5 V (*vs* SCE), one of the experimentally defined limits of the electrochemical window and determined by CV of the electrolytic environment without active species. Among the structures considered only structure **3,** with the ATCUN motif, provides a SRP value that is compatible with the experimental observations (-1.48 V, *vs* SCE). Whereas structures **1, 2** and **4** present SRP values that would appear in the voltammogram.

7.3.2. Cu^{2+}-HWH COMPLEXES

Considering the results obtained in the last section for Cu^{2+}-HAH complexes and the fact that experimental results do not exhibit major changes between the CV analysis of HAH and HWH complexes, configuration **3**, which shown ATCUN motif, has been considered the most probable structure for Cu^{2+}-HWH complexes. However, a conformational search consisting in modifying the lateral chains orientation of the amino acids allows us to analyze different conformations. The most stable structure for the oxidized and the reduced complex is shown in *Figure 7.10*, while geometris of the other configurations can be found in *Figure C2* of *Appendix C* section. Relative energies and SRP of all the conformers of Cu-HWH complexes are reported in *Table 7.2*. Particularly, interesting is the analysis of Cu^{2+}-π interactions with Trp, which could play a role in the SRP values.

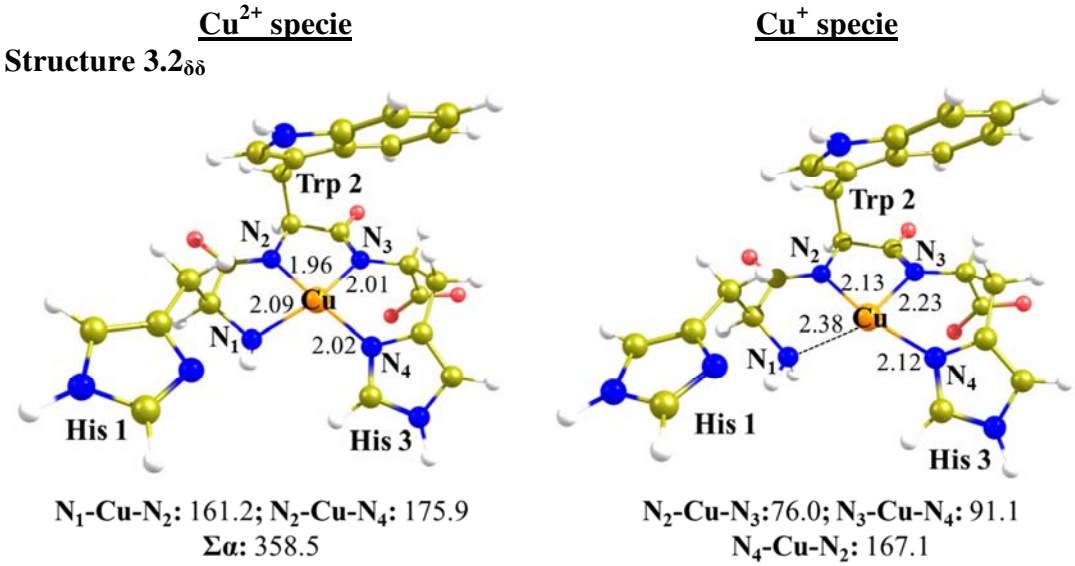

Figure 7.10. Optimized configuration for the most stable configuration of structure **3** of Cu-HWH complex. Distances are in angstroms and angles in degrees. Σα means the sum of all the angles around Cu.

The Cu^{2+}-HWH structures exhibit a distorted square planar coordination with Cu-ligands distances around 2.00 Å and Σα near 360º, which means that the structures are almost planar. Moreover, the N_1-Cu-N_3 and N_2-Cu-N_4 angles are between 143.0 and 176.5º, near 180º. In all structures, Cu^{2+} spin densities are around 0.70.

After the reduction, all the structures present the elongation of the N-terminal, similarly to structure **3** of Cu-HAH complex, leading to a quasi-tricoordinated structure which exhibit T-shaped geometries. However, the structure is stable enough to not completely decoordinate the ligand leading Cu-N^{term} distances shorter than 3.00 Å.

Table 7.2. Relative energy summary for Cu^{2+} binding HWH complexes (in kcal·mol^{-1}), as well as SRP (in V) vs SHE (E^0_{SHE}) and vs SCE (E^0_{SCE}) for the different considered structures of Cu^{2+}/Cu^{+} HWH couple and distances (in Å) between Cu and the centroid of the indol group of Trp.

Structures	$\Delta E^{Cu^{2+}}$	$\Delta G^{Cu^{2+}}$	E^0_{SHE}	E^0_{SCE}	$d_{Cu\text{-}Centroid\ of\ Trp}$
3.1$_{\delta\delta}$	3.6	4.9	-1.29	-1.53	6.89
3.2$_{\delta\delta}$	**0.0**	**0.0**	-1.46	-1.70	4.43
3.3$_{\delta\delta}$	0.4	4.5	-1.46	-1.70	4.98
3.4$_{\delta\delta}$	1.6	5.2	-1.22	-1.46	6.80

The computed SRP are very similar (differ in ~0.3 V) and negative, which indicate that these complexes inhibit the ROS formation because Cu^{2+}-HWH cannot be reduced by any of the reducing external agents to start the catalytic H_2O_2 formation cycle. In agreement with these low SRP values, the reduction process of the complex is not experimentally observed in the considered potential range of the CV. In addition, the distance between the metal center and the centroid of the indol group indicates that when the Trp is near to Cu (around 4.50 – 5.00 Å) the reduction potential is lower than when the Trp is further from Cu (~7.00 Å). This means that the indol group interacts with Cu through π-interaction when the distance is shorter.

The CV analysis shows two anodic peaks: the oxidation peak of Cu^{2+} to Cu^{3+}, at 0.67 V (*vs* SCE), and the oxidation peak of Trp at 0.78 V (*vs* SCE). Then, the SRP of this Cu^{2+} to Cu^{3+} couple has been also computed for the most stable structure, which is structure **3.2**. As Cu^{3+} complex can be triplet or singlet, both states have been considered. In the two spin states, Cu^{3+} structure present minor changes compared to Cu^{2+} structure (see *Figure C3* from *Appendix C* section). The value theoretically obtained for the oxidation process of Cu^{2+} to Cu^{3+} (triplet) is 0.96 V (*vs* SCE). The Cu^{3+}-HWH complex in the triplet state presents a Cu spin density around 0.71 and a Trp spin density of about 0.99, which means that this state corresponds to the oxidation of the Trp and the computed SRP value (0.96 V, *vs* SCE) is near to the experimental one (0.78 V, *vs* SCE). However, the singlet state for the Cu^{3+}-HWH complex shows an empty HOMO (*Highest Occupied Molecular Orbital*) orbital corresponding to the d_{z^2} of the copper, which implies that the oxidation process of the Cu has taken place. The value obtained from theoretical calculations for this state (1.77 V, *vs* SCE) is far away from the experimental result (0.67 V, *vs* SCE). This may be related with the fact that the electron correlation effects in Cu^{3+} are much more important than in Cu^{2+} and this effects are not well described by

this functional. In this line, the second ionization energy of Cu with M06-2X is 37.4 eV; that is, 0.6 eV more than the experimental value, which is 36.8 eV.

7.3.3. Cu^{2+}-Ac-HWH COMPLEXES

The Ac-HWH peptide has been chosen to show the crucial role played by the N-terminal amino group for copper binding. In this case considering all the ligands proposed by NMR experiments (N^{term}, His1, His3, N^- from the amide or O from the carbonyl group of the backbone) and excluding the N^{term}, only two different structures are likely, one simulating the ATCUN-like motif with the coordination of His1 instead of the N-terminal, called structure **5**, and another involving only one N deprotonation of the amide of Trp2 and the coordination of the carbonyl group of Trp2 besides the coordination of the two histidines, which means a 3N1O coordination environment. This last configuration is named structure **6** (see *Figure 7.11*). Moreover, because of the results shown above, only δ nitrogen coordination of the histidines is considered and the Trp orientation was similar to structure **3.2**.

The Cu^{2+} coordination sphere in structure **5** is overly distorted square-planar (Σα > 360º and N_1-Cu-N_2 and N_2-Cu-N_4 angles near 160º). However, structure **6** presents a less distorted square-planar metal coordination (Σα ~360º and N_1-Cu-O_1 and N_2-Cu-N_3 near to 170º) than structure **5**. In all cases, Cu-ligand distances are around 2.00 Å, and all the Cu^{2+} spin densities are around 0.7. After the reduction, structure **6** loses the coordination of the carbonyl group, equal to what has been observed in the reduction of Cu^{2+}-$A\beta_{1-16}$ complexes with the same coordination environment, obtaining a tricoordinated geometry. Nevertheless, structure **5** only suffers a slight elongation of the coordinated ligands. In this case, there is neither decoordination nor larger elongation of one of the ligands, only greater distortion of the planarity of the metal coordination sphere (Σα higher in Cu^+ species than in Cu^{2+}). However, the reduction does not lead in a tetrahedral geometry because of the restrictions imposed by the peptide backbone.

The CV analysis show a cathodic peak of E_c = -0.24, these result allow us to discard the structure **5** due to its low computed SRP (-1.34 V, *vs* SCE) and suggest structure **6** as the most plausible structure due to the great agreement between its computed SRP (-0.19 V, *vs* SCE) and the experimental potential. The SRP value that corresponds to a 3N1O coordination is higher than those presented by the external reducing agents.

Hence, complexation of Cu^{2+} by Ac-HWH would not inhibit ROS formation. These results show also that a second amide deprotonation is favored by the presence of two rings of 5 members, like in the ATCUN motif, when the N-terminal can coordinate.

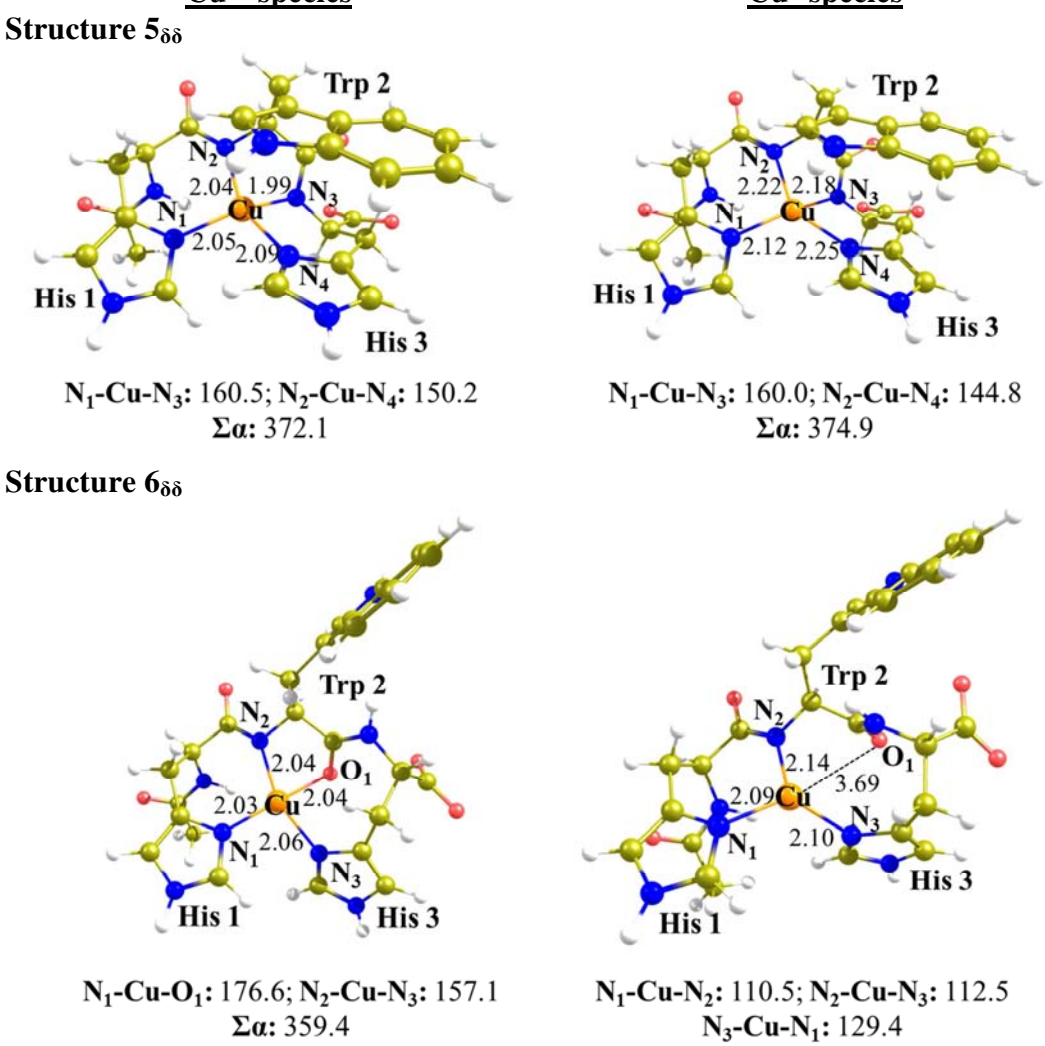

Figure 7.11. Optimized structures for the Cu-Ac-HWH complexes. Distances are in angstroms and angles in degrees. Σα means the sum of all the angles around Cu.

In addition, the experimental study show the cathodic peak (-0.24 V, vs SCE) shifted from the anodic peak (0.22 V, vs SCE), which is explained as pseudo-reversible reduction of Cu^{2+} to Cu^{+}. The separation between these peaks implies coordination changes in the metal sphere. In fact, the computed Cu^{+} complex of structure **6** shows a decoordination of the carbonyl group showing a coordination change in the reduction process. Hence, the oxidation of Cu^{+} to Cu^{2+} has also studied for this structure. In this case, the SRP obtained for this process is 0.74 V (*vs* SCE), which is far away from the experimental value (0.22 V). The Cu^{2+} specie obtained by the oxidation of Cu^{+} complex,

which is shown in *Figure 7.12*, present a spin density over the Cu near zero and over the Trp around 0.9. This means that the oxidation takes place on the Trp moiety and, thus, Cu^{2+} complex is not recovered from the Cu^{+} specie. Moreover, the geometry is similar to Cu^{+} specie.

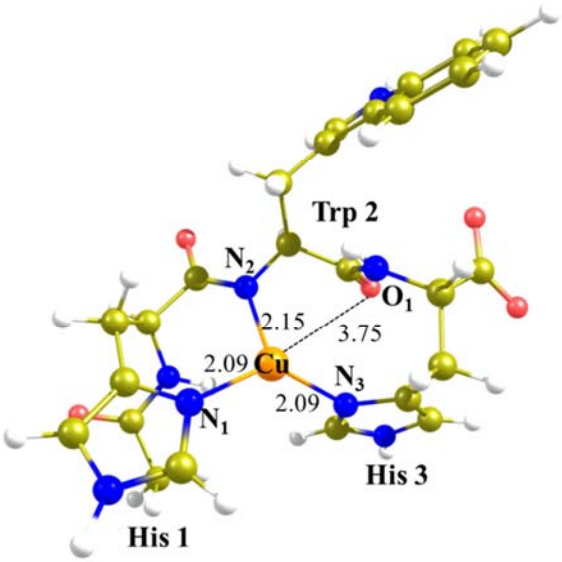

Figure 7.12. Structure **6** of Cu^{2+} obtained from the oxidation of Cu^{+} specie.

However, if the Trp is substituted by Ala leading a Cu^{2+}-Ac-HAH complex with structure **6** coordination environment (see *Figure C4* of *Appendix C* section), the Cu^{2+} structure obtained from the oxidation of Cu^{+} specie is found achieving a potential of -0.07 V (*vs* SCE), which is nearer to the experimental one. In this case, both the Cu^{2+} and the Cu^{+} geometries are very similar. Nevertheless, the spin density over Cu in the Cu^{2+} complex is around 0.80. This fact shows the influence of Trp in electronic transfers due to its π character, which leads a delicate balance between the HOMO orbital of Cu and Trp. On the other hand, the accurate calculation of the oxidation potential would require MD simulations of the reduced species considering explicit solvent to account for the conformational changes in solution.

7.3.4. Cu^{2+}-HHW COMPLEXES

The tripeptide His–His–Trp (HHW) has been selected to confirm the importance of the histidine residue at position 3 for obtaining an ATCUN arrangement. For the complex formed between HHW and Cu^{2+}, the X-Ray results, obtained by Ana Belén Caballero and Patrick Gámez, shown in *Figure 7.13*, indicate that this complex does not present

an ATCUN motif in the metal coordination sphere in solid state. It seems more like a polimeric species where the N-terminal, the deprotonated N from the amide of Ala2 and His2 are coordinated from one peptide and the forth position comes from a histidine of a second peptide.

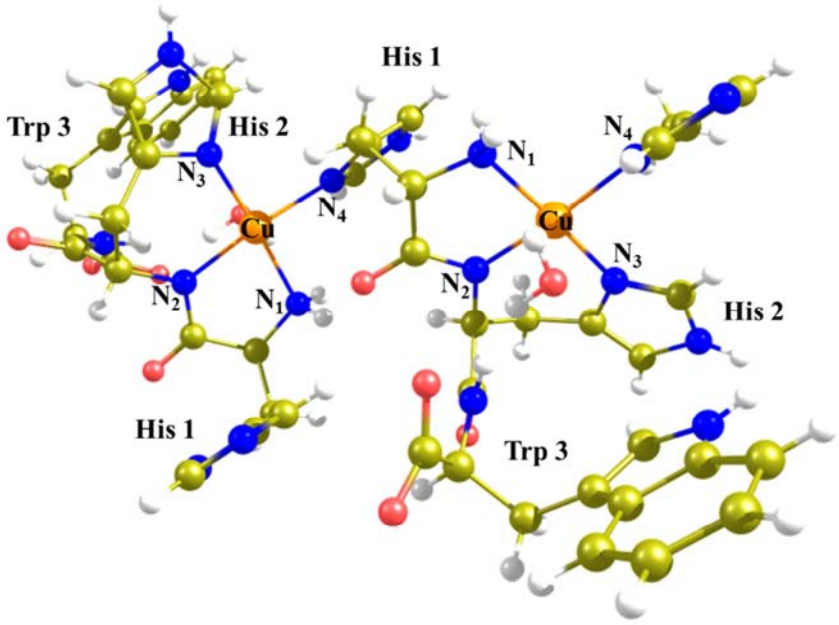

Figure 7.13. Representation of the X-ray structure for the Cu-HHW complex.

In solution, it would be possible to have a 1:2 species, which involve one Cu atom and two peptides considering a 4N coordination without ATCUN motif, or 1:1 complexes, which involve one Cu atom and one peptide with a water molecule in the fourth position giving a 3N1O coordination. As a consequence, and in order to embrace all the possibilities, it has been computationally considered the possibility that Cu^{2+} is bound to one HHW peptide with a water molecule in the fourth position, trying to simulate a general O ligand (structure **7**); or bound to two HHW peptides, as in the X-ray approach, considering only the methyl imidazole that interacts in this fourth position simulating a second peptide (structure **8**). Moreover, as in the X-ray structure seems to interact a water molecule in an apical position, the combination of methyl imidazole as fourth ligand and water in an apical coordination has been also considered. This structure, named structure **9**, is shown in *Figure C5* of the *Appendix C* section. However, the results achieved for this coordination environment are very similar to those obtained for structure **8**. Thus, it is not considered in the discussion. Again, only δ nitrogen coordination of the histidines is considered in all cases. The geometrical parameters are reported in *Figure 7.14*.

Structures **7** and **8** show a distorted square-planar Cu^{2+} coordination ($\Sigma\alpha$ ~360º and N_1-Cu-N_2/N_3 and N_2-Cu-O_1/N_4 near 180º). However, structure **9** present a penta-coordinated geometry due to the presence of the water molecule as fifth ligand. All the Cu-ligand distances are around 2.00 Å, except the Cu-H_2O distance in structure **9** which is around 2.60 Å. The Cu^{2+} spin density for all the structures is between 0.67 and 0.75. After the reduction, the decoordination of one of the ligands occurs leading a tricoordinated structure, which exhibit T-shaped geometries, also for structure **9**. If there is an oxygen binding ligand, this is the one decoordinated. If not, the N terminal is the ligand that is elongated. In the case of structure **9** both processes, the oxygen decoordination and the N elongation, occurs.

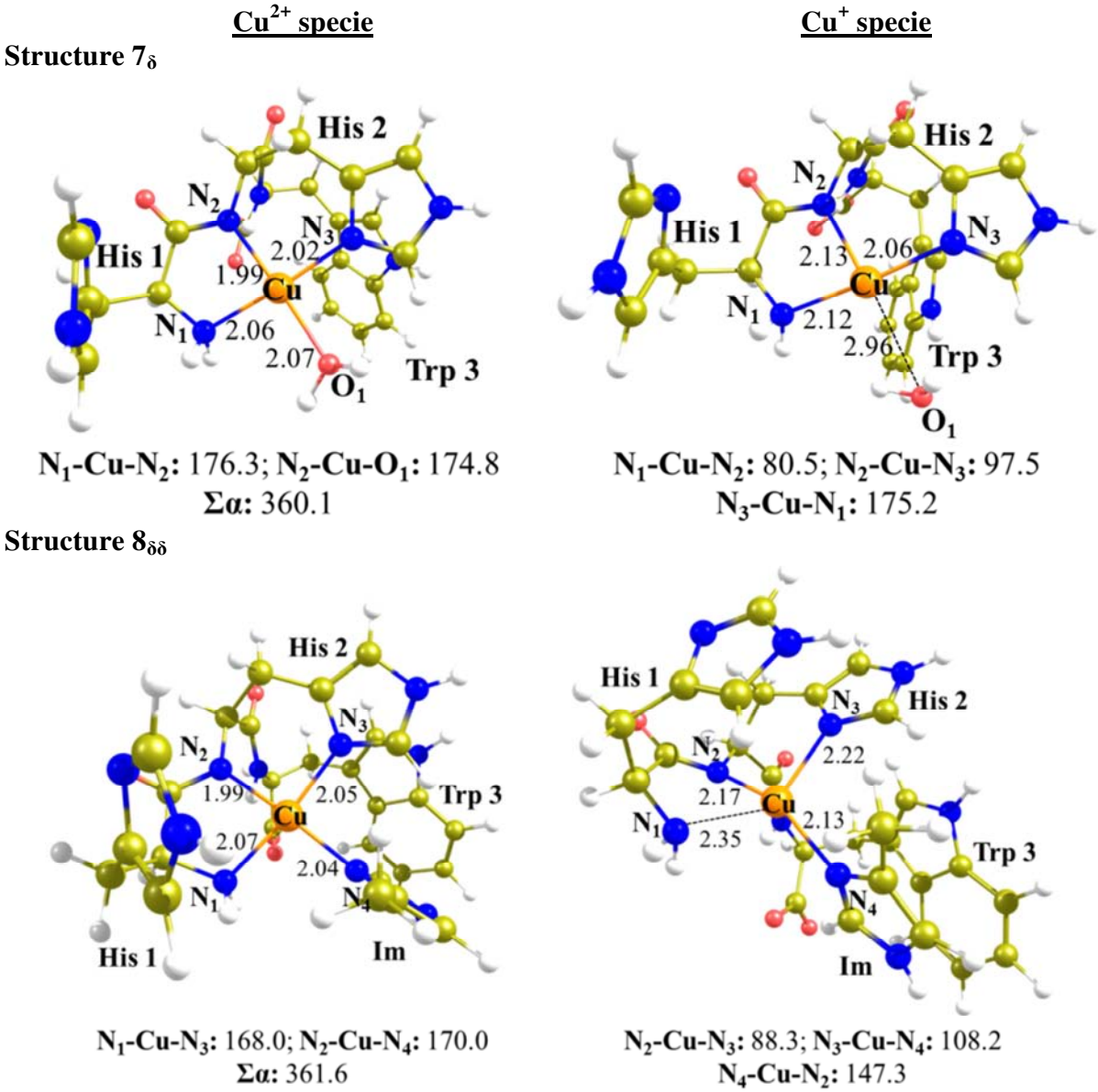

Figure 7.14. Optimized structures for the Cu-HHW complexes. Distances are in angstroms and angles in degrees. Σα means the sum of all the angles around Cu.

The computed SRP values for structure **7** and **8** (-0.87 V and -1.03 V, *vs* SCE, respectively) are closer and are in agreement with the experimental reduction potential (E_c = -0.90). Moreover, structure **8** and **9** show very similar SRP value (-1.03 V and -1.02 V, *vs* SCE, respectively), which is expected that both complexes present similar behavior. However, structure **7,** which has an O as fourth ligand, presents the nearest potential value to the experimental result. Therefore, it seems that there is a preference for an O atom as fourth ligand.

The anodic and the cathodic peaks are shifted as in the CV analysis of Cu-Ac-HWH complexes, which means conformational changes in the metal coordination sphere. In order to further confirm the structure of the reduced species, the oxidation of Cu^{+} to Cu^{2+} has also studied for these structures. In this case, the SRP values obtained for this process are 0.79 V and -1.05 V (*vs* SCE) for structure **7** and **8**, respectively, which are not close to the experimental value (0.23 V, *vs* SCE). In fact, the structure obtained from the oxidation of the Cu^{+} complex of structure **7** present a Cu spin density around 0 and spin density over the indol group of Trp about 0.90. Hence, the oxidation has taken place on the Trp moiety. However, the oxidation of Cu^{+} species of structure **8** comes back to the starting Cu^{2+} complex with a Cu spin density of about 0.60 and the SRP value is very similar to the obtained in the reduction process of Cu^{2+} to Cu^{+}. Therefore, equally to what has been commented for the Cu-Ac-HWH complexes, it is necessary to perform more studies in order to theoretically reproduce the anodic peak.

7.3.4. Cu^{2+}-WHH COMPLEXES

In this case, the CV analysis shows different behavior depending on the pH, which is probably related to different Cu coordination modes. As the CV experiments showed, at high pH only two oxidation peaks are observed, similarly to HWH complexes; while at low pH, a pseudo-reversible process is noticed, as for Ac-HWH and HHW complexes. Therefore, different structures have been theoretically considered. On the one hand, the ATCUN motif has been analyzed (structure **10**). On the other hand, structures analogous to those tested in Cu-HHW complex, considering either a water molecule or methyl imidazole in the fourth position (structures **11** and **12**, respectively), have been studied. Since the cathodic potential for Cu-WHH at low pH is considerably higher than for Cu-HHW complexes, another two structures with no deprotonated amide were tested. These structures involve the coordination of the N-terminal, the O from carbonyl

group of His2, His3 and either a water molecule or methyl imidazole that simulates a histidine ligand from another peptide (structures **13** and **14**, respectively). Equally to the last section, only δ nitrogen coordination of the histidines is considered in all cases. The geometrical parameters are reported in *Figure 7.15*.

Structure 10_{δ}

Cu^{2+} specie

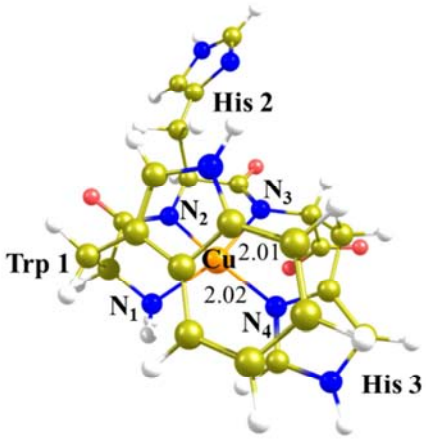

N_1-Cu: 2.11; **N_2-Cu:** 1.97
N_1-Cu-N_3: 161.1; **N_2-Cu-N_4:** 175.8
Σα: 359.9

Cu^{+} specie

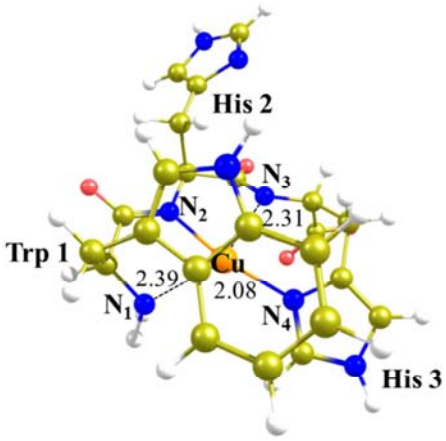

N_2-Cu: 2.12
N_2-Cu-N_3: 75.7; **N_3-Cu-N_4:** 90.3
N_4-Cu-N_2: 164.1

Structure 11_{δ}

Cu^{2+} specie

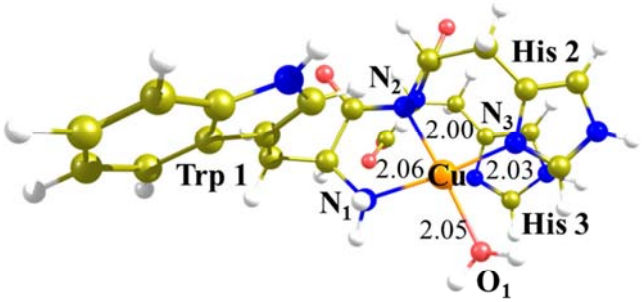

N_1-Cu-N_3: 173.8; **N_2-Cu-O_1:** 176.5
Σα: 360.2

Cu^{+} specie

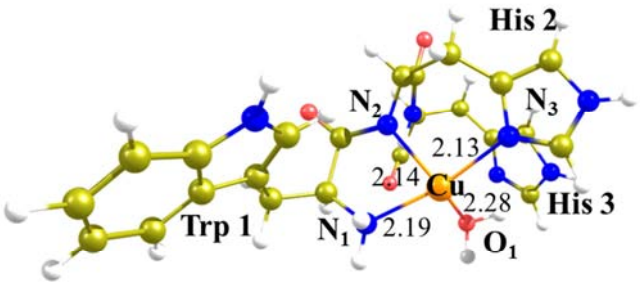

N_1-Cu-N_2: 77.4; **N_2-Cu-N_3:** 92.8
N_3-Cu-N_1: 150.7

Figure 7.15. Optimized structures for the Cu-HHW complexes. Distances are in angstroms and angles in degrees. Σα means the sum of all the angles around Cu.

Structure $12_{\delta\delta}$

Cu^{2+} specie

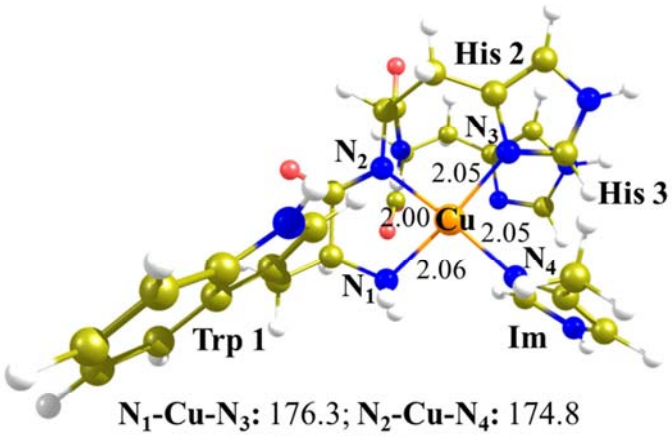

N_1-Cu-N_3: 176.3; **N_2-Cu-N_4:** 174.8
Σα: 360.1

Cu^{+} specie

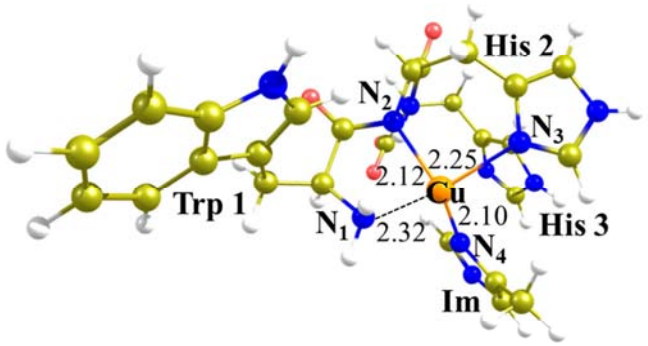

N_2-Cu-N_3: 90.6; **N_3-Cu-N_4:** 105.7
N_4-Cu-N_2: 143.0

Cu^{2+} specie **Cu^{+} specie**

Structure $13_{\delta\delta}$

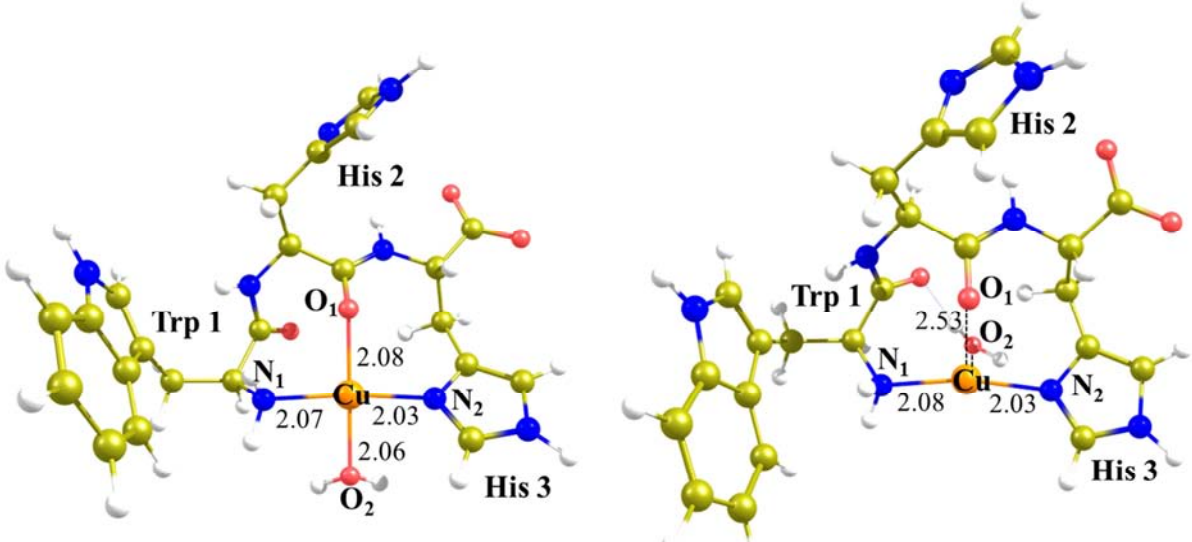

N_1-Cu-N_2: 166.0; **O_1-Cu-O_2:** 178.6
Σα: 360.4

Cu-O_2: 2.97
N_1-Cu-N_2: 168.4

Figure 7.15. Continuation.

Structure 14$_{\delta\delta\delta}$

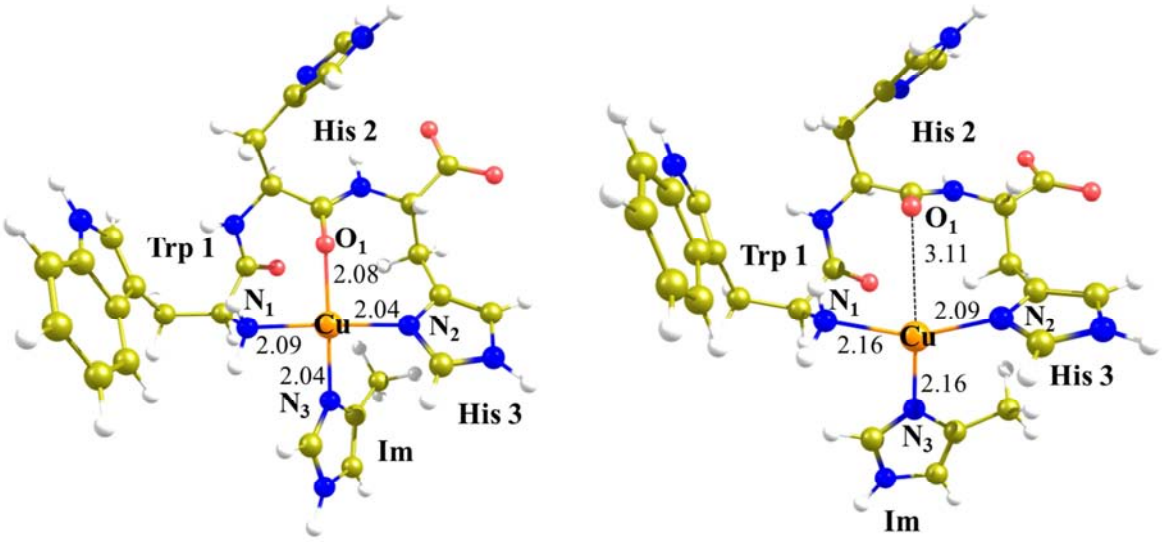

Figure 7.15. Continuation.

All the structures show a distorted square-planar Cu^{2+} coordination (Σα ~360º and N_1-Cu-N_2/N_3 and N_2-Cu-O_1/N_4 near 180º) with all the Cu-ligand distances around 2.00 Å and the Cu^{2+} spin density between 0.71 and 0.81. Similarly to what has been observed in the previous complexes, the N_1-Cu distance is elongated upon reduction, if there is not any O ligand. Moreover, for structure **10**, also the N_3-Cu distance is lengthened. Structure **13**, which present two O ligands, show the elongation of Cu-O_1 distance and the decoordination of water molecule due to the fact that the O_1 ligand corresponds to the carbonyl group of the backbone of the peptide. Hence, it presents more hindrance to get away from Cu than the water molecule that has free movement.

The electrochemical behavior observed for this complex is more complicated than for the others since it depends on the pH and the metal coordination sphere involved. Then, the different theoretical SRP values can be related with the cathodic peaks obtained at different pH value. For instance, structure **10** that corresponds to the ATCUN motif is the configuration that presents a more negative potential (-1.60 V, *vs* SCE). Hence, the reduction process of the complex is not experimentally observed because the SRP value is out of the limits of the electrochemical window, similarly to the HWH complex. The voltammogram for Cu-WHH complex that not present any cathodic peak is that recorded at basic pH, near pH 10.2. At this pH, experiments show only the oxidation peaks at E_{a1} = 0.65 V (oxidation of Cu^{2+} to Cu^{3+}) and E_{a2} = 0.79 V (oxidation of Trp).

however, equal to Cu-HWH complexes, the theoretical potential for the first anodic peak (1.73 V *vs* SCE) is not in agreement with the experimental one (0.65 V, *vs* SCE). Whereas the computational value for the second anodic peak (0.94 V, *vs* SCE) is near to the experimental (0.79 V, *vs* SCE).

The SRP values obtained for structures **11** and **12** (-0.91 V and -1.01 V, *vs* SCE, respectively), which present one deprotonated amide, are not as negative as in structure **10** but are lower than those proposed for the acid pH, it is possible that these structures are referred to intermediate pH values. Moreover, the experimentalists observe that the potentials are shifted to intermediate values at pH between 5.5 and 9. Similarly to those structures obtained for Cu-HHW complexes, more studies would be necessary to reproduce the potential related to the anodic peaks.

Finally, structures **13** and **14**, which do not present any deprotonated amide, show a SRP value of -0.01 V and -0.32 V (*vs* SCE), respectively. The first potential value is near to the experimental cathodic peak (E_c = -0.08 V) reported for Cu-WHH complexes at low pH. Therefore, structure **13**, which shows a 2N2O coordination environment, seems to be the most plausible one at low pH values.

7.4. GENERAL TRENDS

In this section, a breve summary of all obtained results is discussed. The computed and experimental values obtained for the redox potentials are shown in *Table 7.3*. This table includes the cathodic potential (E_c) that corresponds to the reduction potential of Cu^{2+} to Cu^{+}, the anodic potential referred to the oxidation of Cu^{+} to Cu^{2+} (E'_{a1}), to the oxidation of Cu^{2+} to Cu^{3+} (E_{a1}) and to the oxidation of Trp (E_{a2}) and the number of deprotonated amides ($N^{deprot.}$ amide). For complex HHW, two numbers are shown for the E_c; the first one corresponds to the 3N1O environment and the second one to 4N metal coordination sphere (similarly to WHH complex for pH ranged between 5.5 and 9).

The calculation of the potentials has allowed us to determine the most plausible structure of the complexes considered in this work by comparison with the experimental results. As it is already known, the N-terminal and His 3 are crucial in the ATCUN motif formation, as in **Cu-HAH**, **Cu-HWH** and **Cu-WHH** (basic pH) complexes. However, when any of both ligands is not available, three possible coordination modes seem to be

formed: one that involves 3N1O metal coordination sphere, such as in **Cu-Ac-HWH** and **Cu-HHW** complexes, another with 4N coordination environment different from the ATCUN motif, as in **Cu-HHW** and **Cu-WHH** (at intermediate pH) complexes and, finally, one that involves 2N2O metal coordination sphere, such as in **Cu-WHH** (acid pH) complex.

Table 7.3. Summary of all obtained results. *E* refers to the potentials (in V). Values in parenthesis correspond to the experimental results. *corresponds to Cu-Ac-HAH complex. For HHW and WHH complexes two values are shown to E_c, the first one corresponding to 3N1O coordination and the other corresponding to the 4N coordination.

Peptide sequence	Coordination mode	$N^{deprot.}$ amide	E_c	E'_{a1}	E_{a1}	E_{a2}
HAH	ATCUN (4N)	2	-1.48	–	(0.73)	–
HWH	ATCUN (4N)	2	-1.70	–	1.77 (0.67)	0.96 (0.78)
Ac-HWH	No ATCUN (3N1O)	1	-0.19 (-0.24)	0.07* (0.22)	–	0.74 (0.80)
HHW	No ATCUN (3N1O or 4N)	1	-0.87/-1.03 (-0.90)	(0.23)	–	–
WHH	ATCUN (4N)	2 (pH > 9)	-1.60	–	1.73 (0.65)	0.94 (0.79)
	No ATCUN (3N1O or 4N)	1 (5.5 < pH >9)	-0.91/-1.01	–	–	–
	No ATCUN (2N2O)	0 (pH < 5.5)	-0.01 (-0.08)	(0.23)	–	(0.92)

As it has been mentioned in Chapter 5, redox potentials are deeply affected by the presence of negatively charged ligands. For these complexes, the negatively charged ligands are the deprotonated amides of the metal coordination sphere. Moreover, the number of deprotonations depends on the stability of the resulting complex. For example, if the ATCUN motif can be assembled (Cu-binding Xaa–Xaa–His complexes), the deprotonation of two amides is compensated by the high stability of the complex formed. In this case, the reduction potential of the complex is not observed in the range experimentally studied and computed values are between -1.48 and -1.70 V. However, if the peptide cannot adopt an ATCUN type structure, two deprotonation are not compensated and only one is observed (systems with protonated N-terminal group, **Cu-Ac-HWH**, systems with no available His3, **Cu-HHW**, or even **Cu-WHH** at intermediate pH values). This is reflected in intermediate values of the reduction potentials (between -0.24 and -0.90 V, depending on the coordination or not of the N-terminal). Finally, for

Cu-WHH at low pH values no deprotonation is observed and, consequently, the experimental and theoretical value of the reduction potential is around zero.

Although the theoretical results achieved for the cathodic potentials are in good agreement with those obtained experimentally, the anodic potential is not always well described by this methodology. In all the cases, the oxidation of the Trp moiety is experimentally observed at about 0.80 V (E_{a2}) and it is reasonably well reproduced by the calculations. However, the ATCUN complexes can stabilize a +3 charge on Cu. Therefore, an anodic peak corresponding to the oxidation process of Cu^{2+} to Cu^{3+} is experimentally observed. This oxidation of the metal center is not well described theoretically by the considered functional because the theoretical results are far from the experimental value. Probably, the compact nature of the Cu^{3+} cation makes necessary a suitable description of the exchange energy. Thus, a proper balance of Cu^{+}, Cu^{2+} and Cu^{3+} states is needed to accurately reproduce the experimental values and a deeper calibration study of different functionals is required.

In addition, complexes with only one or none deprotonated coordination sites show an anodic peak that corresponds to the oxidation of Cu^{+} to Cu^{2+} after the reduction of this same complexes at different potential (pseudo-reversible process), whose experimental values are around 0.2 V. In this case, computation of potential values is hard because the presence of aromatic amino acids that can interfere in the electron transfer process. For instance, when computing the anodic potential for the oxidation of Cu^{+} to Cu^{2+} (E'_{a1}) of complex **Cu-Ac-HWH**, oxidation is always located in the Trp moiety and only when the Trp is not in the peptidic sequence; that is, when the **Cu-Ac-HAH** complex is considered, the computed value is in good agreement with the experimental one. Therefore, the Trp influences the electronic transfers due to its π character, allowing it to take the electron and leave a Cu^{+} complex. Moreover, the accurate calculation of the oxidation potential would require MD simulations of the reduced species considering explicit solvent to account for the conformational changes in solution.

7.5. CONCLUSIONS

In this chapter, a series tripeptides that include two histidines and either one tryptophan or alanine have been analyze to understand the influence of the peptidic sequence on the

copper-binding and the redox properties of these complexes by performing optimizations and frequency calculations at M06-2X/LB level of theory.

The thorough computational and experimental study reported herein clearly reveals that different metal coordination environments present different behaviors, which can be demonstrated by the cathodic potential value related to the reduction of Cu^{2+} to Cu^{+} complexes. In fact, the potentials values are affected by both the peptidic sequence and the charge of the complex leading the lowest values for the ATCUN motif (as in **Cu-HAH**, **Cu-HWH** and **Cu-WHH** at basic pH complexes) and the highest ones for 2N2O metal coordination environment (such as in **Cu-WHH** at acid pH complexes), with a 3N1O and 4N metal coordination spheres in the intermediate values (like in **Cu-Ac-HWH**, **Cu-HHW** and **Cu-WHH** at intermediate pH complexes). However, more studies would be necessary to reproduce the anodic peaks related to the oxidation of Cu^{+} to Cu^{2+} and Cu^{2+} to Cu^{3+}.

To summarize, the different studied peptides can adopt different coordination metal spheres, ATCUN motif, 3N1O, 4N different from ATCUN motif and 2N2O coordination, depending on the pH and the availability of N-terminal to coordinate and position of both the His and Trp. If this complexes show an ATCUN coordination, the complexes will inhibit the ROS formation, while 3N1O, 4N or 2N2O coordination might produce it.

8

FINAL REMARKS

This thesis has focused on understanding the structure of both Cu^{2+}-Aβ_{1-16} and Cu^{+}-Aβ_{1-16} complexes to get a better knowledge of the oxidative stress process which is one of the earliest and the most fatal symptoms observed in the development of the AD. In addition, small peptides have been studied as potential metal chelates for employing as possible treatment for AD. Specifically, we have used quantum mechanical calculations based on density functional theory to provide atomistic insights of these complexes to elucidate how these processes take place. In any case, results are very sensitive both to the method calculation and to the models used. Therefore, the sparse of energetic results can dramatically affect the predictions and trends provided by the numerical models. However, with the obtained results the following questions have been answered:

- How important is the influence of both the copper sphere coordination and the peptide configuration in the Cu^{2+}-Aβ_{1-16} complexes formation?

  During the last years, different coordination spheres on the Cu^{2+}-Aβ complexes have been proposed. The combination of homology modeling and quantum mechanics calculations has provided us with the exploration of the conformational space and the modelling of the fine electronic effects necessary to generate plausible 3D structures of Cu^{2+}-Aβ_{1-16} complexes, involving the metal sphere coordination experimentally proposed at different pH range. The results show that the final stability of the complexes derives from a balance between the metal coordination site and amyloid folding upon complexation, illustrating the importance of the second coordination sphere in defining the relative stability between complexes.

- Can the Cu^{+}-Aβ_{1-16} complexes catalyze the H_2O_2 formation?

  Reduction of Cu^{2+}-Aβ complex has been proposed as the previous step in the production of ROS that lead to the oxidative stress typical of AD. The computed SRP values for all complexes are lower than 0.30 V, and thus reduction of O_2 to H_2O_2 is thermodynamically favored. In addition, results demonstrate that an external reducing agent is necessary to perform this first step of the process. However, the nature of the ligands effect on the SRP values causes that all systems would not be favorable reduced. For instance, those structures which exhibit negatively charged ligands present significantly lower SRP values than those which present neutral ligands and would not participate in the H_2O_2 production.

  It has been reported that Cu^{+} systems tend to adopt near-linear two coordinate structures which seem to be inert toward dioxygen, hindering the redox cycling of $Cu^{+/2+}$-Aβ. Results show that, after the reduction, the Cu^{+}-Aβ_{1-16} complexes exhibit a tricoordinate structures with the $CO_{backbone}$ decoordination that are stable for a period of time long enough to be attached by dioxygen. For all these reasons, Cu^{+}-Aβ_{1-16} complexes can catalyze the H_2O_2 formation.

- Which is the role of the first and the second coordination sphere of the $Cu^{+/2+}$-Aβ_{1-16} complexes in the O_2 activation?

  The H_2O_2 formation is a global down-hill reaction, where the most favorable reaction is the electron and proton transfer process. Therefore, the activation of O_2 by the resulting Cu^{+}-Aβ have been proposed as key step in the production of ROS. Thus, superoxide formation can be influenced by ligands present both in the first and second sphere of the $Cu^{+/2+}$-Aβ_{1-16} complexes. Results show that superoxide formation is more favorable in His rich metal coordination environments or when there is a negatively charged coordinating ligand. In addition, second sphere negatively charged groups in vicinity of the metal center disfavors the superoxide formation, while positively charged ligands favors it.

- What is the importance of the peptidic sequencein the redox potentials of the small peptide as potential chelates?

  ATCUN motif is a typical peptidic sequence of type Xaa–Xaa–His present in several proteins with high affinity for metals, such as Cu^{2+} and Ni^{2+}. Small peptides that show variations on this peptidic sequence have been studied as possible copper chelates. Results enable to assign an atomic detailed structure for the different peaks obtained in the CV experiments. Moreover, the potential values highlight the influence of the peptidic sequence on the redox properties of the resulting Cu-peptide complexes, which also depends on the pH. Therefore, the reduction potentials values are affected by both the peptidic sequence and the charge of the complex leading the lowest values for the ATCUN motif (systems with two deprotonated amides) and the highest ones for 2N2O metal coordination environment (complexes with no deprotonation), leaving an intermediate values for the 3N1O and 4N metal coordination spheres (systems with only one deprotonation). In conclusion, different metal coordination sphere involves differences in the SRP values. In fact, if the metal coordination is in ATCUN form, these complexes can inhibit ROS formation.

REFERENCES

1 Wilson RS, Segawa E, Boyle PA, Anagnos SE, Hizel LP, Bennett DA. The natural history of cognitive decline in Alzheimer's disease. *Psychol Aging* 2012; **27**: 1008–17.

2 Halpert BP. Development of the term senility as a medical diagnosis. *Minn Med* 1983; **66**: 421–424.

3 Torack R. *The early history of senile dementia*. New York : The Free Press, 1983.

4 Blocq P, Marinesco G. Sur les lésions et la pathogénie de l'épilepsie dite essentielle. *Sem Médical* 1892; **12**: 445–446.

5 Redlich E. Ueber miliare Sklerose der Hirnrinde bei seniler Atrphie. *J Psychiat Neurol* 1898; **17**: 208–216.

6 Fischer O. Miliare Nekrosen mit drusigen Wucherungen der Neurofibrillen, eine regelmässige Veränderung der Hirnride bei seniler Demenz. *Mschr Psychiat Neurol* 1907; **22**: 361–372.

7 Haymarker W, Schiller F. *The Founders of Neurology*. Springfield, Illinois, 1970.

8 Amaducci LA, Rocca WA, Schoenberg BS. Origin of the Distinction Between Alzheimers-Disease and Senile Dementia - How History Can Clarify Nosology. *Neurology* 1986; **36**: 1497–1499.

9 Schorer CE. Historical essay: Kraepelin's description of Alzheimer's disease. *Int J Aging Hum Dev* 1985; **21**: 235–238.

10 Hebert LE, Weuve J, Scherr PA, Evans DA. Alzheimer disease in the United States (2010-2050) estimated using the 2010 census. *Neurology* 2013; **80**: 1778–83.

11 Alzheimer's Association. Early onset dementia: a national challenge, a future crisis. *Alzheimer's Assoc* 2006.

12 Statistical WHO. *International problems. Classification of diseases and related health 10th revision.* 2nd editio. Geneva, Switzerland, 2004.

13 Batsch N, Mittelman M. World Alzheimer Report 2012: Overcoming the sitgma of dementia. *Alzheimer's Dis Int* 2012.

14 Alzheimer's Association. Alzheimer's Disease Facts and Figures. Alzheimer's &Dementia:USA. 2015.

15 Cummings JL, Cole G. Alzheimer disease. *JAMA* 2002; **287**: 2335–8.

16 Mandelkow EM, Mandelkow E. Tau in Alzheimer's disease. *Trends Cell Biol* 1998; **8**: 425–7.

17 Goedert M, Klug A, Crowther RA. Tau protein, the paired helical filament and Alzheimer's disease. *J Alzheimers Dis* 2006; **9**: 195–207.

18 Blennow K, de Leon MJ, Zetterberg H. Alzheimer's disease. *Lancet* 2006; **368**: 387–403.

19 Joachim CL, Morris JH, Selkoe DJ. Diffuse senile plaques occur commonly in the cerebellum in Alzheimer's disease. *Am J Pathol* 1989; **135**: 309–19.

20 Selkoe DJ. The cell biology of beta-amyloid precursor protein and presenilin in Alzheimer's disease. *Trends Cell Biol* 1998; **8**: 447–53.

21 Thinakaran G, Koo EH. Amyloid precursor protein trafficking, processing, and function. *J Biol Chem* 2008; **283**: 29615–9.

22 Mattson MP. Pathways towards and away from Alzheimer's disease. *Nature* 2004; **430**: 631–9.

23 Duthey B. Background Paper 6.11: Alzheimer disease and other dementias. *World Heal Organ* 2013.

24 Jack CR, Knopman DS, Jagust WJ, Shaw LM, Aisen PS, Weiner MW *et al.* Hypothetical model of dynamic biomarkers of the Alzheimer's pathological cascade. *Lancet Neurol* 2010; **9**: 119–28.

25 Big Think Editors. The brain plaques and tangles that cause Alzheimer's disease. Big Think Ed. 2010.

26 Braak H, Braak E. Neuropathological stageing of Alzheimer-related changes. *Acta*

Neuropathol 1991; **82**: 239–59.

27 Roy S, Rauk A. Alzheimer's disease and the 'ABSENT' hypothesis: mechanism for amyloid beta endothelial and neuronal toxicity. *Med Hypotheses* 2005; **65**: 123–37.

28 Lovell MA. A potential role for alterations of zinc and zinc transport proteins in the progression of Alzheimer's disease. *J Alzheimers Dis* 2009; **16**: 471–83.

29 Hardy JA, Higgins GA. Alzheimer's disease: the amyloid cascade hypothesis. Science. 1992; **256**: 184–185.

30 Sommer B. Alzheimer's disease and the amyloid cascade hypothesis: ten years on. *Curr Opin Pharmacol* 2002; **2**: 87–92.

31 LaFerla FM, Green KN, Oddo S. Intracellular amyloid-beta in Alzheimer's disease. *Nat Rev Neurosci* 2007; **8**: 499–509.

32 Karran E, Mercken M, De Strooper B. The amyloid cascade hypothesis for Alzheimer's disease: an appraisal for the development of therapeutics. *Nat Rev Drug Discov* 2011; **10**: 698–712.

33 De Ferrari and G V., Inestrosa NC. Wnt signaling function in Alzheimer's disease. *Brain Res Rev* 2000; **33**: 1–12.

34 Kang J, Lemaire HG, Unterbeck A, Salbaum JM, Masters CL, Grzeschik KH *et al.* The precursor of Alzheimer's disease amyloid A4 protein resembles a cell-surface receptor. *Nature* 1987; **325**: 733–736.

35 Kepp KP. Bioinorganic chemistry of Alzheimer's disease. *Chem Rev* 2012; **112**: 5193–239.

36 Hardy J, Selkoe DJ. The amyloid hypothesis of Alzheimer's disease: progress and problems on the road to therapeutics. *Science* 2002; **297**: 353–6.

37 Torreilles F, Touchon J. Pathogenic theories and intrathecal analysis of the sporadic form of Alzheimer's disease. *Prog Neurobiol* 2002; **66**: 191–203.

38 Faller P, Hureau C. A bioinorganic view of Alzheimer's disease: when misplaced metal ions (re)direct the electrons to the wrong target. *Chemistry* 2012; **18**: 15910–

20.

39 Esch FS, Keim PS, Beattie EC, Blacher RW, Culwell AR, Oltersdorf T *et al.* Cleavage of amyloid β peptide during constitutive processing of its precursor. *Science* 1990; **248**: 1122–1124.

40 Nunan J, Small DH. Regulation of APP cleavage by α-, β- and γ-secretases. *FEBS Lett* 2000; **483**: 6–10.

41 Chow VW, Mattson MP, Wong PC, Gleichmann M. An overview of APP processing enzymes and products. *Neuromolecular Med* 2010; **12**: 1–12.

42 Bitan G, Kirkitadze MD, Lomakin A, Vollers SS, Benedek GB, Teplow DB. Amyloid -protein (A) assembly: A 40 and A 42 oligomerize through distinct pathways. *Proc Natl Acad Sci* 2002; **100**: 330–335.

43 Rauk A. The chemistry of Alzheimer's disease. *Chem Soc Rev* 2009; **38**: 2698–715.

44 Vigo-Pelfrey C, Lee D, Keim P, Lieberburg I, Schenk DB. Characterization of beta-amyloid peptide from human cerebrospinal fluid. *J Neurochem* 1993; **61**: 1965–8.

45 Hardy J. Amyloid, the presenilins and Alzheimer's disease. *Trends Neurosci* 1997; **20**: 154–9.

46 Hureau C, Dorlet P. Coordination of redox active metal ions to the amyloid precursor protein and to amyloid-β peptides involved in Alzheimer disease. Part 2: Dependence of Cu(II) binding sites with Aβ sequences. *Coord Chem Rev* 2012; **256**: 2175–2187.

47 Karran E, Mercken M, De Strooper B. The amyloid cascade hypothesis for Alzheimer's disease: an appraisal for the development of therapeutics. *Nat Rev Drug Discov* 2011; **10**: 698–712.

48 Rajan MT, Jagannatha Rao KS, Mamatha BM, Rao R V, Shanmugavelu P, Menon RB *et al.* Quantification of trace elements in normal human brain by inductively coupled plasma atomic emission spectrometry. *J Neurol Sci* 1997; **146**: 153–66.

49 Dobrowolska J, Dehnhardt M, Matusch A, Zoriy M, Palomero-Gallagher N, Koscielniak P *et al.* Quantitative imaging of zinc, copper and lead in three distinct regions of the human brain by laser ablation inductively coupled plasma mass

spectrometry. *Talanta* 2008; **74**: 717–723.

50 Bush AI, Tanzi RE. Therapeutics for Alzheimer's disease based on the metal hypothesis. *Neurotherapeutics* 2008; **5**: 421–32.

51 Bush AI. The metallobiology of Alzheimer's disease. *Trends Neurosci* 2003; **26**: 207–14.

52 Suzuki K, Miura T, Takeuchi H. Inhibitory effect of copper(II) on zinc(II)-induced aggregation of amyloid beta-peptide. *Biochem Biophys Res Commun* 2001; **285**: 991–6.

53 Atwood CS, Moir RD, Huang X, Scarpa RC, Bacarra NM, Romano DM *et al.* Dramatic aggregation of Alzheimer abeta by Cu(II) is induced by conditions representing physiological acidosis. *J Biol Chem* 1998; **273**: 12817–26.

54 Faller P, Hureau C, Berthoumieu O. Role of metal ions in the self-assembly of the Alzheimer's amyloid-β peptide. *Inorg Chem* 2013; **52**: 12193–206.

55 Lovell MA, Robertson JD, Teesdale WJ, Campbell JL, Markesbery WR. Copper, iron and zinc in Alzheimer's disease senile plaques. *J Neurol Sci* 1998; **158**: 47–52.

56 Miller LM, Wang Q, Telivala TP, Smith RJ, Lanzirotti A, Miklossy J. Synchrotron-based infrared and X-ray imaging shows focalized accumulation of Cu and Zn co-localized with beta-amyloid deposits in Alzheimer's disease. *J Struct Biol* 2006; **155**: 30–7.

57 House E, Collingwood J, Khan A, Korchazkina O, Berthon G, Exley C. Aluminium, iron, zinc and copper influence the in vitro formation of amyloid fibrils of Abeta42 in a manner which may have consequences for metal chelation therapy in Alzheimer's disease. *J Alzheimers Dis* 2004; **6**: 291–301.

58 Dong J, Atwood CS, Anderson VE, Siedlak SL, Smith MA, Perry G *et al.* Metal binding and oxidation of amyloid-beta within isolated senile plaque cores: Raman microscopic evidence. *Biochemistry* 2003; **42**: 2768–73.

59 Huang X, Atwood CS, Moir RD, Hartshorn MA, Tanzi RE, Bush AI. Trace metal contamination initiates the apparent auto-aggregation, amyloidosis, and

oligomerization of Alzheimer's Abeta peptides. *J Biol Inorg Chem* 2004; **9**: 954–60.

60 Minicozzi V, Stellato F, Comai M, Dalla Serra M, Potrich C, Meyer-Klaucke W *et al.* Identifying the minimal copper- and zinc-binding site sequence in amyloid-beta peptides. *J Biol Chem* 2008; **283**: 10784–92.

61 Syme CD, Nadal RC, Rigby SEJ, Viles JH. Copper binding to the amyloid-beta (Abeta) peptide associated with Alzheimer's disease: folding, coordination geometry, pH dependence, stoichiometry, and affinity of Abeta-(1-28): insights from a range of complementary spectroscopic techniques. *J Biol Chem* 2004; **279**: 18169–77.

62 Talmard C, Leuma Yona R, Faller P. Mechanism of zinc(II)-promoted amyloid formation: zinc(II) binding facilitates the transition from the partially alpha-helical conformer to aggregates of amyloid beta protein(1-28). *J Biol Inorg Chem* 2009; **14**: 449–55.

63 Tõugu V, Karafin A, Zovo K, Chung RS, Howells C, West AK *et al.* Zn(II)- and Cu(II)-induced non-fibrillar aggregates of amyloid-beta (1-42) peptide are transformed to amyloid fibrils, both spontaneously and under the influence of metal chelators. *J Neurochem* 2009; **110**: 1784–95.

64 Waggoner DJ, Bartnikas TB, Gitlin JD. The role of copper in neurodegenerative disease. *Neurobiol Dis* 1999; **6**: 221–30.

65 Karr JW, Szalai VA. Role of aspartate-1 in Cu(II) binding to the amyloid-beta peptide of Alzheimer's disease. *J Am Chem Soc* 2007; **129**: 3796–7.

66 Ghosh C, Dey SG. Ligand-field and ligand-binding analysis of the active site of copper-bound Aβ associated with Alzheimer's disease. *Inorg Chem* 2013; **52**: 1318–27.

67 Curtain CC, Ali F, Volitakis I, Cherny RA, Norton RS, Beyreuther K *et al.* Alzheimer's disease amyloid-beta binds copper and zinc to generate an allosterically ordered membrane-penetrating structure containing superoxide dismutase-like subunits. *J Biol Chem* 2001; **276**: 20466–73.

68 Drew SC, Barnham KJ. The heterogeneous nature of Cu2+ interactions with Alzheimer's amyloid-β peptide. *Acc Chem Res* 2011; **44**: 1146–55.

69 El Khoury Y, Dorlet P, Faller P, Hellwig P. New insights into the coordination of Cu(II) by the amyloid-B 16 peptide from Fourier transform IR spectroscopy and isotopic labeling. *J Phys Chem B* 2011; **115**: 14812–21.

70 Beauchemin D, Kisilevsky R. A method based on ICP-MS for the analysis of Alzheimer's amyloid plaques. *Anal Chem* 1998; **70**: 1026–9.

71 Huang X, Cuajungco MP, Atwood CS, Hartshorn MA, Tyndall JDA, Hanson GR *et al.* Cu(II) Potentiation of Alzheimer Aβ Neurotoxicity: Correlation with Cell-Free Hydrogen Peroxide Production and Metal Reduction. *J Biol Chem* 1999; **274**: 37111–37116.

72 Kowalik-Jankowska T, Ruta M, Wiśniewska K, Lankiewicz L. Coordination abilities of the 1-16 and 1-28 fragments of beta-amyloid peptide towards copper(II) ions: a combined potentiometric and spectroscopic study. *J Inorg Biochem* 2003; **95**: 270–82.

73 Miura T, Suzuki K, Kohata N, Takeuchi H. Metal binding modes of Alzheimer's amyloid beta-peptide in insoluble aggregates and soluble complexes. *Biochemistry* 2000; **39**: 7024–31.

74 Drew SC, Noble CJ, Masters CL, Hanson GR, Barnham KJ. Pleomorphic copper coordination by Alzheimer's disease amyloid-beta peptide. *J Am Chem Soc* 2009; **131**: 1195–207.

75 Karr JW, Akintoye H, Kaupp LJ, Szalai VA. N-Terminal deletions modify the Cu2+ binding site in amyloid-beta. *Biochemistry* 2005; **44**: 5478–87.

76 Guilloreau L, Damian L, Coppel Y, Mazarguil H, Winterhalter M, Faller P. Structural and thermodynamical properties of CuII amyloid-beta16/28 complexes associated with Alzheimer's disease. *J Biol Inorg Chem* 2006; **11**: 1024–38.

77 Alí-Torres J, Maréchal J-D, Rodríguez-Santiago L, Sodupe M. Three dimensional models of Cu(2+)-Aβ(1-16) complexes from computational approaches. *J Am Chem Soc* 2011; **133**: 15008–14.

78 Drew SC, Masters CL, Barnham KJ. Alanine-2 carbonyl is an oxygen ligand in Cu2+ coordination of Alzheimer's disease amyloid-beta peptide--relevance to N-terminally

truncated forms. *J Am Chem Soc* 2009; **131**: 8760–1.

79 Shin B, Saxena S. Substantial contribution of the two imidazole rings of the His13-His14 dyad to Cu(II) binding in amyloid-β(1-16) at physiological pH and its significance. *J Phys Chem A* 2011; **115**: 9590–602.

80 Hureau C, Coppel Y, Dorlet P, Solari PL, Sayen S, Guillon E *et al.* Deprotonation of the Asp1-Ala2 peptide bond induces modification of the dynamic copper(II) environment in the amyloid-beta peptide near physiological pH. *Angew Chem Int Ed Engl* 2009; **48**: 9522–5.

81 Faller P, Hureau C. Bioinorganic chemistry of copper and zinc ions coordinated to amyloid-beta peptide. *Dalton Trans* 2009; **7**: 1080–94.

82 Dorlet P, Gambarelli S, Faller P, Hureau C. Pulse EPR spectroscopy reveals the coordination sphere of copper(II) ions in the 1-16 amyloid-beta peptide: a key role of the first two N-terminus residues. *Angew Chem Int Ed Engl* 2009; **48**: 9273–6.

83 Raffa DF, Gómez-Balderas R, Brunelle P, Rickard GA, Rauk A. Ab initio model studies of copper binding to peptides containing a His-His sequence: relevance to the beta-amyloid peptide of Alzheimer's disease. *J Biol Inorg Chem* 2005; **10**: 887–902.

84 Azimi S, Rauk A. On the Involvement of Copper Binding to the N-Terminus of the Amyloid Beta Peptide of Alzheimer's Disease: A Computational Study on Model Systems. *Int J Alzheimers Dis* 2011.

85 Raffa DF, Rauk A. Molecular dynamics study of the beta amyloid peptide of Alzheimer's disease and its divalent copper complexes. *J Phys Chem B* 2007; **111**: 3789–99.

86 Floyd RA. Antioxidants, oxidative stress, and degenerative neurological disorders. *Proc Soc Exp Biol Med* 1999; **222**: 236–45.

87 Halliwell B, Gutteridge JMC. *Free Radicals in Biology and Medicine*. Oxford University Press: Oxford, 1999.

88 Freinbichler W, Colivicchi MA, Stefanini C, Bianchi L, Ballini C, Misini B *et al.* Highly reactive oxygen species: detection, formation, and possible functions. *Cell*

Mol Life Sci 2011; **68**: 2067–2079.

89 Cadet J, Loft S, Olinski R, Evans MD, Bialkowski K, Richard Wagner J *et al.* Biologically relevant oxidants and terminology, classification and nomenclature of oxidatively generated damage to nucleobases and 2-deoxyribose in nucleic acids. *Free Radic Res* 2012; **46**: 367–381.

90 Lane N. *Oxygen: the Molecule that Made the World*. Oxford University Press: Oxford, 2006.

91 Finkel T, Holbrook NJ. Oxidants, oxidative stress and the biology of ageing. *Nature* 2000; **408**: 239–47.

92 Betteridge DJ. What is oxidative stress? *Metabolism* 2000; **49**: 3–8.

93 Beal MF. Aging, energy, and oxidative stress in neurodegenerative diseases. *Ann Neurol* 1995; **38**: 357–66.

94 Dumont M, Beal MF. Neuroprotective strategies involving ROS in Alzheimer disease. *Free Radic Biol Med* 2011; **51**: 1014–26.

95 Markesbery WR. Oxidative Stress Hypothesis in Alzheimer's Disease. *Free Radic Biol Med* 1997; **23**: 134–147.

96 Gaggelli E, Kozlowski H, Valensin D, Valensin G. Copper Homeostasis and Neurodegenerative Disorders (Alzheimer's, Prion, and Parkinson's Diseases and Amyotrophic Lateral Sclerosis). *Chem Rev* 2006; **106**: 1995–2044.

97 Barnham KJ, Masters CL, Bush AI. Neurodegenerative diseases and oxidative stress. *Nat Rev Drug Discov* 2004; **3**: 205–14.

98 Hewitt N, Rauk A. Mechanism of hydrogen peroxide production by copper-bound amyloid beta peptide: a theoretical study. *J Phys Chem B* 2009; **113**: 1202–9.

99 Jiang D, Men L, Wang J, Zhang Y, Chickenyen S, Wang Y *et al.* Redox Reactions of Copper Complexes Formed with Different β-Amyloid Peptides and Their Neuropathalogical Relevance. *Biochemistry* 2007; **46**: 9270–9282.

100 Alí-Torres J, Rodríguez-Santiago L, Sodupe M, Rauk A. Structures and stabilities of

Fe2+/3+ complexes relevant to Alzheimer's disease: an ab initio study. *J Phys Chem A* 2011; **115**: 12523–30.

101 Guilloreau L, Combalbert S, Sournia-Saquet A, Mazarguil H, Faller P. Redox chemistry of copper-amyloid-beta: the generation of hydroxyl radical in the presence of ascorbate is linked to redox-potentials and aggregation state. *Chembiochem* 2007; **8**: 1317–25.

102 Nunomura A, Perry G, Aliev G, Hirai K, Takeda A, Balraj EK *et al.* Oxidative damage is the earliest event in Alzheimer disease. *J Neuropathol Exp Neurol* 2001; **60**: 759–67.

103 Mecocci P, MacGarvey U, Kaufman AE, Koontz D, Shoffner JM, Wallace DC *et al.* Oxidative damage to mitochondrial DNA shows marked age-dependent increases in human brain. *Ann Neurol* 1993; **34**: 609–16.

104 Paola D, Domenicotti C, Nitti M, Vitali A, Borghi R, Cottalasso D *et al.* Oxidative stress induces increase in intracellular amyloid beta-protein production and selective activation of betaI and betaII PKCs in NT2 cells. *Biochem Biophys Res Commun* 2000; **268**: 642–6.

105 Sanaullah, Wilson S, Glass RS. The effect of pH and complexation of amino acid functionality on the redox chemistry of methionine and X-ray structure of [Co(en)2(L-Met)](ClO4)2.H2O. *J Inorg Biochem* 1994; **55**: 87–99.

106 Opazo C, Huang X, Cherny RA, Moir RD, Roher AE, White AR *et al.* Metalloenzyme-like Activity of Alzheimer's Disease β-Amyloid: Cu-Dependent Catalytic Conversion of Dopamine, Cholesterol, and Biological Reducing Agents to Neurotoxic H2O2. *J Biol Chem* 2002; **277**: 40302–40308.

107 Streltsov VA, Varghese JN. Substrate mediated reduction of copper-amyloid-beta complex in Alzheimer's disease. *Chem Commun (Camb)* 2008; : 3169–71.

108 Huang X, Cuajungco MP, Atwood CS, Hartshorn MA, Tyndall JDA, Hanson GR *et al.* Cu(II) Potentiation of Alzheimer A Neurotoxicity: correlation with cell-free hydrogen peroxide production and metal reduction. *J Biol Chem* 1999; **274**: 37111–37116.

109 Bondy SC, Guo-Ross SX, Truong AT. Promotion of transition metal-induced reactive oxygen species formation by beta-amyloid. *Brain Res* 1998; **799**: 91–6.

110 Nelson DL, Cox MM. *Lehninger Principles of Biochemistry*. W. H. Freeman: New York, 2005.

111 Trujano-Ortiz LG, González FJ, Quintanar L. Redox cycling of copper-amyloid β 1-16 peptide complexes is highly dependent on the coordination mode. *Inorg Chem* 2015; **54**: 4–6.

112 Duce JA, Bush AI. Biological metals and Alzheimer's disease: implications for therapeutics and diagnostics. *Prog Neurobiol* 2010; **92**: 1–18.

113 Rodríguez-Rodríguez C, Telpoukhovskaia M, Orvig C. The art of building multifunctional metal-binding agents from basic molecular scaffolds for the potential application in neurodegenerative diseases. *Coord Chem Rev* 2012; **256**: 2308–2332.

114 Huang X, Atwood CS, Moir RD, Hartshorn MA, Vonsattel J-P, Tanzi RE *et al.* Zinc-induced Alzheimer's A 1-40 Aggregation Is Mediated by Conformational Factors. *J Biol Chem* 1997; **272**: 26464–26470.

115 Cherny RA, Legg JT, McLean CA, Fairlie DP, Huang X, Atwood CS *et al.* Aqueous dissolution of Alzheimer's disease Abeta amyloid deposits by biometal depletion. *J Biol Chem* 1999; **274**: 23223–8.

116 Lee J-Y, Friedman JE, Angel I, Kozak A, Koh J-Y. The lipophilic metal chelator DP-109 reduces amyloid pathology in brains of human beta-amyloid precursor protein transgenic mice. *Neurobiol Aging* 2004; **25**: 1315–21.

117 Badrick AC, Jones CE. Reorganizing metals: the use of chelating compounds as potential therapies for metal-related neurodegenerative disease. *Curr Top Med Chem* 2011; **11**: 543–52.

118 Choi J-S, Braymer JJ, Nanga RPR, Ramamoorthy A, Lim MH. Design of small molecules that target metal-A{beta} species and regulate metal-induced A{beta} aggregation and neurotoxicity. *Proc Natl Acad Sci U S A* 2010; **107**: 21990–5.

119 Cherny RA, Atwood CS, Xilinas ME, Gray DN, Jones WD, McLean CA *et al.*

Treatment with a copper-zinc chelator markedly and rapidly inhibits beta-amyloid accumulation in Alzheimer's disease transgenic mice. *Neuron* 2001; **30**: 665–76.

120 Adlard PA, Cherny RA, Finkelstein DI, Gautier E, Robb E, Cortes M *et al.* Rapid restoration of cognition in Alzheimer's transgenic mice with 8-hydroxy quinoline analogs is associated with decreased interstitial Abeta. *Neuron* 2008; **59**: 43–55.

121 Barnham KJ, Gautier ECL, Kok GB, Krippner G. 8-hydroxy quinoline derivatives. 2009.

122 Crouch PJ, Savva MS, Hung LW, Donnelly PS, Mot AI, Parker SJ *et al.* The Alzheimer's therapeutic PBT2 promotes amyloid-β degradation and GSK3 phosphorylation via a metal chaperone activity. *J Neurochem* 2011; **119**: 220–30.

123 Martell AE, Smith RM. *Critical Stability Constants*. vol. 1-6. Plenum: New York.

124 Boldron C, Van der Auwera I, Deraeve C, Gornitzka H, Wera S, Pitié M *et al.* Preparation of cyclo-phen-type ligands: chelators of metal ions as potential therapeutic agents in the treatment of neurodegenerative diseases. *Chembiochem* 2005; **6**: 1976–80.

125 Oliveri V, Vecchio G. 8-Hydroxyquinolines in medicinal chemistry: A structural perspective. *Eur J Med Chem* 2016; **120**: 252–274.

126 Jin H, Randazzo J, Zhang P, Kador PF. Multifunctional antioxidants for the treatment of age-related diseases. *J Med Chem* 2010; **53**: 1117–27.

127 Grundman M, Delaney P. Antioxidant strategies for Alzheimer's disease. *Proc Nutr Soc* 2002; **61**: 191–202.

128 Devore EE, Grodstein F, van Rooij FJA, Hofman A, Stampfer MJ, Witteman JCM *et al.* Dietary antioxidants and long-term risk of dementia. *Arch Neurol* 2010; **67**: 819–25.

129 Gray SL, Anderson ML, Crane PK, Breitner JCS, McCormick W, Bowen JD *et al.* Antioxidant vitamin supplement use and risk of dementia or Alzheimer's disease in older adults. *J Am Geriatr Soc* 2008; **56**: 291–5.

130 Rice-Evans C. Flavonoid antioxidants. *Curr Med Chem* 2001; **8**: 797–807.

131 Rezai-Zadeh K, Shytle D, Sun N, Mori T, Hou H, Jeanniton D *et al.* Green tea epigallocatechin-3-gallate (EGCG) modulates amyloid precursor protein cleavage and reduces cerebral amyloidosis in Alzheimer transgenic mice. *J Neurosci* 2005; **25**: 8807–14.

132 Shimmyo Y, Kihara T, Akaike A, Niidome T, Sugimoto H. Three distinct neuroprotective functions of myricetin against glutamate-induced neuronal cell death: involvement of direct inhibition of caspase-3. *J Neurosci Res* 2008; **86**: 1836–45.

133 Rao A V, Balachandran B. Role of oxidative stress and antioxidants in neurodegenerative diseases. *Nutr Neurosci* 2002; **5**: 291–309.

134 Hamaguchi T, Ono K, Yamada M. REVIEW: Curcumin and Alzheimer's disease. *CNS Neurosci Ther* 2010; **16**: 285–97.

135 Yang F, Lim GP, Begum AN, Ubeda OJ, Simmons MR, Ambegaokar SS *et al.* Curcumin Inhibits Formation of Amyloid Oligomers and Fibrils, Binds Plaques, and Reduces Amyloid in Vivo. *J Biol Chem* 2004; **280**: 5892–5901.

136 Barik A, Mishra B, Shen L, Mohan H, Kadam RM, Dutta S *et al.* Evaluation of a new copper(II)-curcumin complex as superoxide dismutase mimic and its free radical reactions. *Free Radic Biol Med* 2005; **39**: 811–22.

137 Huang H-C, Lin C-J, Liu W-J, Jiang R-R, Jiang Z-F. Dual effects of curcumin on neuronal oxidative stress in the presence of Cu(II). *Food Chem Toxicol* 2011; **49**: 1578–83.

138 Charkoudian LK, Pham DM, Franz KJ. A pro-chelator triggered by hydrogen peroxide inhibits iron-promoted hydroxyl radical formation. *J Am Chem Soc* 2006; **128**: 12424–5.

139 Dickens MG, Franz KJ. A prochelator activated by hydrogen peroxide prevents metal-induced amyloid Beta aggregation. *Chembiochem* 2010; **11**: 59–62.

140 Folk DS, Franz KJ. A prochelator activated by beta-secretase inhibits Abeta aggregation and suppresses copper-induced reactive oxygen species formation. *J Am Chem Soc* 2010; **132**: 4994–5.

141 Rodríguez-Rodríguez C, Rimola A, Alí-Torres J, Sodupe M, González-Duarte P. In silico strategies for the selection of chelating compounds with potential application in metal-promoted neurodegenerative diseases. *J Comput Aided Mol Des* 2011; **25**: 21–30.

142 Rimola A, Alí-Torres J, Rodríguez-Rodríguez C, Poater J, Matito E, Solà M *et al.* Ab initio design of chelating ligands relevant to Alzheimer's disease: influence of metalloaromaticity. *J Phys Chem A* 2011; **115**: 12659–66.

143 Rodríguez-Santiago L, Alí-Torres J, Vidossich P, Sodupe M. Coordination properties of a metal chelator clioquinol to Zn(2+) studied by static DFT and ab initio molecular dynamics. *Phys Chem Chem Phys* 2015; **17**: 13582–9.

144 Rodriguez-Rodriguez C, De Groot NS, Rimola A, Alvarez-Larena A, Lloveras V, Vidal-Gancedo J *et al.* Design, selection, and characterization of thioflavin-based intercalation compounds with metal chelating properties for application in alzheimer's disease. *J Am Chem Soc* 2009; **131**: 1436–1451.

145 Dixon JW, Sarkar B. Isolation, amino acid sequence and copper(II)-binding properties of peptide (1-24) of dog serum albumin. *J Biol Chem* 1974; **249**: 5872–5877.

146 Harford C, Sarkar B. Amino Terminal Cu(II)- and Ni(II)-Binding (ATCUN) Motif of Proteins and Peptides: Metal Binding, DNA Cleavage, and Other Properties. *Acc Chem Res* 1997; **30**: 123–130.

147 Sankararamakrishnan R, Verma S, Kumar S. ATCUN-like metal-binding motifs in proteins: Identification and characterization by crystal structure and sequence analysis. *Proteins Struct Funct Bioinforma* 2004; **58**: 211–221.

148 Gasmi G, Singer A, Forman-Kay J, Sarkar B. NMR structure of neuromedin C, a neurotransmitter with an amino terminal CuII-, NiII-binding (ATCUN) motif. *J Pept Res* 1997; **49**: 500–509.

149 Melino S, Gallo M, Trotta E, Mondello F, Maurizio Paci A, Petruzzelli R. Metal-Binding and Nuclease Activity of an Antimicrobial Peptide Analogue of the Salivary Histatin 5. *Biochemistry* 2006; **45**: 15373–15383.

150 McKay DJ, Renaux BS, Dixon GH. Human sperm protamines. Amino-acid sequences of two forms of protamine P2. *Eur J Biochem* 1986; **156**: 5–8.

151 Laussac JP, Sarker B. Characterization of the copper(II) and nickel(II) transport site of human serum albumin. Studies of copper(II) and nickel(II) binding to peptide 1-24 of human serum albumin by carbon-13 and proton NMR spectroscopy. *Biochemistry* 1984; **23**: 2832–2838.

152 Bal W, Sokołowska M, Kurowska E, Faller P. Binding of transition metal ions to albumin: Sites, affinities and rates. *Biochim Biophys Acta - Gen Subj* 2013; **1830**: 5444–5455.

153 Munteanu CR, Vázquez JM, Dorado J, Sierra AP, Sánchez-González Á, Prado-Prado FJ *et al.* Complex Network Spectral Moments for ATCUN Motif DNA Cleavage: First Predictive Study on Proteins of Human Pathogen Parasites. *J Proteome Res* 2009; **8**: 5219–5228.

154 Jin Y, Cowan JA. DNA Cleavage by Copper−ATCUN Complexes. Factors Influencing Cleavage Mechanism and Linearization of dsDNA. *J Am Chem Soc* 2005; **127**: 8408–8415.

155 Kimoto E, Tanaka H, Gyotoku J, Morishige F, Pauling L. Enhancement of antitumor activity of ascorbate against Ehrlich ascites tumor cells by the copper:glycylglycylhistidine complex. *Cancer Res* 1983; **43**: 824–8.

156 Chiou SH. DNA- and protein-scission activities of ascorbate in the presence of copper ion and a copper-peptide complex. *J Biochem* 1983; **94**: 1259–67.

157 Mjos KD, Orvig C. Metallodrugs in Medicinal Inorganic Chemistry. *Chem Rev* 2014; **114**: 4540–4563.

158 Joyner JC, Cowan JA, Joyner JC, Cowan JA. Target-directed catalytic metallodrugs. *Brazilian J Med Biol Res* 2013; **46**: 465–485.

159 Bradford S, Cowan JA. Catalytic metallodrugs targeting HCV IRES RNA. *Chem Commun* 2012; **48**: 3118–3120.

160 Bradford SS, Ross MJ, Fidai I, Cowan JA. Insight into the Recognition, Binding, and

Reactivity of Catalytic Metallodrugs Targeting Stem Loop IIb of Hepatitis C IRES RNA. *ChemMedChem* 2014; **9**: 1275–1285.

161 Schrödinger E. An Undulatory Theory of the Mechanics of Atoms and Molecules. *Phys Rev* 1926; **28**: 1049–1070.

162 Tannor DJ. *Introduction to Quantum Mechanics: A Time-Dependent Perspective*. University Science Book: California, 2006.

163 Jensen F. *Introduction to Computational Chemistry*. UK, 2002http://catdir.loc.gov/catdir/enhancements/fy0826/2006023998-b.html.

164 Born M, Oppenheimer R. Zur quantentheorie der molekeln. *Ann Phys* 1927; **20**: 457–484.

165 Szabo A, Ostlund NS. *Modern Quantum Chemistry: Introduction to Advanced Electronic Structure Theory*. 1996.

166 Cramer CJ. *Essentials of Computational Chemistry Theories and Models*. 2004 doi:10.1021/ci010445m.

167 Roothaan CCJ. New developments in molecular orbital theory. *Rev Mod Phys* 1951; **23**: 69–89.

168 Hall GG. The Molecular Orbital Theory of Chemical Valency. VIII. A Method of Calculating Ionization Potentials. *Proc R Soc A Math Phys Eng Sci* 1951; **205**: 541–552.

169 Saxe P, Schaeffer III HF, Handy NC. Exact solution (within a double-zeta basis set) of the Schrödinger electronic equation for water. *Chem Phys Lett* 1981; **79**: 202–204.

170 Møller C, Plesset MS. Note on an Approximation Treatment for Many-Electron Systems. *Phys Rev* 1934; **46**: 618–622.

171 Hoffmann MR, Schaefer III HF. A Full Coupled-Cluster Singles, Doubles, and Triples Model for the Description of Electron Correlation. *Adv Quantum Chem* 1986; **18**: 207–279.

172 Raghavachari K, Trucks GW, Pople JA, Head-Gordon M. A fifth-order perturbation

comparison of electron correlation theories. *Chem Phys Lett* 1989; **157**: 479–483.

173 Scuseria GE, Schaefer HF. Is coupled cluster singles and doubles (CCSD) more computationally intensive than quadratic configuration interaction (QCISD)? *J Chem Phys* 1989; **90**: 3700.

174 Thomas LH. The calculation of atomic fields. Proc. Camb. Philos. Soc. 1927; **23**: 542.

175 Fermi E. Eine statistische Methode zur Bestimmung einiger Eigenschaften des Atoms und ihre Anwendung auf die Theorie des periodischen Systems der Elemente. *Zeitschrift für Phys* 1928; **48**: 73–79.

176 Slater JC. A Generalized Self-Consistent Field Method. *Phys Rev* 1953; **91**: 528–530.

177 Hohenberg P, Kohn W. The Inhomogeneous Electron Gas. *Phys Rev* 1964; **136**: B864.

178 Kohn W. Electronic structure of matter—wave functions and density functionals. *Rev Mod Phys* 1999; **71**: 1253–1266.

179 Kohn W, Sham LJ. Self-consistent equations including exchange and correlation effects. *Phys Rev* 1965; **140**.

180 Martin RM. *Electronic Structure: Basic Theory and Practical Methods*. 2005 doi:10.1080/00107514.2010.509989.

181 Fermi E. Statistical method to determine some properties of atoms. *Rend Accad Naz Lincei* 1927; **6**: 602–607.

182 Dirac P a. M. Note on Exchange Phenomena in the Thomas Atom. *Math Proc Cambridge Philos Soc* 1930; **26**: 376.

183 Ceperley DM, Alder BJ. Ground State of the Electron Gas by a Stochastic Method. *Phys Rev Lett* 1980; **45**: 566–569.

184 Vosko SH, Wilk L, Nusair M. Accurate spin-dependent electron liquid correlation energies for local spin density calculations: a critical analysis. *Can J Phys* 1980; **58**:

1200–1211.

185 Becke AD. Density-functional exchange-energy approximation with correct asymptotic behavior. *Phys Rev A* 1988; **38**: 3098–3100.

186 Adamo C, Barone V. Exchange functionals with improved long-range behavior and adiabatic connection methods without adjustable parameters: The mPW and mPW1PW models. *J Chem Phys* 1998; **108**: 664–675.

187 Handy NC, Cohen AJ. Left-right correlation energy. *Mol Phys* 2001; **99**: 403–412.

188 Levy M, Perdew JP. Success of quantum mechanical approximations for molecular geometries and electron–nuclear attraction expectation values: Gift of the Coulomb potential? *J Chem Phys* 1986; **84**: 4519.

189 Becke AD. Density functional calculations of molecular bond energies. *J Chem Phys* 1986; **84**: 4524.

190 Lee C, Yang W, Parr RG. Development of the Colle-Salvetti correlation-energy formula into a functional of the electron density. *Phys Rev B* 1988; **37**: 785–789.

191 Perdew JP, Ernzerhof M, Burke K. Generalized gradient approximation made simple. *Phys Rev Lett* 1996; **77**: 3865–3868.

192 Schmider HL, Becke AD. Optimized density functionals from the extended G2 test set. *J Chem Phys* 1998; **108**: 9624–9631.

193 Tao J, Perdew JP, Staroverov VN, Scuseria GE. Climbing the Density Functional Ladder: Nonempirical Meta–Generalized Gradient Approximation Designed for Molecules and Solids. *Phys Rev Lett* 2003; **91**: 146401.

194 Van Voorhis T, Scuseria GE. A novel form for the exchange-correlation energy functional. *J Chem Phys* 1998; **109**: 400–410.

195 Zhao Y, Truhlar DG. The M06 suite of density functionals for main group thermochemistry, thermochemical kinetics, noncovalent interactions, excited states, and transition elements: two new functionals and systematic testing of four M06-class functionals and 12 other function. *Theor Chem Acc* 2008; **120**: 215–241.

196 Zhao Y, Truhlar DG. A new local density functional for main-group thermochemistry, transition metal bonding, thermochemical kinetics, and noncovalent interactions. *J Chem Phys* 2006; **125**: 194101.

197 Zhao Y, Truhlar DG. Density functional for spectroscopy: no long-range self-interaction error, good performance for Rydberg and charge-transfer states, and better performance on average than B3LYP for ground states. *J Phys Chem A* 2006; **110**: 13126–30.

198 Grimme S. Accurate description of van der Waals complexes by density functional theory including empirical corrections. *J Comput Chem* 2004; **25**: 1463–73.

199 Von Lilienfeld OA, Tavernelli I, Rothlisberger U, Sebastiani D. Optimization of effective atom centered potentials for london dispersion forces in density functional theory. *Phys Rev Lett* 2004; **93**: 153004.

200 Sato T, Tsuneda T, Hirao, K. Van der Waals interactions studied by density functional theory. *Mol Phys* 2005; **103**: 1151–1164.

201 Sun YY, Kim Y-H, Lee K, Zhang SB. Accurate and efficient calculation of van der Waals interactions within density functional theory by local atomic potential approach. *J Chem Phys* 2008; **129**: 154102.

202 Grimme S. Semiempirical GGA-type density functional constructed with a long-range dispersion correction. *J Comput Chem* 2006; **27**: 1787–99.

203 Grimme S, Antony J, Ehrlich S, Krieg H. A consistent and accurate ab initio parametrization of density functional dispersion correction (DFT-D) for the 94 elements H-Pu. *J Chem Phys* 2010; **132**: 154104.

204 Grimme S, Ehrlich S, Goerigk L. Effect of the damping function in dispersion corrected density functional theory. *J Comput Chem* 2011; **32**: 1456–65.

205 Poater J, Sola M, Rimola A, Rodr??guez-Santiago L, Sodupe M. Ground and low-lying states of Cu2+-H2O. A difficult case for density functional methods. *J Phys Chem A* 2004; **108**: 6072–6078.

206 Georgieva I, Trendafilova N, Rodríguez-Santiago L, Sodupe M. Coordination

properties of the oxime analogue of glycine to Cu(II). *J Phys Chem A* 2005; **109**: 5668–76.

207 Rimola A, Rodríguez-Santiago L, Sodupe M. Cation-π interactions and oxidative effects on Cu+ and Cu2+ binding to Phe, Tyr, Trp, and His amino acids in the gas phase. Insights from first-principles calculations. *J Phys Chem B* 2006; **110**: 24189–24199.

208 Rimola A, Constantino E, Rodríguez-Santiago L, Sodupe M. Binding properties of Cu(+/2+)-(glycyl)n glycine complexes (n = 1-3). *J Phys Chem A* 2008; **112**: 3444–53.

209 Trucks GW, Pople JA, Head-Gordon M. A fifth-order perturbation comparison of electron correlation theoriesA1 - Raghavachari,K. *Chem Phys Lett* 1989; **157**: 479–483.

210 Leach AR. *Molecular Modelling: Principles and Applications*. 2nd editio. Pearson Education, 2001.

211 Burkert U, Allinger NL. Molecular Mechanics. ACS Monogr. Ser. 1982.

212 Dinur U, Hagler A. New approaches to empirical force fields. *Rev Comput Chem* 1991.

213 Rappé AK, Casewit CJ. *Molecular Mechanics Across Chemistry*. 1997.

214 Levitt M, Lifson S. Refinement of protein conformations using a macromolecular energy minimization procedure. *J Mol Biol* 1969; **46**: 269–279.

215 Warshel A. Consistent Force Field Calculations. II. Crystal Structures, Sublimation Energies, Molecular and Lattice Vibrations, Molecular Conformations, and Enthalpies of Alkanes. *J Chem Phys* 1970; **53**: 582.

216 Allinger NL, Sprague JT. Conformational analysis. XC. Calculation of the structures of hydrocarbons containing delocalized electronic systems by the molecular mechanics method. *J Am Chem Soc* 1973; **95**: 3893–3907.

217 Li D-W, Brüschweiler R. NMR-based protein potentials. *Angew Chem Int Ed Engl* 2010; **49**: 6778–80.

218 Case DA, Berryman JT, Betz RM, Cerutti DS, III TEC, Darden TA *et al.* AMBER 2015. 2015.

219 Brooks BR, Brooks CL, Mackerell AD, Nilsson L, Petrella RJ, Roux B *et al.* CHARMM: The biomolecular simulation program. *J Comput Chem* 2009; **30**: 1545–1614.

220 Reif MM, Winger M, Oostenbrink C. Testing of the GROMOS Force-Field Parameter Set 54A8: Structural Properties of Electrolyte Solutions, Lipid Bilayers, and Proteins. *J Chem Theory Comput* 2013; **9**: 1247–1264.

221 Jorgensen WL, Maxwell DS, Tirado-Rives J. Development and testing of the OPLS all-atom force field on conformational energetics and properties of organic liquids. *J Am Chem Soc* 1996; **118**: 11225–11236.

222 Price DJ, Brooks CL. Modern protein force fields behave comparably in molecular dynamics simulations. *J Comput Chem* 2002; **23**: 1045–57.

223 Garcia-Viloca M, Gao J, Karplus M, Truhlar DG. How enzymes work: analysis by modern rate theory and computer simulations. *Science (80-)* 2004; **303**: 186–195.

224 Senn HM, Thiel W. QM/MM methods for biomolecular systems. *Angew Chem Int Ed Engl* 2009; **48**: 1198–229.

225 Reuter N, Dejaegere A, Maigret B, Karplus M. Frontier Bonds in QM/MM Methods: A Comparison of Different Approaches. *J Phys Chem A* 2000; **104**: 1720–1735.

226 Antes I, Thiel W. Adjusted Connection Atoms for Combined Quantum Mechanical and Molecular Mechanical Methods. *J Phys Chem A* 1999; **103**: 9290–9295.

227 Zhang Y. Improved pseudobonds for combined ab initio quantum mechanical/molecular mechanical methods. *J Chem Phys* 2005; **122**: 24114.

228 DiLabio GA, Hurley MM, Christiansen PA. Simple one-electron quantum capping potentials for use in hybrid QM/MM studies of biological molecules. *J Chem Phys* 2002; **116**: 9578.

229 Thery V, Rinaldi D, Rivail JL, Maigret B, Ferenczy GG. Quantum-mechanical computations on very large molecular systems: the local self-consistent field method.

J Comput Chem 1994; **15**: 269.

230 Gao J, Amara P, Alhambra C, Field MJ. A Generalized Hybrid Orbital (GHO) Method for the Treatment of Boundary Atoms in Combined QM/MM Calculations. *J Phys Chem A* 1998; **102**: 4714.

231 Bizzarri AR, Cannistraro S. Molecular Dynamics of Water at the Protein−Solvent Interface. *J Phys Chem B* 2002; **106**: 6617–6633.

232 Jorgensen WL, Chandrasekhar J, Madura JD, Impey RW, Klein ML. Comparison of simple potential functions for simulating liquid water. *J Chem Phys* 1983; **79**: 926.

233 Berendsen H. The missing term in effective pair potentials. *J Phys* 1987; **21**: 6269–6271.

234 Bernal JD, Fowler RH. A Theory of Water and Ionic Solution, with Particular Reference to Hydrogen and Hydroxyl Ions. *J Chem Phys* 1933; **1**: 515.

235 Stillinger FH, Rahman A. Improved simulation of liquid water by molecular dynamics. *J Chem Phys* 1974; **60**: 1545–1557.

236 Orozco M, Luque FJ. Theoretical Methods for the Description of the Solvent Effect in Biomolecular Systems. *Chem Rev* 2000; **100**: 4187–4226.

237 Tomasi J, Persico M. Molecular Interactions in Solution: An Overview of Methods Based on Continuous Distributions of the Solvent. *Chem Rev* 1994; **94**: 2027–2094.

238 Miertus S, Scrocco E, Tomasi J. Electrostatic interaction of a solute with a continuum. A direct utilizaion of AB initio molecular potentials for the prevision of solvent effects. *Chem Phys* 1981; **55**: 117–129.

239 Klamt A, Schüürmann G. COSMO: A new approach to dielectric screening in solvents with explicit expressions for the screening energy and its gradient. *J Chem Soc Trans 2* 1993; : 799–805.

240 Marenich A V., Cramer CJ, Truhlar DG. Performance of SM6, SM8, and SMD on the SAMPL1 test set for the prediction of small-molecule solvation free energies. *J Phys Chem B* 2009; **113**: 4538–4543.

241 Frediani L, Cammi R, Corni S, Tomasi J. A polarizable continuum model for molecules at diffuse interfaces. *J Chem Phys* 2004; **120**: 3893–907.

242 Marenich A V, Cramer CJ, Truhlar DG. Universal solvation model based on solute electron density and on a continuum model of the solvent defined by the bulk dielectric constant and atomic surface tensions. *J Phys Chem B* 2009; **113**: 6378–96.

243 Barone V, Cossi M, Tomasi J. A New Definition of Cavities for the Computation of Solvation Free Energies by the Polarizable Continuum Model. *J~Chem\ Phys* 1997; **107**: 3210–3221.

244 Zuo C-S, Wiest O, Wu Y-D. Parameterization and validation of solvation corrected atomic radii. *J Phys Chem A* 2009; **113**: 12028–34.

245 Frisch MJ, Trucks GW, Schlegel HB, Scuseria GE, Robb MA, Cheeseman JR *et al.* Gaussian 09, Revision A.2. Gaussian Inc Wallingford CT. 2009; **34**: Wallingford CT.

246 Tuckerman ME. *Statistical Mechanics: Theory and Molecular Simulation.* 2010.

247 Verlet L. Computer 'experiments' on classical fluids. I. Thermodynamical properties of Lennard-Jones molecules. *Phys Rev* 1967; **159**: 98–103.

248 Hockney RW. The potential calculation and some applications. *Methods Comput Phys* 1970; 135–211.

249 Car R, Parrinello M. Unified approach for molecular dynamics and density-functional theory. *Phys Rev Lett* 1985.

250 Kühne TD. Second generation Car-Parrinello molecular dynamics. *Wiley Interdiscip Rev Comput Mol Sci* 2014; **4**: 391–406.

251 Beard DA, Qian H. *Chemical Biophysics: Quantitative Analysis of Cellular Systems*. Cambridge University Press, 2008.

252 Nose S. A unified formulation of the constant temperature molecular dynamics methods. *J Chem Phys* 1984; **81**: 511.

253 Hoover WG. Canonical dynamics: Equilibrium phase-space distributions. *Phys Rev*

A 1985; **31**: 1695–1697.

254 http://www.rcsb.org. http://www.rcsb.org. 2016.

255 Berman HM, Westbrook J, Feng Z, Gilliland G, Bhat TN, Weissig H *et al.* The Protein Data Bank. Nucleic Acids Res. 2000; **28**: 235–242.

256 The UniProt Consortium. The Universal Protein Resource (UniProt) in 2010. *Nucleic Acids Res* 2010; **38**: D142-8.

257 Blundell TL, Sibanda BL, Sternberg MJ, Thornton JM. Knowledge-based prediction of protein structures and the design of novel molecules. *Nature* 1987; **326**: 347–352.

258 Johnson MS, Srinivasan N, Sowdhamini R, Blundell TL. Knowledge-based protein modeling. *Crit Rev Biochem Mol Biol* 1994; **29**: 1–68.

259 Bajorath J, Aruffo A. Three-Dimensional Protein Models: Insights into Structure, Function, and Molecular Interactions. *Bioconjug Chem* 1994; **5**: 173–181.

260 Šali A. Modelling mutations and homologous proteins. *Curr Opin Biotechnol* 1995; **6**: 437–451.

261 Chothia C, Lesk a M. The relation between the divergence of sequence and structure in proteins. *EMBO J* 1986; **5**: 823–826.

262 Sánchez R, Sali A. Advances in comparative protein-structure modelling. *Curr Opin Struct Biol* 1997; **7**: 206–14.

263 Kiefer F, Arnold K, Kuenzli M, Bordoli L, Schwede T. The SWISS-MODEL Repository and associated resources. *Nucleic Acids Res* 2009; **37**.

264 Sutcliffe MJ, Haneef I, Carney D, Blundell TL. Knowledge based modelling of homologous proteins, Part I: Three-dimensional frameworks derived from the simultaneous superposition of multiple structures. *Protein Eng* 1987; **1**: 377–384.

265 Sutcliffe MJ, Hayes FR, Blundell TL. Knowledge based modelling of homologous proteins, Part II: Rules for the conformations of substituted sidechains. *Protein Eng* 1987; **1**: 385–392.

266 Bates PA, Kelley LA, MacCallum RM, Sternberg MJ. Enhancement of protein

modeling by human intervention in applying the automatic programs 3D-JIGSAW and 3D-PSSM. *Proteins* 2001; **Suppl 5**: 39–46.

267 Sali A, Blundell TL. Comparative protein modelling by satisfaction of spatial restraints. *J Mol Biol* 1993; **234**: 779–815.

268 Snow M. A novel parameterization scheme for energy equations and its use to calculate the structure of protein molecules. *Proteins Struct Funct Bioinforma* 1993.

269 Brocklehurst SM, Perham RN. Prediction of the three-dimensional structures of the biotinylated domain from yeast pyruvate carboxylase and of the lipoylated H-protein from the pea leaf glycine cleavage system: a new automated method for the prediction of protein tertiary structure. *Protein Sci* 1993; **2**: 626–39.

270 Sali a, Overington JP. Derivation of rules for comparative protein modeling from a database of protein structure alignments. *Protein Sci* 1994; **3**: 1582–1596.

271 MacKerell AD, Bashford D, Bellott M, Dunbrack RL, Evanseck JD, Field MJ *et al.* All-atom empirical potential for molecular modeling and dynamics studies of proteins. *J Phys Chem B* 1998; **102**: 3586–616.

272 Hestenes M, Stiefel E. Methods of conjugate gradients for solving linear systems. 1952.

273 Kirkpatrick S, Gelatt CD, Vecchi MP. Optimization by simulated annealing. *Science* 1983; **220**: 671–80.

274 Wilson SR, Cui WL. Applications of simulated annealing to peptides. *Biopolymers* 1990; **29**: 225–35.

275 Tryfos P. Cluster Analysis. In: *Methods for Business Analysis and Forecasting: Text & Cases*. Wiley, 1998.

276 Kelley L, Gardner S, Sutcliffe M. An automated approach for clustering an ensemble of NMR-derived protein structures into conformationally related subfamilies. *Protein Eng* 1996; **9**: 1063–1065.

277 Ali-Torres J. *Estudio Teórico de la Estructura Electrónica y Molecular de Complejos Cu+/2+ y Fe2+/3+ Relevantes en la Enfermedad del Alzheimer*. 2011.

278 Rayner-Canham G, Overton T. Descriptive inorganic chemistry. *Vasa* 2003.

279 Rios-Font R, Sodupe M, Rodríguez-Santiago L, Taylor PR. The role of exact exchange in the description of Cu(2+)-(H(2)O)(n) (n = 1-6) complexes by means of DFT methods. *J Phys Chem A* 2010; **114**: 10857–63.

280 Hay PJ, Wadt WR. Ab initio effective core potentials for molecular calculations. Potentials for K to Au including the outermost core orbitals. *J Chem Phys* 1985; **82**: 299.

281 Roy LE, Hay PJ, Martin RL. Revised Basis Sets for the LANL Effective Core Potentials. *J Chem Theory Comput* 2008; **4**: 1029–1031.

282 Ehlers AW, Böhme M, Dapprich S, Gobbi A, Höllwarth A, Jonas V *et al.* A set of f-polarization functions for pseudo-potential basis sets of the transition metals Sc-Cu, Y-Ag and La-Au. *Chem Phys Lett* 1993; **208**: 111–114.

283 Zirah S, Kozin S a., Mazur AK, Blond A, Cheminant M, Segalas-Milazzo I *et al.* Structural Changes of Region 1-16 of the Alzheimer Disease Amyloid beta-Peptide upon Zinc Binding and in Vitro Aging. *J Biol Chem* 2006; **281**: 2151–2161.

284 Šali A, Webb B, Madhusudhan MS, Shen M-Y, Dong G, Martı-Renom MA *et al.* MODELLER A Program for Protein Structure Modeling 9v11. 2012.

285 Pettersen EF, Goddard TD, Huang CC, Couch GS, Greenblatt DM, Meng EC *et al.* UCSF Chimera--a visualization system for exploratory research and analysis. *J Comput Chem* 2004; **25**: 1605–1612.

286 Ali-Torres J, Dannenberg JJ. The folding of acetyl(Ala)28NH2 and acetyl(Ala) 40NH2 extended strand peptides into antiparallel β-sheets. a density functional theory study of β-sheets with β-turns. *J Phys Chem B* 2012; **116**: 14017–14022.

287 Himes RA, Ga YP, Barry AN, Blackburn NJ, Karlin KD. Synthesis and x-ray absorption spectroscopy structural studies of Cu(I) complexes of HistidylHistidine peptides: The predominance of linear 2-coordinate geometry. *J Am Chem Soc* 2007; **129**: 5352–5353.

288 Peck KL, Clewett HS, Schmitt JC, Shearer J. Copper ligation to soluble oligomers of

the English mutant of the amyloid-β peptide yields a linear Cu(I) site that is resistant to O2 oxidation. *Chem Commun (Camb)* 2013; **49**: 4797–9.

289 Cassagnes LE, Herve V, Nepveu F, Hureau C, Faller P, Collin F. The catalytically active copper-amyloid-beta state: Coordination site responsible for reactive oxygen species production. *Angew Chemie - Int Ed* 2013; **52**: 11110–11113.

290 Shearer J, Szalai VA. The amyloid-beta peptide of Alzheimer's disease binds cu 1 in a linear bis-his coordination environment: Insight into a possible neuroprotective mechanism for the amyloid-beta peptide. *J Am Chem Soc* 2008; **130**: 17826–17835.

291 Balland V, Hureau C, Savéant J-M. Electrochemical and homogeneous electron transfers to the Alzheimer amyloid-beta copper complex follow a preorganization mechanism. *Proc Natl Acad Sci U S A* 2010; **107**: 17113–17118.

292 Wagemann DD, Evans WH, Parker VB, Schumm RH, Halow I, Baily SM *et al.* The NBS tables of chemical thermodynamic properties: selected values for inorganic and C1 and C2 organic substances in SI units. *J Phys Chem Ref Data* 1982; **11 Supplem**: 1–392.

293 Bard AJ, Parsons R, Jordan J. *Standard Potentials in Aqueous Solution*. New York, 1985.

294 VandeVondele J, Krack M, Mohamed F, Parrinello M, Chassaing T, Hutter J. Quickstep: Fast and accurate density functional calculations using a mixed Gaussian and plane waves approach. *Comput Phys Commun* 2005; **167**: 103–128.

295 VandeVondele J, Hutter J. Gaussian basis sets for accurate calculations on molecular systems in gas and condensed phases. *J Chem Phys* 2007; **127**: 114105.

296 Blöchl PE. Electrostatic decoupling of periodic images of plane-wave-expanded densities and derived atomic point charges. *J Chem Phys* 1995; **103**: 7422.

297 Goedecker S, Teter M, Hutter J. Separable dual-space Gaussian pseudopotentials. *Phys Rev B* 1996; **54**: 1703–1710.

298 Hartwigsen C, Goedecker S, Hutter J. Relativistic separable dual-space Gaussian pseudopotentials from H to Rn. *Phys Rev B* 1998; **58**: 3641–3662.

299 Krack M. Pseudopotentials for H to Kr optimized for gradient-corrected exchange-correlation functionals. *Theor Chem Acc* 2005; **114**: 145–152.

300 VandeVondele J, Hutter J. An efficient orbital transformation method for electronic structure calculations. *J Chem Phys* 2003; **118**: 4365.

301 Laino T, Mohamed F, Laio A, Parrinello M. An Efficient Real Space Multigrid QM/MM Electrostatic Coupling. *J Chem Theory Comput* 2005; **1**: 1176–84.

302 Laino T, Mohamed F, Laio A, Parrinello M. An Efficient Linear-Scaling Electrostatic Coupling for Treating Periodic Boundary Conditions in QM/MM Simulations. *J Chem Theory Comput* 2006; **2**: 1370–8.

303 Himes RA, Park GY, Siluvai GS, Blackburn NJ, Karlin KD. Structural studies of copper(I) complexes of amyloid-beta peptide fragments: Formation of two-coordinate bis(histidine) complexes. *Angew Chemie - Int Ed* 2008; **47**: 9084–9087.

304 Raffa DF, Rickard GA, Rauk A. Ab initio modelling of the structure and redox behaviour of copper(I) bound to a His-His model peptide: Relevance to the ??-amyloid peptide of Alzheimer's disease. *J Biol Inorg Chem* 2007; **12**: 147–164.

305 Furlan S, Hureau C, Faller P, La Penna G. Modeling the Cu+ binding in the 1-16 region of the amyloid-β peptide involved in Alzheimer's disease. *J Phys Chem B* 2010; **114**: 15119–33.

306 Dryhurst G, Kadish KM, ScHeller F, Renneberg R. *Biological Electrochemistry*. Academic Press: New York, 1982.

307 Wallace D. Diseases of the mitochondrial DNA. *Annu Rev Biochem* 1992.

308 Conway BE. *Electrochemical data*. Greenwood Press: Wesport, CT, 1969.

309 Parthasarathy S, Yoo B, McElheny D, Tay W, Ishii Y. Capturing a reactive state of amyloid aggregates: NMR-based characterization of copper-bound Alzheimer disease amyloid β-fibrils in a redox cycle. *J Biol Chem* 2014; **289**: 9998–10010.

310 Reybier K, Ayala S, Alies B, Rodrigues J V., Bustos Rodriguez S, La Penna G *et al.* Free Superoxide is an Intermediate in the Production of H2O2 by Copper(I)-Aβ Peptide and O2. *Angew Chemie Int Ed* 2015; **55**: 1085–1089.

311 La Penna G, Hureau C, Andreussi O, Faller P. Identifying, by first-principles simulations, Cu[Amyloid-β] species making Fenton-type reactions in Alzheimer's disease. *J Phys Chem B* 2013; **117**: 16455–16467.

312 Kramida A. National Institute of Standards and Technology. At. Spectrosc. Gr. 2003.

313 Ervin KM, Anusiewicz I, Skurski P, Simons J, Lineberger WC. The Only Stable State of O 2 - Is the X 2 Π g Ground State and It (Still!) Has an Adiabatic Electron Detachment Energy of 0.45 eV. *J Phys Chem A* 2003; **107**: 8521–8529.

314 Steinmann SN, Piemontesi C, Delachat A, Corminboeuf C. Why are the Interaction Energies of Charge-Transfer Complexes Challenging for DFT? *J Chem Theory Comput* 2012; **8**: 1629–40.

315 National Institut of Standards and Technology. U.S. Dep. Commer. 2013.http://cccbdb.nist.gov/exp2.asp.

316 Peters T. Interaction of one mole of copper with the alpha amino group of bovine serum albumin. *Biochim Biophys Acta* 1960; **39**: 546–547.

317 Peters T, Blumenstock FA. Copper-binding properties of bovine serum albumin and its amino-terminal peptide fragment. *J Biol Chem* 1967; **242**: 1574–8.

318 Appleton DW, Sarkar B. The absence of specific copper (II)-binding site in dog albumin. A comparative study of human and dog albumins. *J Biol Chem* 1971; **246**: 5040–6.

319 Neupane KP, Aldous AR, Kritzer JA. Metal-binding and redox properties of substituted linear and cyclic ATCUN motifs. *J Inorg Biochem* 2014; **139**: 65–76.

320 Mena S. *Entendiendo las propiedades redox de complejos CuII-péptido involucrados en la enfermedad del Alzheimer*. 2016.

ARTICLES DERIVED FROM THIS THESIS

Chapter 4: Alí-Torres, J.; Mirats, A.; Maréchal, J-D.; Rodríguez-Santiago, L.; Sodupe, M. Modeling Cu^{2+}-Aβ complexes from computational approaches. *AIP Adv* 2015; **5**. doi:10.1063/1.4921072.

Chapter 4 and 5: Alí-Torres, J.; Mirats, A.; Maréchal, J-D.; Rodríguez-Santiago, L.; Sodupe, M. 3D Structures and Redox Potentials of Cu(2+)-Aβ(1-16) Complexes at Different pH: A Computational Study. *J Phys Chem B* 2014; **118**: 4840–50.

Chapter 5 and 6: Mirats, A.; Alí-Torres, J.; Rodríguez-Santiago, L.; Sodupe, M. Stability of transient Cu+Aβ (1–16) species and influence of coordination and peptide configuration on superoxide formation. *Theor Chem Acc* 2016; **135**: 75.

Chapter 6: Mirats, A.; Alí-Torres, J.; Rodríguez-Santiago, L.; Sodupe, M.; La Penna, G. Dioxygen activation in the Cu–amyloid b complex. *Phys Chem Chem Phys* 2015; **17**: 27270–27274.

Chapter 7: This article is in progress.

APPENDIX A. FURTHER DETAILS ON 3D Cu^{2+}-Aβ_{1-16} STRUCTURES

Further detail on the building of the 3D Cu^{2+}-Aβ_{1-16} structures for both model systems and the entire Cu^{2+}-Aβ_{1-16} complexes.

A.1. MODEL SYSTEMS

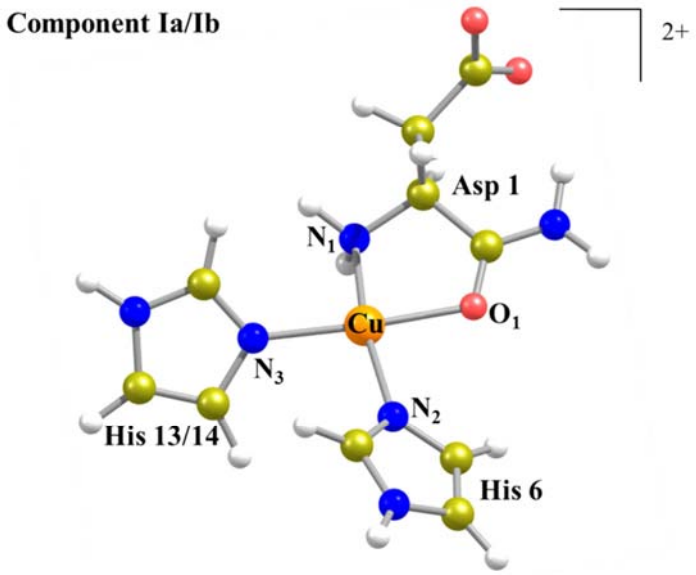

	*Distances** (Å)				*Angles** (º)					
	d_1	d_2	d_3	d_4	θ_1	θ_2	θ_3	θ_4	θ_5	θ_6
M06-L	2.04 (2.04)	2.03 (2.05)	2.00 (1.99)	2.02 (2.01)	79.9 (79.2)	91.1 (90.8)	93.1 (93.9)	95.8 (96.1)	170.8 (169.9)	174.2 (173.7)
M06	2.03 (2.02)	2.00 (2.04)	2.00 (1.98)	2.00 (1.99)	80.6 (80.0)	90.9 (90.8)	94.4 (93.9)	94.3 (95.3)	171.3 (170.6)	172.4 (174.6)
M06-2X	2.06 (2.07)	2.01 (2.04)	2.03 (2.03)	2.04 (2.03)	80.6 (79.7)	90.9 (90.6)	94.4 (94.2)	94.1 (95.3)	170.2 (168.7)	170.4 (174.7)

*d_1 corresponds to the distance formed by N_1-Cu; d_2: O_1-Cu; d_3: N_2-Cu; d_4: N_3-Cu; d_5: O_2-Cu; θ_1 corresponds to the angle formed by N_1-Cu-O_1; θ_2: O_1-Cu-N_2; θ_3: N_2-Cu-N_3; θ_4: N_3-Cu-N_1; θ_5: N_1-Cu-N_2 and θ_6: O_1-Cu-N_3

Figure A1. Optimized geometries with the M06 functional family and the SB_1 basis set. In parenthesis, there are the obtained LB basis set values.

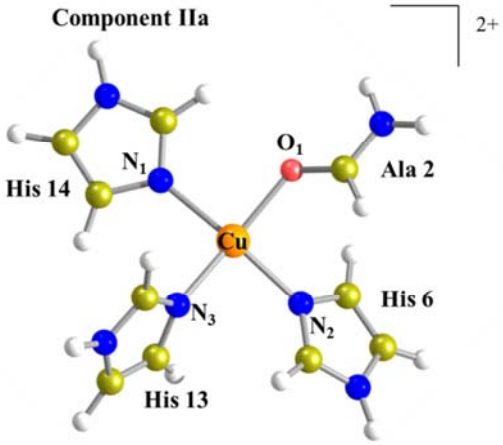

	*Distances** (Å)				*Angles** (º)					
	d_1	d_2	d_3	d_4	θ_1	θ_2	θ_3	θ_4	θ_5	θ_6
M06-L	2.02 (1.99)	2.03 (2.03)	2.02 (1.99)	2.03 (2.00)	88.3 (88.9)	89.4 (90.1)	91.1 (93.2)	90.5 (91.0)	175.6 (164.9)	177.9 (167.8)
M06	2.01 (1.99)	2.02 (2.03)	2.01 (1.99)	2.01 (2.00)	88.9 (88.8)	90.5 (90.1)	93.0 (93.2)	90.6 (91.0)	164.4 (164.9)	168.6 (167.8)
M06-2X	2.05 (1.99)	2.04 (2.03)	2.05 (1.99)	2.05 (2.00)	89.3 (88.9)	91.1 (90.1)	92.5 (93.2)	91.2 (91.0)	160.8 (164.9)	164.7 (167.8)

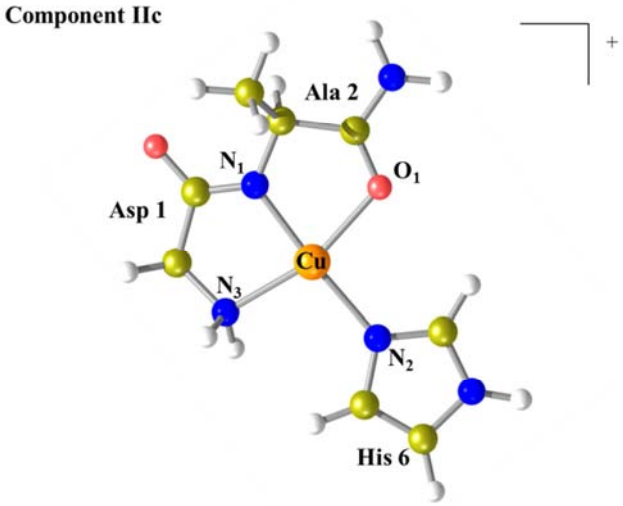

	*Distances** (Å)				*Angles** (º)					
	d_1	d_2	d_3	d_4	θ_1	θ_2	θ_3	θ_4	θ_5	θ_6
M06-L	1.92 (1.92)	2.08 (2.08)	2.00 (1.99)	2.08 (2.08)	81.1 (80.8)	96.7 (96.8)	100.6 (100.6)	81.6 (82.0)	175.9 (175.9)	162.5 (162.7)
M06	1.90 (1.91)	2.07 (2.07)	1.97 (1.97)	2.06 (2.06)	81.7 (81.2)	96.7 (96.9)	98.8 (99.0)	82.8 (82.9)	177.2 (178.0)	163.9 (163.8)
M06-2X	1.94 (1.95)	2.08 (2.07)	2.02 (2.01)	2.11 (2.10)	81.1 (80.4)	96.0 (96.5)	100.7 (100.9)	82.1 (82.0)	174.2 (174.3)	162.0 (162.3)

*d_1 corresponds to the distance formed by N_1-Cu; d_2: O_1-Cu; d_3: N_2-Cu; d_4: N_3-Cu; θ_1 corresponds to the angle formed by N_1-Cu-O_1; θ_2: O_1-Cu-N_2; θ_3: N_2-Cu-N_3; θ_4: N_3-Cu-N_1; θ_5: N_1-Cu-N_2 and θ_6: O_1-Cu-N_3

Figure A1. Continuation.

A.2. COMPUTATIONAL DETAILS

Table A1. Representative structure evaluation of the most populated clusters for component Ia and Ib. Cluster column reflects the element numbers of a cluster and, in parenthesis, the most representative structure of such cluster. *Refers to the *loop* refinement. The energies are in kcal·mol^{-1}.

	Cluster	E_{CHARMM}	E_{DOPE}
Structure	**Component Ia**		
δε	**167(405)**	**259.7**	**-585.2**
	121(308)	246.9	-553.4
	88(285)	398.2	-520.4
	28(447)	393.9	-519.5
δε*	36(41)	24.0	-653.6
	16(14)	**35.6**	**-689.6**
	13(39)	38.3	-623.6
εδ	**238(496)**	**273.9**	**-617.2**
	69(180)	429.9	-550.2
	53(499)	264.6	-512.1
	24(279)	401.6	-430.2
εδ*	**21(90)**	**15.9**	**-693.1**
	15(48)	39.4	-667.5
	10(51)	9.2	-647.8
εε	**220(384)**	**222.7**	**-659.1**
	57(413)	368.2	-522.1
	39(388)	358.4	-503.3
	36(176)	375.9	-546.1
	33(261)	231.7	-504.3
	26(58)	379.2	-554.8
εε*	**17(52)**	**26.3**	**-694.3**
	14(32)	10.7	-686.5
	11(56)	34.7	-647.1
	11(46)	12.6	-660.5
	11(51)	16.3	-641.9

	Cluster	E_{CHARMM}	E_{DOPE}
Structure	**Component Ib**		
δδ	**272(177)**	**204,1**	**-651,2**
	94(436)	371,1	-516,7
	27(498)	405,5	-425,6
	20(245)	415,7	-565,1
δδ*	18(20)	25,8	-596,2
	16(34)	**32,7**	**-672,3**
	16(17)	31,6	-656,7
δε	**253(460)**	**188,5**	**-657,3**
	70(9)	309,2	-517,4
	52(279)	317,8	-493,8
	31(450)	421,7	-556,3
	25(432)	403,8	-432,5
	20(472)	238,3	-595,1
δε*	23(99)	42,5	-613,1
	10(72)	**13,2**	**-713,0**
	9(85)	460,7	-296,2
	9(74)	40,3	-595,3
εδ	**130(88)**	**230,0**	**-625,2**
	78(5)	432,7	-450
	50(67)	459,0	-514,9
	42(142)	467,3	-563,0
	33(464)	246,2	-581,9
	26(409)	374,7	-555,4
εδ*	**21(88)**	**53,6**	**-570,2**
	12(71)	40,6	-542,2
	12(81)	49,1	-539,4
εε	205(251)	338,7	-619,1
	163(217)	**221,7**	**-622,3**
	17(180)	342,6	-494,5
εε*	27(100)	26,8	-631,6
	16(62)	**36,5**	**-639,2**
	15(40)	32,1	-576,9

Table A2. Representative structure evaluation of the most populated clusters for component IIc. Cluster column reflects the element numbers of a cluster and, in parenthesis, the most representative structure of such cluster. *Refers to the *loop* refinement. The energies are in kcal·mol^{-1}.

	Cluster	E_{CHARMM}	E_{DOPE}
Structure	**Component IIc**		
δ	192 (485)	220,3	-613,0
	131(106)	244,5	-630,6
	61(121)	235,5	-597,9
	20(416)	**369,1**	**-751,3**
δ*	**23(1)**	**29,5**	**-690,5**
	20(94)	42,2	-561,2
	7(82)	29,6	-579,5
ε	202(351)	221,1	-566,7
	40(52)	**242,8**	**-630,2**
	40(308)	204,1	-597,2
	21(420)	225,5	-605,9
	17(270)	212,3	-621,4
ε*	34(44)	27,0	-562,3
	13(78)	**37,9**	**-662,8**
	10(36)	34,8	-631,7

A.3. Cu^{2+}-$A\beta_{1-16}$ COMPLEXES

Structure $Ia_{\delta\delta}$

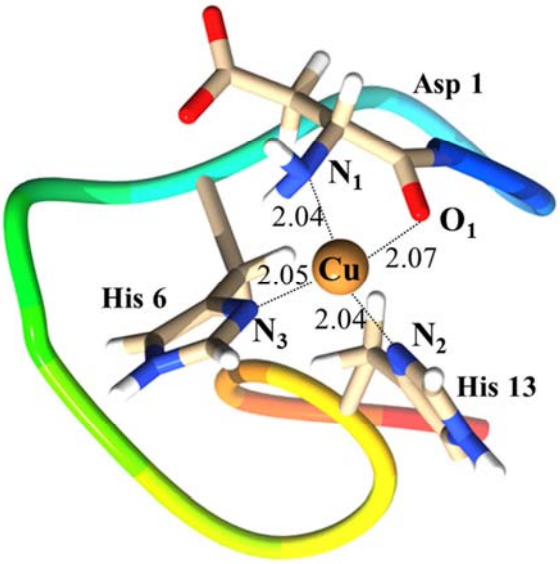

N_1-Cu-N_2: 168.0, **O_1-Cu-N_3:** 151.5
Σα: 362.5

Structure $Ia_{\delta\varepsilon}$

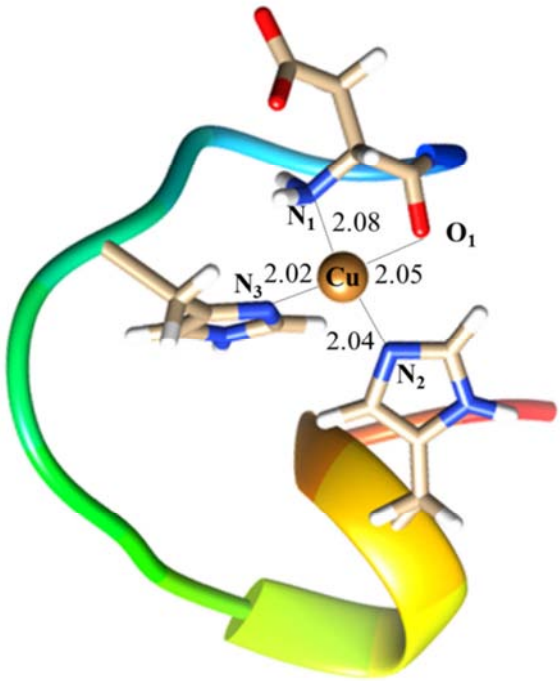

N_1-Cu-N_2: 169.4, **O_1-Cu-N_3:** 151.0
Σα: 360.5

Structure $Ia_{\varepsilon\delta}$

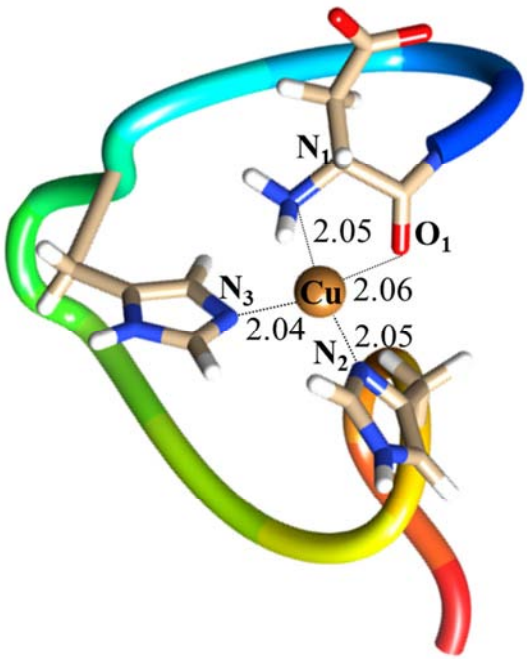

N_1-Cu-N_2: 153.0, **O_1-Cu-N_3:** 163.9
Σα: 363.3

Structure $Ia_{\varepsilon\varepsilon}$

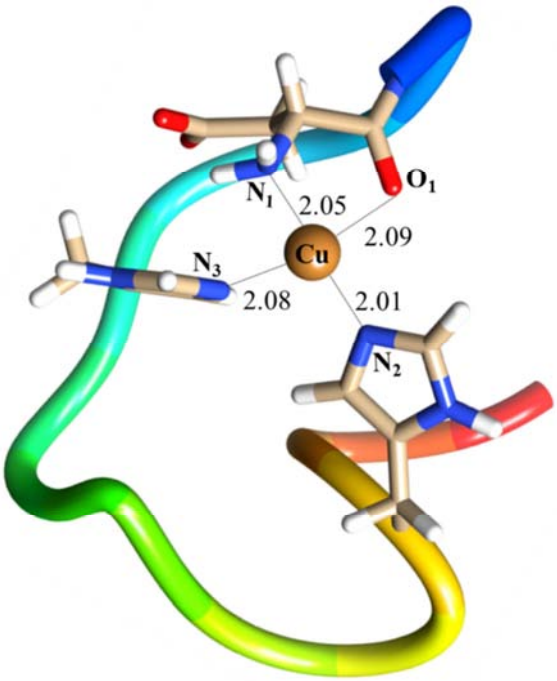

N_1-Cu-N_2: 168.1, **O_1-Cu-N_3:** 154.7
Σα: 363.6

Figure A2. Geometric details of the most representative structures for the different configurations of component Ia. Distances are in angstroms and angles in degrees. Σα means the sum of all the angles around Cu.

Structure Ib$_{\delta\delta}$

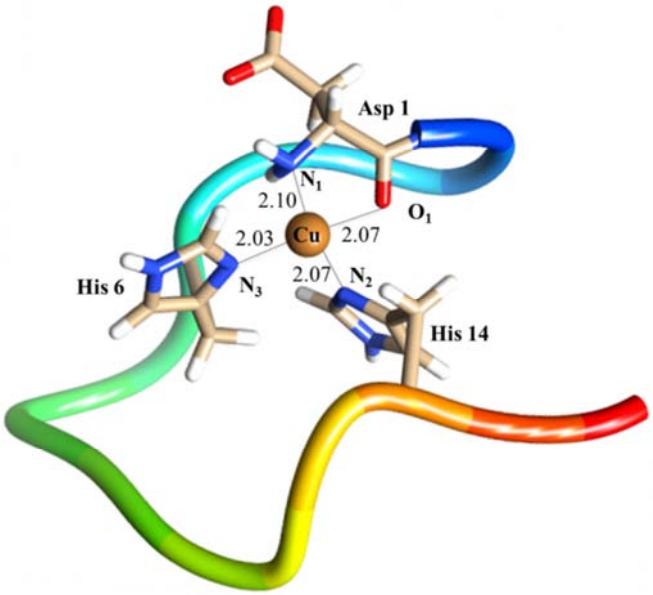

N_1-Cu-N_2: 164.7, **O_1-Cu-N_3:** 164.9
Σα: 360.0

Structure Ib$_{\delta\varepsilon}$

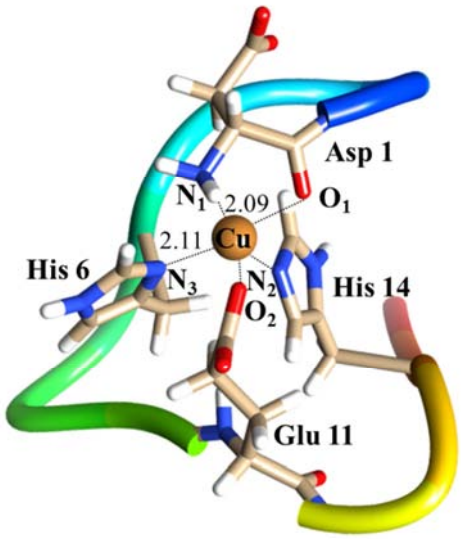

O_1-Cu: 2.08, **N_2-Cu:** 2.05, **O_2-Cu:** 2.19
N_1-Cu-N_2: 156.6, **O_1-Cu-N_3:** 167.5
Σα: 356.8

Structure Ib$_{\varepsilon\delta}$

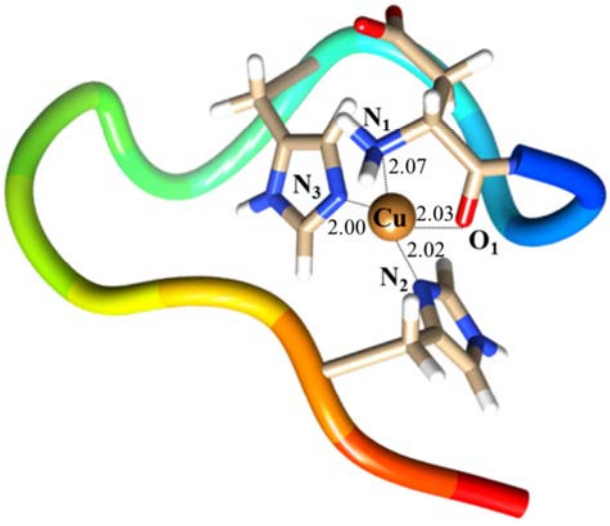

N_1-Cu-N_2: 163.8, **O_1-Cu-N_3:** 160.8
Σα: 361.4

Structure Ib$_{\varepsilon\varepsilon}$

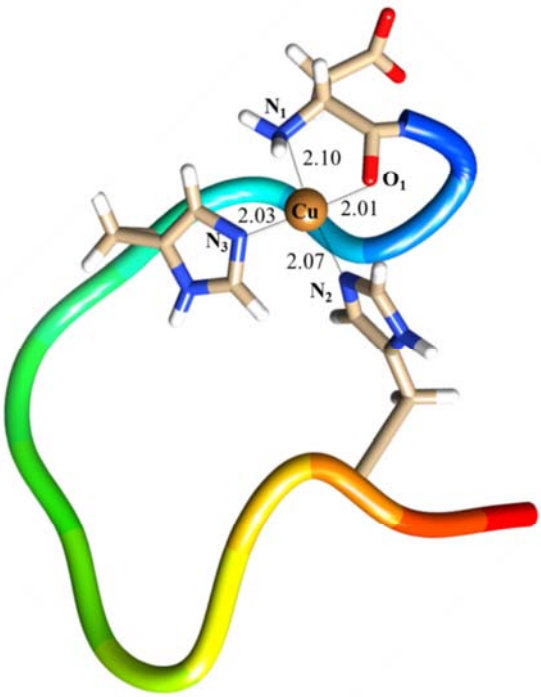

N_1-Cu-N_2: 163.4, **O_1-Cu-N_3:** 175.0
Σα: 359.8

Figure A3. Geometric details of the most representative structures for the different configurations of component Ib. Distances are in angstroms and angles in degrees. Σα means the sum of all the angles around Cu.

Structure IIa$_{\delta\delta\delta}$

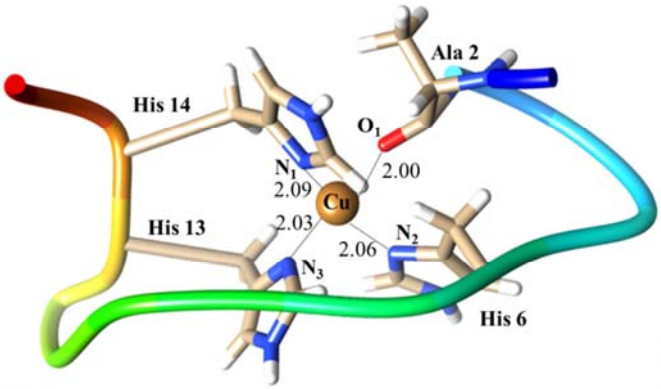

N_1-Cu-N_2: 143.7, **O_1-Cu-N_3:** 169.6
Σα: 365.4

Structure IIa$_{\delta\delta\varepsilon}$

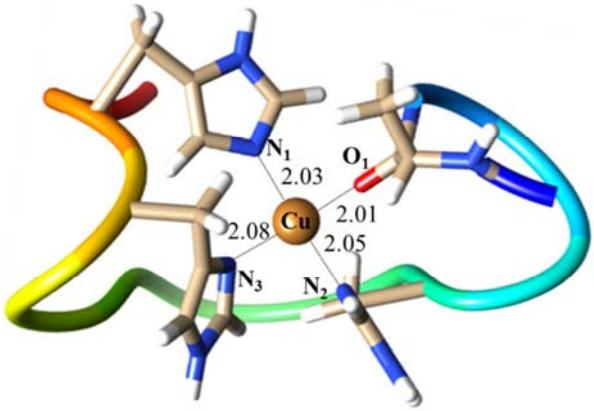

N_1-Cu-N_2: 174.8, **O_1-Cu-N_3:** 176.4
Σα: 359.9

Structure IIa$_{\delta\varepsilon\delta}$

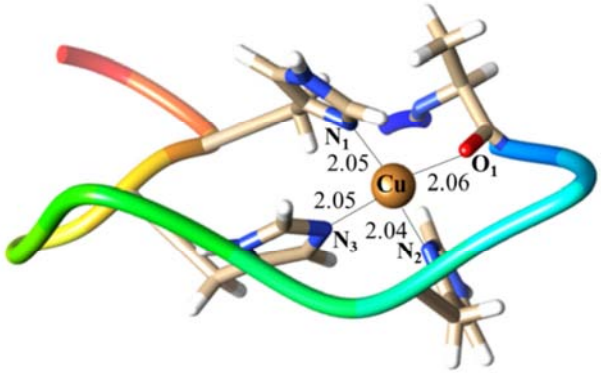

N_1-Cu-N_2: 174.2, **O_1-Cu-N_3:** 174.2
Σα: 360.1

Structure IIa$_{\delta\varepsilon\varepsilon}$

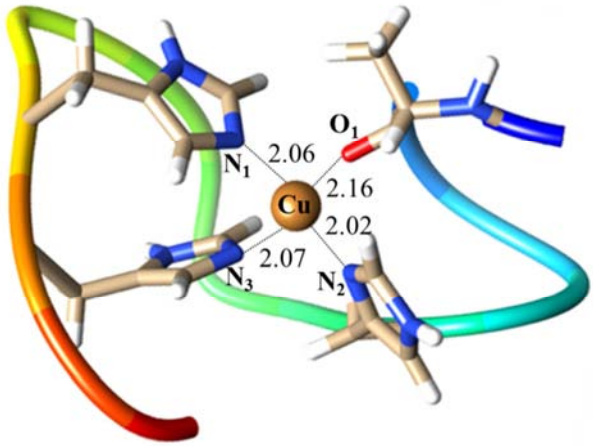

N_1-Cu-N_2: 156.9, **O_1-Cu-N_3:** 109.7
Σα: 385.8

Figure A4. Geometric details of the most representative structures for the different configurations of component IIa. Distances are in angstroms and angles in degrees. Σα means the sum of all the angles around Cu.

Structure IIa$_{\varepsilon\delta\delta}$

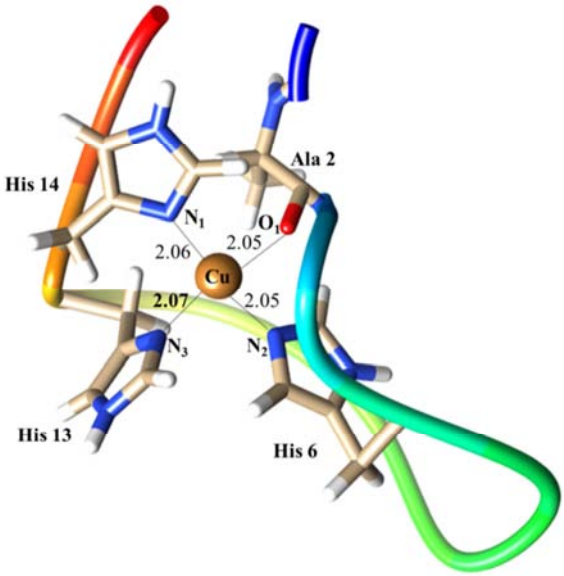

N_1-Cu-N_2: 167.3, **O_1-Cu-N_3:** 169.9
Σα: 365.3

Structure IIa$_{\varepsilon\delta\varepsilon}$

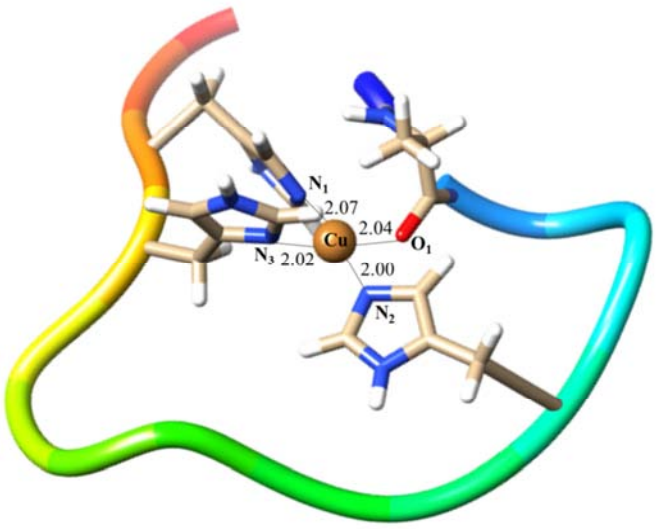

N_1-Cu-N_2: 174.4, **O_1-Cu-N_3:** 166.6
Σα: 361.3

Structure IIa$_{\varepsilon\varepsilon\delta}$

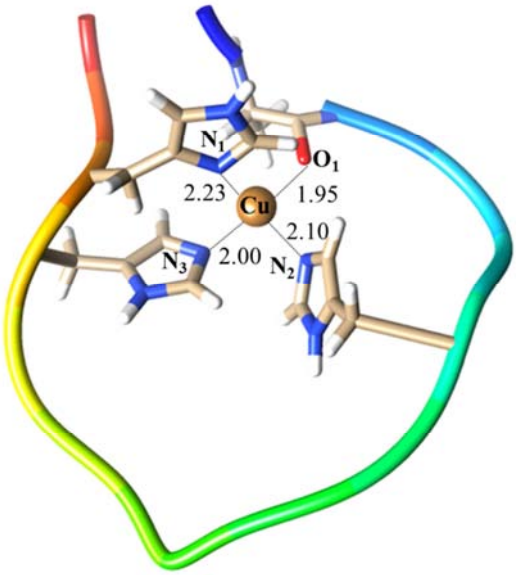

N_1-Cu-N_2: 119.8, **O_1-Cu-N_3:** 161.2
Σα: 378.6

Structure IIa$_{\varepsilon\varepsilon\varepsilon}$

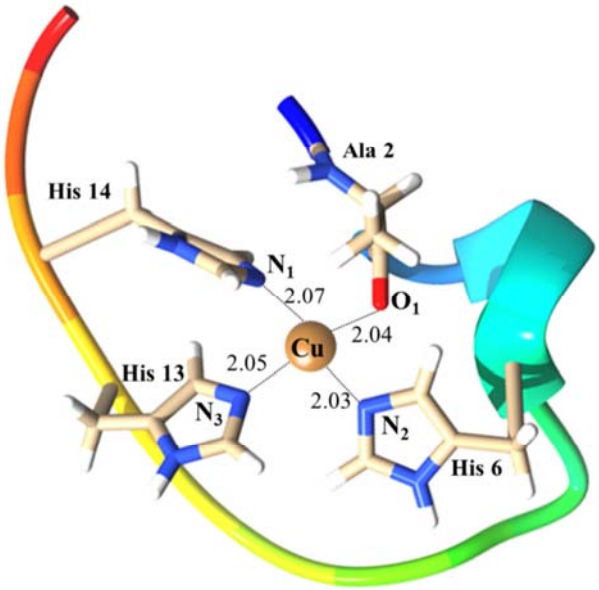

N_1-Cu-N_2: 165.2, **O_1-Cu-N_3:** 165.2
Σα: 364.8

Figure A4. Continuation.

Structure IIc$_\delta$

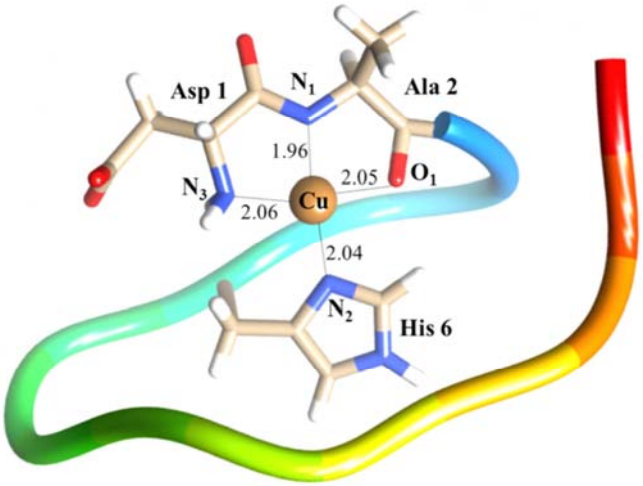

N_1-Cu-N_2: 169.6, **O_1-Cu-N_3:** 162.3
Σα: 359.7

Structure IIc$_\varepsilon$

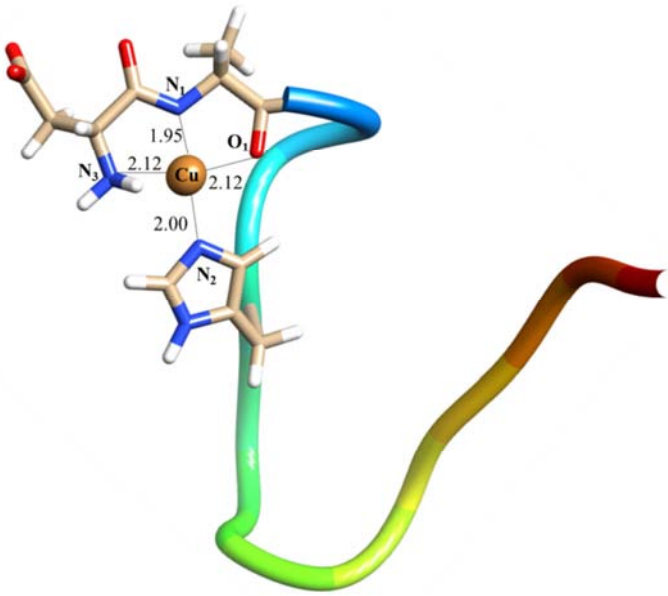

N_1-Cu-N_2: 174.6, **O_1-Cu-N_3:** 162.0
Σα: 362.4

Figure A5. Geometric details of the most representative structures for the different configurations of component IIc. Distances are in angstroms and angles in degrees. Σα means the sum of all the angles around Cu.

A.4. INFRARED SPECTRA

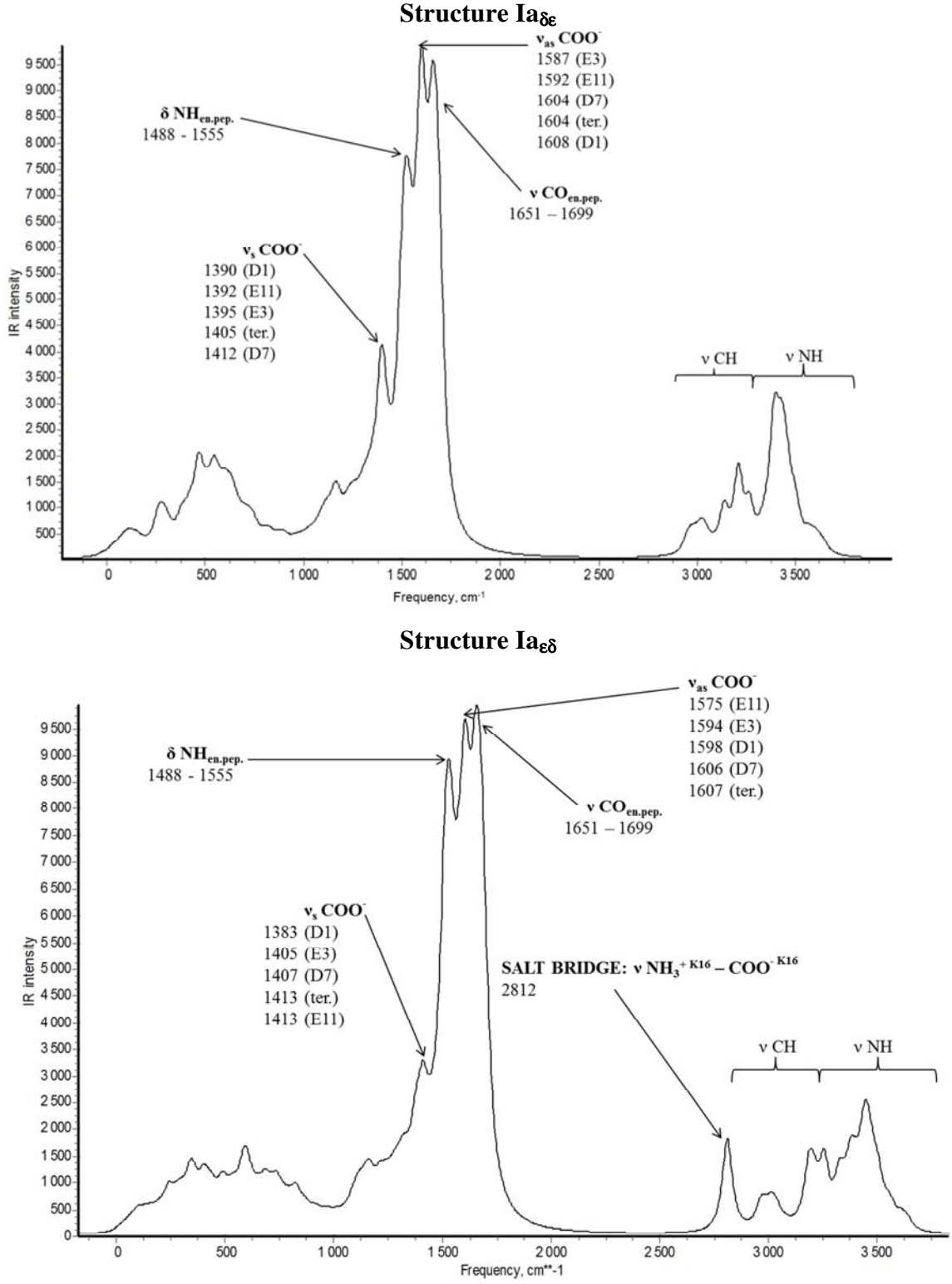

Figure A6. IR spectra of the less stable conformations of components Ia and Ib.

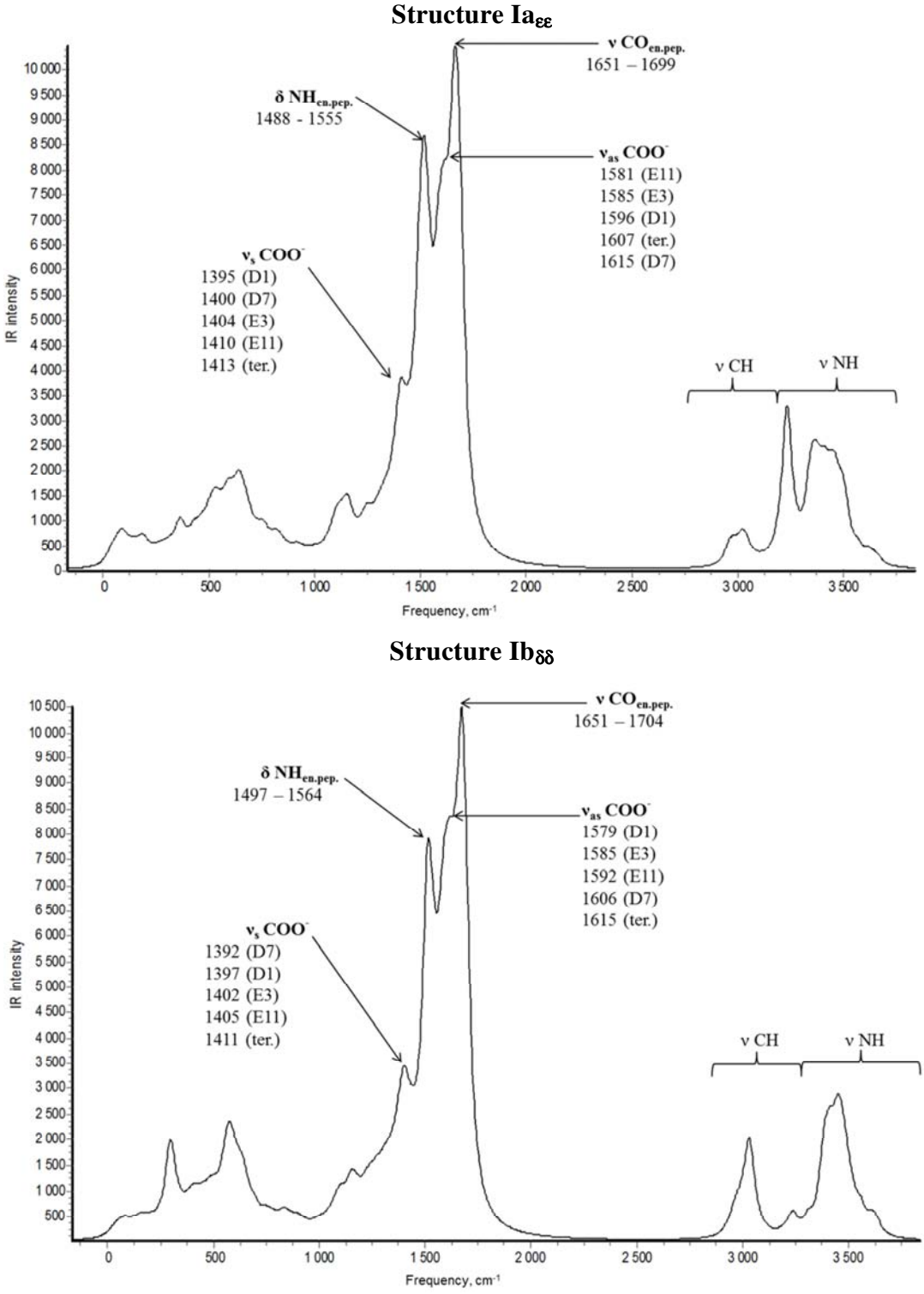

Figure A6. Continued.

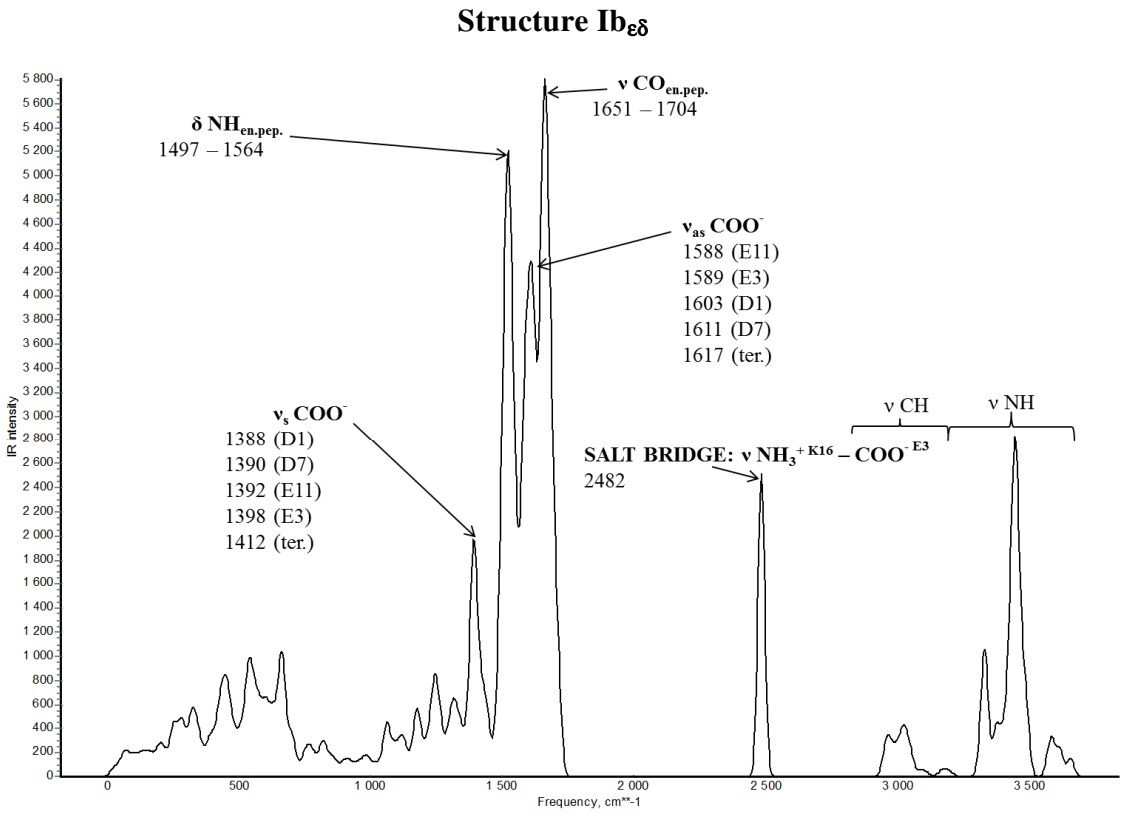

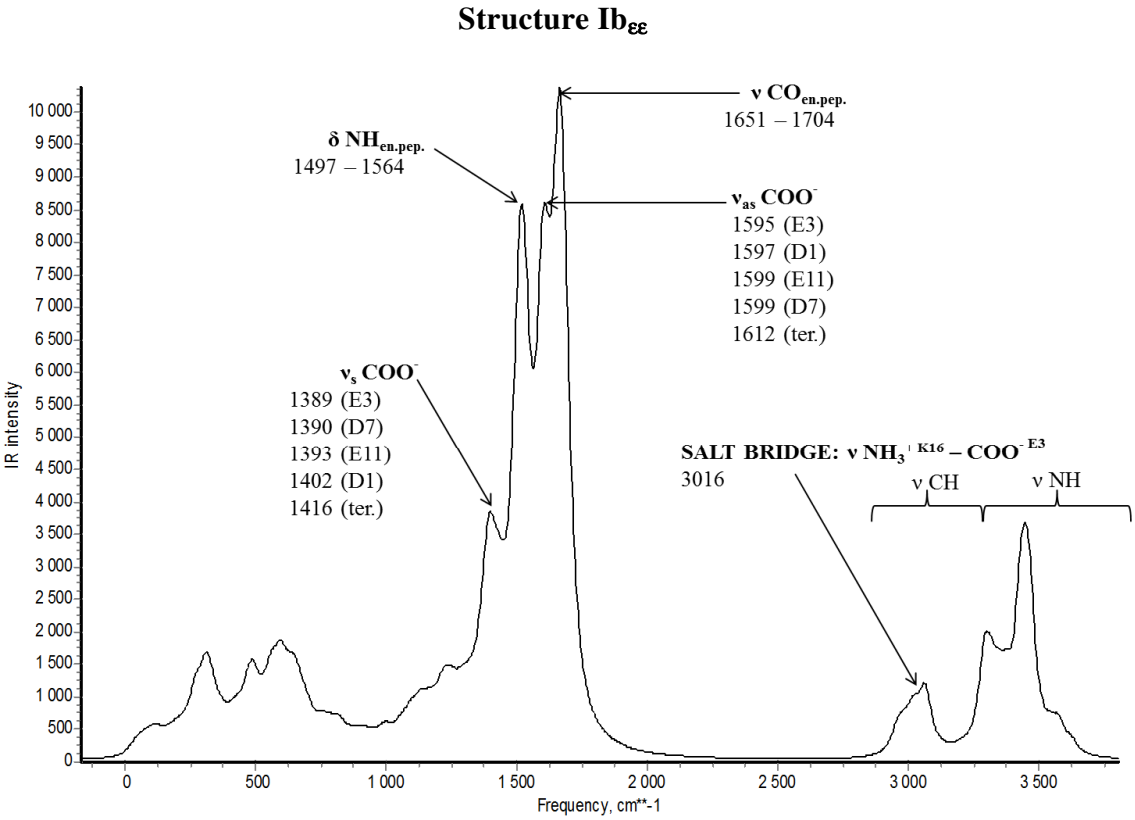

Figure A6. Continued.

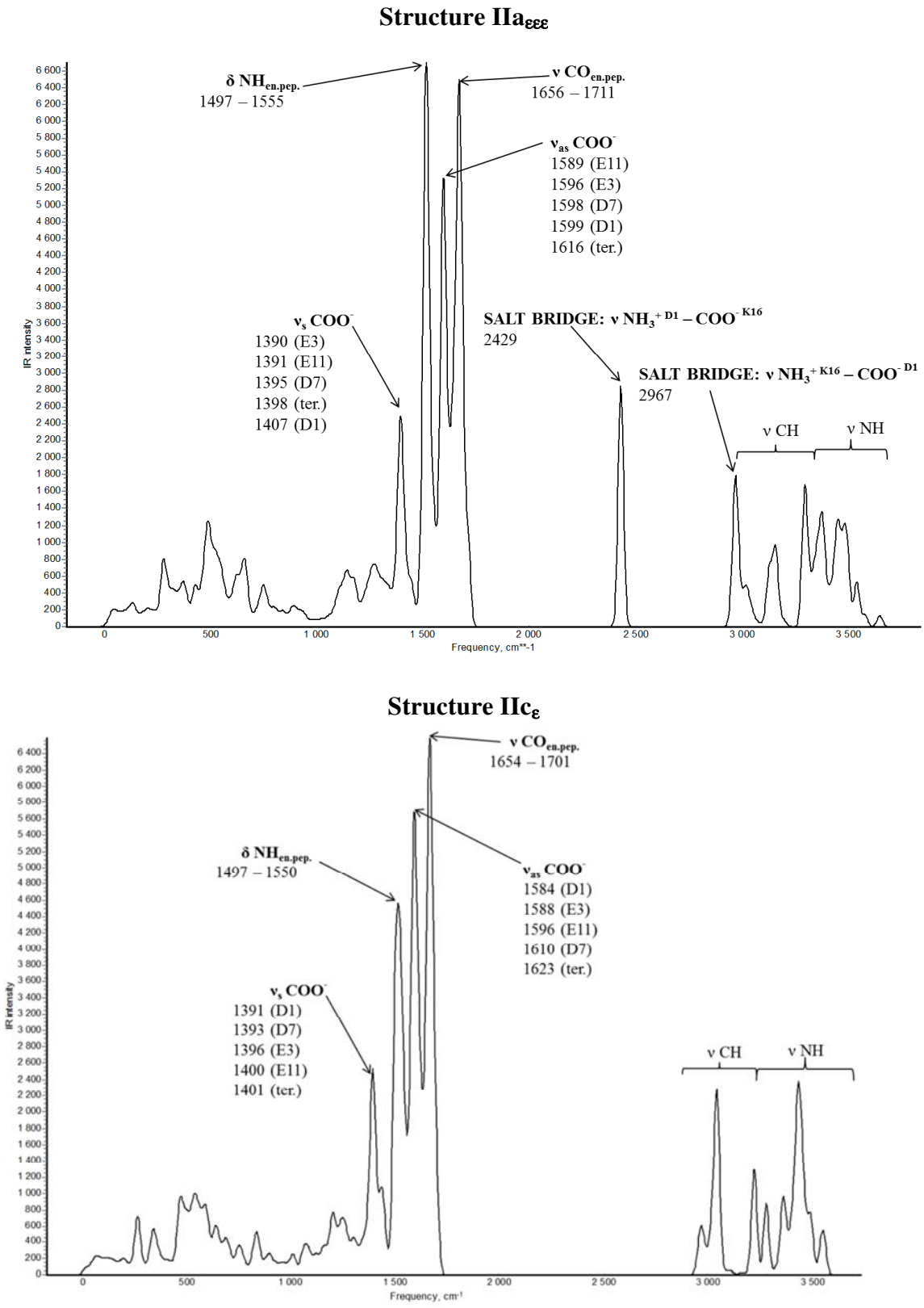

Figure A7. IR spectra of the less stable conformations of components IIa and IIc.

APPENDIX B. FURTHER DETAILS ON O_2 ACTIVATION

Further detail on the description of model systems interacting with O_2.

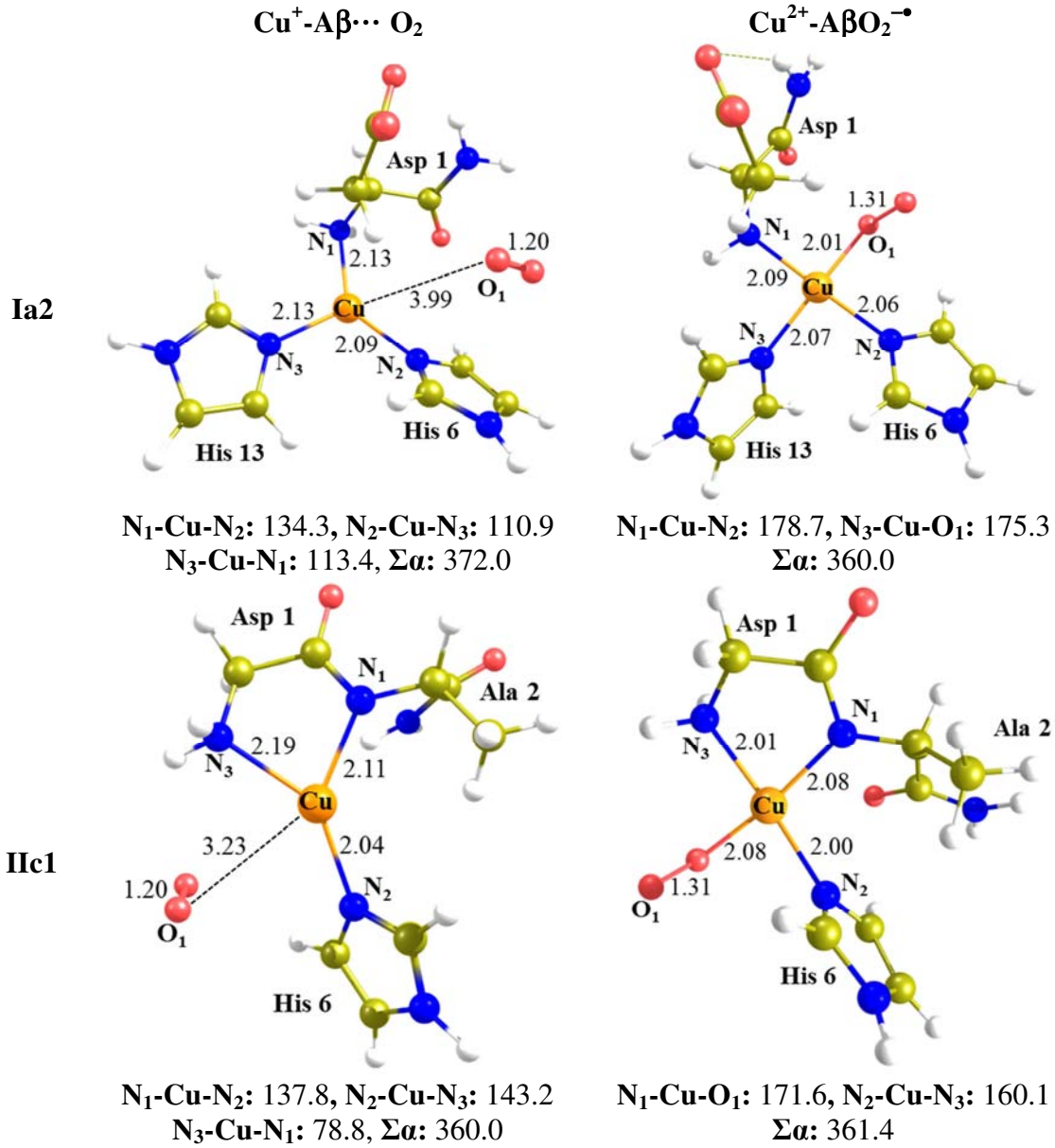

Figure B1. Geometric parameters for Cu^{+}-Aβ···O_2 and Cu^{2+}-A$\beta O_2^{-\bullet}$ species of the considered model systems.

	Cu^{+}-Aβ··· O_2	Cu^{2+}-A$\beta O_2^{-\bullet}$
1	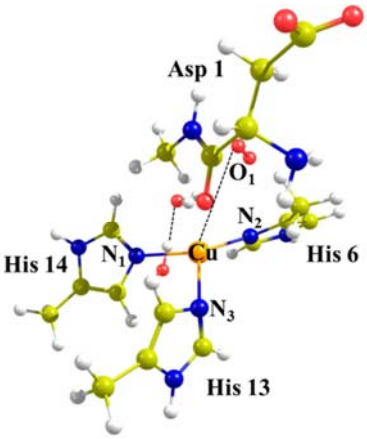	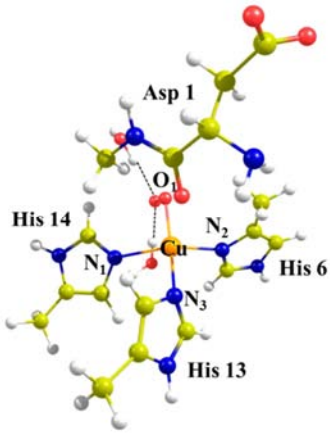

Distances (Å)*					
d_1	d_2	d_3	d_4	d_5	Σα (º)*
2.13	2.08	2.20	4.10	1.20	373.4

Distances (Å)*					
d_1	d_2	d_3	d_4	d_5	Σα (º)*
2.09	2.06	2.04	2.00	1.31	368.4

2	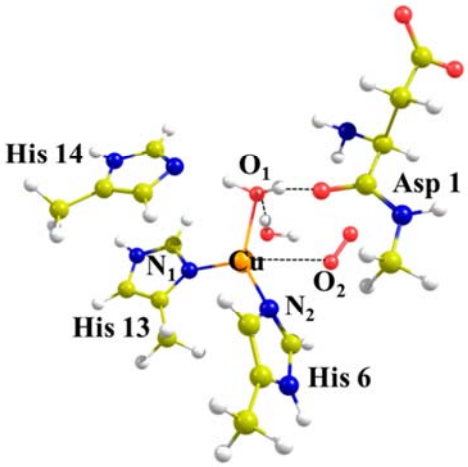	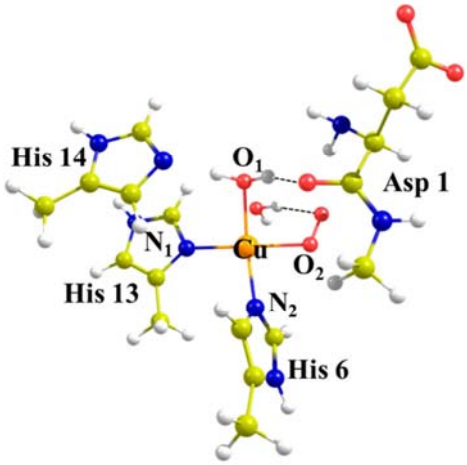

Distances (Å)*					
d_1	d_2	d_3	d_4	d_5	Σα (º)*
2.01	2.08	2.85	2.18	1.20	381.0

Distances (Å)*					
d_1	d_2	d_3	d_4	d_5	Σα (º)*
2.05	2.05	2.01	2.07	1.31	369.5

5	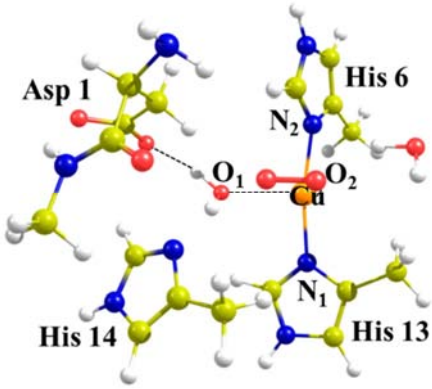	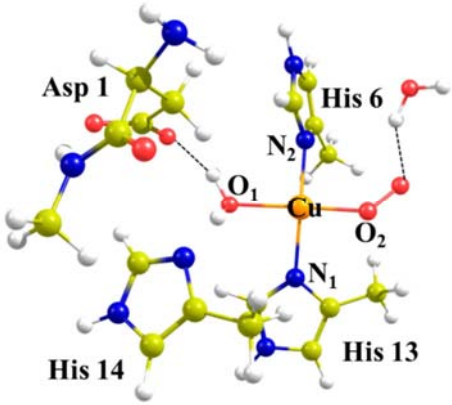

Distances (Å)*					
d_1	d_2	d_3	d_4	d_5	Σα (º)*
2.02	2.03	2.90	2.50	1.20	371.1

Distances (Å)*					
d_1	d_2	d_3	d_4	d_5	Σα (º)*
2.07	2.03	2.00	2.03	1.30	368.3

*d_1 corresponds to the distance formed by N_1-Cu; d_2: N_2-Cu; d_3: N_3-Cu; d_4: O_1-Cu; d_5: O-O of the O_2 moiety and Σα corresponds to the sum of the angles around Cu. For structure 2 and 5, d_3: O_2-Cu.

Figure B2. Cu^{+}-Aβ···O_2 and Cu^{2+}-A$\beta O_2^{-\bullet}$ structures of LA Penna's models.

	Cu^{+}-Aβ··· O_2	Cu^{2+}-Aβ$O_2^{-\bullet}$
7	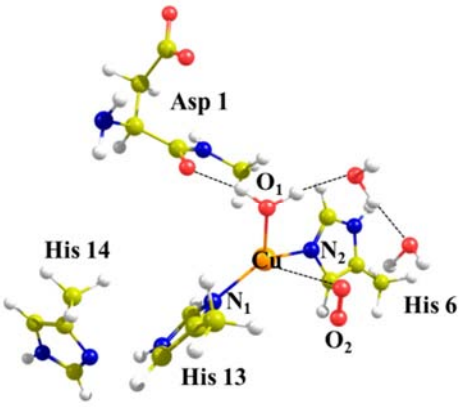	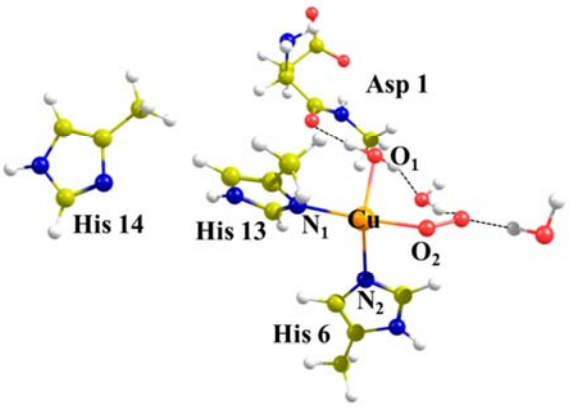
	Distances (Å)* / **Σα (º)***	**Distances (Å)*** / **Σα (º)***
	d_1 = 2.06; d_2 = 2.07; d_3 = 2.90; d_4 = 2.30; d_5 = 1.20; Σα = 400.7	d_1 = 2.04; d_2 = 2.09; d_3 = 2.02; d_4 = 2.09; d_5 = 1.30; Σα = 378.8
8	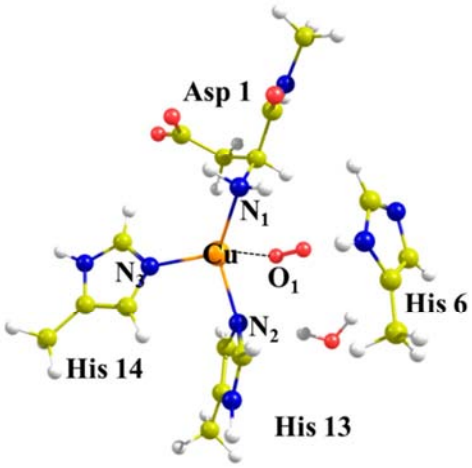	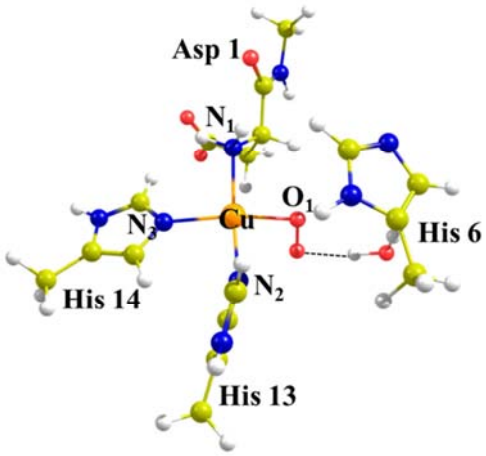
	Distances (Å)* / **Σα (º)***	**Distances (Å)*** / **Σα (º)***
	d_1 = 2.11; d_2 = 2.14; d_3 = 2.15; d_4 = 2.87; d_5 = 1.20; Σα = 390.4	d_1 = 2.07; d_2 = 2.06; d_3 = 2.08; d_4 = 2.02; d_5 = 1.31; Σα = 366.4
9	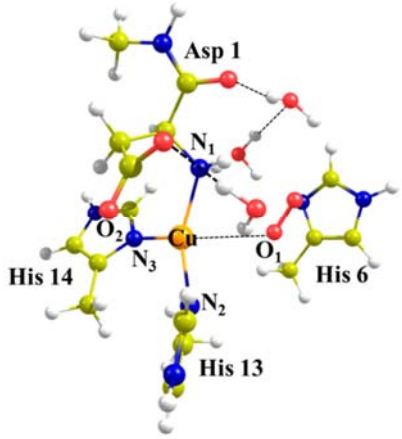	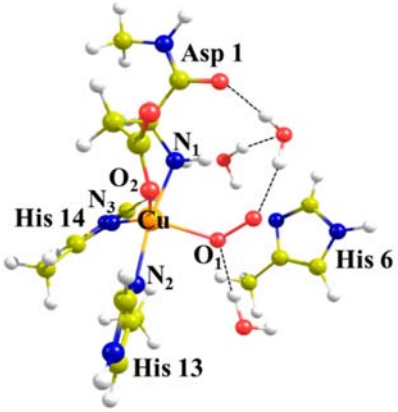
	Distances (Å)* / **Σα (º)***	**Distances (Å)*** / **Σα (º)***
	d_1 = 2.15; d_2 = 2.10; d_3 = 2.16; d_4 = 2.86; d_5 = 1.20; Σα = 375.4	d_1 = 2.06; d_2 = 2.05; d_3 = 2.11; d_4 = 2.21; d_5 = 1.32; Σα = 362.1

*d_1 corresponds to the distance formed by N_1-Cu; d_2: N_2-Cu; d_3: O_2-Cu; d_4: O_1-Cu; d_5: O-O of the O_2 moiety and Σα corresponds to the sum of the angles around Cu. For structure 8 and 9, d_3: N_3-Cu.

Figure B2. Continuation.

	Cu^{+}-Aβ··· O_2	Cu^{2+}-A$\beta O_2^{-\bullet}$
10	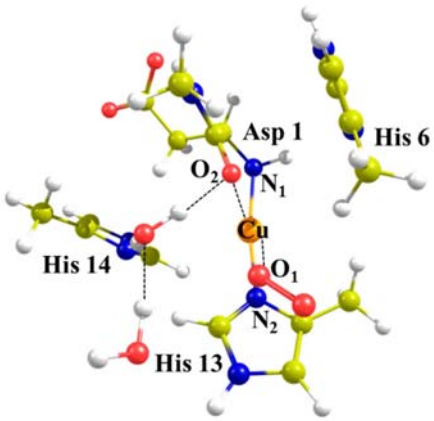	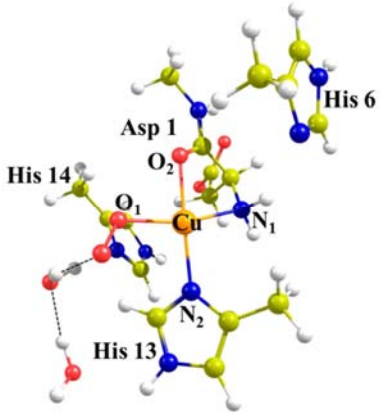
13	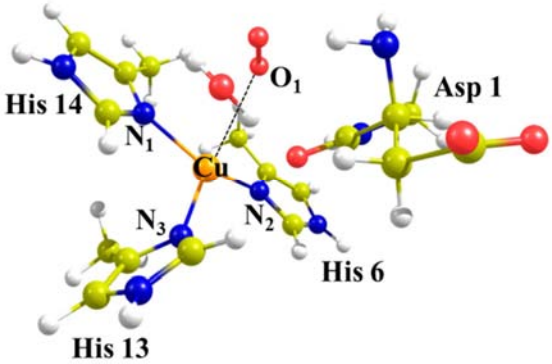	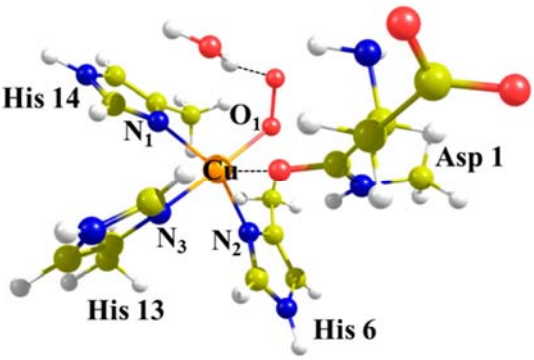
14	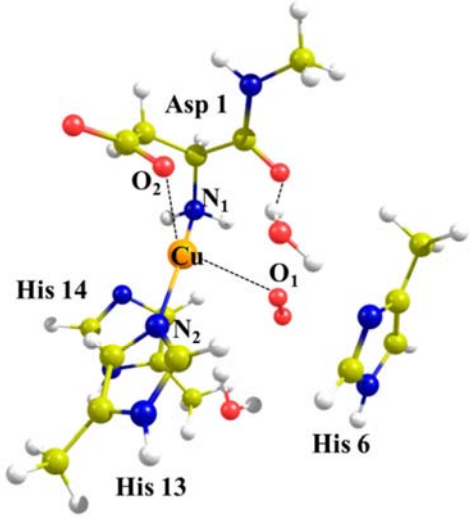	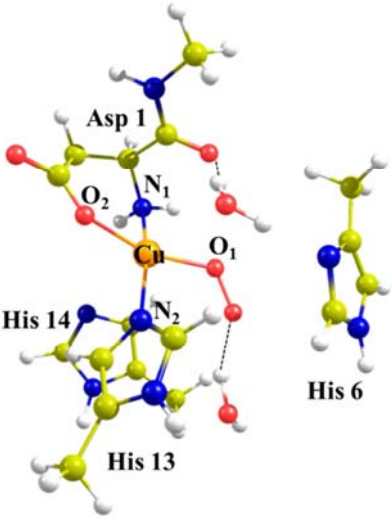

Distances (Å)*					
d_1	d_2	d_3	d_4	d_5	Σα (º)*
2.07	2.01	2.36	4.00	1.20	353.3

Distances (Å)*					
d_1	d_2	d_3	d_4	d_5	Σα (º)*
2.07	2.03	2.05	2.00	1.31	359.8

Distances (Å)*					
d_1	d_2	d_3	d_4	d_5	Σα (º)*
2.07	2.03	2.38	2.84	1.20	375.3

Distances (Å)*					
d_1	d_2	d_3	d_4	d_5	Σα (º)*
2.08	2.07	2.02	2.02	1.30	364.5

Distances (Å)*					
d_1	d_2	d_3	d_4	d_5	Σα (º)*
2.08	2.07	2.20	2.92	1.20	373.6

Distances (Å)*					
d_1	d_2	d_3	d_4	d_5	Σα (º)*
2.11	2.17	2.06	1.99	1.31	370.1

*d_1 corresponds to the distance formed by N_1-Cu; d_2: N_2-Cu; d_3: O_2-Cu; d_4: O_1-Cu; d_5: O-O of the O_2 moiety and Σα corresponds to the sum of the angles around Cu. For structure 13, d_3: N_3-Cu.

Figure B2. Continuation.

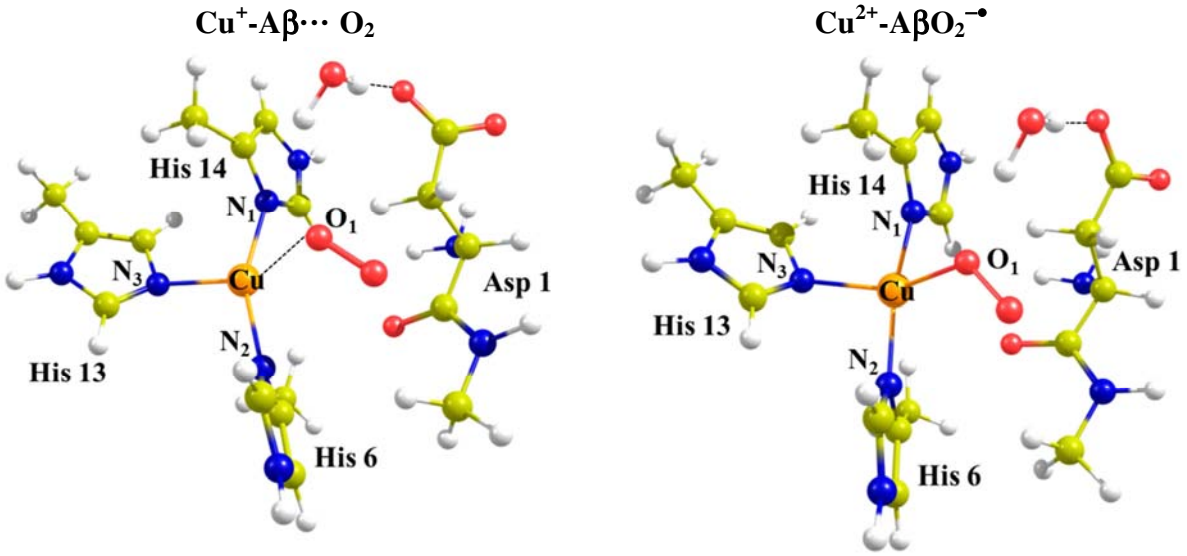

15

Distances (Å)*					
d_1	d_2	d_3	d_4	d_5	Σα (º)*
2.08	2.07	2.21	2.93	1.20	369.0

Distances (Å)*					
d_1	d_2	d_3	d_4	d_5	Σα (º)*
2.04	2.05	2.10	2.04	1.30	369.1

*d_1 corresponds to the distance formed by N_1-Cu; d_2: N_2-Cu; d_3: N_3-Cu; d_4: O_1-Cu; d_5: O-O of the O_2 moiety and Σα corresponds to the sum of the angles around Cu.

Figure B2. Continuation.

APPENDIX C. FURTHER DETAILS ON COPPER CHELATES

Further details on the geometric parameters of Cu-chelate complexes.

C.1. Cu^{2+}-HAH

Structure 1

δδ

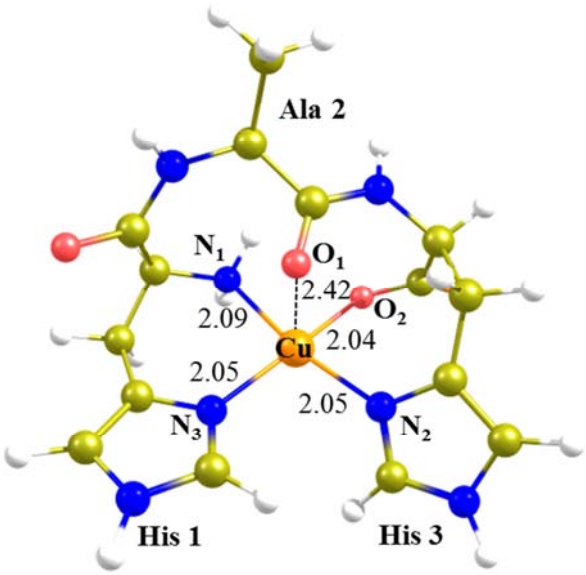

N_1-Cu-N_2: 169.7, **O_1-Cu-N_3:** 172.1
Σα: 360.9

δε

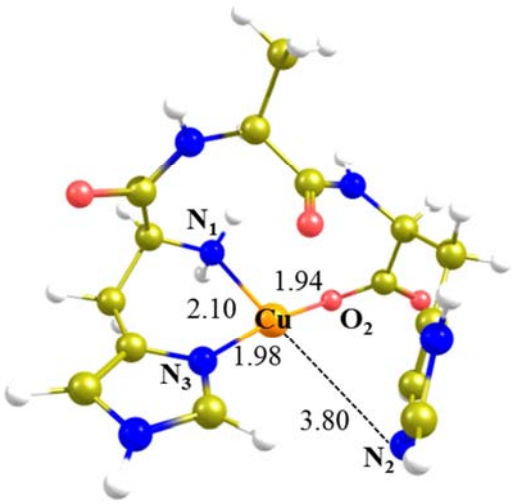

N_1-Cu-N_2: 166.2, **O_1-Cu-N_3:** 170.4
Σα: 361.6

εδ

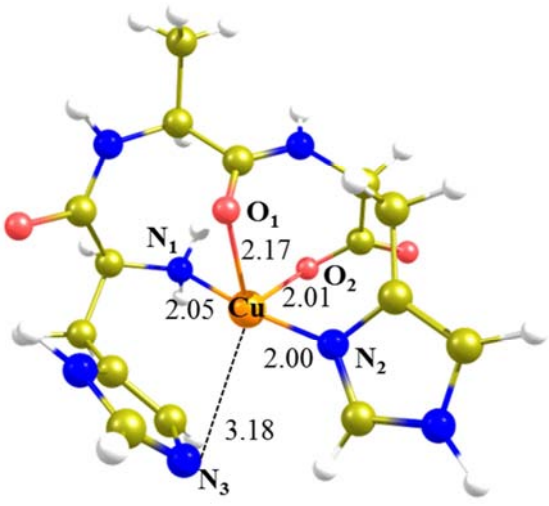

N_1-Cu-N_2: 173.6, **O_2-Cu-N_3:** 152.3
Σα: 360.8

εε

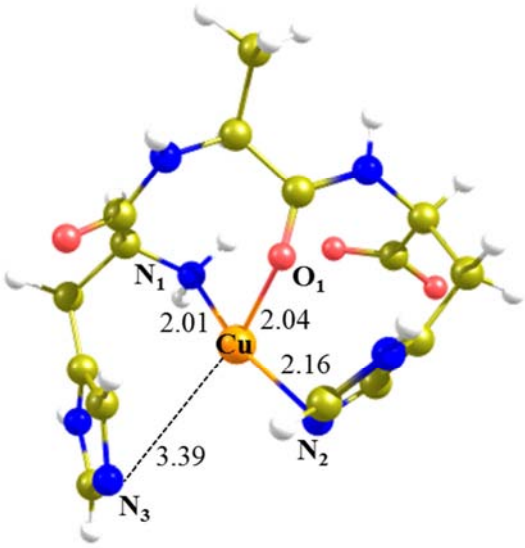

N_1-Cu-N_2: 164.8, **O_1-Cu-N_3:** 136.7
Σα: 369.3

Figure C.1. Geometric details of all the proposed structures of Cu^{2+}-HAH complexes considering all the combination of the histidine nitrogen coordination. Distances are in angstroms and angles in degrees. Σα means the sum of all the angles around Cu.

Structure 2

δ

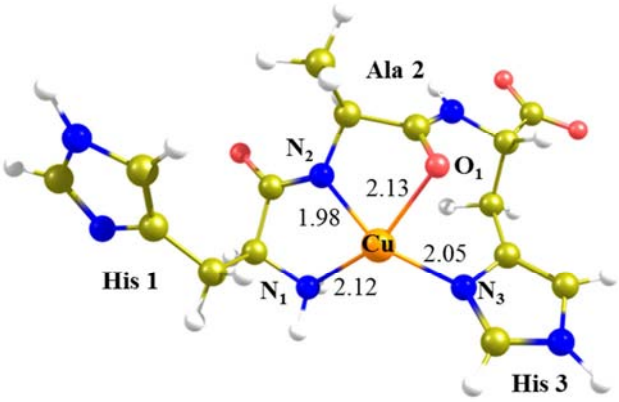

N_1-Cu-O_1: 159.2, **N_2-Cu-N_3:** 152.8
Σα: 358.5

ε

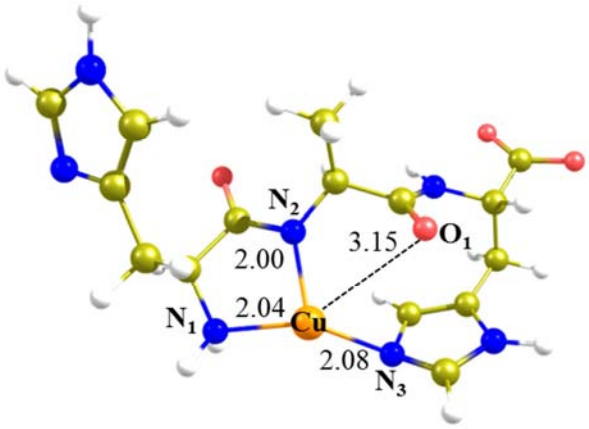

N_1-Cu-O_1: 145.6, **N_2-Cu-N_3:** 118.3
Σα: 360.7

Structure 3

δ

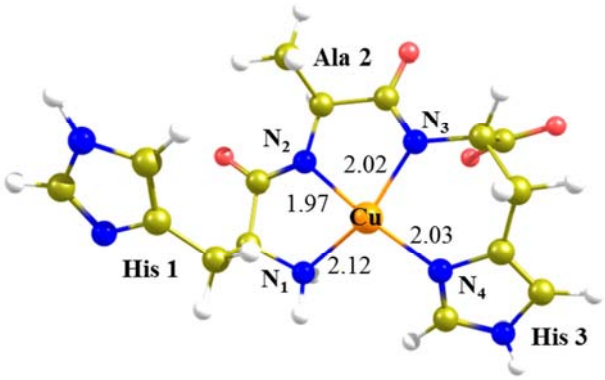

N_1-Cu-N_3: 160.6, **N_2-Cu-N_4:** 171.3
Σα: 358.5

ε

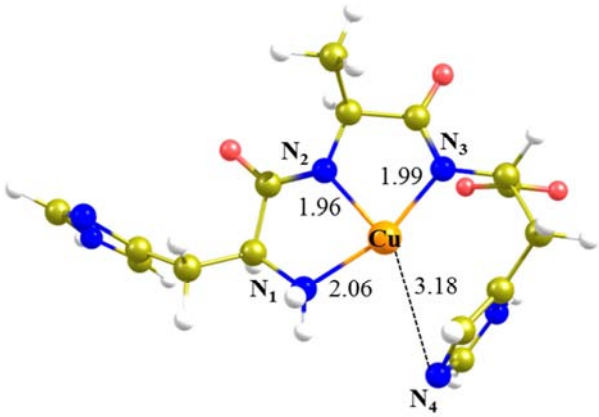

N_1-Cu-N_3: 163.3, **N_2-Cu-N_4:** 157.0
Σα: 360.0

Figure C1. Continuation.

Structure 4

δδ

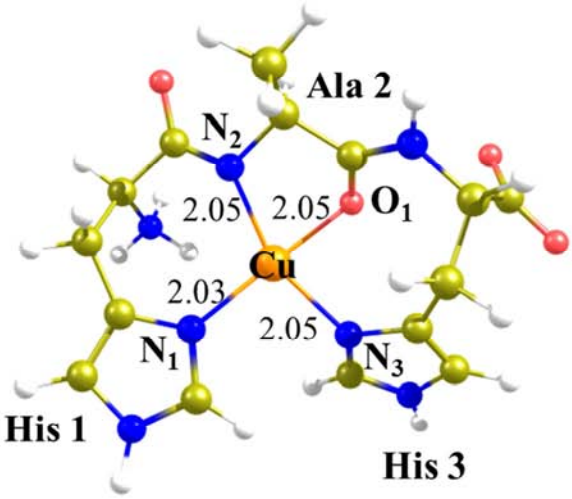

N_1-Cu-O_1: 178.3, **N_2-Cu-N_3:** 157.0
Σα: 359.8

δε

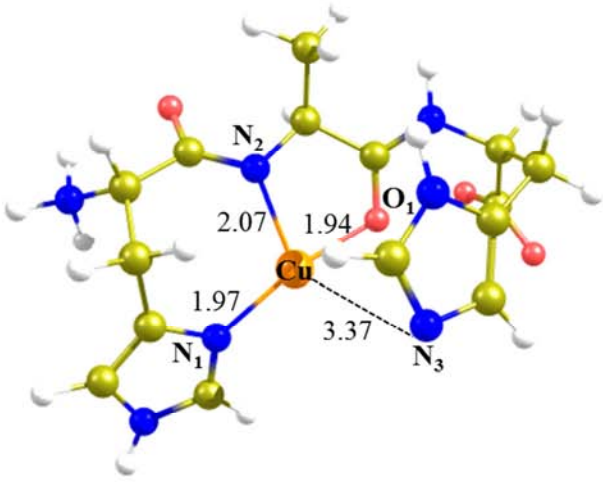

N_1-Cu-O_1: 166.8, **N_2-Cu-N_3:** 111.5
Σα: 359.8

εδ

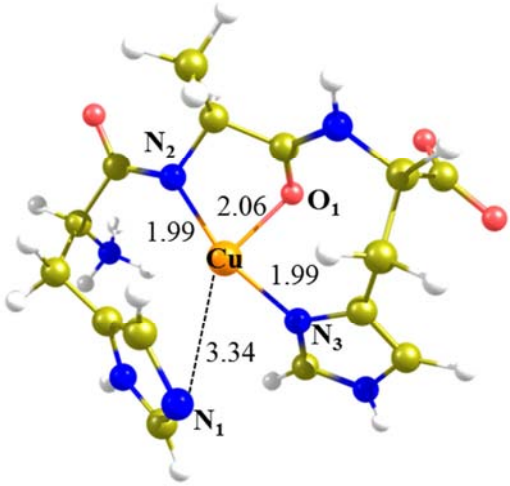

N_1-Cu-O_1: 143.4, **N_2-Cu-N_3:** 162.1
Σα: 352.9

εε

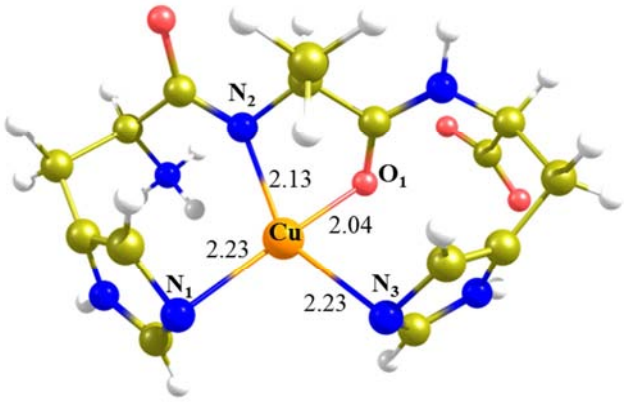

N_1-Cu-O_1: 177.7, **N_2-Cu-N_3:** 144.9
Σα: 360.7

Figure C1. Continuation.

C.2. Cu^{2+}-HWH

Structure 3.1

Cu^{2+} specie

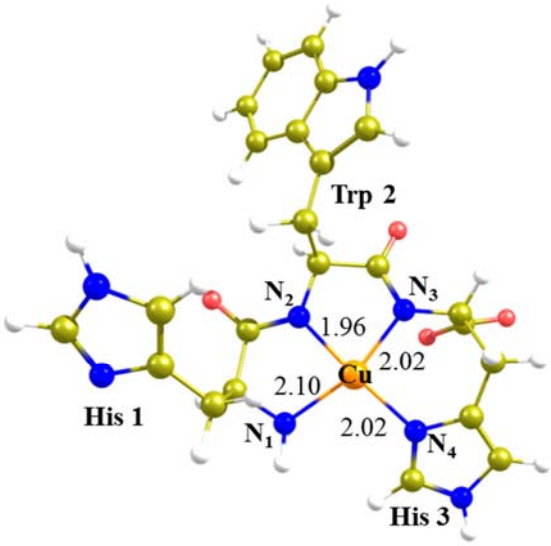

N_1-Cu-N_3: 160.0, **N_2-Cu-N_4:** 173.8
Σα: 359.0

Cu^{+} specie

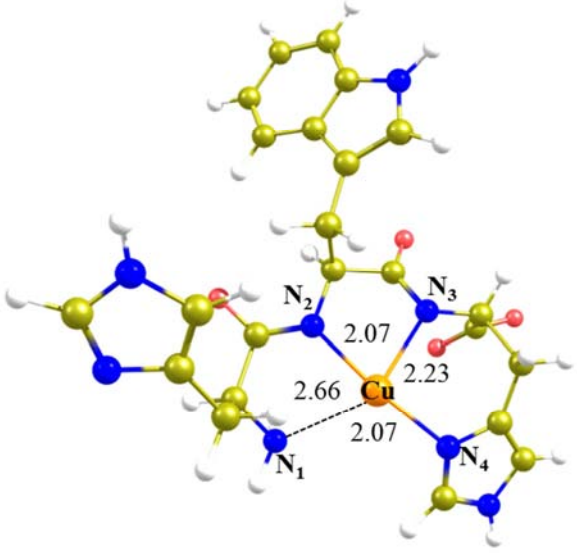

N_2-Cu-N_3: 78.5, **N_3-Cu-N_4:** 93.3
N_4-Cu-N_2: 167.7

Structure 3.2

Cu^{2+} specie

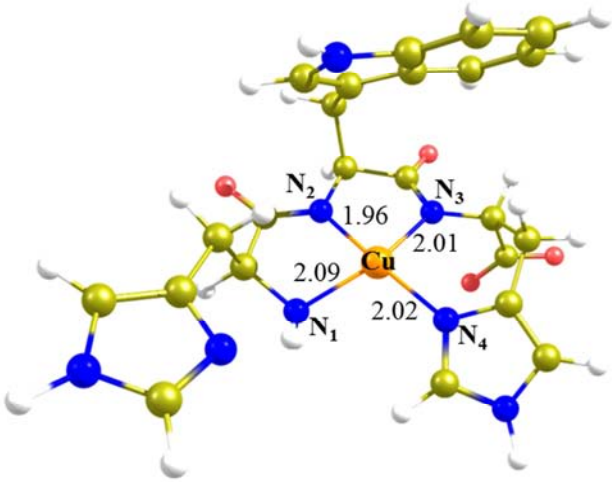

N_1-Cu-N_3: 161.2, **N_2-Cu-N_4:** 175.9
Σα: 358.5

Cu^{+} specie

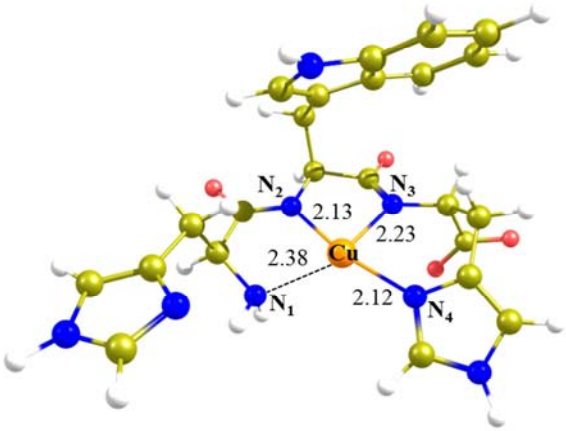

N_2-Cu-N_3: 76.0, **N_3-Cu-N_4:** 91.1
N_4-Cu-N_2: 167.1

Figure C2. Geometric parameters for different configurations of Cu-HWH complex. Distances are in angstroms and angles in degrees.

Structure 3.3

Cu^{2+} specie

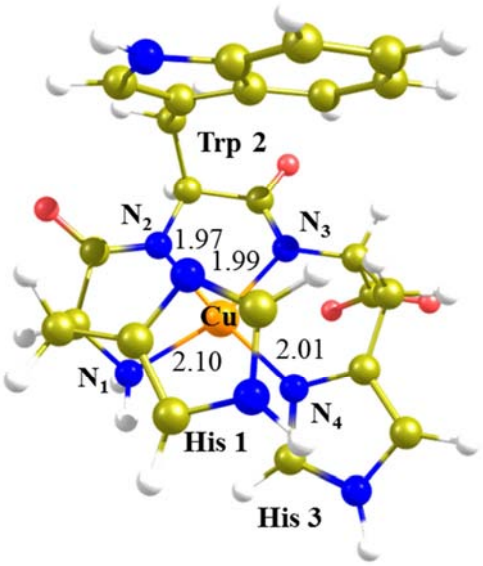

N_1-Cu-N_3: 162.1, **N_2-Cu-N_4:** 170.5
Σα: 360.6

Cu^{+} specie

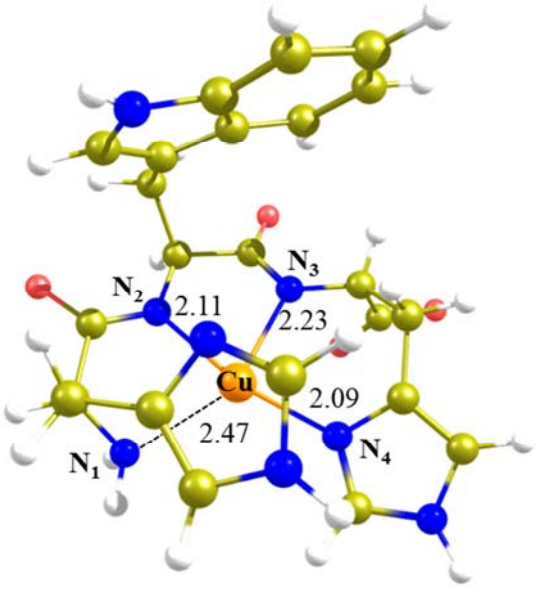

N_2-Cu-N_3: 75.8, **N_3-Cu-N_4:** 91.4
N_4-Cu-N_2: 167.1

Structure 3.4

Cu^{2+} specie

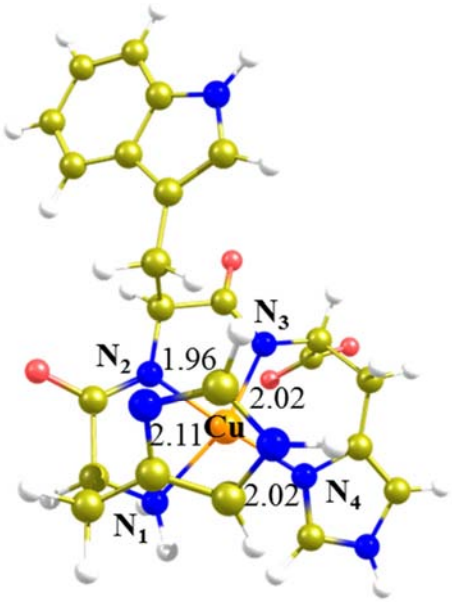

N_1-Cu-N_3: 160.5, **N_2-Cu-N_4:** 176.5
Σα: 359.9

Cu^{+} specie

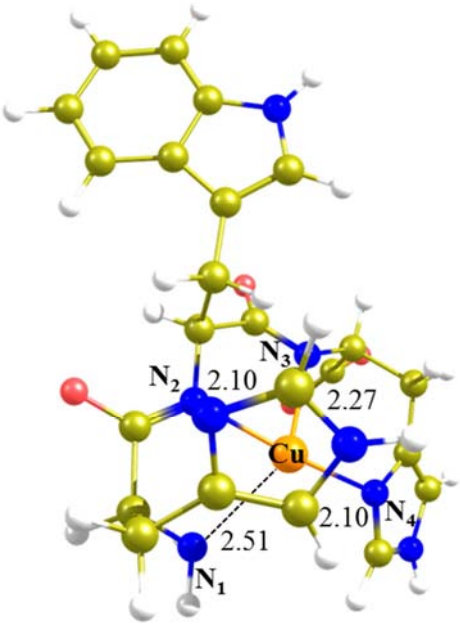

N_2-Cu-N_3: 77.4, **N_3-Cu-N_4:** 91.4
N_4-Cu-N_2: 163.9

Figure C2. Continuation.

Structure 3.2

$Cu^{3+\,(T)}$ specie | **$Cu^{3+\,(S)}$ specie**

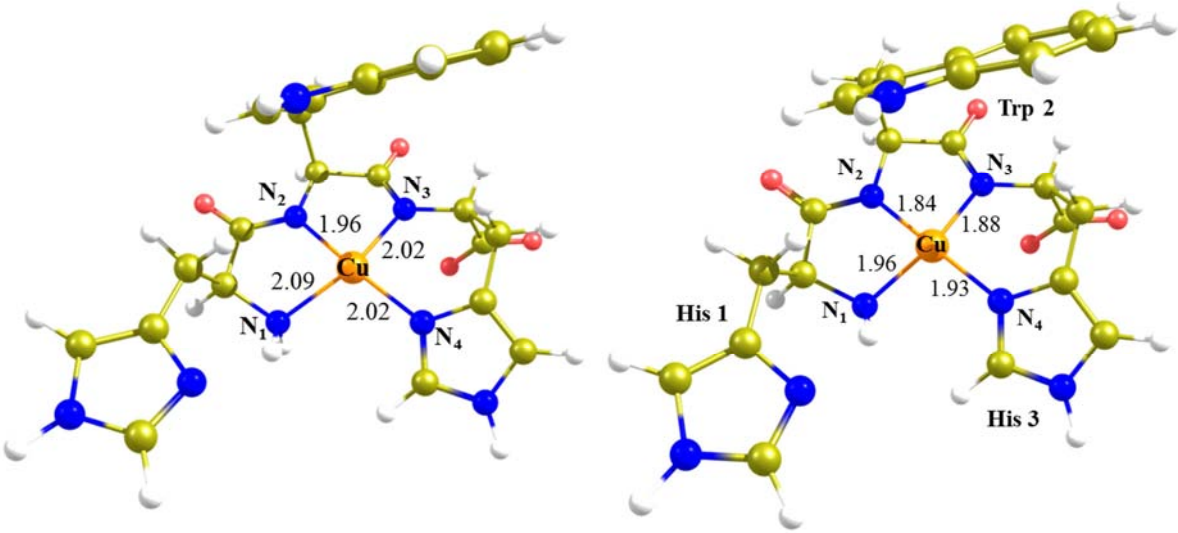

N_1-Cu-N_3: 159.9, **N_2-Cu-N_4:** 174.8
Σα: 359.4

N_1-Cu-N_3: 167.4, **N_2-Cu-N_4:** 178.4
Σα: 360.0

Figure C3. Geometric parameters for the different states of Cu^{3+}-HWH complex. Distances are in angstroms and angles in degrees.

C.3. Cu^{2+}-Ac-HWH

Structure 6 (HAH-Ac)

Cu^{2+} specie | **Cu^{+} specie**

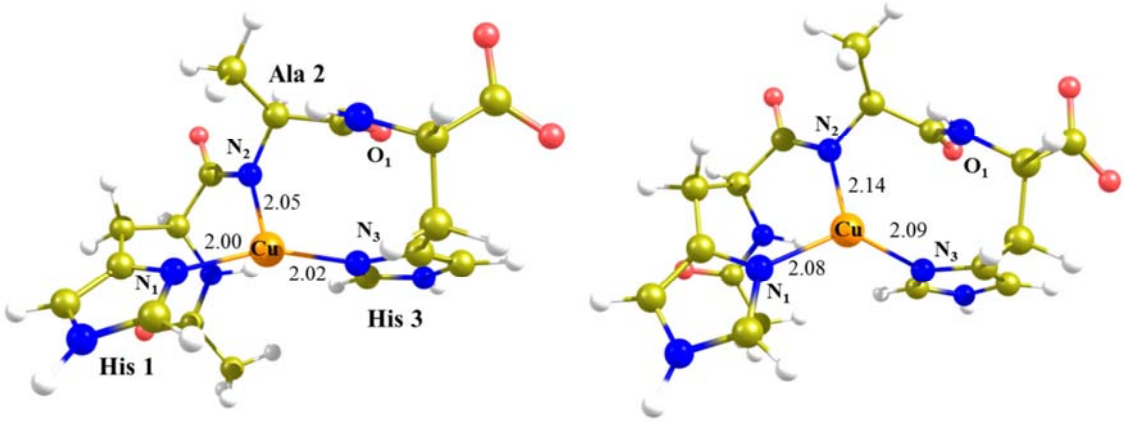

N_1-Cu-N_2: 99.9, **N_2-Cu-N_3:** 100.6
N_3-Cu-N_1: 158.1

N_1-Cu-N_2: 109.8, **N_2-Cu-N_3:** 111.4
N_3-Cu-N_1: 132.5

Figure C4. Geometric parameters for the $Cu^{2+/+}$-Ac-HAH complexes. Distances are in angstroms and angles in degrees.

C.4. Cu^{2+}-HHW

Cu^{2+} specie **Cu^{+} specie**

Structure $9_{\delta\delta}$

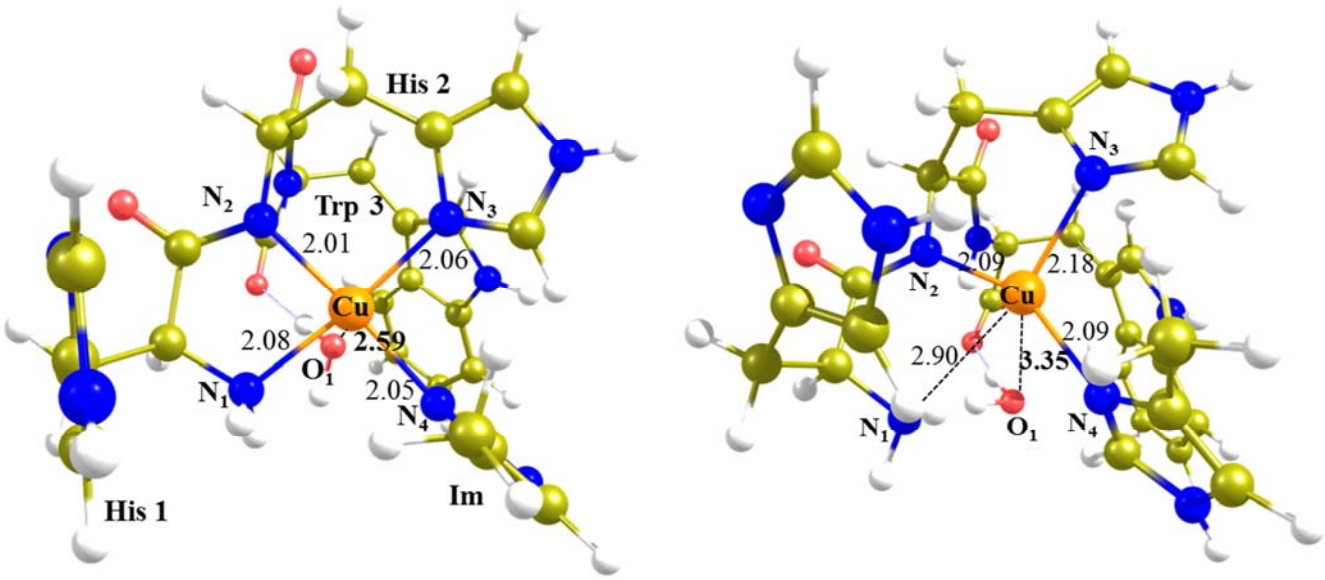

N_1-Cu-N_3: 166.0, **N_2-Cu-N_4:** 176.5
Σ*α*: 360.3

N_2-Cu-N_3: 101.0, **N_3-Cu-N_4:** 107.0
N_4-Cu-N_2: 151.9

Figure C5. Geometric details of Cu-HHW complex with methyl imidazole as fourth ligand and water molecule in apical position. Distances are in angstroms and angles in degrees.